

A Numerical Study of Entropy Generation in Nanofluid Flow in Different Flow Geometries



A THESIS SUBMITTED TO THE UNIVERSITY OF KWAZULU-NATAL
FOR THE DEGREE OF DOCTOR OF PHILOSOPHY
IN THE COLLEGE OF AGRICULTURE, ENGINEERING & SCIENCE

By

Zachariah Mbugua Mburu

School of Mathematics, Statistics and Computer Science

June 2021

Contents

Abstract	iii
Declaration 1: Plagiarism	iv
Declaration 2: Publications	v
Acknowledgment	vi
Dedication	vii
1 Introduction and motivation	1
1.1 Literature on entropy generation	2
1.2 Selected studies on Newtonian and non-Newtonian fluids	4
1.3 The thermophysical properties of nanofluids	6
1.4 The rate of heat and mass transfer in nanofluids	8
1.5 The effect of thermal radiation and a magnetic field	10
1.6 The effects of double-diffusive convection on fluid properties	13
1.7 Numerical methods of solution	16
1.7.1 The bivariate spectral quasilinearization method	17
1.7.2 The overlapping grid spectral collocation method	18
1.8 Thesis objectives	18
2 A numerical study of entropy generation in Oldroyd-B nanofluid flow past a Riga plate	21
3 Numerical study on combined thermal radiation and magnetic field effects on entropy generation in unsteady fluid flow past an inclined cylinder	44
4 Impact of irreversibility ratio and entropy generation on three-dimensional Oldroyd- B fluid flow with relaxation-retardation viscous dissipation	66

5	Entropy generation in double-diffusive convective magnetic nanofluid flow in the stagnation region of a rotating sphere with viscous dissipation	84
6	A numerical study of the fluid velocity, heat, and mass transfer in an unsteady nanofluid flow past parallel porous plates	110
7	Conclusion	137
	References	140


Abstract

This thesis is concerned with the mathematical modelling and numerical solution of equations for boundary layer flows in different geometries with convective and slip boundary conditions. We investigate entropy generation, heat and mass transport mechanisms in non-Newtonian fluids by determining the influence of important physical and chemical parameters on nanofluid flows in various flow geometries, namely, an Oldroyd-B nanofluid flow past a Riga plate; the combined thermal radiation and magnetic field effects on entropy generation in unsteady fluid flow in an inclined cylinder; the impact of irreversibility ratio and entropy generation on a three-dimensional Oldroyd-B fluid flow along a bidirectional stretching surface; entropy generation in a double-diffusive convective nanofluid flow in the stagnation region of a spinning sphere with viscous dissipation and a study of the fluid velocity, heat and mass transfer in an unsteady nanofluid flow past parallel porous plates. We assumed that the nanofluids are electrically conducting and that the velocity slip and shear stress at the boundary have a linear relationship. We also consider different boundary conditions for all the flow models. The study further analyzes and quantifies the influence of each source of irreversibility on the overall entropy generation.

The transport equations are solved using two recent numerical methods, the overlapping grid spectral collocation method and the bivariate spectral quasilinearization method, first to determine which of these methods is the most accurate, and secondly to authenticate the numerical accuracy of the results. Further, we determine the skin friction coefficient and the changes in the heat and mass transfer coefficients with various system parameters. The results show, *inter alia* that reducing the heat transfer coefficient, the particle Brownian motion parameter, chemical reaction parameter, Brinkman number, thermophoresis parameter and the Hartman number all lead individually to a reduction in entropy generation. The overlapping grid spectral collocation method gives better computational accuracy and converge faster than the bivariate spectral quasilinearization method. The fluid flow problems have engineering and industrial applications, particularly in the design of cooling systems and in aerodynamics.

Declaration 1: Plagiarism

I, Zachariah Mbugua Mburu, declare that the research reported in this thesis, except where otherwise indicated, is my original research. This thesis has not been submitted for any other degree or examination at any other university. This thesis does not contain other persons' pictures, graphs, or other information unless expressly acknowledged as being sourced from those persons. This thesis does not contain other persons' writing unless expressly acknowledged as being sourced from them. Where other sources have been quoted, the words have been rewritten, while attributing the general information to the authors as referenced, or, where their exact words have been used, then the quotation appears in quotation marks and has been referenced. This thesis does not contain information, graphics or tables copied and pasted from the internet unless specifically acknowledged. The sources are detailed in the thesis and the reference sections.



Zachariah Mbugua Mburu

20/06/2021

Date



Prof. P. Sibanda

21-June-2021

Date

Declaration 2: Publications

1. **Z. M. Mburu**, S. Mondal, P. Sibanda, R.P. Sharma. A numerical study of entropy generation in Oldroyd-B nanofluid flow past a Riga plate. *Journal of Thermal Engineering*, 7 (4): 845-866, 2021, <https://DOI:10.18186/thermal.930653>.
2. **Z. M. Mburu**, S. Mondal, and P. Sibanda. Numerical study on combined thermal radiation and magnetic field effects on entropy generation in unsteady fluid flow past an inclined cylinder. *Journal of Computational Design and Engineering*, 8(1):149–169, 2021, <https://doi.org/10.1093/jcde/qwaa068>.
3. **Z. M. Mburu**, M.K.Nayak, S. Mondal, P. Sibanda. Impact of irreversibility ratio and entropy generation on three-dimensional Oldroyd-B fluid flow with relaxation–retardation viscous dissipation. *Indian Journal of Physics*, 2(1):1–17, 2021, <https://doi.org/10.1007/s12648-020-01950-w>.
4. M. Almakki, H. Mondal, **Z. M. Mburu**, P. Sibanda. Entropy generation in double diffusive convective magnetic nanofluid flow in the stagnation region of a rotating sphere with viscous dissipation. *Theoretical and Computational Fluid Dynamics*, TCFD-D-20-00065, under review.
5. **Z. M. Mburu**, S. Mondal, P. Sibanda. The numerical study of the fluid velocity, heat and mass transfer in an unsteady nanofluid flow past parallel porous plates. *Nanoscience & Nanotechnology-Asia*, BMS-NNA-2021-20, under review.

In all these publications, I formulated the flow problem, obtained the numerical solutions and drafted the manuscripts.



20/06/2021

Zachariah Mbugua Mburu

Date

Acknowledgment

First and foremost, I thank God for giving me the strength, knowledge, ability and opportunity to undertake this research study and complete it satisfactorily. Without His blessings, this achievement would not have been possible.

I would like to sincerely thank my supervisor, Prof. Precious Sibanda, from the bottom of my heart. His financial support, laptop purchase, valuable advice, guidance and comprehensive insights in this field have made this an inspiring experience for me. Special thanks to Dr. Sabyasachi Mondal, Prof. Henry Mwambi, Prof. Stephen Mutula, Dr. Felix Mutua, Dr. Mohammed Almakki, Dr. Elphas Okango, Mr. Francis Thuo and Dr. Ibukun Oyelakin for their valuable insights and support in making this work successful. Special thanks to the editor Mrs. Sheelagh Halstead.

Special thanks go to the administrators in the School of Mathematics, Statistics and Computer science, University of KwaZulu-Natal, and all the colleagues with whom I shared the office, for their incredible support throughout my Ph.D journey.

I sincerely thank my entire family for their love and support. My sincere thanks to my son John Peters Mbugua for his lovely character that made the home a friendly and hospitable atmosphere for studying.

Finally, I would like to sincerely thank my lovely wife, Sarah Atieno Ogutu, who has throughout gave unconditional love and endless support. Her daily concerns and encouragement are the reasons for every single success I have had thus far. You have been amazing, and I will now clear all the dishes as promised.

Dedication

This thesis is dedicated to my dear wife Sarah A. Ogutu, son John P. Mbugua and the entire Mburu family.

Chapter 1

Introduction and motivation

Over the past few decades, there has been an overwhelming interest in the study of entropy generation in non-Newtonian flows due to their many applications in industries such as plastic manufacturing, metal cooling, food processing, aerodynamics and medicine [1]. Nanofluids fall under the broad category of non-Newtonian fluids. They exhibit stability, minimal clogging and high heat flux capabilities when used in industrial applications [2]. However, despite their wide applications, the physics of the flow of such fluids is not well understood compared to the rheology of Newtonian fluids. This study determines entropy generation in non-Newtonian fluid flows in different geometries with convective and velocity slip boundary conditions. The Oldroyd-B fluid [3], nanofluids, and magneto fluids are the fluids of interest. We analyze the influence of variable physical and chemical parameters on entropy production and fluid properties.

Numerous studies on entropy generation, and heat and mass transfer in non-Newtonian fluids have been reported in the literature, see for instance [4–8]. These studies considered entropy production in various flow geometries, with varying boundary conditions using different solution techniques for the mathematical models. As Dalir et al.[9] pointed out, entropy generation due to non-Newtonian fluid motion has applications and consequences in processing such as blade coating, dyeing of textiles, electronic cooling and could also explain physical phenomenon such as wear and tear in moving machine parts. Other consequential examples of heat and mass flux occur in catalytic reactors, MHD heat pumps, crude oil extraction and chemical reaction chambers as reported by Lee et al.[10]. Here we suggest new solution methods, that include, the overlapping grid spectral collocation and the bivariate spectral quasilinearization methods that have not yet been tested extensively in the literature

for systems of highly nonlinear differential equations that describe boundary layer flow problems in various geometries. Through the solution of various flow model equations, we aim to show that these chosen methods are accurate, robust and provide rapid convergence.

1.1 Literature on entropy generation

The research on entropy generation due to nanofluid flow has recently become a priority concern in the study of thermodynamic systems for applications such as radiator coils, steam turbines, turbo machines, electronic cooling, porous materials and combustion [11]. In the last few decades, there has been an increased desire for reliable and sustainable systems that make optimal use of scarce energy resources. The optimization of entropy generation has then been found to be more appropriate and reliable than the traditional energy balance approaches in utilizing the scarce resources. More so, the study of entropy generation allows major causes of inefficiencies to be identified and so opens up the possibility for the design of more effective and efficient models of thermodynamic systems. Further, because entropy generation optimization is based on fundamental thermodynamic principles, it can, in principle, be used for any type of energy conversion system [12]. These desirable attributes have made entropy production optimization a leading thermodynamic tool for designing and optimizing systems.

The optimization of entropy generation in any thermodynamic system may not be successfully achieved without considering the limitations posed by the second law of thermodynamics. The law states that all real processes are irreversible [13]. As entropy generation is a measure of irreversibility associated with processes, the quality and quantity of energy produced is always reduced [14]. Accordingly, in a thermodynamic system involving fluid motion, preserving the energy produced implies a reduction of the amount of entropy produced. It is essential to analyse the generation of entropy in different flow geometries and boundary conditions for application in a wide range of processes, including electronic cooling, heat exchangers, thermal insulation engineering and water flow in geothermal turbines. During the design of thermal and electrical devices, engineers need to be concerned with irreversible processes that decrease the efficiency of the system [15]. It is therefore important to consider both the

geometry of the system and the thermo-physical properties that tend to reduce entropy production and optimize the system efficiency.

A number of investigations of entropy production in non-Newtonian flows in different domains have been reported in the literature. Entropy production in a nanofluid flow due to forced convective currents was considered by Abolbashi et al. [16]. They found that entropy generation was directly correlated to frictional forces between the cylinder walls and the liquid layers. Siavashi et al. [17] studied entropy production in nanofluid flow in a horizontal porous pipe using a two-phase model. They reported that increased permeability generated higher entropy than low permeability. In simple terms, higher permeability increases the ease of flow through the porous pipe, which in turn increases the flow velocity, resulting in increased frictional forces which leads to a higher rate of entropy generation. Butt et al. [18] extended the study by considering entropy generated in a hydrodynamic flow past a vertical porous surface. Their results differed from those of Siavashi et al. [17]. Notably, they found the opposite effect for the permeability parameter, with a reduction in the rate of entropy production occurring with an increment in permeability. They showed that the velocity of the upward flow reduced, leading to small frictional forces between the plate's wall and the fluid layer. This minimized the rate of entropy generation. The difference could also be ascribed to the alteration in the geometry of the flow and varying the boundary constraints.

The study of the combined influence of convective forces and thermal radiation on entropy production is important in fluid flow through channels with permeable walls as pointed out by Makinde and Egunjobi [19]. Chinyoka and Makinde [20] modelled the effect of thermal radiation on entropy production in an unsteady magneto fluid flow with convective cooling and Navier slip conditions. Qasim et al. [21] researched the impact of thermal radiation on entropy production in a methanol-aluminium oxide nanofluid flowing in a wavy channel. These studies indicated that increased thermal radiation contributed significantly to entropy production in a fluid flow model. Additional contributions to the study of entropy production can also be found in [22–26].

From the literature, the numerical simulations of entropy production due to nanofluid flow in

different geometries, with convective and boundary velocity slip conditions using the overlapping grid spectral collocation and the bivariate spectral quasilinearization methods has not received adequate attention to date. The current study seeks to enhance our understanding of such problems. We adopt modelling techniques to investigate entropy generation mechanisms in boundary layer problems and use computationally efficient and accurate spectral methods to determine the influence of a variety of physical and chemical parameters on the entropy production.

1.2 Selected studies on Newtonian and non-Newtonian fluids

The investigation of Newtonian and non-Newtonian fluid flow problems is essential in relation to entropy production, heat and mass transport in commercial and industrial processes. A Newtonian fluid is one whose viscous stress is linearly correlated to the rate of deformation over time [27]. Examples of Newtonian fluids include water, crude oil and air. Newtonian fluids are used primarily to reduce friction in slider bearings and cooling processes [28].

On the other hand, a non-Newtonian fluid does not follow Newton's law of viscosity [29]. They exhibit non-isothermal behaviour and their viscosity is dependent on the applied shear stress. Some examples of non-Newtonian fluids considered in this study are the Oldroyd-B fluid, magneto fluids and nanofluids. They are of great interest to researchers because of their wide variety of applications in science and engineering. They play a significant role in, for instance, food processing, chemical engineering, polymer mixing and medicinal product production. The complexity of the constitutive equations that describe these non-Newtonian fluids presents challenges to understanding their behaviour [30]

The rheological characteristics of non-Newtonian fluids were researched by Hojjat et al. [31]. They reported that such fluids exhibit pseudoplastic behaviour and their rheological characteristics are functions of temperature and particle concentration. Heris et al. [32] extended the study by investigating the convective heat transport in a non-Newtonian flow in a circular tube with a constant wall temperature. They reported that increased advection forces

steered an increase in the rate of heat transport. In a theoretical study using the finite difference approach to solve the transport equations, Behaabadi et al. [33] studied the problem of convective heat transport in non-Newtonian flow in a circular pipe. They showed that the viscosity and elastic modulus of the fluid decreased significantly with an increase in the temperature suggesting that the non-Newtonian rheological behaviour is directly related to the temperature change. They also found that the temperature-dependence of the viscosity of the fluid had to be taken into account for accurate analysis of thermal physical properties. An analysis of the rheological behaviour of a non-Newtonian hybrid nano-coolant was reported by Eshgarf and Afrand [34], who found that the nano-coolant exhibited pseudoplastic behaviour, with power law index less than unity. The viscosity of the fluid was found to increase with the rise in the concentration and reduce with temperature. However, assuming convective boundary conditions and applying the finite difference technique, Rostami et al. [35] obtained contrary results for the temperature distribution. This was explained as due to the difference in the accuracy of the method of solution and the different boundary domains. Khan et al. [36] studied entropy production in a steady Darcy-Forchheimer non-Newtonian flow with a chemical reaction, using the Runge-Kutta technique to solve the transport equations. They showed that increasing the Darcy and electric field parameters suppressed the flow velocity and increased the entropy production rate. In their study, Riaz et al. [37] found that the Williamson flow model could be reduced to a Newtonian model by taking the Weissenberg number as the ratio of elastic force to viscous force being less than one. Wang et al. [38] studied non-Newtonian radiative flow with entropy generation and a binary chemical reaction.

Heat transport in non-Newtonian and Newtonian fluids with velocity slip boundary conditions was analyzed by Shojaeian and Kosar [39]. They showed that, in the non-Newtonian fluid, entropy generation is strongly influenced by the magnetic field and the Brinkman number, whereas the Newtonian fluid was affected only by a change in the boundary conditions. The power-law index and Bejan number were found to suppress entropy production in both cases. Waqas [40] used the finite element approach to investigate the rate of heat conveyance in a ferromagnetic non-Newtonian fluid flow, with heterogeneous chemical reaction. For a non-Newtonian fluid flow in a cylinder with a porous surface, Yoshino et al. [41] applied the

Boltzmann technique in solving the system of differential equations. They reported that the approach could be used for optimization applications involving non-Newtonian fluid models with shear thickening and pseudoplastic characteristics although it had a small rate of convergence. We shall focus in this thesis on determining the rate of entropy generation in non-Newtonian fluids varying velocity slip boundary domains. This of great significance because of its numerous applications in science and engineering.

1.3 The thermophysical properties of nanofluids

In this study, we investigate the flow of nanofluids with binary reactions. The term nanofluid refers to nanometer-sized solid particles suspended in a base fluid. The base fluids are normally oil, water or ethylene glycol. The nanoparticles consist of stable metals, metal oxides or carbon nanotubes [42]. The nanoparticles have been shown, experimentally, to enhance heat transfer of the base fluids. The low heat transport properties of the base fluids can be enhanced by as much as 70% with 1% suspended nanoparticles by volume [43]. Nanofluids are used in several engineering and industrial applications, including, thermal insulation, floor heating, nuclear reactors and cooling processes.

The importance of nanofluids has led to an increasing body of literary work on the convective heat conveyance of nanofluids, and the associated flow problems related to entropy production. Choi [44] initiated the study of the thermophysical properties of nanofluids. He discovered that adding nanoparticles to a base fluid increased the thermal conductivity of the fluid and thus improved the rate of heat transport . Other benefits of adding nanoparticles to base fluids include being able to reduce the overall size of the heat transfer system, minimize clogging, and improve micro-channel cooling.

There have been numerous theoretical studies on nanofluids. One such study by Saha and Paul [45] used single and multi-phase models to investigate heat and mass transfer, and the entropy production in the flow of a titanium oxide-water fluid in a pipe. They reported that the nanofluid had a larger heat transfer coefficient in the multi-phase model than in a single phase

model. Although they noted that there was no optimal Reynolds number that would minimize entropy production, they found, however, that varying the boundary conditions would help in obtaining optimal results. Domairry and Hatami [46] applied the differential transformation technique with a Padé approximation to solve the equations for a copper-water fluid flowing along parallel plates. They showed that heat transfer in the nanofluid was accelerated with a rise in the nanoparticle volume fraction, the Eckert number and the squeeze number. However, the Pade approximation method gave poor convergence results. To address this, Hatami and Ganji [47] used the Runge–Kutta method to solve the equations, when investigating fluid flow through a permeable medium between two cylinders. They considered the fluid viscosity to be a function of the temperature. However, they still faced the challenge of the viscoelasticity of the fluid leading to intractable higher order nonlinear differential equations.

MHD nanofluid flow in parallel plates was investigated by Derakhshan et al. [48]. They determined through numerical simulations the effect of thermophoresis and the Brownian motion on the heat and mass transport in the nanofluid. They established that heat transfer was reduced with an increase in the thermophoresis and Brownian motion parameters. Nevertheless, such results have a poor theoretical basis. The rapidly moving nanoparticles have greater kinetic energy resulting in increased collisions, which in turn would lead to an increased rate of heat and mass transport. Waqas et al. [49] applied the shooting approach to solve the nonlinear governing equations arising from the Buongiorno model [50] for a thermally radiating nanofluid flow in a magnetic field with heat generation. They reported that the flow velocity dropped with higher magnetic parameter value, which they could explain in terms of an increase in the Lorentz force, thereby increasing the shear stress that slows the fluid motion. Li and Kleinstreuer [51] studied nanofluid flow and entropy generation using a computer simulated model. They focused on micro-channel heat source application and volumetric entropy rate due to thermal and frictional effects. They established that an optimal Reynolds number range exists for a system with two different entropy sources. In addition, using nanofluids rather than base fluids minimized the rate of entropy generation due to their improved thermal properties. Shah et al. [52] investigated thermal radiation and Hall current parameter effects on a micropolar nanofluid flow past rotating surface. They reported a decline in the velocity profiles when the Hall current increased, and the temperature of the fluid

increased significantly with a rise in thermophoresis.

To improve the efficiency of a compact heat exchanger Li et al. [53] used an aluminum oxide nanofluid in a micro-channel with protrusion and dimples. They reported that the fanning friction factor and the thermal performance of the heat exchanger increased with increasing velocity of the nanofluid. In addition, the rate of heat conveyance increased when the radius of the micro-channel was reduced. Kameswaran et al. [54] researched on the combined effect of binary reaction, Soret and viscous dissipation on MHD nanofluid flow along a shrinking surface using the finite difference method. Using a copper-water nanofluid reduced the rate of heat transport compared to a mercury-water nanofluid. However, such results are at odds with theory, because copper has a higher thermal conductivity than mercury. The effects of the Casson parameter, thermal dissipation and magnetic field on unsteady nanofluid flow past a stretching plate with convective boundary domains were investigated by Oyelakin et al. [55]. They showed that a rise in the Casson parameter suppressed the temperature and velocity of the fluid. Increasing the velocity slip parameter slowed the velocity of the fluid. Dhlamini et al. [56] studied the effects of thermal energy and chemical reactions in a convective nanofluid flow past infinite plates. They showed that increased thermophoretic parameter accelerated mass transfer away from the plate surface, thus reducing the concentration boundary layer.

1.4 The rate of heat and mass transfer in nanofluids

This study analyzes the rate of heat and mass transfer in nanofluid flows. Heat and mass conveyance plays a vital role in cooling systems, fiber coating and electromagnetic drug treatment [57]. In energy plant production and industrial processing, the design of apparatus must take into consideration the attainable rate of mass and heat transfer. For example, the operation of equipment such as air-conditioning units and refrigerants must account for heat and mass exchange efficiency. An effective design for a dynamic system must make adequate provisions for maintaining suitable temperatures through efficient heat transport from a heat sink to the ambient fluid layers [58]. The heat transfer model equations for boundary layer

fluid flow problems is written as follows [59]

$$Q_t = -\hat{k}A_t \frac{d\hat{T}}{dy}. \quad (1.1)$$

Here \hat{k} is the thermal conductivity of the material, $d\hat{T}/dy$ is the temperature gradient and A_t is the heat conduction coefficient. Heat transfer can occur via convection from a hot to a cold layer of fluid. Convection is the total energy transport caused by the random vibration of fluid particles and the movement of bulk fluids. When a fluid is forced to flow by an external force such as a fan, pump or body pressure, it is referred to as forced convection. However, if fluid movement is due to buoyancy forces induced by the difference in fluid density, it is called free or natural convection. Mixed convection results when both forced and free convection are present. The rate of heat transport is directly correlated to the temperature difference, expressed according to the Newton's law of cooling as [60]

$$Q_c = h_t A (T_s - T_\infty), \quad (1.2)$$

where h_t , A , T_s , T_∞ and T_∞ represent the heat transfer coefficient, heat transfer surface area, surface temperature and free-stream temperature, respectively.

Mass transfer refers to the movement of species from a region of higher concentration to a lower one, relative to the other species available in the medium. The rate of mass transport of species is determined by the Fick's law, expressed as [61]

$$M_d = -DA \frac{d\hat{C}}{dy}, \quad (1.3)$$

here D is the mass diffusivity coefficient, A is the heat transfer surface area, and $d\hat{C}/dy$ is the concentration gradient. The rate of mass transfer by convection in a nanofluid through both diffusion and bulk fluid motion can be expressed as [62]

$$M_c = h_m A (C_s - C_\infty), \quad (1.4)$$

where h_m is the mass transfer coefficient, A is the cross-sectional area and $C_s - C_\infty$ is the species concentration difference. Heat and mass transport are analogous in several ways and, as such, the mathematical terms for heat and mass conveyance for a particular geometry can have a similar form.

There is currently a large body of research on heat and mass transport in nanofluids that includes among others Makinde et al. [63] who studied the effect of the buoyancy forces on heat and mass transport in a nanofluid fluid over a heated shrinking plate. Tlili et al. [64] studied the rate of heat and mass transport in nanofluid flow in a static wedge with the Navier slip and convective boundary constraints. Khan et al. [65] studied heat and mass movement in a third grade nanofluid in a heated vertical plate. Ali et al. [66] investigated heat transport in MHD fluid flow over a rotating system with convective cooling. They showed that the rate of heat and mass conveyance is directly proportional to the velocity slip conditions. These investigations follow closely of others such as Mabood et al. [67] who studied MHD stagnation point nanofluid flow in a porous surface with thermal radiation and viscous dissipation. Anwar et al. [68] studied the effect of solutal buoyancy and thermal radiation parameters on heat and mass transfer in a nanofluid flow. Yang et al. [69] investigated the heat transport in a nanofluid flow in a wavy sinusoidal tube using a two-phase model. Reddy et al. [70] considered the problem of heat and mass transport in a copper-water fluid flow over a rotating disk with thermal radiation and the magnetic field effect. In these investigations, the nonlinear transport equations were solved using the Hermite-Padé approximations, the homotopy analysis approach and the Adomian decomposition methods. However, these methods cannot guarantee convergence of series solutions and, may be valid only for weakly nonlinear problems. Spectral collocation methods have been used in this study to solve the boundary layer problems with heat and mass transfer. These methods may guarantee high levels of convergence and accurate results.

1.5 The effect of thermal radiation and a magnetic field

The overall influence of thermal radiation and a magnetic field on entropy production is a classical problem in fluid dynamics. Thermal radiation in fluids refers to the electromagnetic radiation produced by the thermal variations of fluid particles. The study of magnetic properties and characteristics of an electrically conducting fluid is referred to as magnetohydrodynamics. Examples of such magnetofluids are electrolytes, plasmas, liquid metals and salt solutions. The rate of entropy generation depends on the thermal radiation flux [71] and the magnetic

field number [72] defined respectively by

$$Q^r = -\frac{4\sigma_1}{3\chi} \frac{\partial T^4}{\partial y} \quad \text{and} \quad M = \frac{UL}{\hat{d}}, \quad (1.5)$$

where Q^r , σ_1, χ , $\partial T^4/\partial y$, M , U , L and \hat{d} represent the rate of thermal radiation, Stefan-Boltzmann constant, mean absorption coefficient, temperature gradient, magnetic number, velocity, unit length and the magnetic diffusivity, respectively. The impact of thermal radiation and a magnetic field are combined in various processes found in astrophysics, hydrogeology and during material science and thus sparking interest in investigating their impact. Sakiadis [73] focused on the influence of thermal radiation on laminar and turbulent nanofluid flows. The results showed that an increment in thermal radiation increased the wall temperature for both flows. However, these results were inconsistent with those of [74]; the disparity being ascribed to the difference in the boundary constraints used for the two studies. Rahimi et al. [75] researched on the impact of a magnetic field on an Eyring-Powell nanofluid flow past a stretching plate. Their results indicated that increasing the magnetic field slowed down the rate of fluid flow due to the increased skin friction. Investigations by Loper [76] on the influence of vortex magnetic field with rigid-free boundary constraints on the fluid flow indicated that a boost in the magnetic field decreased the rate of heat conveyance in the system. Furthermore, the model's entropy production was reported to be greater for rigid-free boundary conditions than for free-free boundary constraints.

In the study by Makinde [77] into the influence of thermal radiation and Newtonian heating on a boundary layer flow, the effects of the magnetic field were ignored, whereas Hussanan et al. [78] incorporated the magnetic effects. They noticed that an increment in the magnetic field generated a Lorentz force that retarded the velocity of the fluid, steering a decline in entropy production rate. The recent study by Afridi and Qasim [79] focused on the impact of thermal radiation on heat transport and entropy production in a boundary layer flow around a needle in motion in a tube with zero nanoparticle flux at the walls. They ascertained that the rate of heat conveyance and entropy generation increased with an increase in the Prandtl number, rate of thermal radiation and the Eckert number. A study of the impact of a magnetic field and Brownian motion on Williamson nanofluid flow past a stretching plate was investigated by Rasool et al. [80]. They reported that the heat flux intensified with an increase in the

Brownian motion parameter and reduced with an increase in the magnetic field.

The combined influence of thermal radiation and a magnetic field on entropy production were by considered by Berrehal et al. [81] in a radiating nanofluid flow with convective boundary constraints and by Mondal et al. [82] in a boundary layer nanofluid flow along a stretching plate. They solved the system of equation using the spectral quasilinearization method and found that the rate of entropy generation intensified as a result of an increase in thermal radiation. Heat was transferred to the fluid from the walls of the stretching plate, which consequently raised the temperature of the fluid leading to an increase in the rate of entropy generation. The study by Mir et al. [83] focused on entropy production and heat transfer in a silver-water nanofluid in an elliptical channel. Vijaybabu [84] researched on the impact of thermal radiation in a copper-water nanofluid, buoyancy-driven flow, with entropy production. Here, they found that entropy generation occurred due to buoyancy forces and the effect of nanoparticles. They also noted an inconsistency in the rate of heat transport as with a rise in thermal radiation, it decreased rather than increased as would have been expected.

Aghakhani et al. [85] investigated the rate of entropy production in a nanofluid flow along a tilted enclosure with a magnetic field and thermal radiation. They noted that the thermal boundary layer increased with an increase in the radiation parameter while a boost in the magnetic field enhanced the rate of entropy generation. The study by Aziz and Shams [86] focused on the combined effects of the thermal conductivity, internal heat source and velocity slip in fluid flow along a porous stretching plate. They reported a decline in the rate of entropy generation with an increase in thermal radiation, permeability, nanoparticle concentration and the magnetic number. A study of entropy generation in a nanofluid flow past a rotating disk with a magnetic effect was investigated by Rashidi et al. [87]. Eid and Mabood [88] studied carbon nanotubes suspended in a micro-polar fluid flowing through a permeable surface with thermal radiation and magnetic field effects. The velocity and temperature profiles of the fluid decreased with an increase in the suction parameter and magnetic field parameter. The study by Lopez et al. [89] focused on the combined influence of thermal radiation and viscous dissipation on entropy generation in a fluid flow through a porous vertical microchannel. They reported a reduction in the rate of entropy production when thermal radiation was increased,

while a reduction in the viscous dissipation parameter enhanced the rate of entropy generation. Baag et al. [90] investigated entropy production in MHD flow along a stretching plate, taking into account the influence of the Brownian motion, thermophoresis, and a magnetic field. They established that the rate of entropy generation could be increased by increasing the Brownian motion, magnetic strength and thermophoresis parameter.

1.6 The effects of double-diffusive convection on fluid properties

The majority of the studies above have considered heat transfer by natural convection means. There are, however, several scenarios where convection leads to both heat and mass transfer. Such convection processes are determined by the buoyancy forces. The form of convection caused by buoyancy forces is generally referred to as thermosolutal or double-diffusive convection. Double-diffusive convection plays a vital role in engineering applications and the transport of heat and salt in oceans. In double-diffusion convection, the density of the fluid depends linearly on the temperature and solute concentration, as is expressed in [91]

$$\rho = \rho_0[1 - \beta_v(T - T_0) - \beta_s(C - C_0)], \quad (1.6)$$

where ρ_0 , β_v , β_s , T , and C represent the density at reference state, volumetric thermal expansion coefficient, solute concentration expansion coefficient, temperature and concentration, respectively.

Substantial focus has been given to the study of the effects of double-diffusive convection on entropy generation in fluid flow. Yang et al.[92] studied double-diffusive and thermo- haline convection in a nanofluid flow regime that occurs where warm water lies above cold water. They assumed that fluid quantities vanish at the boundary region of the flow and found that double-diffusive convection leads to enhanced heat transfer at low Rayleigh number. The onset of convective fluid flows induced by buoyancy forces due to a temperature gradient was considered by Turner [93] for a thin horizontal flow in a fluid heated from top and cooled from

the bottom. Mondal et al. [94] extended the study of double-diffusion by considering entropy production in a lid-driven duct with different aspect ratios. They used the finite difference method to find the approximate solutions predicting the rate of heat transfer and entropy production in the model. They noted that the rate of entropy generation was a linear combination of the buoyancy forces and the magnetic parameter.

The entropy production in double-diffusive convection depends on several dimensionless parameters in the flow equations. The double-diffusive convection is complex when there is interaction between fluid particles and a porous medium, and this has generated research attention. For instance, Chen et al. [95] investigated entropy production in a double-diffusive convective nanofluid flow. They considered the impact of the Rayleigh number, buoyancy forces and nanoparticle volume fraction and observed that when buoyancy effects and thermal Rayleigh number opposed each other, the entropy generation pattern differed from that which had been reported by Sohail et al. [96]. The study of entropy generation and heat transport in Darcy-Forchheimer double-diffusive convection in an inclined cylinder was reported by Siavashi et al. [97]. They ascertained that the onset of convective forces at the porous surface was marked by an upward shift in the entropy generation and heat transfer. Hussain [98] used the finite difference approach to predict entropy production at the onset of convection in a double-diffusive natural convection within a corrugated enclosure. The effects of parameter values such as the buoyancy ratio, Hartmann number, Darcy number and the Lewis number on entropy generation were determined. The Lewis number is a significant parameter for double-diffusive convection and is expressed as [99]

$$Le = \frac{\varphi}{D}, \quad (1.7)$$

where φ and D represent thermal diffusivity and mass diffusivity, respectively. The equation is often used to describe fluid flow where convection heat transfer and mass transport occurs simultaneously.

The diffusion of mass due to the temperature gradient is known as the Soret or thermo-diffusion effect, while the transfer of energy due to the solute concentration gradient is defined as the Dufour effect. A number of studies have assumed the influence of Dufour and the Soret

numbers to be negligible when analyzing the effects of double-diffusion convection on entropy generation in fluid flow problems. However, such effects are critical where there exists a fluid density difference within the flow regime. For instance, when Torabi et al. [100] studied entropy production in a double-diffusive convection flow in a porous horizontal channel with thick walls and the Soret effect, they observed that the rate of entropy production was directly related to the lower thickness of the wall. They also noted that the total entropy generated could be minimized if the thicknesses of both walls was chosen appropriately. However, their observations differed from those reported by Kefayati [101]. This was attributed to the differences in the boundary conditions and the numerical method used. Khan et al. [102] researched on the influence of the Soret and Dufour numbers on entropy generation in MHD fluid flow over a rotating cone using the finite element method. They found that a rise in the Dufour number caused the concentration gradient to increase, resulting in temperature increase in the fluid causing greater entropy generation. For the Soret number an opposite trend was observed, which confirmed the reciprocal relationship between the two phenomena. Other studies related to double-diffusion convection on entropy generation in nanofluids with the Soret and Dufour effects include, those of Shit et al. [103], Seth et al. [104] and Oueslati et al. [105].

The case of entropy generation in a double-diffusive magnetic nanofluid flow subjected to temperature and concentration gradients is often encountered in oceanography where the temperature differences and salt concentrations exist with different gradients and heat and salt diffuse at different rates. In free convection flow, the heat diffusivity is intrinsically higher than the solute diffusivity. Mchirgui et al. [106] used the Darcy-Brinkman formulation for double-diffusive convection flow in a square duct. Using the volume finite element technique, they found that the rate of entropy production depended significantly on the Darcy number. They also observed that for higher Rayleigh numbers, entropy production increased due to the increase in the buoyancy forces. Similar results were obtained by Jing et al. [107] for MHD fluid flow in a rectangular cavity fitted with fins of different shapes, using the finite difference approach to solve the governing equations. For double-diffusive convective flow in a Casson fluid, Ahmed et al. [108] used the bvp4c solver to compute the entropy generation number and found that, increasing the Casson parameter suppressed the rate of entropy generation and

enhanced the concentration profiles.

1.7 Numerical methods of solution

Most of the studies reported in the literature on boundary layer problems still make use of traditional numerical methods, such as the finite difference method [109], finite volume method [110] and finite element method [111] to solve the transport equations. However, these approaches have certain weaknesses, for instance, they may require a great number of grid points to yield accurate results [112–115]. Another challenge lies in using basis functions that are nonzero only over small domains. Therefore, obtaining accurate results requires a more reliable and robust numerical method that demands fewer grid points and allows a global approach. Accordingly, in recent years some authors [116–119] have used spectral methods to overcome these challenges. Spectral methods have been acknowledged by researchers, such as Motsa and Makukula [120] as having a global approach and require few grid points compared to traditional methods to achieve accurate results, Polynomial spectral methods have been used to solve finite and unbounded flow problems, pseudospectral methods adapt well to highly nonlinear problems, and spectral iteration methods are suitable for boundary value problems [121]. Among the possible spectral methods are the collocation, the Galerkin and the Tau methods [122].

In this thesis we focus on spectral collocation methods to solve highly nonlinear differential equations with excellent error properties and accurate results. The principle when using spectral methods is to write the approximate solution to a differential equation as a sum of the polynomial basis function and select the coefficient in the sum that satisfy the differential equation as closely as possible. However, in practice, the polynomials have a disadvantage in that the matrices resulting from discretization may have a large condition number which reduces the expected theoretical accuracy, as reported in [123, 124]. Further, the discretized matrices are generally densely populated. These weaknesses can, nevertheless, be easily resolved by the use of *inter alia*, Hermite, Laguerre, Lagrange and Chebyshev polynomials [125, 126] as the basis functions. In this study we use the overlapping grid spectral collocation

method (OGSQLM) and the bivariate spectral quasilinearization method (BSQLM) with Chebyshev and Lagrange polynomial as basis functions.

1.7.1 The bivariate spectral quasilinearization method

Quasilinearization refers to a numerical tool for linearizing differential equations. When the spectral method is used to solve a linearized system of equations, it is referred to as the spectral quasilinearization method (SQLM). The application of the method assumes a small difference between the previous and current iterations of the approximate solution. Further, it assumes a small difference between the derivatives at subsequent iterations levels. Motsa et al. [127] compared the accuracy of the spectral quasilinearization method with that of spectral local linearization method by solving the Blasius boundary layer problem. They reported that the spectral quasilinearization method converged faster, with a quadratic convergence rate, than did the spectral local linearization method with a linear rate of convergence. Nevertheless, despite the SQLM having a better rate of convergence, it has a weakness, namely that with a poor initial guess made, the SQLM performs poorly. Further, the method may not be suitable for highly nonlinear partial differential equations. To overcome the latter challenge, which results from introducing a second variable, we introduce the bivariate spectral quasilinearization method (BSQLM). In some previous studies, researchers have discretized the space variable using the SQLM and the time variable using finite differences [128]. However, this approach has some disadvantages in that this may lead to difficulties in matrix inversion. This may be overcome by discretizing using the bivariate spectral quasilinearization method in both space and time. Motsa and Animasaun [129] used the bivariate spectral quasilinearization method to solve the equations for the heat transfer problem in a micropolar fluid flow with concentrated solid particles. The method was found to be computationally efficient and gave stable and accurate results from a few iterations. The bivariate spectral quasilinearization method has also been shown to give solutions that are uniformly accurate and valid over large space and small time domains [130]. This favours the use of the Chebyshev polynomials as the basis functions and restricting the domain to the interval $[0,1]$. In this study the bivariate spectral quasilinearization method is discussed

further in Chapters 5 and 6.

1.7.2 The overlapping grid spectral collocation method

The overlapping grid spectral collocation method (OGSCM) is used to overcome some weaknesses observed when using the bivariate spectral quasilinearization method. For example, in the bivariate spectral quasilinearization method, increasing the number of nodes to achieve greater accuracy creates an exponential increase in the computational effort required to solve the system of matrix equations. In this regard, one way of ensuring accurate solutions over large domains is to limit the overall size of the matrix equations. Thus, a more computationally efficient and robust approach, namely the overlapping grid spectral collocation method was introduced [131]. In this method, the large spatial computational domain is divided into a sequence of overlapping subintervals and the large time domain subdivided into equal non-overlapping subintervals. This leads to a sparse coefficient matrix that is easier to invert and has a smaller condition number. The overlapping grid spectral collocation method has been reported to be accurate and computationally efficient when applied to boundary value problems that are defined on a large computational domains [132]. Mkhathswa et al. [133] used the method to solve conjugate problems of conduction and free convection flow and reported the method as giving accurate numerical results and converging rapidly. Using the same method to solve a problem of MHD Eyring-Powell fluid flow, Mkhathswa et al. [134] noted that the method was stable and computationally efficient. They ascribed the accuracy of the method to the use of overlapping grids, which led to a less dense matrix that is easy to invert. A search of the literature indicates that the method has not been extensively used to solve entropy generation problems in boundary layer flows. The overlapping grid spectral collocation method is further discussed in Chapters 2, 3 and 4.

1.8 Thesis objectives

The primary objective of this thesis is to investigate and quantify entropy generation in unsteady MHD nanofluid flows in various bounded and unbounded domains. The specific problems investigated include entropy generation in an Oldroyd-B nanofluid flow over a Riga

plate, entropy generation in an unsteady MHD nanofluid past an inclined cylinder using Buongiorno's model [135], irreversibility impact and entropy generation in a three-dimensional magnetohydrodynamic Oldroyd-B fluid flow past a stretching sheet, entropy generation in an unsteady magnetic nanofluid flow in the stagnation region of an impulsively rotating sphere, and the fluid velocity, heat and mass transfer in an unsteady nanofluid flow past parallel porous plates. We explore the significance of the various models and emphasize the physical implications of the mathematical results.

The secondary objective is to conduct numerical simulations to verify and demonstrate the accuracy, convergence and computational efficiency of the modified spectral methods used in solving boundary layer flow problems arising in fluid dynamics. From the literature, the spectral methods of interest have not been widely used to solve systems of highly coupled differential equations. The specific methods include the overlapping grid spectral collocation method and the bivariate spectral quasilinearization method. The application of these methods is extended for the first time to the transport equations modelling entropy generation in boundary layer flow problems.

We further seek to determine the impact of physical and chemical parameters, including *inter alia*, the Brinkman number, chemical reaction parameter, thermophoresis parameter, magnetic number, Eckert number and Reynolds number on fluid properties and entropy generation.

The thesis consists of seven chapters. In Chapter 2, we investigate entropy generation due to the unsteady boundary layer flow of an Oldroyd-B nanofluid past a Riga plate, taking into account the effects of varying, *inter alia* the convective boundary conditions, the dimensions of the Riga plate, the Brownian motion parameter and the Brinkman number. The overlapping grid spectral collocation approach is used to find approximate solutions of the transport equations.

In Chapter 3, we analyze entropy generation, heat and mass transfer in an unsteady MHD nanofluid over an inclined cylinder using Buongiorno's model [135] with velocity slip conditions. The effects of varying various chemical and physical parameters on fluid

properties have been investigated. The overlapping grid spectral collocation method is used to find the numerical solution to the highly nonlinear PDEs, and the rate of convergence is presented.

In Chapter 4, the impact of the irreversibility ratio and entropy generation in a three-dimensional Oldroyd-B fluid with relaxation-retardation viscous dissipation and velocity slip boundary condition is considered. The effects of varying various chemical and physical parameters on fluid properties have been investigated. The overlapping grid spectral collocation method is used to solve the transport equations.

In Chapter 5, we investigate entropy generation in a double-diffusive convective magnetic nanofluid flow in the stagnation region of a rotating sphere with viscous dissipation. The bivariate spectral quasilinearization method is used to solve the system of highly coupled PDEs. The impact of various physical parameters on entropy production, heat, and mass transfer is determined and discussed.

In Chapter 6, the combined impact of chemical reaction, momentum diffusivity and the magnetic fields on the fluid velocity, heat and mass transfer in an unsteady nanofluid flow over inclined porous plates is considered. The system of equations governing the flow of the model are solved numerically using the bivariate spectral quasilinearization method.

We summarize and discuss the major findings of the study in Chapter 7.

Chapter 2

A numerical study of entropy generation in Oldroyd-B nanofluid flow past a Riga plate

In this chapter, we investigate entropy generation due to the unsteady boundary layer flow of an Oldroyd-B nanofluid past a Riga plate, taking into account the effect of varying convective boundary conditions, thermophoretic motion, varying the dimensions of the Riga plates, the Brownian motion parameter and the Brinkman number. The transport equations modelling the flow are solved to a high degree of accuracy using the overlapping grid spectral collocation method.

A NUMERICAL STUDY OF ENTROPY GENERATION ON OLDROYD-B NANOFUID FLOW PAST A RIGA PLATE

Zachariah Mbugua Mburu¹, Sabyasachi Mondal^{2*}, Precious Sibanda³, Ramprakash Sharma⁴

ABSTRACT

This study investigates entropy generation due to the unsteady boundary layer flow of an Oldroyd-B nanofluid past a Riga plate. The velocity, temperature and concentration fields are obtained and the flow equations solved numerically using the spectral collocation method with overlapping grids. The local entropy generation distribution is obtained by solving the entropy generation equation numerically. Sensitivity and convergence analysis is performed to demonstrate the accuracy and convergence of the numerical method. The effect of principal flow parameters on entropy generation is investigated and it is established that entropy generation is directly proportional to the width of the Riga plate, Brinkman number, Prantl number and the Brownian motion parameter. It is further shown that the entropy generation is inversely proportional to the Eckert number and Deborah number in relaxation time. The range of parameter values were obtained from the reported literature. The current study may have applications of physics, including in the design of both cooling and heating devices.

Keywords: Entropy Generation, Overlapping Grids, Relaxation and Retardation Time, Oldroyd-B Nanofluid, Hyperbolic Time-Varying Boundary Conditions, Riga Plate

INTRODUCTION

The quantity of energy produced in any thermodynamic process is conserved from the second law of thermodynamics, although the quality may degrade with the process. The reduction in the quality of energy produced in any thermodynamic process is measured by entropy generation. The quality and quantity of energy produced in a thermodynamic process reduce with the increase in entropy generation. A Riga plate, also commonly known as an electromagnetic actuator is a device consisting of permanent magnets and electrodes of equal width. The flow control device was first developed by Gailitis et al. [1] and Avilov [2] renamed it a Riga plate. Hayat et al. [3] investigated the impact of nonlinear mixed convection and radiation along a Riga plate with double stratification. The homotopy method was used to solve the system of differential equations. It was established that the effects of radiation and temperature ratio variables enhanced heat distribution. The buoyancy ratio and the modified Hartman number had the opposite effect on the rate of heat transfer. The study of entropy generation due to the unsteady nanofluid flow past a Riga plate is of great interest to researchers. It has applications such as in cooling of automotive vehicles, heat exchangers and heat sinks, solar energy collectors and cooling towers. Heat and mass transfer are often accompanied by entropy production, which often reduces energy in many thermodynamic processes. For this reason, focusing on the irreversibility of heat transfer processes and seeking to understand the impact of entropy generation makes engineering sense. For example, a good heat exchanger design essentially means thermodynamic efficiency. The art of modifying a dynamical system so that it destroys the least available work subject to different boundary constraints is the key focus of entropy generation minimization.

Rana et al. [4] reported on a study of entropy generation due to Ohmic heating in a nanofluid flow under the influence of a varying magnetic field. Nayak et al. [5] used the Buongiorno model of a nanofluid to study the influence of magnetic forces on the slip flow over a Riga plate with internal heating. The influence of variable thermal conductivity on nonlinear Sisko fluid flow past an electromagnetic sheet with entropy production was reported by Shaw et al. [6]. Das et al. [7] determined the effects of Soret and Dufour parameters on unsteady Casson fluid flow past a Riga plate. They reported that the skin friction coefficient is enhanced by increasing the Dufour parameter and the Biot number. Recent studies on energy produced

This paper was recommended for publication in revised form by Regional Editor Hatice Mercan

^{1,3} School of Mathematics, Statistics and Computer Science, University of KwaZulu-Natal, Pietermaritzburg, South Africa

² Department of Mathematics, Amity University Kolkata, Newtown - 700135, West Bengal, India

⁴ Department of Mechanical Engineering, National Institute of Technology, Arunachal Pradesh, India

*E-mail address: sabya.mondal.2007@gmail.com

Orcid id: 0000-0002-2916-2922, 0000-0003-4666-0568, 000-0003-2115-4642, 0000-0002-3359-1316

Manuscript Received 05 December 2019, Accepted 09 May 2020

in a thermodynamic process are given by [8–13].

The use of nanofluids is one of the modern techniques used to enhance heat transfer in thermodynamic devices [14, 15]. To improve the sustainability of heat transfer devices and improve their efficiency, researchers have investigated the major causes of entropy generation in different dynamical systems [16, 17]. Entropy generation has been shown to be linked to the geometry of a device and the thermophysical properties of the working fluid [18]. Rehman et al. [19] investigated entropy generation in a radiative rotating nanofluid with thermal slip. The shooting method was used in solving the system of differential equations. It was established that the Bejan number has the effect of reducing the nanoparticle volume fraction. Also, gold nanoparticles produced the maximum entropy when compared to silver and copper oxide nanoparticles. Nanofluids are efficient energy transfer with marginal entropy generation. Related studies on heat transfer in nanofluids are given by [20–25].

Esfahani et al. [26] investigated the influence of a wavy wall and nanoparticles on entropy generation in flow past a heat exchanger plate. The finite volume technique was used to solve the system of differential equations. The simulations were done using the Ansys-fluent software. The entropy generation reduced along the centerline where friction does not play a significant role. Bhatti et al. [27] studied entropy generation in a magneto hydrodynamic boundary layer generated by a rotating surface using the successive linearization method to solve the flow equations. They found that with an increase in the suction parameter, both the velocity profiles and entropy generation increased. Shashikumar et al. [28] investigated entropy generation analysis in magneto-nanofluids containing aluminum and titanium alloy nanoparticles in a micro-channel with partial slip and convective conditions. The dimensionless flow equations were solved by applying the Runge-Kutta numerical method. They found that entropy production can be reduced by increasing radiative parameter, Joule heating parameter and viscous dissipation.

Moreover, entropy generation was higher in the case of titanium-water nanofluids than aluminum-water nanofluids. Related literature on nanofluids and entropy generation can be found in ref. [29–33].

The impact of entropy generation and nonlinear thermal radiation on Darcy-Forchheimer flow of a Manganese Iron Oxide ($MnFe_2O_4$) Casson-water nanofluid due to a rotating disk and its application to brain dynamics was reported by Shaw et al. [34]. They found that entropy generation affects how the brain functions. Farooq et al. [35] investigated transpiration and viscous dissipation impact on entropy generation in nanofluid flow past a nonlinear radially stretching sheet. The numerical solution was obtained using the shooting technique and the `bvp4c` Matlab solver. It was found that entropy generation within the laminar flow was high compared to the surface of the stretching sheet. The laminar motion of an electrically conducting fluid can be reduced by applying an external magnetic field. The applied magnetic field was shown to reduce entropy generation in the fluid flow.

Recently, Gupta et al. [36] investigated the MHD flow of an Oldroyd-B nanofluid past a bi-directional stretching sheet. The differential equations were solved using the differential transformation technique and Padé approximations. It was found that the velocity decreased with an increasing magnetic parameter, the temperature profiles increased with an increase in the magnetic parameter, Deborah number of the first kind and the Brownian motion parameter. However, it decreased with an increase in the Deborah number of the second kind. Alshomrani et al. [37] investigated chemically reactive MHD flow and energy transport in an Oldroyd-B nanofluid subject to stratifications. The homotopy method was used for the computation of solutions of the nonlinear flow equations. They found that an increase in both the Biot number and chemical reaction parameter led to a mass transfer reduction.

Gireesha et al. [38] recently investigated chemical reaction effects on fluid flow and concentration transport past a Riga plate with solutal slip impact. The system of differential equations was solved using the Runge-Kutta method. Nayak et al. [39] investigated the effects of homogeneous- heterogeneous reactions on radiative sodium chloride-carbon nanofluid flow past a heated vertical plate. They noted that the momentum, thermal and concentration boundary layer thicknesses reduced due to a Lorentz force's effect. Related studies are reported by [40–42].

The analysis of heat transfer in boundary layer problems is fundamental in industrial processes. Heat

transfer in fluids involving open and closed systems is mainly explained by the first law of thermodynamics [43]. The law of thermodynamics is useful for investigating the temperature distribution within a thermodynamic system and the rate of heat transfer at the solid boundary [44]. There are several causes for entropy generation in any thermodynamic process, including fluid friction, chemical reactions, mixing of fluids, dissipative forces, among others, Bejan [45].

Entropy generation due to unsteady Oldroyd-B nanofluid flow past a Riga Plate has not received much attention in the literature. The current study investigates the impact of principal parameters such as the width parameter of the Riga plate, Brinkman number, Eckert number, Hartman number, Reynolds number and Brownian motion parameter on entropy generation for Oldroyd-B nanofluid past a Riga plate. We further present an analysis of accuracy and convergence of the spectral collocation numerical method with overlapping grids. This study may have applications in the cooling of machine parts, food processing and drying of cylinder-shaped bodies, considering shrinkage at different drying temperatures.

MATHEMATICAL FORMULATION

In the study, we consider an incompressible boundary layer time-varying flow of an Oldroyd-B nanofluid past a Riga plate. The study takes into account entropy generation, thermophoretic motion and Brownian diffusion. We take u and v to be respectively the velocity components in the x and y directions where the x -axis is measured along the plate and the y -axis is at right angle to it as shown in Figure 1, see [46]. The electromagnetic field M_h of the Riga-plate yields a wall-parallel Lorentz force of exponentially decaying nature. The boundary layer equations with Boussinesq approximation and the assumptions set out above are

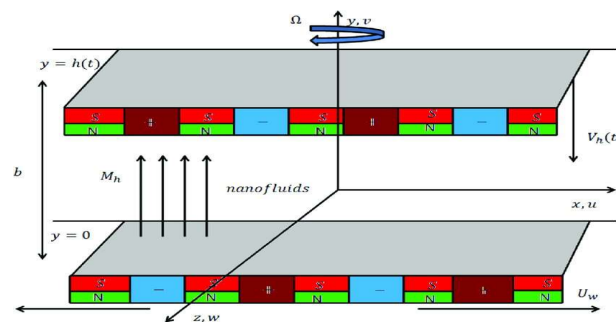


Figure 1. Flow configuration, where N and S are the North pole and the South pole, respectively of the magnet

Continuity equation

$$\frac{\partial u}{\partial x} + \frac{\partial v}{\partial y} = 0 \quad (1)$$

Momentum equation

$$\begin{aligned} \frac{\partial u}{\partial t} + u \frac{\partial u}{\partial x} + v \frac{\partial u}{\partial y} + \Gamma_1 \left(u^2 \frac{\partial^2 u}{\partial x^2} + v^2 \frac{\partial^2 u}{\partial y^2} + 2uv \frac{\partial^2 u}{\partial x \partial y} \right) &= \frac{\pi j_0 M_h}{8 \rho_f} \exp\left(-\frac{\pi}{d}y\right) + \\ v_f \left[\frac{\partial^2 u}{\partial y^2} + \Gamma_2 \left(u \frac{\partial^3 u}{\partial x \partial y^2} + v \frac{\partial^3 u}{\partial y^3} - \frac{\partial u}{\partial x} \frac{\partial^2 u}{\partial y^2} - \frac{\partial u}{\partial y} \frac{\partial^2 v}{\partial y^2} \right) \right] & \end{aligned} \quad (2)$$

Energy equation

$$\frac{\partial T}{\partial t} + u \frac{\partial T}{\partial x} + v \frac{\partial T}{\partial y} = \frac{k_f}{(\rho c_p)_f} \left(\frac{\partial^2 T}{\partial y^2} \right) + \tau \left[D_B \frac{\partial c}{\partial y} \frac{\partial T}{\partial y} + \frac{D_T}{T_\infty} \left(\frac{\partial T}{\partial y} \right)^2 \right] + \frac{\Gamma_1}{\Gamma_2} \frac{\mu}{(\rho c_p)_f} \left(\frac{\partial u}{\partial y} \right)^2 - \frac{1}{(\rho c_p)_f} \left(\frac{\partial q^r}{\partial y} \right) \quad (3)$$

Species concentration equation

$$\frac{\partial C}{\partial t} + u \frac{\partial C}{\partial x} + v \frac{\partial C}{\partial y} = D_B \frac{\partial^2 C}{\partial y^2} + \frac{D_T}{T_\infty} \frac{\partial^2 T}{\partial y^2} - K_1(C - C_\infty) \quad (4)$$

The model time-varying boundary conditions are given by

$$t = 0: u = v = 0, T = T_\infty, C = C_\infty, (x, y \geq 0),$$

$$u = u_w(t, x), v = 0, T = T_w, C = C_w, (y = 0),$$

$$t > 0: u = u_e(t, x), T \rightarrow T_\infty, C \rightarrow C_\infty, \text{ as } y \rightarrow \infty,$$

where, $u_w(x, t) = \frac{ax}{1+\zeta t}$, $u_e(x, t) = \frac{bx}{1+\zeta t}$, $T_w = T_\infty + \frac{T_0 x^m}{1+\zeta t}$ and $C_w = C_\infty + \frac{C_0 x^n}{1+\zeta t}$. Eqs. (2-4) are transformed to ordinary differential equations using the variables $u = \frac{ax}{1+\zeta t} F_\eta(\eta)$, $v = -\sqrt{\frac{av_f}{1+\zeta t}} F(\eta)$, $\theta(\eta) = \frac{T-T_\infty}{T_w-T_\infty}$, $\phi(\eta) = \frac{C-C_\infty}{C_w-C_\infty}$ and $\eta = y \sqrt{\frac{a}{v_f(1+\zeta t)}}$. From Eq.(3), the radiative heat flux q^r is described by the Rosseland approximation, [47]

$$q^r = -\frac{4\sigma_1}{3\chi} \frac{\partial T^4}{\partial y} \quad (5)$$

The fluid-phase temperature difference within the flow is assumed to be sufficiently small [47] such that T^4 may be expanded in a Taylor series about the free-stream temperature T_∞ and neglecting higher-order terms to yield

$$T^4 = 4T_\infty^3 T - 3T_\infty^4 \quad (6)$$

Substituting Eq. (5) in the last term of Eq. (3) yields

$$\frac{\partial q^r}{\partial y} = -\frac{16}{3\chi} T_\infty^3 \frac{\partial^2 T}{\partial y^2} \quad (7)$$

We then substitute the transformation variables into Eqs. (2-5) to have

$$F_{\eta\eta\eta} + \Omega_2[(F_{\eta\eta})^2 - FF_{\eta\eta\eta}] + \Omega_1(2FF_\eta F_{\eta\eta} - F^2 F_{\eta\eta\eta}) + FF_{\eta\eta} - (F_\eta)^2 + \frac{1}{2}\varepsilon\eta F_{\eta\eta} + \varepsilon F_\eta + H_a e^{-\delta\eta} = 0 \quad (8)$$

$$\left(1 + \frac{4R_d}{3}\right)\theta_{\eta\eta} + Pr \left[N_b \theta_\eta \phi_\eta + N_t (\theta_\eta)^2 + F\theta_\eta + \frac{1}{2}\varepsilon\eta\theta_\eta + 2Ec \frac{\Omega_2}{\Omega_1} (F_{\eta\eta})^2\right] = 0 \quad (9)$$

$$\phi_{\eta\eta} + \frac{N_t}{N_b} \theta_{\eta\eta} - S_c \left(F\phi_\eta + \frac{1}{2}\varepsilon\eta\phi_\eta + \gamma\phi\right) = 0. \quad (10)$$

The boundary conditions for Eqs. (8-10) are obtained as $F_\eta = 1$, $F = 0$, $\theta = 1$, $\phi = 1$ at $\eta = 0$ and $F_\eta = \beta$, $\theta \rightarrow 0$, $\phi \rightarrow 0$ as $\eta \rightarrow \infty$.

The parameters in Eqs. (8-10) are given by $\Omega_1 = \frac{a\Gamma_1}{1+\zeta t}$, $\Omega_2 = \frac{a\Gamma_2}{1+\zeta t}$, $\varepsilon = \frac{\tau}{a}$, $H_a = \frac{\pi j_0 M_H x(1+\zeta t)^2}{8\rho_f u_w^2}$, $\delta = \frac{\pi}{d \sqrt{\frac{a}{v_f(1+\zeta t)}}}$, $Pr = \frac{v}{\alpha}$, $Ec = \frac{u_w^2}{(c_p)_f(T_w - T_\infty)}$, $N_b = \frac{\tau D_B (C_w - C_\infty)}{v_f}$, $N_t = \frac{\tau D_T (T_w - T_\infty)}{T_\infty v_f}$, $S_c = \frac{v}{D_B}$, $\gamma = \frac{K_0}{a}$, $\beta = \frac{b}{a}$ and $R_d = \frac{\sigma_1 T_\infty^3}{3k\chi}$.

ENTROPY GENERATION ANALYSIS

There are several causes of entropy production: fluid friction, dissipative forces, mixing of chemical particles, heat transfer, viscous forces, unrestrained expansion and contraction. In this study, the volumetric rate of local entropy generation for an Oldroyd-B nanofluid past an electromagnetic actuator with thermal radiation and the magnetic fields can be expressed as, see [48]

$$S_{gen} = \underbrace{\frac{k_f}{T_\infty^2} \left[\left(\frac{\partial T}{\partial y} \right)^2 + \frac{16\sigma_1 T_\infty^3}{3\chi} \frac{\partial^2 T}{\partial y^2} \right]}_{1^{st} \text{ part}} + \underbrace{\frac{\nu_f}{T_\infty} \left(\frac{\partial u}{\partial y} \right)^2}_{2^{nd} \text{ part}} + \underbrace{\frac{Ha_0^2}{T_\infty} u^2}_{3^{rd} \text{ part}} + \underbrace{\frac{R_d D_B}{C_\infty} \left(\frac{\partial C}{\partial y} \right)^2 + \frac{R_d D_B}{T_\infty} \left(\frac{\partial T}{\partial y} \frac{\partial C}{\partial y} \right)}_{4^{th} \text{ part}} \quad (11)$$

In Eq.(11), the entropy is in four parts. The first term is the entropy due to thermal radiation irreversibility, the second is entropy due to viscous dissipation irreversibility, the third is entropy due to the applied magnetic field irreversibility and the fourth part is entropy due to diffusive irreversibility. Entropy generation is defined as the ratio of local volumetric entropy generation to the characteristic rate of entropy generation expressed as

$$N_G = \frac{S_{gen}}{S_0} \quad (12)$$

where,

$$S_0 = \frac{k_f (T_w - T_\infty)^2}{T_\infty^2} \quad (13)$$

Using Eqs. (11-13), the dimensionless entropy generation is expressed as

$$N_G = Re_e (1 + N_b) (\theta_\eta)^2 + \frac{Br}{\psi} (F_\eta)^2 + \frac{Br(Ha)^2}{\psi} (F_\eta)^2 + \Lambda \left(\frac{\rho}{\psi} \right)^2 (\phi_\eta)^2 + \Lambda \left(\frac{\rho}{\psi} \right) (\phi_\eta \theta_\eta) \quad (14)$$

The dimensionless terms in Eq. (14) are defined as $Re = \frac{v_0 u}{\nu}$, $Br = \frac{\mu_f u_w^2}{k \Delta T_\infty}$, $\psi = \frac{T_w - T_\infty}{T_\infty}$, $\rho = \frac{c_w - c_\infty}{c_\infty}$ and $\Lambda = \frac{R_d D_B}{C_\infty}$

METHOD OF SOLUTION

This section describes the spectral collocation method with overlapping grids for a system of highly nonlinear ordinary differential equations defined over a large computational domain. The nonlinear system of ODEs is first linearized using the quasilinearization method (QLM) of Bellman and Kalaba [49]. The linearized system is then solved using the spectral collocation method applied on overlapping grids. The truncated computational domain is subdivided into equal overlapping subintervals and an approximate solution computed over the entire domain. The overlapping is such that two grid points at the end of each subinterval coincide with neighboring subintervals. The grid points lead to less dense matrices that require less computational time to invert, leading to an efficient method. The well-posed nature of the resulting linear ODEs is demonstrated by calculating the condition number of the coefficient matrices. A well-conditioned system guarantees stability, which consequently leads to accurate results.

The system of Eqs. (8-10) are first simplified using QLM to give

$$a_{0,r} f_{r+1}''' + a_{1,r} f_{r+1}'' + a_{2,r} f_{r+1}' + a_{3,r} f_{r+1} = R_{1,r}, \quad (15)$$

$$b_{0,r} \theta_{r+1}'' + b_{1,r} \theta_{r+1}' + b_{2,r} f_{r+1}'' + b_{3,r} f_{r+1}' + b_{4,r} \phi_{r+1}' = R_{2,r}, \quad (16)$$

$$c_{0,r} \phi_{r+1}'' + c_{1,r} \phi_{r+1}' + c_{2,r} \phi_{r+1} + c_{3,r} f_{r+1} + c_{4,r} \theta_{r+1}'' = R_{3,r}. \quad (17)$$

The boundary conditions are expressed as $f' = 1, f = 0, \theta = 1, \phi = 1$, at $\eta = 0$ and $f' = \beta, \theta \rightarrow 0, \phi \rightarrow 0$ as $\eta \rightarrow \infty$. The variable coefficients on the left-hand side of Eqs. (15-17) are expressed as

$$a_{0,r} = 1 - \Omega_2 f_r - \Omega_1 f_r^2, a_{1,r} = 2(\Omega_2 f_r'' + \Omega_1 f_r f_r') + f_r + \frac{1}{2} \varepsilon \eta, a_{2,r} = 2\Omega_2 f_r f_r'' - 2f_r' + \varepsilon,$$

$$a_{3,r} = -\Omega_2 f_r'' + 2\Omega_1 f_r' f_r'' - \Omega_1 f_r''' + f_r'', b_{0,r} = 1 + \frac{4R_d}{3}, b_{2,r} = 4P_r E_c \frac{\Omega_2}{\Omega_1} f_r'', b_{3,r} = P_r \theta_r',$$

$$b_{1,r} = Pr \left[N_b \phi_r' + 2N_t \theta_r' + f_r + \frac{1}{2} \varepsilon \eta \right], b_{4,4} = P_r N_b \theta_r' c_{0,r} = 1, c_{1,r} = -S_c \left(f_r + \frac{1}{2} \varepsilon \right),$$

$$c_{2,r} = \gamma, c_{3,r} = -S_c \phi_r' \text{ and } c_{4,r} = \frac{N_t}{N_b}.$$

The right-hand side of Eqs. (15-17) consist of nonlinear terms expressed as

$$R_{1,r} = \Omega_2 [(f_r'')^2 - f_r f_r'''] + \Omega_1 (2f_r f_r' f_r'' - f_r^2 f_r''' + f_r f_r'' - (f_r')^2 + H_a e^{-\delta \eta}) \tag{18}$$

$$R_{2,r} = P_r \left[N_b \theta_r' \phi_r' + N_t (\theta_r')^2 + f_r \theta_r' + 2E_c \frac{\Omega_2}{\Omega_1} (f_r'')^2 \right] \tag{19}$$

$$R_{3,r} = -S_c f_r \phi_r' \tag{20}$$

Here, $r = 1, 2 \dots$ denotes the iteration level. Starting with an initial approximation, Eqs. (15-17) are solved iteratively until a solution with the desired accuracy is realized. The spatial domain $\eta \in [0, \infty)$ is first truncated to $[0, L_\eta]$ where L_η is large enough to approximate conditions at infinity. The truncated domain $[0, L_\eta]$ is decomposed into q overlapping subintervals of equal lengths expressed as $\sphericalangle_l = [\eta_{l-1}, \bar{\eta}_l], \eta_{l-1} \eta_l \bar{\eta}_l, \eta_0 = 0, \bar{\eta}_q = L_\eta, l = 1, 2, 3, \dots, q$ where $\eta_l \bar{\eta}_l$ depicts the overlapping nature of the grid points. The overlapping domain decomposition in η is as shown in Figure 2.

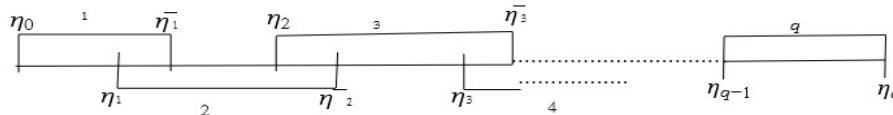


Figure 2. Overlapping grid in η

The computational domain $[\eta_{l-1}, \bar{\eta}_l]$ in the l^{th} subinterval is transformed into $\eta^* \in [-1, 1]$ where the standard Chebyshev differential matrix is defined by applying the linear map

$$\eta^* = \frac{2}{\bar{\eta}_l - \eta_{l-1}} \left[\eta - \frac{1}{2} (\bar{\eta}_l + \eta_{l-1}) \right], \eta \in [\eta_{l-1}, \bar{\eta}_l] \tag{21}$$

Further, each subinterval is discretized into $N_\eta + 1$ Chebyshev Gauss Lobatto points. The subintervals in the decomposed domain overlap such that the last two points in the \sphericalangle_l subinterval overlap with the first two points of the \sphericalangle_{l+1} subinterval and they remain common. The collocation nodes in the l^{th} subinterval in η are defined in [50] by

$$\eta_i = \cos \left(\frac{\pi i}{N_\eta} \right), \text{ for } i = 0, 1, 2, \dots, N_\eta, \eta \in [-1, 1] \tag{22}$$

To obtain an explicit expression for the length of each subinterval given by $L = \bar{\eta}_l - \eta_{l-1}$ in terms of the number of subintervals q , we find

$$qL - L(q-1) \left(\frac{1}{2} - \frac{1}{2} \cos\left\{ \frac{\pi}{N_\eta} \right\} \right) = b - a \quad (23)$$

to obtain

$$L = \frac{b-a}{q+(1-q)\left(\frac{1}{2}-\frac{1}{2}\cos\left\{\frac{\pi}{N_\eta}\right\}\right)} \quad (24)$$

From Eq. (24), we obtain the following relation

$$\bar{\eta}_l = \eta_l + L \left(\frac{1}{2} - \frac{1}{2} \cos\left\{ \frac{\pi}{N_\eta} \right\} \right) \quad (25)$$

Eq.(29) is used in defining the boundaries of the overlapping sub-intervals when performing discretization. The numerical solutions to the system of Eqs. (8-10) are approximated using Lagrange bivariate interpolating polynomials expressed as $f(\eta) \approx \sum_{q=0}^{N_\eta} f(\eta_q)L_q(\eta)$, $\theta(\eta) \approx \sum_{q=0}^{N_\eta} \theta(\eta_q)L_q(\eta)$ and $\phi(\eta) \approx \sum_{q=0}^{N_\eta} \phi(\eta_q)L_q(\eta)$.

Here $L_q(\eta)$ is the standard Lagrange polynomial. The interpolating polynomial is applied in finding the approximation of discrete derivatives of the unknown functions. The derivatives of $F = (f, \theta, \phi)$ with respect to η are approximated at the collocation points (η_i) for $i = 0, 1, 2, \dots, N_\eta$ as

$$\frac{\partial^p F_{r+1}(\eta_i)}{\partial \eta^p} = \mathbf{D}^p \mathbf{F}_{i,r+1} = \left(\frac{2}{L_\eta} \right)^p \sum_{k=0}^{N_\eta} D_{i,k}^l F_{r+1}(\eta_k), \quad (26)$$

where,

$$\mathbf{D}^l = \left(\frac{2}{L_\eta} \right)^l D_{i,k}^l \quad \text{for} \quad i, k = 0, 1, 2, \dots, N_\eta \quad (27)$$

here $D_{i,k}^l$, $j, k = 0, 1, 2, \dots, N_\eta$ denotes an $(N_\eta + 1) \times (N_\eta + 1)$ standard Chebyshev differentiation matrix and the factor $(2/L_\eta)$ is as a result of the application of the chain rule of differentiation, vector $F_{j,r+1}$ can be expressed as

$$F_{i,r+1} = \left[F_{r+1}(\eta_0), F_{r+1}(\eta_1), F_{r+1}(\eta_2), F_{r+1}(\eta_3), \dots, F_{r+1}(\eta_{N_\eta}) \right]^{\check{T}} \quad (28)$$

where \check{T} denotes a matrix transpose. The solution is computed simultaneously across all subintervals and a matrix of coefficients is assembled. To achieve this, since the last two points in the l^{th} subinterval and the first two points in the $(l+1)^{th}$ sub-interval overlap and remain common, we discard the rows corresponding to the repeated grid points and assemble the Chebyshev differentiation matrix as shown below.

$$\begin{bmatrix} A_{1,1}^i & A_{1,2}^i & A_{1,3}^i \\ A_{2,1}^i & A_{2,2}^i & A_{2,3}^i \\ A_{3,1}^i & A_{3,2}^i & A_{3,3}^i \end{bmatrix} \begin{bmatrix} F_{r+1} \\ \Theta_{r+1} \\ \Phi_{r+1} \end{bmatrix} = \begin{bmatrix} R_{1r} \\ R_{2r} \\ R_{3r} \end{bmatrix} \quad (33)$$

The boundary conditions are imposed on the matrix system and evaluated at the collocation points for each subinterval as $f_{r+1}(N_\eta) = 0$, $f'_{r+1}(N_\eta) = 1$, $\theta_{r+1}(N_\eta) = 1$, $\phi_{r+1}(N_\eta) = 1$ and $f'_{r+1}(0) = \beta$, $\theta_{r+1}(0) = 0$, $\phi_{r+1}(0) = 0$.

Starting with the initial approximation, the system is solved iteratively until a solution with the desired accuracy is realized

CONVERGENCE OF SOLUTIONS

A comparison of the numerical results was made against published literature in Table 1. It was found that the findings are consistent with the published results, see [46]. The spectral collocation method with overlapping grids is thus reliable in solving boundary value problems. Sensitivity analysis for the system of differential equations was also done. This is essential for testing the method's accuracy and understanding the impact of small changes to an input variable on the solutions. To test our method's stability, the reciprocal condition number was calculated for the matrices and presented in Table 2. We note that the reciprocal condition number is relatively small that the matrices used are well-conditioned. This is an essential step in confirming the accuracy of the solutions and the overlapping grid spectral collocation method's stability. It was also noted the central processing unit (CPU) time is relatively small, indicating the method is efficient in solving boundary value problems.

Table 1. A comparison of reported literature results with the present results

Pr	Ec	Br	Hayat et al. [46]			Current results		
			$f[0]$	$-\theta[0]$	$-\varphi[0]$	$f[0]$	$-\theta[0]$	$-\varphi[0]$
0.71	10.50	0.10	1.96871	0.237534	0.632846	1.97821781	0.23735723	0.63282430
	1.0		1.54903	0.529374	0.629509	1.54801713	0.52937338	0.62950321
	2.0		1.37220	0.670280	0.622038	1.37211146	0.67027662	0.62102739
0.70	12.10	0.10	1.68425	0.337882	0.633256	1.68423080	0.33788452	0.63325546
	14.10		1.69051	0.29549	0.633719	1.69050310	0.29548573	0.63371797
0.71	10.50	0.70	1.39653	0.352877	0.621139	1.39651831	0.35287083	0.62103738
		1.20	2.01524	0.318826	0.660435	2.01525741	0.31892553	0.66042310

Table 2. Reciprocal condition number using $N_\eta = 30$, $q = 5$

Iterations	t	CPU time (Picoseconds)	Condition number
1	0.4	0.40869	1.2164e+03
2	0.9	0.52877	1.2316e+03
3	1.5	0.59214	1.2328e+03
4	1.9	0.69153	2.2437e+03
5	2.5	0.73419	2.24565e+03
6	3.0	0.81735	2.24634e+03

Convergence analysis is the process of determining the rate at which an approximation approaches the exact solution. To determine the convergence of the numerical method, the infinity error norm is computed between two successive iterations as

$$\|E_{r+1}\|_\infty = \max_{0 \leq \eta \leq T} |F_{r+1}^N - F_r^N| \quad (34)$$

where r is the number of iterations. Tables 3 and 4 show that after the sixth iteration, both the residual and exact

errors are small, implying that the numerical method has converged.

Table 3. Infinity error norm between successive iterations using $N_\eta=30, q=5$

Iterations	Infinity error norm		
	$\ f_{r+1} - f_r\ _\infty$	$\ \theta_{r+1} - \theta_r\ _\infty$	$\ \varphi_{r+1} - \varphi_r\ _\infty$
r			
1.0	2.4312e-2	5.1312e-2	1.2164e-3
2.0	3.2394e-6	3.2402e-3	1.1316e-4
3.0	1.8213e-9	6.6318e-5	1.2328e-6
4.0	1.1347e-12	1.5332e-8	2.2437e-7
5.0	2.4312e-14	2.7372e-12	1.0467e-10
6.0	1.6342e-16	1.0462e-14	1.5233e-15
CPU time (Picoseconds)	0.31273	0.28271	0.25261

Table 4: Overlapping grid spectral collocation approximations using $N_\eta = 30, q = 5$

Iterations	Residual error		
	$\ f_{r+1}\ _\infty$	$\ \theta_{r+1}\ _\infty$	$\ \varphi_{r+1}\ _\infty$
r			
1.0	5.1316e-1	4.0312e-3	2.1164e-2
2.0	4.2394e-4	3.2402e-4	1.8206e-4
3.0	3.1215e-7	2.1318e-6	2.4328e-8
4.0	2.0347e-9	1.4332e-8	2.2437e-9
5.0	2.1312e-11	1.2372e-12	1.0476e-12
6.0	1.2372e-15	1.0562e-16	1.1437e-15
CPU time(picoseconds)	0.24361	0.23347	0.20382

DISCUSSION

The influence of the Hartman number, width parameter, thermophoresis parameter, Reynolds number, Brinkman number, temperature difference parameter, concentration difference parameter, diffusion coefficient, Brownian motion parameter, Deborah number in both relaxation time and retardation time, Eckert number and Prandtl number on entropy generation is presented in Figures 3 – 20. The parameters used in this work is taken from published literature see [46] with air as the fluid. The parameter values are, unless stated otherwise $Ec = 10.5, Pr = 0.71, Sc = 0.5, \varepsilon = 0.5, \delta = 0.41, \beta = 0.3, \Lambda = 0.28, N_t = 0.7$ and $R_d = 0.43$.

Figure 3 demonstrates that an increase in the Brinkman number leads to an increase in entropy generation. The Brinkman number measures the importance of the heat generated by viscous heating to heat transferred by molecular conduction. The higher the value, the slower the conduction of heat produced by viscous dissipation and thus the higher the temperature leading to increased irreversibility. It is also observed that the effects of entropy generation are more prominent near the Riga plate's surface and decrease as the distance from the plate increases. Figure 4 demonstrates the influence of the Eckert number on entropy generation. Increasing the Eckert number leads to a decrease in the entropy generation with minimum values at the centerline of the channel and the opposite occurs near the upper plate. The reduced rate of advective transport is experienced at the plates due to the dominant effects of the magnetic forces leading to higher viscous dissipation causing entropy generation to increase near the Riga plate walls. This effect is expected from the nature of Eq.(12). Figure 5 shows the influence of the concentration difference number on entropy production. Higher values of the concentration difference parameter lead to increased entropy generation. This is expected as more mass is transported, causing both the velocity and thermal boundary layer thickness to increase, leading to a rise in entropy generation

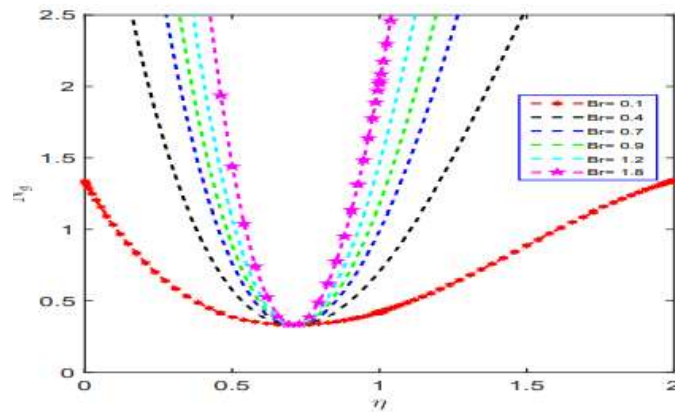


Figure 3. Influence of Brinkmann number on entropy generation

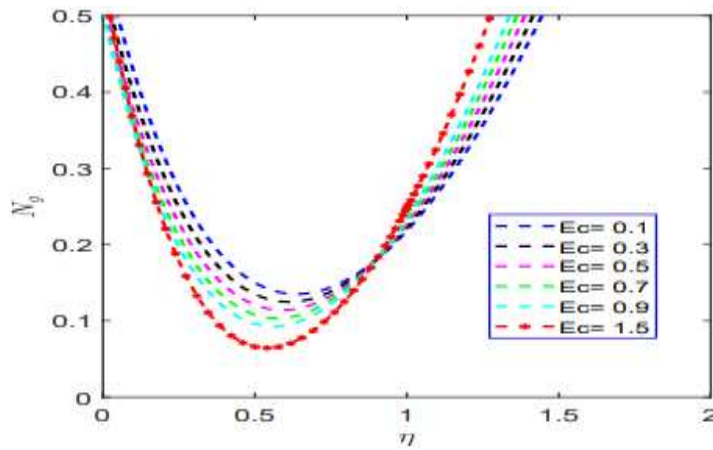


Figure 4. Influence of Eckert number on entropy generation

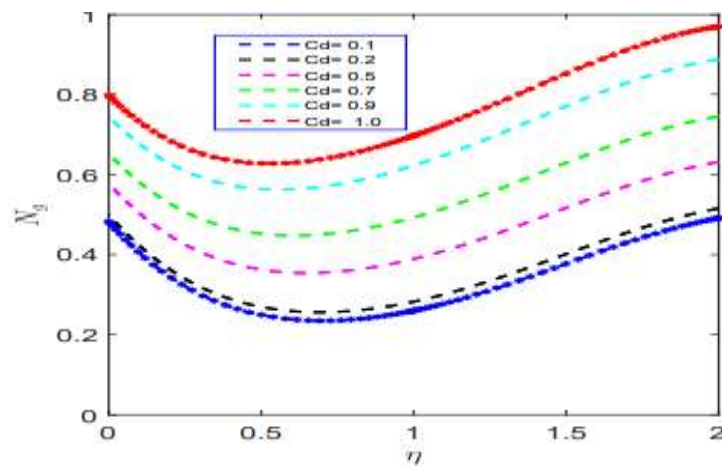


Figure 5. Influence of concentration difference parameter on entropy generation

Figure 6 shows the influence of the diffusion coefficient on entropy generation. An increase in diffusion coefficient leads to an increase in entropy generation. Increased diffusion coefficient parameter causes an increase in both the velocity gradient and temperature gradients of the nanofluid, leading to increased entropy generation. Figure 7 shows the influence of the Prandtl number on entropy production. The Prandtl number increases the entropy generation near the plate due to increased friction irreversibility, while the opposite is observed at the center. Figure 8 shows the influence of the Hartmann number on entropy generation. Increased Hartmann number leads to an increase in the entropy generation. Near the Riga plate, the Hartmann number significantly influences entropy generation, while it has minor effects in the regions far away from the plate. The Hartmann number significantly increases the resistance to fluid motion; thus, the temperature rises, leading to an increase in the entropy production. Figure 9 displays the influence of the Brownian motion parameter on entropy generation. An increase in Brownian motion leads to an increase in entropy generation. The Brownian motion enhances micro-mixing that improves the nanofluid's thermal conductivity causing a temperature increase and an increased entropy generation rate.

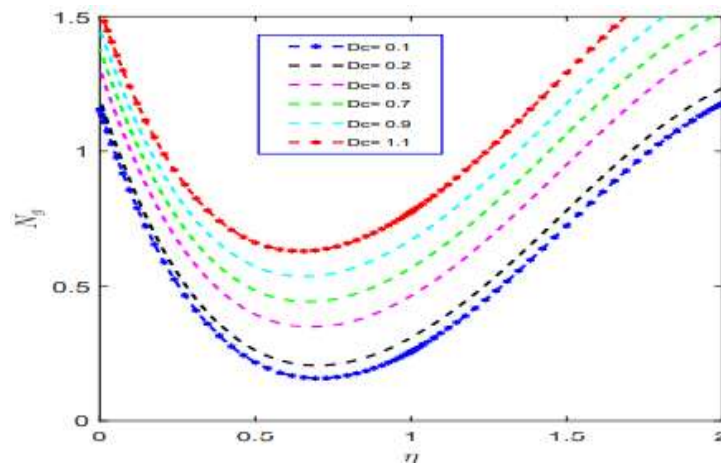


Figure 6. Influence of diffusion coefficient parameter on entropy generation

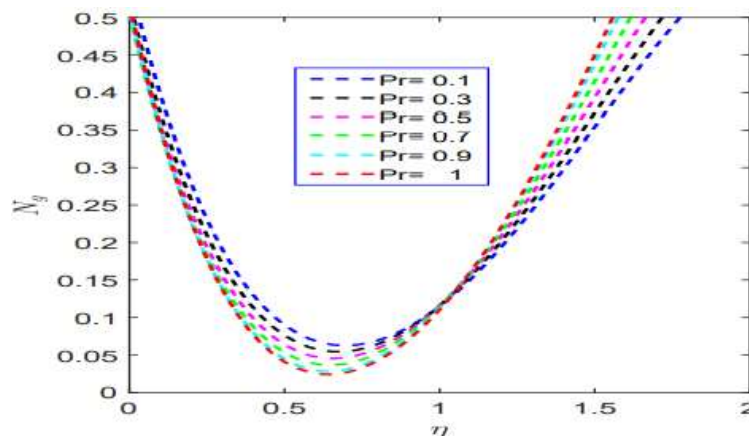


Figure 7. Influence of Prandtl number on entropy generation

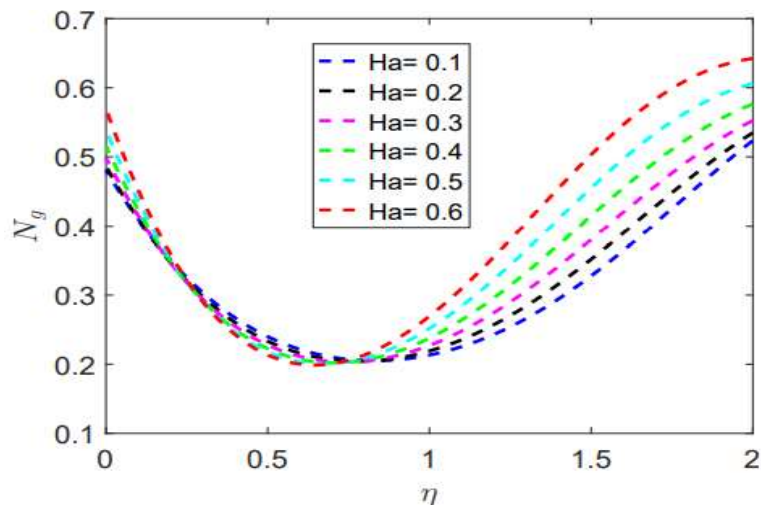


Figure 8. Influence of Hartmann number on entropy generation

Figure 11 shows the influence of the temperature difference parameter on entropy generation. A rise in temperature difference between the fluid particles leads to a fall in the entropy generation. This can be explained by the fact that as the temperature difference between the fluid particles increases, less heat is transferred within the channel leading to less entropy is generated. Figure 12 shows the effect of varying both the Brinkman number and the Reynolds number on entropy generation. A rise in both of the parameters results in a rise in entropy production. This is expected because both the inertia forces and temperature in the fluid increase with an increase in the two parameters resulting in high entropy generation. Figure 13 shows the effect of the Reynolds number and the temperature difference parameter simultaneously. An increase in both parameters leads to an increase in entropy generation. The inertia forces dominate the viscous forces when both the Reynolds number and the temperature difference parameter increases causing a rise in the fluid's temperature boosting entropy production.

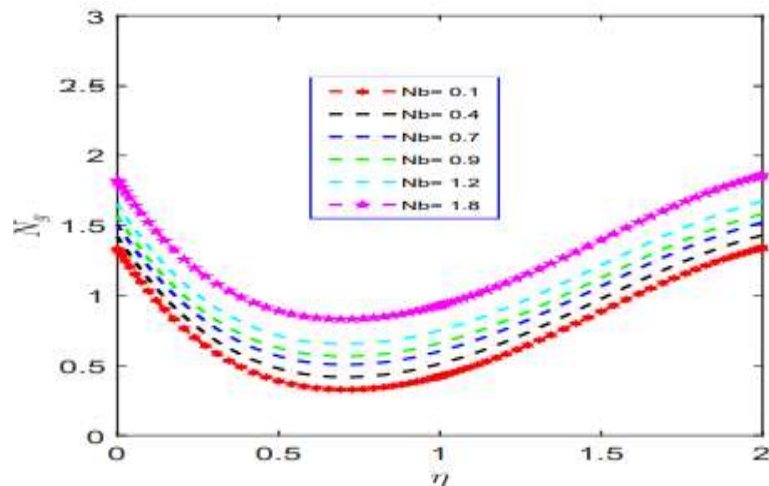


Figure 9. Influence of Brownian motion parameter on entropy generation

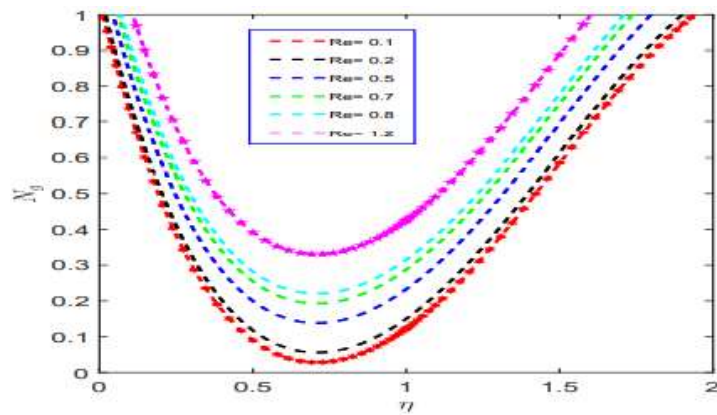


Figure 10. Influence of Reynolds number on entropy generation

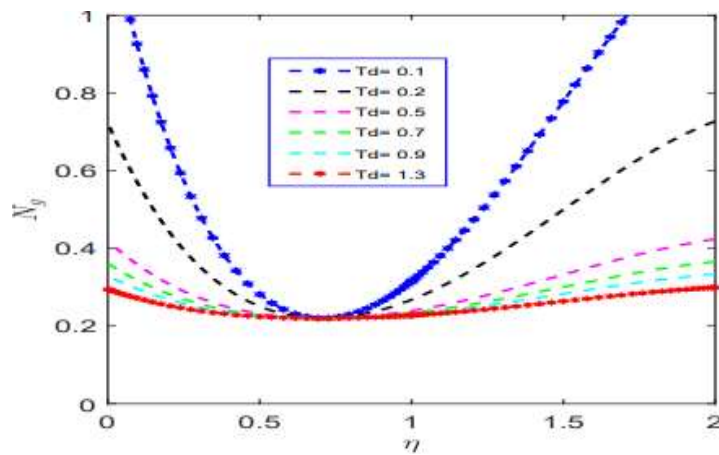


Figure 11. Influence of temperature difference parameter on entropy generation

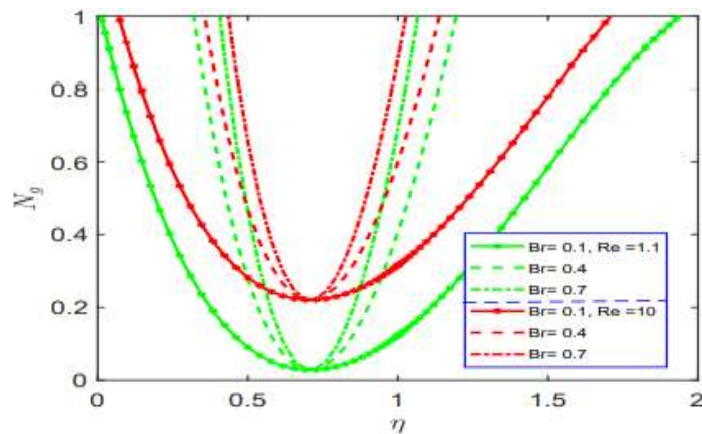


Figure 12. Influence of both Brinkmann number and Reynolds number on entropy generation

Figure 14 shows the effect of both the concentration difference parameter and the Reynolds number on

entropy generation. An increase in both parameters leads to an increase in entropy generation. Figure 15 shows the effect of both the Brinkman number and the Hartmann number on entropy generation. An increase in both parameters translates to a rise in entropy production. An increase in both parameters means both viscous dissipation and electromagnetic force, causing an increase in entropy generation.

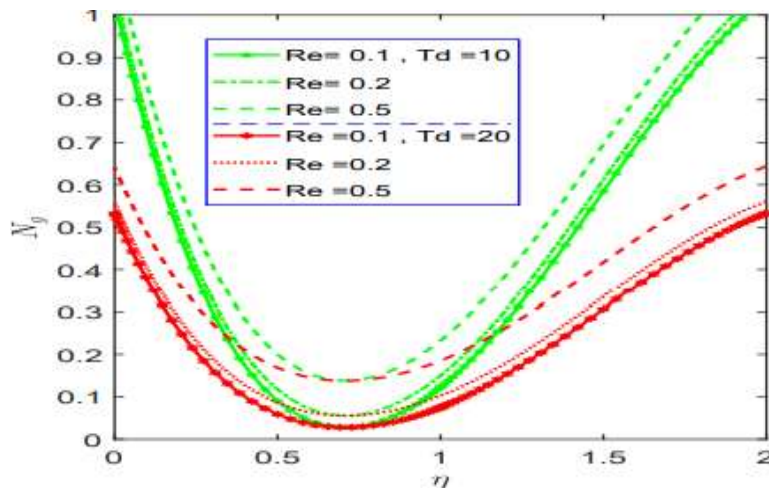


Figure 13. Influence of both temperature difference parameter and Reynolds number on entropy generation

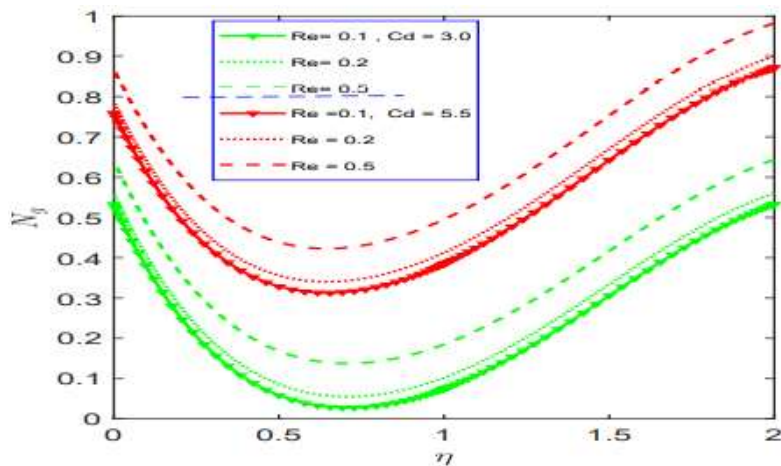


Figure 14. Influence of both concentration difference parameter and Reynolds number on entropy generation

Figure 16 demonstrates the effect of varying both the Reynolds number and the Brownian motion on entropy generation. An increase in both parameters leads to an increase in entropy generation. An increase in both the parameters translates to an increase in molecular collisions and inertial forces, leading to increased entropy generation. Figures 17 and 18 show the Deborah number's influence in both the relaxation time and retardation time, respectively, on the entropy generation rate. The Deborah number quantifies the observation that, with sufficient time, a solid-like material might flow or a fluid-like material may behave like a solid when deformed quickly. Increasing the Deborah's number in relaxation time significantly reduces the fluid motion causing a reduction in the thermal, thermal boundary layer and a decline in the entropy generation. In contrast, the opposite is observed when the Deborah number in retardation time is increased. Figure 19 demonstrates the effect of the Riga plate width parameter on entropy

generation. An increase in the width parameter leads to an increase in entropy generation. Increased width parameter significantly increases the resistance to fluid motion, as a result of which the temperature rises, leading to an increase in the entropy production. Figure 20 shows the influence of the thermophoresis parameter on entropy production. A rise in the thermophoresis parameter leads to a rise in entropy generation. Close to the plate, the entropy generation decreases as the thermophoresis parameter increases. However, the thermophoresis parameter increases the amount of entropy generation away from the plate and within the boundary layer. The amount of entropy produced near the surface is higher, which means the surface is a significant irreversibility source.

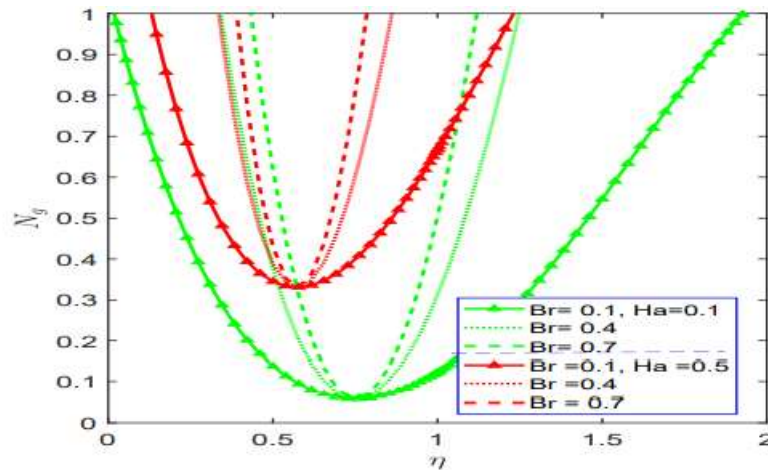


Figure 15. Influence of both Brinkmann number and Hartmann number on entropy generation

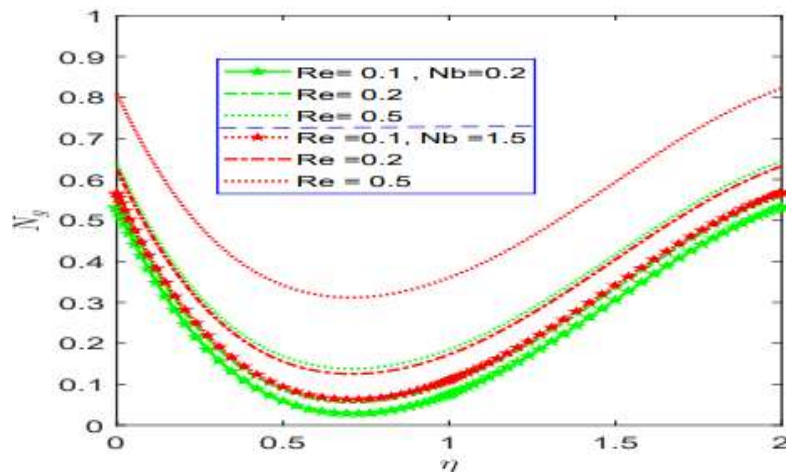


Figure 16. Influence of both Reynolds number and Brownian motion parameter on entropy generation

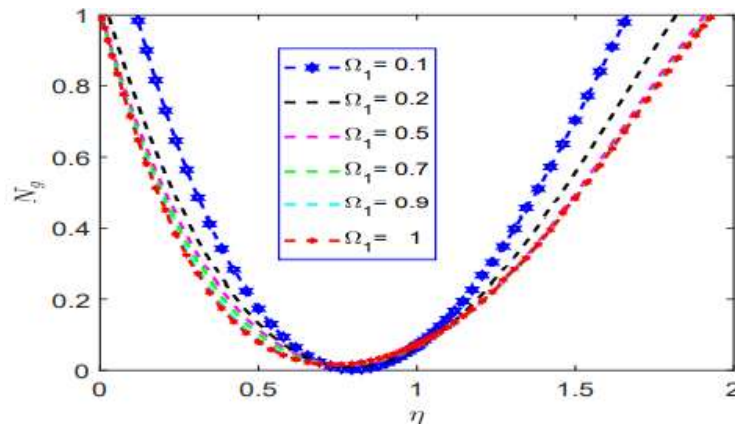


Figure 17. Influence of Deborah number in relaxation time on entropy generation

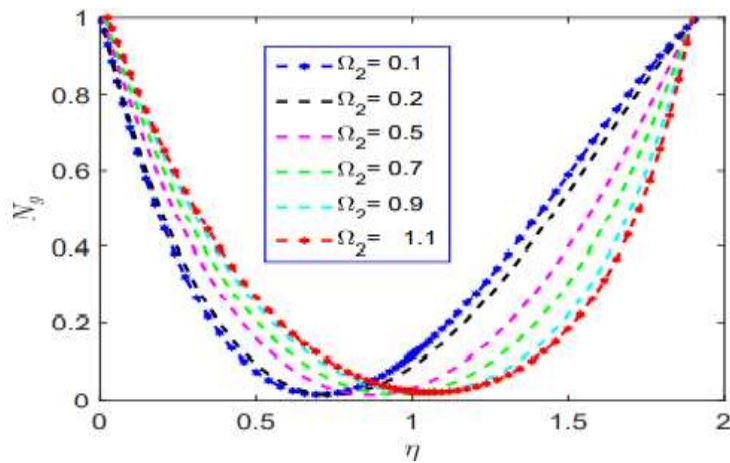


Figure 18. Influence of Deborah number in retardation time on entropy generation

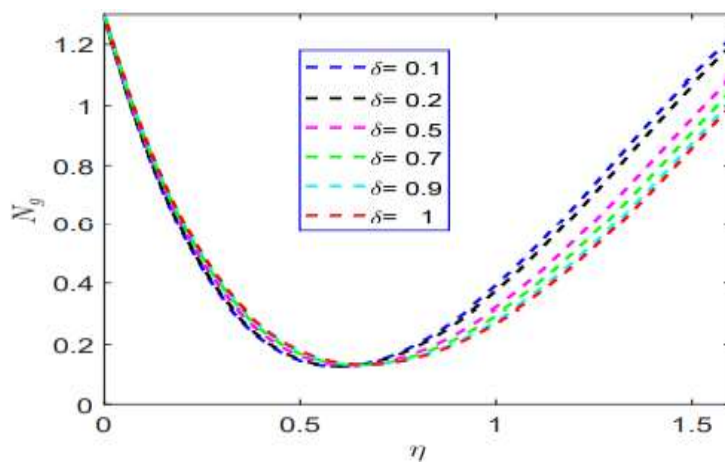


Figure 19. Influence of width parameter on entropy generation

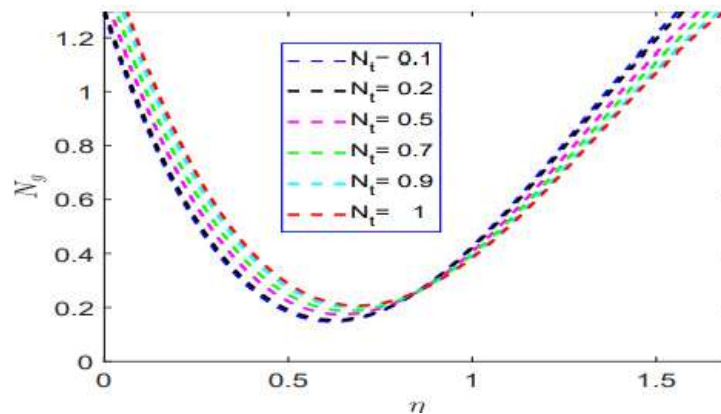


Figure 20. Influence of thermophoresis parameter on entropy generation

CONCLUSION

The study presented a numerical investigation of entropy generation in an Oldroyd-B nanofluid flow past a Riga plate. The highly nonlinear differential equations system was linearized using the QLM scheme and solved numerically using a new spectral collocation method with overlapping grids. Sensitivity and convergence analysis for the method was presented, and the method was confirmed to be stable and convergent for a system of ODEs. The impact of several parameters on entropy generation was determined. The following are the main conclusions drawn from this study:

- An increase in the Hartman number lead to an increase in entropy generation.
- An increase in the width of the Riga plate lead to an increase in entropy generation.
- An increase in Brinkman number leads to an increase in entropy generation.
- Increasing the thermophoresis parameter leads to an increase in entropy generation.
- Increasing the Eckert number leads to a decrease in entropy generation.
- Increasing the Brownian motion parameter leads to an increase in entropy generation.
- The overlapping grid spectral collocation method is accurate and converges fast.

NOMENCLATURE

u	Velocity component in the x direction
v	Velocity component in the y direction
M_h	Electromagnetic field of the Riga-plate
$u_w(x, t)$	Plate velocity
$u_e(x, t)$	Free stream velocity
T	Fluid temperature
T_∞	Temperature of the ambient fluid
T_w	Constant temperature on the surface of the plate
C	Fluid concentration
C_∞	Concentration of the ambient fluid
C_w	Constant concentration on the surface of the plate
$F(\eta)$	Dimensionless stream function with respect to η

q^r	Rosseland approximation
H_a	Modified Hartman number
Pr	Prandtl number
Ec	Eckert number
N_b	Brownian motion parameter
N_t	Thermophoresis parameter
Sc	Schmidt number
Rd	Conduction-radiation parameter
Re	Reynolds number
Br	Brinkmann number
N_G	Entropy generation

Greek symbols

η	Non-dimensional vertical distance
σ_1	Stefan–Boltzmann constant
χ	Mean absorption coefficient
Ω_1	Deborah numbers in terms of relaxation time
Ω_2	Deborah numbers in terms of retardation time
ε	Variable viscosity parameter
δ	Width parameter
γ	Chemical reaction parameter
β	Velocity ratio parameter
ψ	Dimensionless temperature difference
ϱ	Dimensionless concentration difference
Λ	Diffusion coefficient

Subscripts

f	Refers to fluid
-----	-----------------

REFERENCES

- [1] Gailitis AK, Lielausis OA. On the possibility of drag reduction of a flat plate in an electrolyte. Appl. Magneto hydrodyn. Trudy Inst. Fiziky AN Latvia SSR. 1961;12:143.
- [2] Avilov VV. Electric and magnetic fields for the Riga plate. FZR Interner Bericht. 1998.
- [3] Hayat T, Ullah I, Alsaedi A, Ahamad B. Simultaneous effects of nonlinear mixed convection and radiative flow due to Riga-plate with double stratification. Journal of Heat Transfer. 2018; 140 (10):102008. <https://doi.org/10.1115/1.4039994>.
- [4] Rana P, Shukla N. Entropy generation analysis for the non-similar analytical study of nanofluid flow and heat transfer under the influence of the aligned magnetic field. Alexandria engineering journal. 2018; 57(4),3299–3310. <https://doi.org/10.1016/j.aej.2017.12.007>.
- [5] Nayak MK, Shaw S, Makinde OD, Chamkha AJ. Investigation of partial slip and viscous dissipation effects on the radiative tangent hyperbolic nanofluid flow past a vertical permeable Riga plate with internal heating: Buongiorno model. Journal of Nanofluids. 2019; 8(1):51–62.
- [6] Shaw S, Sen SS, Nayak MK, Makinde OD. Boundary layer nonlinear convection flow of Sisko

- nanofluid with melting heat transfer over an inclined permeable electromagnetic sheet. *Journal of Nanofluids*. 2019; 8(5):917–928. <https://doi.org/10.1166/jon.2019.1649>.
- [7] Das M, Mahanta G, Shaw S, Parida SB. Unsteady MHD chemically reactive double-diffusive Casson fluid past a flat plate in a porous medium with heat and mass transfer. *Heat Transfer—Asian Research*. 2019; 48(5):1761–1777. <https://doi.org/10.1002/htj.21456>.
- [8] Nayak MK, Shaw S, Chamkha AJ. 3D MHD free convective stretched flow of a radiative nanofluid inspired by a variable magnetic field. *Arabian Journal for Science and Engineering*. 2019; 44(2): 1269–1282. <https://doi.org/10.1007/s13369-018-3473-y>.
- [9] Kundu B. Semi-analytical methods for heat and fluid flow between two parallel plates. *Journal of Thermal Engineering*. 2015; 1(3):175–181. <https://doi.org/10.18186/jte.12495>.
- [10] Hussein AK, Mustafa AW. Natural convection in a parabolic enclosure with an internal vertical heat source filled with Cu–water nanofluid. *Heat Transfer—Asian Research*. 2018; 47(2):320–336. <https://doi.org/10.1002/htj.21305>.
- [11] Kerme E, Orfi J. Exergy-based thermodynamic analysis of solar-driven organic Rankine cycle. *Journal of Thermal Engineering*. 2015; 1(5):192–202. <https://doi.org/10.18186/jte.25809>.
- [12] Gaikwad VP, Mohite SS, Shinde SS, Dherange ML. Enhancement in thermo-hydraulic performance of microchannel heat sink with secondary flows of leaf venation pattern. *Journal of Thermal Engineering*. 2020; 6(5):677–696.
- [13] Nashine P, Singh TS. Effect of dean number on the heat transfer characteristics of a helical coil tube with variable velocity and pressure inlet. *Journal of Thermal Engineering*. 2020; 6(2):128–139. <https://doi.org/10.18186/thermal.729149>.
- [14] Rudolf E, Eckert G, Drake RM. *Analysis of heat and mass transfer*. 1987.
- [15] Gunn DJ. Transfer of heat or mass to particles in fixed and fluidized beds. *International Journal of Heat and Mass Transfer*. 1978; 21(4):467–476. [https://doi.org/10.1016/0017-9310\(78\)90080-7](https://doi.org/10.1016/0017-9310(78)90080-7).
- [16] Singh PK, Anoop KB, Sundararajan T, Das SK. Entropy generation due to flow and heat transfer in nanofluids. *International Journal of Heat and Mass Transfer*. 2010; 53(21-22):4757–4767. <https://doi.org/10.1016/j.ijheatmasstransfer.2010.06.016>.
- [17] Chen S, Tian Z. Entropy generation analysis of thermal micro-Couette flows in slip regime. *International Journal of Thermal Sciences*. 2010; 49(11):2211–2221.
- [18] Lucia U. Molecular machine as chemical-thermodynamic devices. *Chemical Physics Letters*. 2013; 556:242–244. <https://doi.org/10.1016/j.cplett.2012.11.064>.
- [19] Rehman AU, Mehmood R, Nadeem S. Entropy analysis of radioactive rotating nanofluid with thermal slip. *Applied Thermal Engineering*. 2017; 112:832–840.
- [20] Rashed AA, Kalidasan K, Kolsi L, Velkennedy R, Aydi A, Hussein AK, Malekshah EH. Mixed convection and entropy generation in a nanofluid filled cubical open cavity with a central isothermal block. *International Journal of Mechanical Sciences*. 2018; 135:362–375. <https://doi.org/10.1016/j.ijmecsci.2017.11.033>.
- [21] Ahmed SE, Hussein AK, Mansour MA, Raizah ZA, Zhang X. MHD mixed convection in trapezoidal enclosures filled with micropolar nanofluids. *Nanoscience and Technology: An International Journal*. 2018; 9(4).
- [22] Chand R, Rana GC, Hussein AK. Effect of suspended particles on the onset of thermal convection in a nanofluid layer for more realistic boundary conditions. *International Journal of Fluid Mechanics Research*. 2015; 42(5). 10.1615/InterJFluidMechRes.v42.i5.10.
- [23] Hussein AK, Hussain SH. Heat line visualization of natural convection heat transfer in an inclined wavy cavity filled with nanofluids and subjected to a discrete isoflux heating from its left sidewall. *Alexandria Engineering Journal*. 2016; 55(1):169–186.
- [24] Hussein AK, Bakier M, Hamida MB, Sivasankaran S. Magneto-hydrodynamic natural convection in an inclined t-shaped enclosure for different nanofluids and subjected to a uniform heat source. *Alexandria Engineering Journal*. 2016; 55(3):2157–2169.
- [25] Shaw S, Nayak MK, Makinde OD. The transient rotational flow of radiative nanofluids over an impermeable Riga plate with variable properties. In *Defect and Diffusion Forum*. 2018; volume 387, pages 640–652. <https://doi.org/10.4028/www.scientific.net/DDF.387.640>.
- [26] Esfahani JA, Akbarzadeh M, Rashidi S, Rosen MA, Ellahi R. Influences of wavy wall and nanoparticles on entropy generation overheat exchanger plat. *International Journal of Heat and*

- Mass Transfer. 2017; 109:1162–1171.
- [27] Bhatti MM, Rashidi MM, Pop I. Entropy generation with nonlinear heat and mass transfer on MHD boundary layer over a moving surface using SLM. *Nonlinear Engineering*. 2017; 6(1):43–52. <https://doi.org/10.1515/nleng-2016-0021>.
- [28] Shashikumar NS, Gireesha BJ, Mahanthesh B, Prasannakumara BC, Chamkha AJ. Entropy generation analysis of magneto-nanofluids embedded with aluminum and titanium alloy nanoparticles in a microchannel with partial slips and convective conditions. *International Journal of Numerical Methods for Heat & Fluid Flow*. 2018.
- [29] Walvekar R, Singh A, Khalid M, Gupta TCSM, Yin W. Thermophysical properties of deep eutectic solvent-carbon nanotubes (descent) based nano lubricant. *Journal of Thermal Engineering*. 2018; 6(2):53–64. <https://doi.org/10.18186/thermal.726059>.
- [30] Almakki M, Mondal H, Sibanda P. Entropy generation in MHD flow of viscoelastic nanofluids with homogeneous-heterogeneous reaction, partial slip and nonlinear thermal radiation. *Journal of Thermal Engineering*. 2020;6(3):327–345. <https://doi.org/10.18186/thermal.712452>
- [31] Selimefendigil F. Experimental investigation of nano compressor oil effect on the cooling performance of a vapor-compression refrigeration system. *Journal of Thermal Engineering*. 2019; 5(1):100–104. <https://doi.org/10.18186/thermal.513023>.
- [32] Akinshilo A. Analytical decomposition solutions for heat transfer on straight fins with temperature-dependent thermal conductivity and internal heat generation. *Journal of Thermal Engineering*. 2019; 5(1):76–92. <https://doi.org/10.18186/thermal.505489>.
- [33] Ekiciler R, Aydeniz E, Arslan K. A CFD investigation of Al_2O_3 /water flow in a duct having a backward-facing step. *Journal of Thermal Engineering*. 2019; 5(1):31–41.
- [34] Shaw S, Dogonchi AS, Nayak MK, Makinde OD. Impact of entropy generation and nonlinear thermal radiation on Darcy–Forchheimer flow of $MnFe_2O_4$ -Casson/water nanofluid due to a rotating disk: Application to brain dynamics. *Arabian Journal for Science and Engineering*. 2020; pages 1–20.
- [35] Farooq U, Afridi M, Qasim M, Lu D. Transpiration and viscous dissipation effects on entropy generation in hybrid nanofluid flow over a nonlinear radially stretching disk. *Entropy*. 2018; 20(9):668. <https://doi.org/10.3390/e20090668>.
- [36] Gupta S, Sandeep G. MHD three-dimensional flow of Oldroyd-B nanofluid over a bidirectional stretching sheet: DTM-Padé solution. *Nonlinear Engineering*. 2019;8(1):744–754. <https://doi.org/10.1515/nleng-2018-0047>.
- [37] Alshomrani AS, Irfan M, Salem A, Khan M. Chemically reactive flow and heat transfer of magnetite Oldroyd-B nanofluid subject to stratifications. *Applied Nanoscience*. 2018; 8(7):1743–1754.
- [38] Gireesha BJ, Kumar KG, Prasannakumar BC. Scrutinization of chemical reaction effect on flow and mass transfer of Prandtl liquid over a Riga plate in the presence of solutal slip effect. *International Journal of Chemical Reactor Engineering*. 2018;16(8). <https://doi.org/10.1515/ijcre-2018-0009>.
- [39] Nayak MK, Shaw S, Makinde OD, Chamkha AJ. Effects of homogenous–heterogeneous reactions on radiative NaCl-CNP nanofluid flow past a convectively heated vertical Riga plate. *Journal of Nanofluids*. 2018; 7(4):657–667. <https://doi.org/10.1166/jon.2018.1501>.
- [40] Kasmani RM, Sivasankaran S, Bhuvaneshwari M, Hussein AK. Analytical and numerical study on convection of nanofluid past a moving wedge with Soret and Dufour effects. *International Journal of Numerical Methods for Heat & Fluid Flow*. 2017.
- [41] Karakurt S, Gunes U. A new approach for evaluating the Rankine cycle through entropy generation. *Journal of Thermal Engineering*. 5(6):141–148.
- [42] Bayareh M. Numerical simulation and analysis of heat transfer for different geometries of corrugated tubes in a double pipe heat exchanger. *Journal of Thermal Engineering*. 2019; 5(4):293–301. <https://doi.org/10.18186/thermal.581775>.
- [43] Afridi M, Qasim M, Hussanan A. Second law analysis of dissipative flow over a Riga plate with nonlinear Rosseland thermal radiation and variable transport properties. *Entropy*. 2018; 20(8): 615. <https://doi.org/10.3390/e20080615>.
- [44] Seini IY, Makinde OD. Boundary layer flow near stagnation-points on a vertical surface with slip in the presence of a transverse magnetic field. *International Journal of Numerical Methods for Heat & Fluid Flow*. 2014; 24(3):643–653.

Journal of Thermal Engineering, Research Article, Vol. 7, No. 4, pp. 845-866, May, 2021

- [45] Bejan A. The thermodynamic design of heat and mass transfer processes and devices. *International Journal of Heat and Fluid Flow*. 1987;8(4):258–276. [https://doi.org/10.1016/0142-727X\(87\)90062-2](https://doi.org/10.1016/0142-727X(87)90062-2).
- [46] Hayat T, Khan M, Imtiaz M, Alsaedi A. Squeezing flow past a Riga plate with chemical reaction and convective conditions. *Journal of Molecular Liquids*. 2017;225:569–576. <https://doi.org/10.1016/j.molliq.2016.11.089>.
- [47] Raptis A. Radiation and free convection flow through a porous medium. *International Communications in Heat and Mass Transfer*. 1998; 25(2):289–295.
- [48] Waqas M, Ijaz M, Khan, Hayat T, Alsaedi A. Stratified flow of an Oldroyd-B nanoliquid with heat generation. *Results in Physics*. 2017; 7:2489–2496.
- [49] Bellman RE, Kalaba. *Quasilinearization and nonlinear boundary value problems*. 1965.
- [50] Trefethen LN. *Spectral methods in MATLAB*. 2000; volume 10. Siam.

Chapter 3

Numerical study on combined thermal radiation and magnetic field effects on entropy generation in unsteady fluid flow past an inclined cylinder

In Chapter 2, we reported on entropy generation in an unsteady Oldroyd-B nanofluid flow past horizontally placed parallel Riga plates. The study incorporated the influence of particle Brownian motion parameter and changes in the dimensions of the Riga plates. Riga plates can be used to regulate heat transfer, mass transfer and entropy generation in heat exchangers and other cooling devices. This chapter extends the work in Chapter 2 by considering entropy generation in an unsteady viscous flow past an inclined cylinder. Compared to flow past parallel plates, there are many more real-life applications of flow past cylinders, such as in piped oil transport and piped water flow for domestic and commercial purposes.

We modify Buongiorno's model [135] to include the influence of viscous dissipation, and a variety of velocity slip conditions, thermal slip conditions and chemical reaction effects. The overlapping grid spectral collocation method is used to find the numerical solution to the highly nonlinear partial differential equations that model the flow.



RESEARCH ARTICLE

Numerical study on combined thermal radiation and magnetic field effects on entropy generation in unsteady fluid flow past an inclined cylinder

Zachariah Mbugua Mburu¹, Sabyasachi Mondal^{2,*} and Precious Sibanda¹

¹School of Mathematics, Statistics, and Computer Science, University of KwaZulu-Natal, Private Bag X01, Scottsville 3209, Pietermaritzburg, South Africa and ²Department of Mathematics, Amity University Kolkata, Newtown 700135, Kolkata, West Bengal, India

*Corresponding author. E-mail: sabya.mondal.2007@gmail.com <http://orcid.org/0000-0003-4666-0568>

Abstract

This study reports on combined thermal radiation, chemical reaction, and magnetic field effects on entropy generation in an unsteady nanofluid flow past an inclined cylinder using the Buongiorno model. We consider the impact of viscous dissipation, velocity slip conditions, thermal slip conditions, and the Brownian motion. The transport equations governing the flow are solved using an overlapping grid spectral collocation method. The results indicate that entropy generation is suppressed significantly by thermal radiation and chemical reaction parameters but enhanced with the magnetic field, viscous dissipation, the Brinkman number, and the Reynolds number. Also, fluid flow variables are affected by the thermophoresis parameter, the angle of cylinder inclination, and the Richardson number. We present the findings of the skin friction coefficient, the Nusselt number, and the Sherwood number. The model is applicable in fields such as the petroleum industry, building industries, and medicine.

Keywords: numerical analysis; entropy generation; overlapping grid spectral collocation method; nanofluid; heat transfer

1. Introduction

Entropy generation refers to the amount of useful energy lost in any irreversible processes such as the motion of nanofluids and inelastic stretching of solids, and in thermodynamic cycles such as power plants, heat engines, air conditioners, heat pumps, and refrigerators. Entropy production minimization techniques are applied in many industries whenever heat and mass transfer is involved. The key objective is always to conserve the limited energy resources available and enhance thermodynamic performance. During the past couple of decades, studies on entropy generation in non-Newtonian fluid flow past different geometries have received undivided attention due to their applications in various fields, such as food processing plants, nuclear reactors, biological sciences, chemical engineering, and microelectronic designs. In general, the ultimate optimal design with no energy loss may not exist; however, scientists have made attempts to reduce the energy loss by varying physical parameters in any thermodynamic process. Several authors in the past few decades have reported on entropy generation in nanofluid flow past different geometries using various numerical methods. Clausius (1867) introduced the concept of entropy generation and considered the transfer of energy between two bodies taking temperature into account. He established that entropy is derived from any thermodynamic process without necessarily relying on temperature changes. Mahian et al. (2013) further defined entropy as a measure of a dynamical system thermal energy per unit temperature unavailable to do useful work. Since work is a measure of the orderly motion of molecules, the amount of entropy

Received: 18 May 2020; Revised: 4 September 2020; Accepted: 14 September 2020

© The Author(s) 2020. Published by Oxford University Press on behalf of the Society for Computational Design and Engineering. This is an Open Access article distributed under the terms of the Creative Commons Attribution License (<http://creativecommons.org/licenses/by/4.0/>), which permits unrestricted reuse, distribution, and reproduction in any medium, provided the original work is properly cited.

produced is a measure of molecular disorder in a thermodynamic system. Bahiraei and Majd (2016) discussed heat transfer and entropy generation in a nanofluid flow past a triangular mini channel using the finite volume approach. The rate of entropy production increased with high Reynolds number and reduced significantly with the small size of nanoparticles. Buongiorno's model (Turkyilmazoglu, 2018) was used to analyze entropy production in an electrically conducting fluid flow past a porous curved surface with slip boundary conditions. An increase in the curvature parameter increased the rate of entropy generation. Further, the Brownian motion parameter, the Bejan number, and the magnetic parameter had a remarkable influence on entropy production, as reported by Muhammad, Khan, Khan, and Jameel (2020). Combined effects of thermal radiation and magnetic field on entropy generation in nanofluid flow in a cavity field cylinder was discussed by Huminic and Angel (2020) using the Buongiorno's model and solved the governing equations using finite difference approach.

Yarmand et al. (2014) reported on the effects of the nanoparticle size and concentration on entropy generation in turbulent flow past a tube with variable heat flux and solved the system of equations using the homotopy analysis approach. They found that an increase in both the particle size and concentration promoted growth in entropy generation. Siavashi, Yousofvand, and Rezanejad (2018) reported on the effects of porous fins, nanofluid concentration, the Rayleigh, and the Darcy numbers on entropy generation for flow inside a cavity and used finite volume approach in solving the system of ordinary differential equations (ODEs). Entropy production increased with the introduction of porous fins and the Darcy number, while the low concentration of the nanoparticles reduced entropy production. Dalir (2014) used the implicit Keller box approach to solve entropy generation in a forced convective flow of the Jeffrey fluid past a stretching surface. Aminian, Moghadasi, and Saffari (2020) discussed the effects of the magnetic field on forced convection flow past a vertical cylinder and solved the equations using the finite volume method. They established that an increase in both the Hartman number and the nanoparticle size leads to an increase in entropy production.

Bhatti, Abbas, and Rashidi (2017) reported on entropy production in Eyring–Powell fluid past a porous surface and applied the spectral method with linearization technique in solving the nonlinear ODEs. Rashidi, Ali, Freidoonimehr, and Nazari (2013) discussed entropy generation optimization in an electrically conducting fluid past a rotating surface with a magnetic field. They applied optimization algorithms to minimize entropy production. They established that the entropy generation reduced with a decrease in the Reynolds number, the Brinkman number, and the Hartmann number, respectively. Abolbashari, Freidoonimehr, Nazari, and Rashidi (2014) discussed entropy generation in the Casson nanofluid flow past a stretching cylinder wall, and they solved the highly nonlinear ODEs using homotopy analysis method. Entropy production increased with an increase in the Brownian motion and thermophoresis parameters and reduced with an increase in the Casson parameter and velocity slip parameter, respectively. Freidoonimehr, Rashidi, Abelman, and Lorenzini (2016) analyzed entropy production in MHD flow past a porous rotating plate with Soret and Dufour effects, and they solved the ODEs governing the flow using the homotopy analysis method (HAM). They reported that entropy generation increased with an increase in magnetic parameter, suction parameter, the Prandtl number, and the Schmidt number. The maximum entropy production occurred when both the Soret and the Dufour numbers were increased by 30%. Kargarnovin, Faghidian, Farjami, and Farrahi (2010) used the HAM technique to solve the system of nonlinear ODEs modeling fluid flow in a circular plate. Faghidian, Goudar, Farrahi, and Smith (2012) applied the finite element method in predicting the stress created during the bending of a steel beam in the construction industry. Das, Chakraborty, Jana, and Makinde (2015) reported on entropy production in MHD nanofluid flow past a stretching cylinder with convective boundary conditions, and solved the equations governing the flow using the Runge–Kutta–Fehlberg shooting method. They found that the metallic nanoparticles in the fluid lead to an increase in entropy generation as compared with the base fluid. Mondal, Almakki, and Sibanda (2019) analyzed MHD nanofluid flow with entropy generation incorporating the effects of viscous dissipation. They used spectral methods to solve the conservation equations. Pourmehran, Rahimi-Gorji, and Ganji (2016) investigated MHD nanofluid flow past a vertical stretching plate considering thermal radiation and buoyancy effects, and solved the ODEs governing the flow using the fourth-order Runge–Kutta method with the shooting technique. An increase in thermal radiation and buoyancy parameters leads to the thickening of the thermal boundary layer leading to increased entropy production. Chamkha and Aly (2010) used the finite difference method to solve the nanofluid flow over a porous vertical plate with the magnetic field and suction/injection effects. Sheikholeslami, Jafaryar, Shafee, and Babazadeh (2020b) reported on thermal entropy on nanofluid flow past a wavy channel, and used the finite volume technique in obtaining the desired output. They found that the addition of nanoparticles in the fluid leads to increased entropy production. Sheikholeslami, Jafaryar, Abohamzeh, Shafee, and Babazadeh (2020a) discussed entropy production in turbulent nanofluid flow with a mixed model, and used a finite volume numerical approach to solve the equations governing the flow. They reported that a rise in the velocity of the fluid flow accelerates an increase in entropy generation. Recently, Abdul Hakeem, Nayak, and Makinde (2019); Delkhosh, Parand, and Ganji (2019); Periyadurai, Selvan, and Doh (2019); and Shamshuddin, Thirupathi, and Satya Narayana (2019) studied different types of nanofluid flow. Dhanai, Rana, and Kumar (2016) investigated MHD free convection nanofluid flow past an inclined cylinder using Buongiorno's model and the partial differential equations (PDEs) governing the flow solved using the fourth-order Runge–Kutta–Fehlberg method with a shooting technique. They established that the rate of heat transfer decreased with an increase in the thermal slip parameter, and the coefficient of skin friction increased with increased buoyancy effects. Related studies on MHD flow were reported by Abolbashari, Freidoonimehr, Nazari, and Rashidi (2015); Kataria and Mittal (2017); and Mahanthesh, Giresha, and Gorla (2016).

Literature shows that there are hardly any studies on the analysis of the combined effects of thermal radiation, chemical reaction, and magnetic field on entropy generation in a nanofluid flow past an inclined cylinder using the Buongiorno's model. The main objective is to determine the rate of entropy production in a nanofluid flow past an inclined cylinder when specific physical parameters of the fluid are varied. Further, we investigate velocity, heat, and mass transfer of the fluid flow. The equations governing the flow will be solved using an overlapping grid spectral collocation method, which to the best of our knowledge, has not been used before to solve this problem. The error bound and convergence of the numerical technique is discussed. The physical properties of the fluid, such as skin friction, the Nusselt number, and the Sherwood number, are presented.

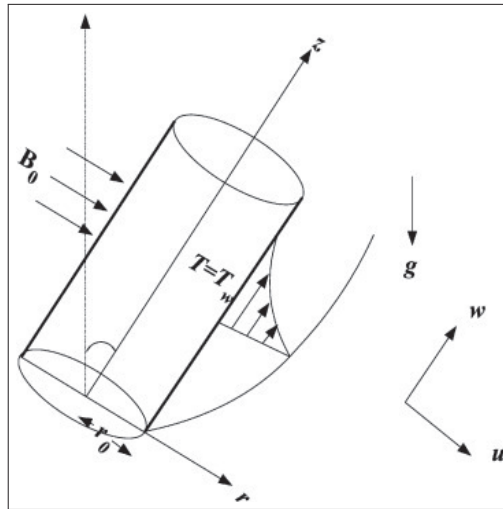


Figure 1: Model of the flow.

2. Mathematical Formulation

We consider a 2D boundary layer unsteady flow of an incompressible fluid past an inclined cylinder with both the velocity slip and convective boundary conditions. The angle of cylinder inclination denoted by α is varied from the z -axis in the clockwise direction, and the walls of the cylinder are assumed to be contracting with velocity W_0z . The physical geometry of the flow with the related cylindrical polar coordinates r and z is as depicted in Fig. 1. The magnetic Reynolds number is assumed to be small such that the induced magnetic field can be neglected compared with the applied magnetic field. The nanofluid is electrically conducting with a material density ρ_p . The magnetic field B_0 is applied in the radial direction perpendicular to the primary fluid flow in the z -axis direction. T_w is assumed to be the convective surface temperature of the cylinder, while T_∞ is the ambient temperature. The surface is heated/cooled by convection from the nanofluid such that $T_w > T_\infty$. The buoyancy force generated due to temperature difference between the surface of the cylinder and the nanofluid tends to accelerate the flow in the upward direction. The concentration of nanoparticles at the surface of the cylinder is controlled by

$$D_B \frac{\partial C}{\partial r} + \frac{D_T}{T_\infty} \frac{\partial T}{\partial r} = 0, \tag{1}$$

where D_B, D_T, C_∞ are the Brownian diffusion coefficient, thermophoresis diffusion coefficient, and ambient concentration, respectively. Applying the boundary layer assumptions, the transport equations become continuity equation

$$\frac{\partial}{\partial r}(rw) + \frac{\partial}{\partial z}(rw) = 0, \tag{2}$$

momentum equation

$$\frac{\partial w}{\partial t} + u \frac{\partial w}{\partial r} + w \frac{\partial w}{\partial z} = \nu \frac{\partial^2 w}{\partial r^2} + \left[-\frac{(\rho_p - \rho)(C - C_\infty)}{\rho} + (1 - C_\infty)(T - T_\infty)\beta \right] g \cos \alpha - \frac{\sigma B_0^2}{\rho} w - \frac{v}{K_p} w, \tag{3}$$

energy equation

$$\frac{\partial T}{\partial t} + u \frac{\partial T}{\partial r} + w \frac{\partial T}{\partial z} = \alpha_m \frac{\partial^2 T}{\partial r^2} - \frac{1}{\rho c_f} \frac{\partial q_r}{\partial r} + \tau \left[D_B \frac{\partial C}{\partial r} \frac{\partial T}{\partial r} + \frac{D_T}{T_\infty} \left(\frac{\partial T}{\partial r} \right)^2 \right] + \frac{\mu}{\rho c_p} \left(\frac{\partial w}{\partial r} \right)^2 + \frac{Q_0}{\rho c_p} (T - T_\infty), \tag{4}$$

and species concentration equation

$$\frac{\partial C}{\partial t} + u \frac{\partial C}{\partial r} + w \frac{\partial C}{\partial z} = D_B \left[\frac{\partial^2 C}{\partial r^2} + \frac{1}{r} \frac{\partial C}{\partial r} \right] + \frac{D_T}{T_\infty} \left[\frac{\partial^2 T}{\partial r^2} + \frac{1}{r} \frac{\partial T}{\partial r} \right] - K_r (C - C_\infty), \tag{5}$$

subject to the boundary conditions (Azam, Khan, & Alshomrani, 2017)

$$\begin{aligned} t > 0: \quad w(z, t) &= \delta W_w + L \frac{\partial w}{\partial r}, \quad u(z, t) = U_w, \quad T(z, t) = T_w + N \frac{\partial T}{\partial r}, \\ C(z, t) &= D_B \frac{\partial C}{\partial r} + \frac{D_T}{T_\infty} \frac{\partial T}{\partial r} \text{ at } r = r_0, \\ t > 0: \quad w &\rightarrow 0, \quad u \rightarrow 0, \quad T \rightarrow T_\infty, \quad C \rightarrow C_\infty \text{ as } r \rightarrow \infty, \end{aligned} \tag{6}$$

where (u, w) are velocity components in radial and axial directions, respectively, ρ is the density of the fluid, ρ_p is the density of nanoparticles, μ is the dynamic viscosity, ν is the kinematic viscosity, g is the acceleration due to gravity, σ is the electrical conductivity,

B_0^2 is the magnetic field strength, K_p is the permeability constant of the porous medium, K_r is the chemical reaction parameter, T is the temperature, C is the concentration, c_f is the heat capacity of the base fluid, c_p is the heat capacity of the nanoparticles, $\alpha_m = k \rho c_p$ is the thermal diffusivity with k as the thermal conductivity, Q_0 is the heat generation constant, q_r is the radiative heat flux, $\tau = (\rho c)_p / (\rho c)_f$ is the ratio of heat capacity of the nanoparticle material to heat capacity of the fluid, t is time, L is the velocity slip, N is the thermal slip, and δ stretching ($\delta > 0$)/shrinking ($\delta < 0$) parameter. The Rosseland approximation (Mansour, 1990) used to describe radiative heat flux in the energy equation is expressed as

$$q_r = -\frac{16\sigma^*}{3k^*} T^4 \frac{\partial T}{\partial r}, \tag{7}$$

where σ^* , k^* represent the Stefan-Boltzmann constant and mean absorption coefficient, respectively. Assuming the temperature difference within the flow is sufficiently small, we express T^4 as a linear function $T^4 \approx 4T_\infty^3 - 3T_\infty^4$ and the derivative of Equation (7) is described as (Das, Sharma, & Sarkar, 2016):

$$\frac{\partial q_r}{\partial r} = -\frac{16\sigma^* T_\infty}{3k^*} \frac{\partial T^2}{\partial r^2}. \tag{8}$$

The system of Equations (2-5) are transformed using the following transformations (Azam et al., 2017):

$$\begin{aligned} \psi &= \sqrt{W_0} \nu z r_0 f(\eta, \xi), \quad \eta = \frac{r^2 - r_0^2}{2r_0} \sqrt{\frac{W_0}{\nu}}, \quad \xi = W_0 t, \quad w = W_0 z f'(\eta, \xi), \\ u &= -\frac{r_0}{r} \sqrt{W_0} \nu f(\eta, \xi), \quad \theta(\eta, \xi) = \frac{T - T_\infty}{T_w - T_\infty}, \quad \phi(\eta, \xi) = \frac{C - C_\infty}{C_\infty}. \end{aligned} \tag{9}$$

Applying the above transformations to Equations (2-5), we have

$$A(1 + 2\eta\vartheta) f''' + 2\vartheta f'' - (f')^2 + ff'' - M^2 f' - \frac{1}{K_p} f' + R_i(\theta - N_c \phi) \cos \alpha - \frac{\partial f'}{\partial \xi} = 0, \tag{10}$$

$$\frac{1}{Pr} [A(1 + 2\eta\vartheta) (\theta'' + N_b \theta' \phi' + N_b \theta'' N_t (\theta')^2) + 3N_t \theta''] + (1 + 2\eta\vartheta) E_c (f'')^2 + He\theta + f\theta' - \frac{\partial \theta}{\partial \xi} = 0, \tag{11}$$

$$A(1 + 2\eta\vartheta) \phi'' + 2\vartheta \phi' + 2\vartheta \frac{N_t}{N_b} \theta' + (1 + 2\eta\vartheta) \theta'' + S_c f \phi' - K_r \phi - \phi. \tag{12}$$

The transformed boundary conditions are expressed as

$$\begin{aligned} f(0, \xi) &= s, \quad f'(0, \xi) = \delta + \lambda f''(0, \xi), \quad \theta(0, \xi) = 1 + \zeta \theta'(0, \xi), \\ N_b \phi'(0, \xi) + N_t \theta'(0, \xi) &= 0 \quad \text{at} \quad \eta = 0, \\ f'(\infty, \xi) &= 0, \quad \theta(\infty, \xi) = 0, \quad \phi(\infty, \xi) = 0 \quad \text{as} \quad \eta \rightarrow \infty. \end{aligned} \tag{13}$$

Here, $0 \leq \xi \leq 1$ and primes denote derivatives with respect to η . The parameters used in Equations (10-13) are defined by

$$\begin{aligned} \vartheta &= \sqrt{\frac{\nu}{r_0^2 W_0}}, & M &= \sqrt{\frac{\sigma B_0^2}{W_0 \rho}}, & K_p &= \frac{k_p^* W_0^3}{\nu^3} \\ Gr &= \frac{\beta g (1 - C_\infty) (T_w - T_\infty) z^2}{\nu^2}, & Re &= \frac{W_0 z^2}{\nu}, & N_c &= \frac{(\rho_p - \rho) C_\infty}{\beta \rho (1 - C_w) (T_w - T_\infty)}, \\ Pr &= \frac{\nu}{\alpha_m}, & N_b &= \frac{\tau D_B (C_w - C_\infty)}{\nu}, & N_t &= \frac{\tau D_T (T_w - T_\infty)}{\nu T_\infty} \\ N_r &= \frac{16\sigma^* T_\infty^3}{3\rho c_f k^* \alpha_m}, & He &= \frac{Q_0 \nu (C_w - C_\infty)}{\nu_0^2 (T_w - T_\infty)}, & Ec &= \frac{W_w^2}{C_f (T_w - T_\infty)}, \\ Ri &= \frac{Gr}{Re^2}, & A &= \frac{\delta r_0^2}{4\nu}, & K_r &= \frac{k_r^* W_0}{\nu^2}, \\ S_c &= \frac{\nu}{D_B}, & s &= -\frac{r u_w}{r_0 \sqrt{W_0 \nu}}, & \lambda &= L \frac{r}{r_0} \sqrt{\frac{W_0}{\nu}}, \\ \zeta &= N \frac{r}{r_0} \sqrt{\frac{W_0}{\nu}}, \end{aligned}$$

where ϑ , M , K_p , Ri , Gr , Re , N_c , A , Pr , N_b , N_t , K_r , N_r , He , Ec , S_c , s , λ , and ζ represent curvature parameter, the Hartman number, permeability parameter, the Richardson number, the Grashof number, the Reynolds number, nanofluid buoyancy ratio, unsteadiness parameter, the Prandtl number, the Brownian motion parameter, thermophoresis parameter, chemical reaction parameter, thermal radiation parameter, heat generation parameter, the Eckert number, the Schmidt number, mass suction/injection, velocity slip, and the thermal slip parameters, respectively.

For practical purpose, the following variables are essential, namely, the local skin friction coefficient

$$\frac{1}{2} \sqrt{Re} C_f = 1 + 3\lambda f(0, \xi) f''(0, \xi), \tag{14}$$

Nusselt number

$$Re^{-\frac{1}{2}} Nu = -(1 + Nr)\theta'(0, \xi), \tag{15}$$

Sherwood number

$$Re^{-\frac{1}{2}} Sh = -\phi'(0, \xi). \tag{16}$$

3. Entropy Generation Analysis

Entropy generation often reduces the amount of energy available for use in most engineering systems and industrial processes. As a result, it is vital to determine entropy generation in a given thermodynamic system to reduce and save the energy lost. Entropy generation can be a result of energy loss through conduction, fluid friction, diffusivity, viscous dissipation, radiation, among others. This study focuses on irreversibility due to chemical reaction, applied external magnetic field, viscous dissipation, and thermal radiation. The volumetric entropy generation equation is expressed by Acharya, Das and Kundu (2019) and Bejan (1982):

$$E_{gen}'' = \frac{k}{T_{\infty}^2} \left[\left(\frac{\partial T}{\partial r} \right)^2 + \frac{16\sigma^* T_{\infty}^3}{3k^*} \left(\frac{\partial T}{\partial r} \right)^2 \right] + \frac{\nu}{T_{\infty}} \frac{\partial^2 w}{\partial r^2} + \frac{\nu}{T_{\infty}} \left(\frac{\partial w}{\partial r} \right)^2 + \frac{\sigma B_0^2}{T_{\infty}} w + \frac{RD}{C_{\infty}} \frac{\partial^2 C}{\partial r^2} + \frac{\nu}{T_{\infty}} Kr(C - C_{\infty}). \tag{17}$$

Equation (17) shows that entropy production is from six sources of irreversibility, namely, thermal radiation, fluid friction, viscous dissipation, magnetic fields, diffusion effects, and chemical reaction, respectively. The characteristic entropy generation equation demonstrates optimal entropy generation at which the thermodynamic performance of a system is optimized and expressed as (Bejan, 2002)

$$E_c''' = \frac{k(T_w - T_{\infty})^2}{r^2 T_{\infty}^2}. \tag{18}$$

Entropy generation (N_G) refers to a ratio of entropy generation rate (E_{gen}''') to characteristic entropy generation rate (E_c''') expressed as

$$N_G = \frac{E_{gen}'''}{E_c'''}. \tag{19}$$

Equation (19) in dimensionless form becomes

$$N_G = Re \left[1 + Nr(1 + \gamma\theta)^3 \right] \theta'^2 + \frac{Re Br}{\gamma^2} (ff''^2 - ff'f''') + \frac{Re Br}{\gamma^2} (f''^2 + Mf'^2) + \frac{Re\psi}{\gamma} \left(\theta'^2 + \frac{Kr\theta'\phi'}{\gamma} \right), \tag{20}$$

where Re , Br , ψ , γ are the Reynolds number, the Brinkman number, diffusion coefficient, and temperature difference parameter, respectively. We define the parameters as

$$Re = \frac{W_0 z^2}{\nu}, \quad Br = \frac{\mu w_0^2(z)}{kT_{\infty}}, \quad \psi = \frac{C_{\infty} RD}{k}, \quad \gamma = \frac{\Delta T}{T_{\infty}} = \frac{T_w - T_{\infty}}{T_{\infty}}. \tag{21}$$

Equation (20) is solved numerically, and we present the results in graphs and tables.

4. Method of Solution

The model consists of a system of highly coupled nonlinear PDEs, which are difficult to solve using both the analytical and semi-analytical numerical techniques. We thus use the overlapping grid spectral collocation method, which involves collocating in both space and time. This method is an advancement of the spectral quasi-linearization method described by Motsa, Dlamini, and Khumalo (2014). We subdivide the semi-infinite domain into smaller domains, and the grid points overlapped. We discard the recurrent grid points leading to a computational matrix that is less dense with zeros for all the repetitive grid points. Therefore, much less computational time is used when solving large matrices, which translates to the efficiency of the method. We define the system of PDEs on a semi-infinite domain $[0, \infty]$, which is then truncated to a finite space $[0, L]$ with L being large enough to approximate conditions at infinity. The system is linearized using quasi-linearization method (QLM) of Bellman and Kalaba (1965) and solved using spectral collocation method applied on overlapping grids of equal length in the computational domain, and the two grid points at the ends of each sub-interval correspond with those of the adjacent sub-intervals canceling out to zero. Applying the QLM to Equations (10)–(12), we obtain the following linearized system :

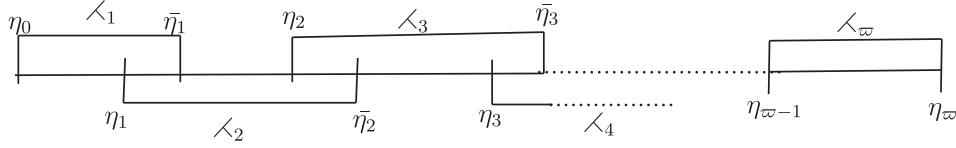
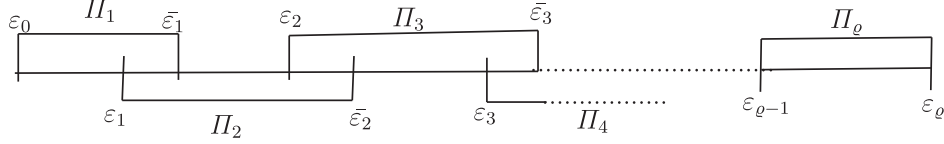
$$a_{0,r} f_{r+1}'' + a_{1,r} f_{r+1}' + a_{2,r} f_{r+1} + a_{3,r} f_{r+1} + a_{4,r} \theta_{r+1} + a_{5,r} \phi_{r+1} - \frac{\partial f}{\partial \xi} = R_{1,r}, \tag{22}$$

$$b_{0,r} \theta_{r+1}'' + b_{1,r} \theta_{r+1}' + b_{2,r} \theta_{r+1} + b_{3,r} f_{r+1} + b_{4,r} f_{r+1} + b_{5,r} \phi_{r+1} - \frac{\partial \theta}{\partial \xi} = R_{2,r}, \tag{23}$$

$$c_{0,r} \phi_{r+1}'' + c_{1,r} \phi_{r+1}' + c_{2,r} \phi_{r+1} + c_{3,r} f_{r+1} + c_{4,r} \phi_{r+1} + c_{5,r} \theta_{r+1} = R_{3,r}. \tag{24}$$

The boundary conditions are

$$\begin{aligned} f_{r+1}(0, \xi) &= s, \quad f_{r+1}'(0, \xi) = \delta + \lambda f_{r+1}''(0, \xi), \quad \theta_{r+1}(0, \xi) = 1 + \zeta \theta_{r+1}'(0, \xi), \\ N_b \phi_{r+1}'(0, \xi) + N_t \theta_{r+1}'(0, \xi) &= 0 \text{ at } \eta = 0, \\ f_{r+1}'(\infty, \xi) &= 0, \quad \theta_{r+1}(\infty, \xi) = 0, \quad \phi_{r+1}(\infty, \xi) = 0 \text{ as } \eta \rightarrow \infty. \end{aligned} \tag{25}$$


 Figure 2: Overlapping grid in η .

 Figure 3: Overlapping grid in ε .

We define the variable coefficients in Equations (22–24) as

$$\begin{aligned} a_{0,r} &= A(1 + 2\eta\vartheta), & a_{1,r} &= 2\vartheta + f_r, & a_{2,r} &= -\left(2f_r' + M^2 + \frac{1}{K_p}\right), & a_{3,r} &= f_r'', \\ a_{4,r} &= R_i \cos\alpha, & a_{5,r} &= R_i N_c \cos\alpha, & b_{0,r} &= \frac{1}{P_r} \left[A(1 + 2\eta\vartheta)(N_b N_t (\theta_r')^2) + 3N_r \right], \\ b_{1,r} &= \frac{1}{P_r} \left[A(1 + 2\eta\vartheta)(N_b \phi_r' + 2N_b N_t \theta_r'' \theta_r') \right] + f_r, & b_{2,r} &= H_e, & b_{3,r} &= 2(1 + 2\eta\vartheta) E_c f_r'', \\ b_{4,r} &= \theta_r', & b_{5,r} &= \frac{1}{P_r} \left[A(1 + 2\eta\vartheta)(N_b \theta_r') \right], & c_{0,r} &= A(1 + 2\eta\vartheta), & c_{1,r} &= 2\vartheta + S_c f_r, \\ c_{2,r} &= -(K_r + 1), & c_{3,r} &= S_c \phi_r', & c_{4,r} &= (1 + 2\eta\vartheta), & c_{5,r} &= 2\vartheta \frac{N_t}{N_b}. \end{aligned}$$

The spatial domain $(\eta, \varepsilon) \in [0, \infty) \times [0, \infty)$ is truncated to $[0, L_\eta] \times [0, L_\varepsilon]$, where L_η and L_ε are large enough to approximate conditions at infinity, and $[0, L_\eta]$ and $[0, L_\varepsilon]$ are broken down into ϖ and ρ overlapping subintervals of equal lengths with

$$\langle l = [\eta_{l-1}, \bar{\eta}_l], \quad \eta_{l-1} < \eta_l < \bar{\eta}_l, \quad \eta_0 = 0, \quad \bar{\eta}_\varpi = L_\eta, \quad l = 1, 2, 3, \dots, \varpi, \quad (26)$$

$$\Pi_l = [\varepsilon_{l-1}, \bar{\varepsilon}_l], \quad \varepsilon_{l-1} < \varepsilon_l < \bar{\varepsilon}_l, \quad \varepsilon_0 = 0, \quad \bar{\varepsilon}_\rho = L_\varepsilon, \quad l = 1, 2, 3, \dots, \rho, \quad (27)$$

where $\eta_l < \bar{\eta}_l$ and $\varepsilon_l < \bar{\varepsilon}_l$ depict the overlapping grid points. Pictorially, the overlapping domain decomposition in both η and ε can be represented as in Figs 2 and 3, respectively.

Further, we divide each subinterval into $(N_\eta + 1)$ and $(N_\varepsilon + 1)$ Chebyshev–Gauss–Lobatto points. The subintervals of the decomposed domain overlap such that the last two points in $\langle l$ and Π_l subintervals overlap with the first two points in $\langle l+1$ and Π_{l+1} subinterval, respectively. Before spectral collocation is applied, we further transform the truncated domain $[0, L_\eta] \times [0, L_\varepsilon]$ to the computational domain $(\eta^*, \varepsilon^*) \in [-1, 1] \times [-1, 1]$ using the linear transformations expressed as

$$\eta^* = \frac{2}{\bar{\eta}_l - \eta_{l-1}} \left[\eta - \frac{1}{2}(\bar{\eta}_l + \eta_{l-1}) \right], \quad \eta \in [\eta_{l-1}, \bar{\eta}_l], \quad (28)$$

$$\varepsilon^* = \frac{2}{\bar{\varepsilon}_l - \varepsilon_{l-1}} \left[\varepsilon - \frac{1}{2}(\bar{\varepsilon}_l + \varepsilon_{l-1}) \right], \quad \varepsilon \in [\varepsilon_{l-1}, \bar{\varepsilon}_l]. \quad (29)$$

We express the grid points as defined by Trefethen (2000) as

$$\eta_i = \cos\left(\frac{\pi i}{N_\eta}\right), \quad \varepsilon_j = \cos\left(\frac{\pi j}{N_\varepsilon}\right), \quad \text{for } i = 0, 1, 2, \dots, N_\eta, \quad j = 0, 1, 2, \dots, N_\varepsilon, \quad \eta, \varepsilon \in [-1, 1]. \quad (30)$$

To obtain an explicit expression for the length of each subinterval given by $L = \bar{\eta}_l - \eta_{l-1}$ in η and $K = \bar{\varepsilon}_l - \varepsilon_{l-1}$ in ε , in terms of the number of subintervals ϖ and ρ , respectively, we solve the equation for L and K in Equation (31) expressed as

$$\varpi L - L(\varpi - 1) \left(\frac{1}{2} - \frac{1}{2} \cos\left\{ \frac{\pi}{N_\eta} \right\} \right) = b - a, \quad \rho K - K(\rho - 1) \left(\frac{1}{2} - \frac{1}{2} \cos\left\{ \frac{\pi}{N_\varepsilon} \right\} \right) = d - c, \quad (31)$$

to obtain

$$L = \frac{d - c}{\varpi + (1 - \varpi) \left(\frac{1}{2} - \frac{1}{2} \cos\left\{ \frac{\pi}{N_\eta} \right\} \right)}, \quad K = \frac{b - a}{\rho + (1 - \rho) \left(\frac{1}{2} - \frac{1}{2} \cos\left\{ \frac{\pi}{N_\varepsilon} \right\} \right)}. \quad (32)$$

Consequently, we obtain the following relations:

$$\bar{\eta}_l = \eta_l + L \left(\frac{1}{2} - \frac{1}{2} \cos\left\{ \frac{\pi}{N_\eta} \right\} \right), \quad \bar{\varepsilon}_l = \varepsilon_l + K \left(\frac{1}{2} - \frac{1}{2} \cos\left\{ \frac{\pi}{N_\varepsilon} \right\} \right). \quad (33)$$

We use Equation (33) to define the boundaries of the overlapping subintervals of the domain and approximate the solution of the system of PDEs using the Lagrange bivariate interpolating polynomial expressed as

$$f(\eta, \varepsilon) \approx \sum_{\varpi=0}^{N_\eta} \sum_{\varrho=0}^{N_\varepsilon} f(\eta_{\varpi}, \varepsilon_{\varrho}) L_{\varpi}(\eta) L_{\varrho}(\varepsilon), \quad \theta(\eta, \varepsilon) \approx \sum_{\varpi=0}^{N_\eta} \sum_{\varrho=0}^{N_\varepsilon} \theta(\eta_{\varpi}, \varepsilon_{\varrho}) L_{\varpi}(\eta) L_{\varrho}(\varepsilon), \quad \phi(\eta, \varepsilon) \approx \sum_{\varpi=0}^{N_\eta} \sum_{\varrho=0}^{N_\varepsilon} \phi(\eta_{\varpi}, \varepsilon_{\varrho}) L_{\varpi}(\eta) L_{\varrho}(\varepsilon), \quad (34)$$

where $L_{\varpi}(\eta)$ and $L_{\varrho}(\varepsilon)$ denote the cardinal standard Lagrange polynomials. The derivatives $F(f, \theta, \phi)$ in respect of η in the l^{th} subinterval for $l = 1, 2, 3 \dots \varpi$ are approximated at the grid points (η_i, ε_j) for $j = 0, 1, 2, \dots, N_\varepsilon$ as

$$\frac{\partial^p F_{r+1}(\eta_i, \varepsilon_j)}{\partial \eta^p} = \overset{l}{D}^p F_{j,r+1} = \left(\frac{2}{L_\eta}\right)^p \sum_{k=0}^{N_\eta} \overset{l}{D}_{i,k}^p F_{r+1}(\eta_k, \varepsilon_j), \quad (35)$$

where,

$$\overset{l}{D} = \left(\frac{2}{L_\eta}\right) \overset{l}{D}_{i,k} \quad \text{for } i, k = 0, 1, 2, \dots, N_\eta, \quad (36)$$

where $\overset{l}{D}_{i,k}$, $j, k = 0, 1, 2, \dots, N_\eta$ represent an $(N_\eta + 1) \times (N_\eta + 1)$ Chebyshev differentiation matrix and the factor $\left(\frac{2}{L_\eta}\right)$ is as a result of application of the chain rule of differentiation. The vector $F_{j,r+1}$ can be expressed as

$$F_{j,r+1} = [F_{r+1}(\eta_0, \varepsilon_j), F_{r+1}(\eta_1, \varepsilon_j), F_{r+1}(\eta_2, \varepsilon_j), \dots, F_{r+1}(\eta_{N_\eta}, \varepsilon_j)]^T, \quad (37)$$

where T denotes the matrix transpose and we approximate the derivatives for ε in the l^{th} subinterval $l = 1, 2, 3 \dots \varrho$ at the grid points (η_i, ε_j) for $i = 0, 1, 2, \dots, N_\eta$ as

$$\frac{\partial F_{r+1}(\eta_i, \varepsilon_j)}{\partial \varepsilon} = \frac{2}{L_\varepsilon} \sum_{\varrho=0}^{N_\varepsilon} \overset{l}{d}_{j,\varrho} F_{r+1}(\eta_i, \varepsilon_{\varrho}) = \sum_{\varrho=0}^{N_\varepsilon} \overset{l}{d}_{j,\varrho} F_{r+1}(\eta_i, \varepsilon_{\varrho}), \quad (38)$$

where $\overset{l}{d}_{j,\varrho} = \left(\frac{N_\varepsilon}{2} \overset{l}{d}_{j,\varrho}\right)$, $j, \varrho = 0, 1, 2, \dots, N_\varepsilon$ are entries of an $(N_\varepsilon + 1) \times (N_\varepsilon + 1)$ standard Chebyshev differentiation matrix. The solution is computed simultaneously across all subintervals. To achieve this, since the last two points in the l^{th} subinterval and the first two points in the $(l + 1)^{\text{th}}$ subinterval overlap and remain common, we discard the rows corresponding to the recurrent grid points and assemble the Chebyshev differentiation matrix D as shown below:

$$D = \begin{bmatrix} \overset{\varpi}{D}_{0,0} & \cdots & \overset{\varpi}{D}_{0,N_\eta-1} & \overset{\varpi}{D}_{0,N_\eta} \\ \overset{\varpi}{D}_{1,0} & \cdots & \overset{\varpi}{D}_{1,N_\eta-1} & \overset{\varpi}{D}_{1,N_\eta} \\ \vdots & \ddots & \vdots & \vdots \\ \overset{\varpi}{D}_{N_\eta-1,0} & \cdots & \overset{\varpi}{D}_{N_\eta-1,N_\eta-1} & \overset{\varpi}{D}_{N_\eta-1,N_\eta} \\ & & \ddots & \ddots \\ & & \overset{2}{D}_{1,0} & \overset{2}{D}_{1,1} & \cdots & \overset{2}{D}_{1,N_\eta-1} & \overset{2}{D}_{1,N_\eta} \\ & & \vdots & \vdots & \ddots & \vdots & \vdots \\ & & \overset{2}{D}_{N_\eta-1,0} & \overset{2}{D}_{N_\eta-1,1} & \cdots & \overset{2}{D}_{N_\eta-1,N_\eta-1} & \overset{2}{D}_{N_\eta-1,N_\eta} \\ & & & & & \overset{1}{D}_{1,0} & \overset{1}{D}_{1,1} & \cdots & \overset{1}{D}_{1,N_\eta} \\ & & & & & \vdots & \vdots & \ddots & \vdots \\ & & & & & \overset{1}{D}_{N_\eta-1,0} & \overset{1}{D}_{N_\eta-1,1} & \cdots & \overset{1}{D}_{N_\eta-1,N_\eta} \\ & & & & & \overset{1}{D}_{N_\eta,0} & \overset{1}{D}_{N_\eta,1} & \cdots & \overset{1}{D}_{N_\eta,N_\eta} \end{bmatrix}.$$

The discarding of the recurrent grid points is key to the method as it leads to a computational matrix that is less dense with zeros for all the repetitive grid points. Thus, a less computational time when solving large matrices and translates to the efficiency of the method. The empty entries of the matrix D are zeros, and $\overset{\varpi}{D}$ is the Chebyshev differentiation matrix in l^{th} subinterval in space variable η . The size of the matrix D is $(N + 1) \times (N + 1)$, and the differentiation matrix in ε assembled similarly. We obtain the higher order differentiation matrices for both η and ε by matrix multiplication $D^2, D^3, D^4, \dots, D^n$. By using the assembled differentiation matrices, we express Equations (22)–(24) as a system of equations given by

$$A_{1,1}^i F_{i,r+1} - \sum_{j=0}^{N_\eta-1} \overset{i}{d}_{i,j} D F_{j,r+1} + A_{1,2}^i \Theta_{i,r+1} + A_{1,3}^i \Phi_{i,r+1} = R_{1,r}, \quad (39)$$

$$A_{2,1}^i F_{i,r+1} + A_{2,2}^i \Theta_{i,r+1} - \sum_{j=0}^{N_\eta-1} \overset{i}{d}_{i,j} \Theta_{j,r+1} + A_{2,3}^i \Phi_{i,r+1} = R_{2,r}, \quad (40)$$

Table 1: Infinity error norm.

t	Error norm	CPU time (picoseconds)	Condition number
0.4	1.4623e-14	0.40869	2.3164e+05
0.9	1.8215e-14	0.52877	2.4716e+05
1.5	2.9241e-11	0.59214	2.5128e+05
1.9	4.4268e-10	0.69153	2.5137e+05
2.5	5.6731e-9	0.73419	2.5265+05
3.0	7.3145e-8	0.81735	2.5734+05

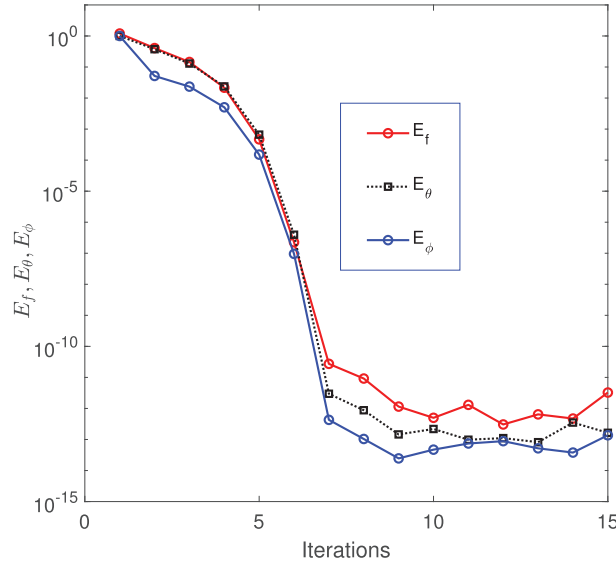


Figure 4: Convergence graph for (f, θ, ϕ) .

$$\mathbf{A}_{3,1}^i \mathbf{F}_{i,r+1} + \mathbf{A}_{3,2}^i \Theta_{i,r+1} + \mathbf{A}_{3,3}^i \Phi_{i,r+1} = \mathbf{R}_{3,r}. \quad (41)$$

The coefficients in Equations (39)–(41) are expressed by

$$\begin{aligned} \mathbf{A}_{1,1}^i &= \mathbf{a}_{0,r} D^3 + \mathbf{a}_{1,r} D^2 + \mathbf{a}_{2,r} D + \mathbf{a}_{3,r} I, & \mathbf{A}_{1,2}^i &= \mathbf{a}_{4,r} I, & \mathbf{A}_{1,3}^i &= \mathbf{a}_{5,r} I, \\ \mathbf{A}_{2,1}^i &= \mathbf{b}_{3,r} D^2 + \mathbf{b}_{4,r} I, & \mathbf{A}_{2,2}^i &= \mathbf{b}_{0,r} D^2 + \mathbf{b}_{1,r} D + \mathbf{b}_{2,r} I, & \mathbf{A}_{2,3}^i &= \mathbf{b}_{5,r} D, \\ \mathbf{A}_{3,1}^i &= \mathbf{c}_{3,r} I, & \mathbf{A}_{3,2}^i &= \mathbf{c}_{4,r} D^2 + \mathbf{c}_{5,r} D, & \mathbf{A}_{3,3}^i &= \mathbf{c}_{0,r} D^2 + \mathbf{c}_{1,r} D + \mathbf{c}_{2,r} I, \end{aligned}$$

where I represents an identity matrix of size $(N_\eta + 1) \times (N_\eta + 1)$. We express the system of Equations (39–41) as a matrix system of the form

$$\begin{bmatrix} \mathbf{A}_{1,1}^i & \mathbf{A}_{1,2}^i & \mathbf{A}_{1,3}^i \\ \mathbf{A}_{2,1}^i & \mathbf{A}_{2,2}^i & \mathbf{A}_{2,3}^i \\ \mathbf{A}_{3,1}^i & \mathbf{A}_{3,2}^i & \mathbf{A}_{3,3}^i \end{bmatrix} \begin{bmatrix} \mathbf{F}_{r+1} \\ \Theta_{r+1} \\ \Phi_{r+1} \end{bmatrix} = \begin{bmatrix} \mathbf{R}_{1r} \\ \mathbf{R}_{2r} \\ \mathbf{R}_{3r} \end{bmatrix}.$$

We impose the boundary conditions in Equation (25) on the matrix and evaluate at the collocation points for each subinterval as

$$\begin{aligned} f_{r+1}(N_\eta, \varepsilon_j) &= s, & f'_{r+1}(N_\eta, \varepsilon_j) &= \delta + \lambda f''_{r+1}(N_\eta, \varepsilon_j), & \theta_{r+1}(N_\eta, \varepsilon_j) &= 1 + \zeta \theta'_{r+1}(N_\eta, \varepsilon_j), & N_b \phi'_{r+1}(0, \varepsilon_j) + N_t \theta'_{r+1}(0, \varepsilon_j) &= 0, \\ f'_{r+1}(0, \varepsilon_j) &= 0, & \theta_{r+1}(0, \varepsilon_j) &= 0. \end{aligned} \quad (42)$$

The system of equations is solved iteratively until we obtain a solution of desired precision. We use the results to find the rate of entropy generation in Equation (20).

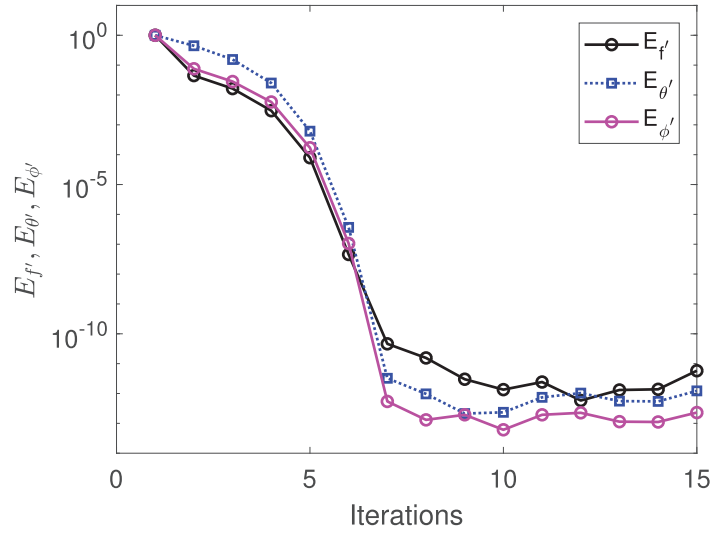


Figure 5: Convergence graph for (f, θ, ϕ) .

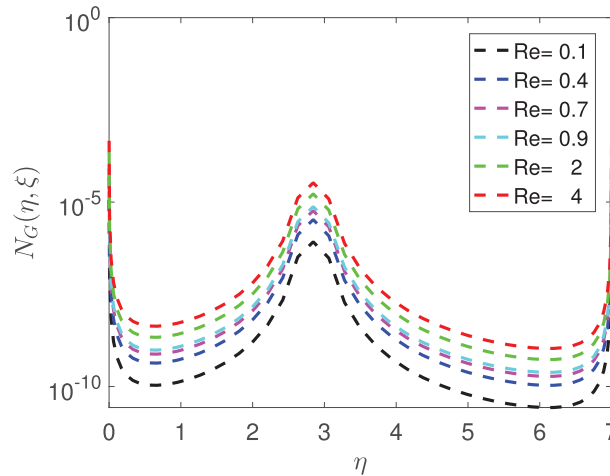


Figure 6: Influence of the Reynolds number on entropy generation.

5. Interpolation Errors and Convergence of Results

Theorem: If $F(\eta, \varepsilon) \in C^{N_\eta+N_\varepsilon+2}([a, b] \times [0, T])$ is a sufficiently smooth function such that at the $(N_\eta + 1)^{\text{th}}$ partial derivative for η , $(N_\varepsilon + 1)^{\text{th}}$ partial derivative for ε and $(N_\eta + N_\varepsilon + 2)^{\text{th}}$ mixed partial derivative for η and ε exist and are continuous, then there exist values $\delta_\eta, \delta'_\eta \in (a, b)$, and $\delta_\varepsilon, \delta'_\varepsilon \in [0, T)$ for which (Samuel & Motsa, 2019)

$$f(\eta, \varepsilon) - F(\eta, \varepsilon) = \frac{\partial^{N_\eta+1} f(\eta, \varepsilon)}{\partial \eta^{N_\eta+1} (N_\eta + 1)!} \prod_{i=0}^{N_\eta} (\eta - \eta_i) + \frac{\partial^{N_\varepsilon+1} f(\eta, \varepsilon)}{\partial \varepsilon^{N_\varepsilon+1} (N_\varepsilon + 1)!} \prod_{i=0}^{N_\varepsilon} (\varepsilon - \varepsilon_i) - \frac{\partial^{N_\eta+N_\varepsilon+2} f(\delta'_\eta, \delta'_\varepsilon)}{\partial \eta^{N_\eta+1} \partial \varepsilon^{N_\varepsilon+1} (N_\eta + 1)! (N_\varepsilon + 1)!} \prod_{i=0}^{N_\eta} (\eta - \eta_i) \prod_{i=0}^{N_\varepsilon} (\varepsilon - \varepsilon_i), \quad (43)$$

where $F(\eta, \varepsilon)$ is the bivariate interpolating polynomial of $f(\eta, \varepsilon)$ at $\{\eta_i\}_{i=0}^{N_\eta}$ grid points in η and $\{\varepsilon_i\}_{i=0}^{N_\varepsilon}$ grid points in the time variable. The remainder formula in Equation (43) is based on the mean value theorem, and we derived recursively from the corresponding univariate error formula given in Equation (46) for a sufficiently smooth function $f(\eta, \varepsilon)$. Taking the absolute value of Equation (43), we obtain

$$\begin{aligned} |f(\eta, \varepsilon) - F(\eta, \varepsilon)| &\leq \max_{(\eta, \varepsilon) \in \Omega} \left| \frac{\partial^{N_\eta+1} f(\eta, \varepsilon)}{\partial \eta^{N_\eta+1}} \right| \frac{\left| \prod_{i=0}^{N_\eta} (\eta - \eta_i) \right|}{(N_\eta + 1)!} + \max_{(\eta, \varepsilon) \in \Omega} \left| \frac{\partial^{N_\varepsilon+1} f(\eta, \varepsilon)}{\partial \varepsilon^{N_\varepsilon+1}} \right| \frac{\left| \prod_{i=0}^{N_\varepsilon} (\varepsilon - \varepsilon_i) \right|}{(N_\varepsilon + 1)!} \\ &+ \max_{(\eta, \varepsilon) \in \Omega} \left| \frac{\partial^{N_\eta+N_\varepsilon+2} f(\delta'_\eta, \delta'_\varepsilon)}{\partial \eta^{N_\eta+1} \partial \varepsilon^{N_\varepsilon+1}} \right| \frac{\left| \prod_{i=0}^{N_\eta} (\eta - \eta_i) \prod_{i=0}^{N_\varepsilon} (\varepsilon - \varepsilon_i) \right|}{(N_\eta + 1)! (N_\varepsilon + 1)!}, \end{aligned} \quad (44)$$

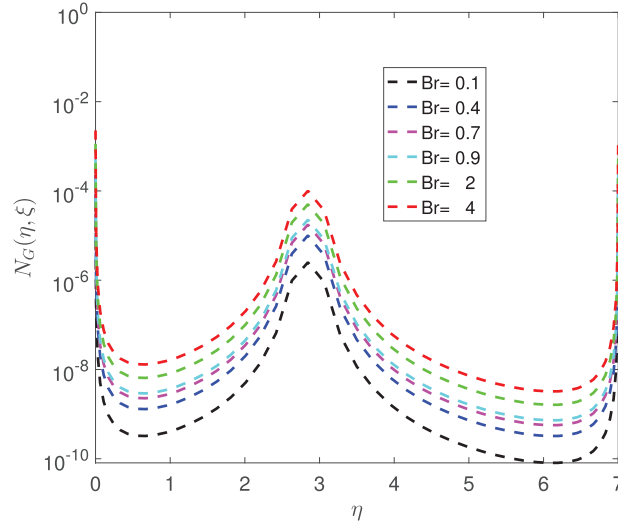


Figure 7: Influence of the Brinkman number on entropy generation.

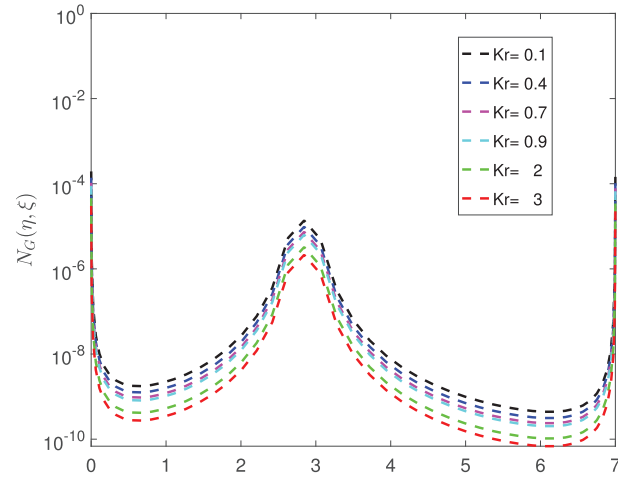


Figure 8: Influence of the chemical reaction parameter on entropy generation.

where $\Omega = [a, b] \times [0, T]$ and since the function $f(\eta, \varepsilon)$ is assumed to be smooth on the defined domain of approximation, it follows that its derivatives are bounded and thus there exist constants C_1, C_2, C_3 such that

$$\max_{(\eta, \varepsilon) \in \Omega} \left| \frac{\partial^{N_\eta+1} f(\eta, \varepsilon)}{\partial \eta^{N_\eta+1}} \right| \leq C_1, \quad \max_{(\eta, \varepsilon) \in \Omega} \left| \frac{\partial^{N_\varepsilon+1} f(\eta, \varepsilon)}{\partial \varepsilon^{N_\varepsilon+1}} \right| \leq C_2, \quad \max_{(\eta, \varepsilon) \in \Omega} \left| \frac{\partial^{N_\eta+N_\varepsilon+2} f(\delta'_\eta, \delta'_\varepsilon)}{\partial \eta^{N_\eta+1} \partial \varepsilon^{N_\varepsilon+1}} \right| \leq C_3. \quad (45)$$

We defined the error bound theorem for the bivariate Lagrange interpolation polynomial using Chebyshev Gauss-Lobatto nodes on the domain $[-1, 1]$. The root of the N^{th} degree Chebyshev Gauss-Lobatto polynomial of the first kind is expressed as $T'_{N_\eta}(\hat{\eta}) = 0$, and that of the $(N_\eta + 1)^{\text{th}}$ degree described as

$$L_{N_\eta+1}(\hat{\eta}) = (1 - \eta^2) T'_{N_\eta}(\hat{\eta}). \quad (46)$$

We further express this relation as

$$L_{N_\eta+1}(\hat{\eta}) = (1 - \eta^2) T'_{N_\eta}(\hat{\eta}) = -N_\eta \hat{\eta} T_{N_\eta}(\hat{\eta}) + N_\eta T_{N_\eta-1}(\hat{\eta}). \quad (47)$$

Using the triangle inequality and noting that $|T_{N_\eta}(\hat{\eta})| \leq 1, \forall \hat{\eta} \in [-1, 1]$, we have

$$|L_{N_\eta+1}(\hat{\eta})| = |-N_\eta \hat{\eta} T_{N_\eta}(\hat{\eta}) + N_\eta T_{N_\eta-1}(\hat{\eta})| \leq |-N_\eta \hat{\eta} T_{N_\eta}(\hat{\eta})| + |N_\eta T_{N_\eta-1}(\hat{\eta})| \leq 2N_\eta. \quad (48)$$

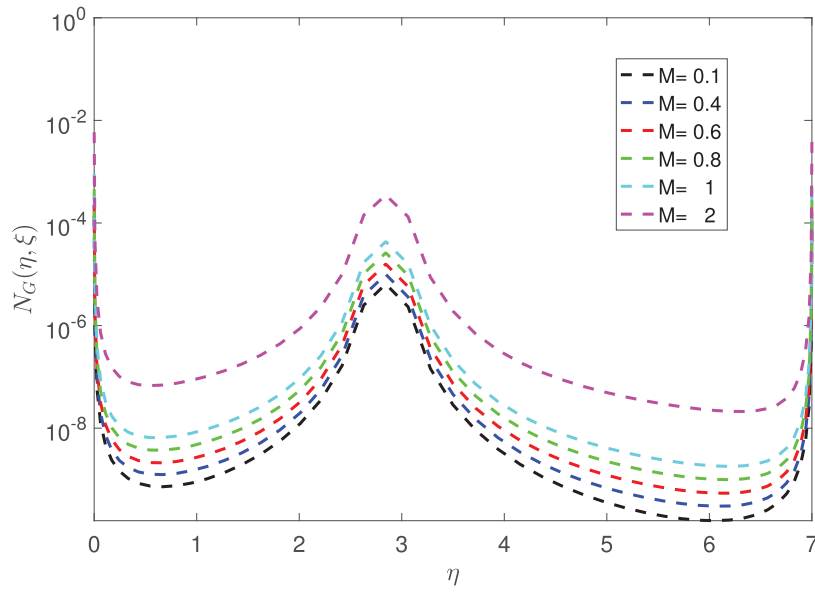


Figure 9: Influence of the magnetic parameter on entropy generation.

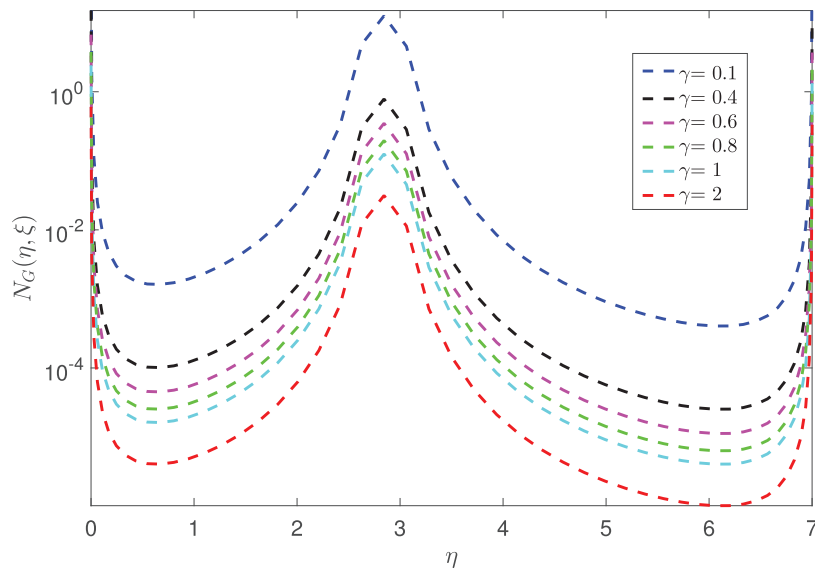


Figure 10: Influence of the temperature difference parameter on entropy generation.

The absolute value of the leading coefficient of $L_{N+1}(\hat{\eta})$ is $2^{N-1}N$. The components 2^{N-1} and N , respectively, come from the $T_N(\hat{\eta})$ leading coefficient and the N^{th} differentiation law applied to $T_N(\hat{\eta})$. We express the product term in the error bound Equation (44) as

$$\prod_{i=0}^{N_\eta} (\hat{\eta} - \hat{\eta}_i) = \frac{L_{N_\eta-1}(\hat{\eta})}{2^{N_\eta-1} N_\eta} = \frac{4}{2^{N_\eta}}. \tag{49}$$

The polynomial in Equation (49) is bounded by

$$\left| \prod_{i=0}^{N_\eta} (\hat{\eta} - \hat{\eta}_i) \right| = \left| \frac{L_{N_\eta-1}(\hat{\eta})}{2^{N_\eta-1} N_\eta} \right| \leq \frac{2N_\eta}{2^{N_\eta-1} N_\eta} = \frac{4}{2^{N_\eta}}. \tag{50}$$

For a general interval, Equation (44) is bounded by

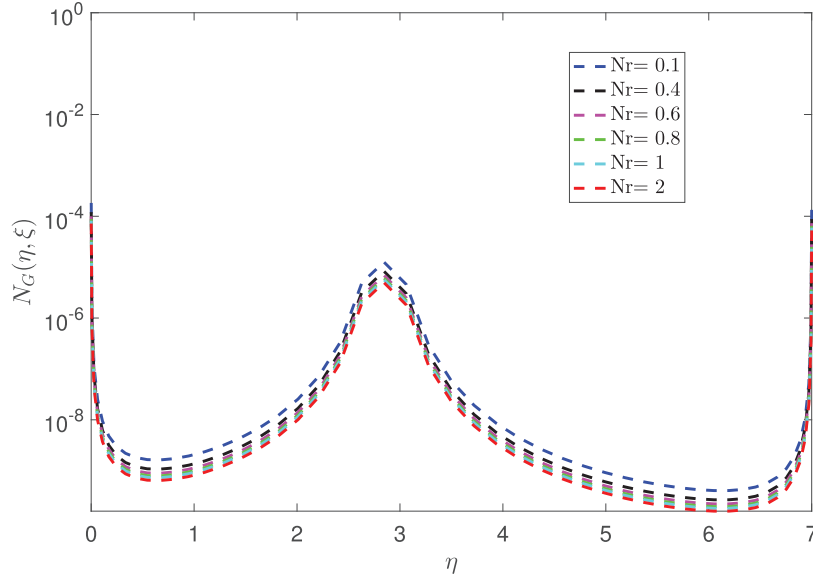


Figure 11: Influence of the thermal radiation parameter on entropy generation.

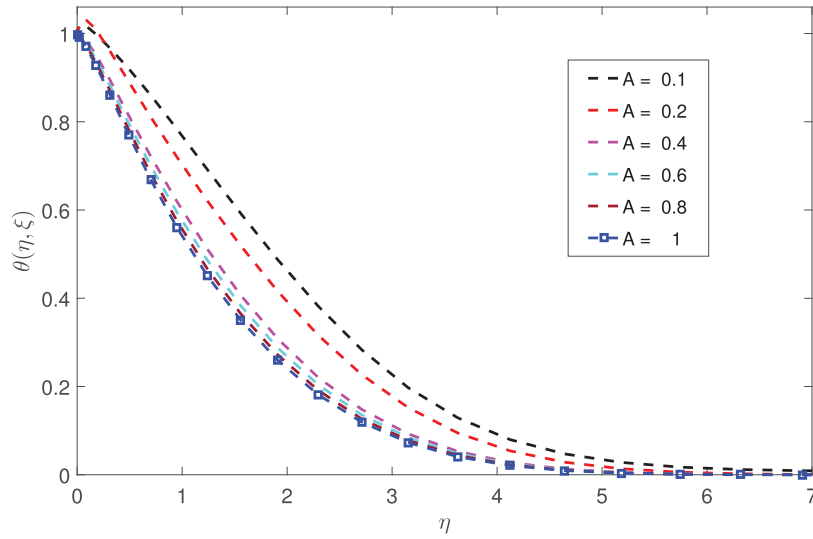


Figure 12: Influence of the unsteadiness parameter on temperature profile.

$$\begin{aligned} \max_{a \leq \eta \leq b} \left| \prod_{i=0}^{N_\eta} (\eta - \eta_i) \right| &= \max_{a \leq \eta \leq b} \left| \prod_{i=0}^{N_\eta} \frac{(b-a)}{2} (\hat{\eta} - \hat{\eta}_i) \right| = \left(\frac{b-a}{2} \right)^{N_\eta+1} \max_{-1 \leq \hat{\eta} \leq 1} \left| \prod_{i=0}^{N_\eta} (\hat{\eta} - \hat{\eta}_i) \right| \\ &= \left(\frac{b-a}{2} \right)^{N_\eta+1} \max_{-1 \leq \hat{\eta} \leq 1} \left| L_{N_\eta-1}(\hat{\eta}) \right| \leq \frac{4 \left(\frac{b-a}{2} \right)^{N_\eta+1}}{2^{N_\eta-1} N_\eta} = 8 \left(\frac{b-a}{4} \right)^{N_\eta+1}. \end{aligned} \quad (51)$$

Similarly, we conclude that the second product factor is bounded by

$$\max_{0 \leq \xi \leq T} \left| \prod_{k=0}^{N_\xi} (\xi - \xi_k) \right| = \left(\frac{T}{2} \right)^{N_\xi+1} \max_{-1 \leq \hat{\xi} \leq 1} \left| L_{N_\xi-1}(\hat{\xi}) \right| \leq \frac{4 \left(\frac{T}{2} \right)^{N_\xi+1}}{2^{N_\xi-1} N_\xi} = 8 \left(\frac{T}{4} \right)^{N_\xi+1}. \quad (52)$$

Using Equations (51)–(52) and (45) in Equation (44), we complete the proof. We carry out the convergence analysis of the Chebyshev differential matrix used to solve the system of differential equations. This analysis is essential in testing the robustness of the algorithm and confirming that the matrix is well conditioned. To determine the convergence of the numerical scheme, we compute

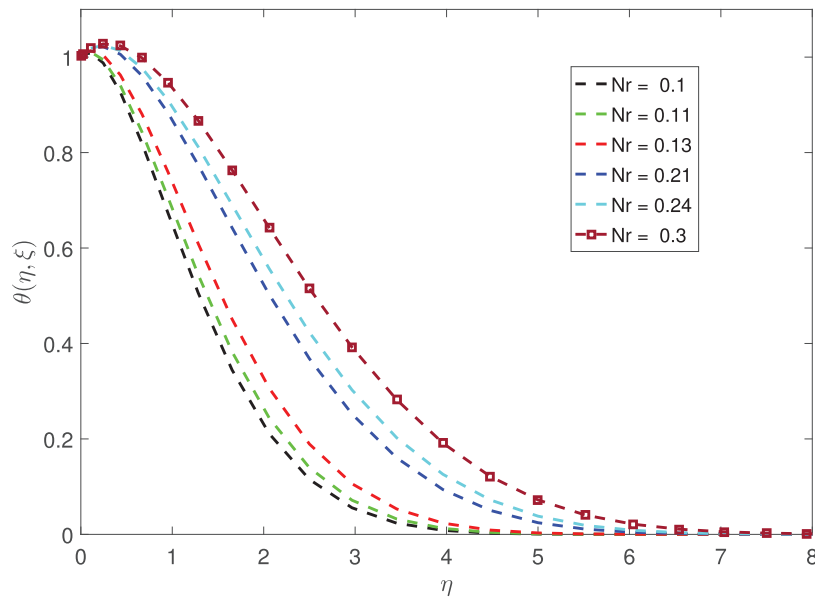


Figure 13: Influence of the thermal radiation parameter on temperature profile.

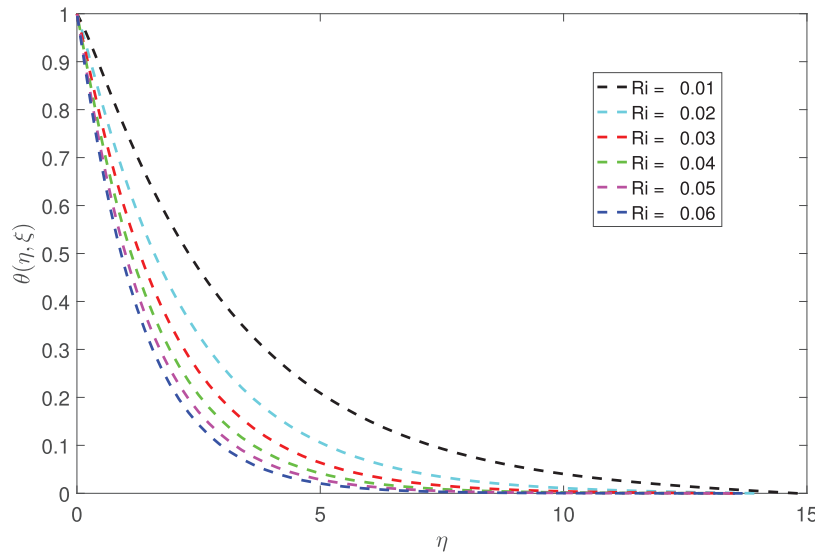


Figure 14: Influence of the Richardson number on temperature profile.

the infinity error norm between two successive iterations as

$$|S_{s+1}|_{\infty} = \max_{0 \leq t \leq T} |u_{s+1}^N - u_s^N|, \tag{53}$$

where the parameter s is the number of iterations made.

6. Results and Discussion

This section presents results for convergence of the method and approximate solutions to the system of PDEs. The results are discussed and presented in tables and graphs. Table 1 shows the error norm, CPU time, and the conditional number of the matrix at different time intervals. The number of grid points in both space and time is kept constant, and the solutions are obtained after the sixth iteration. We found that the accuracy of the numerical scheme deteriorates as the time interval increases indicating that convergence occurs at a short time interval. Further, there is a negligible effect on both the condition number and computation time,

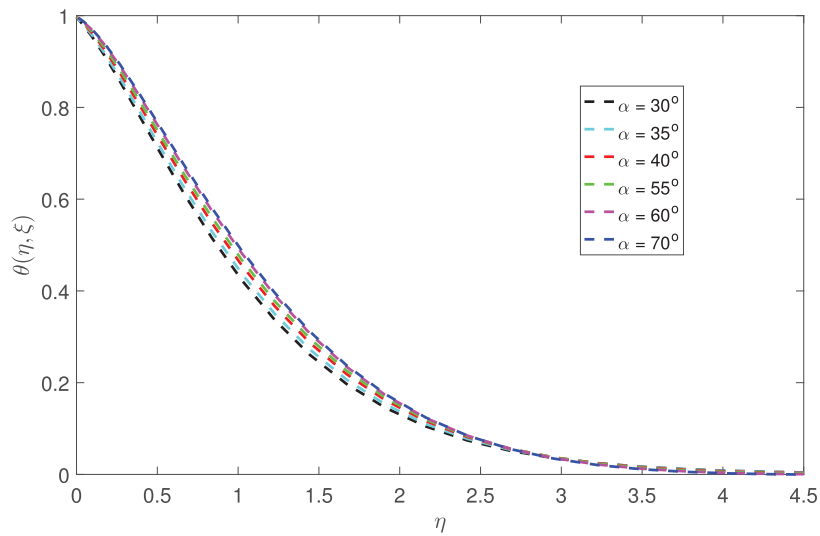


Figure 15: Influence of the angle of inclination on temperature profile.

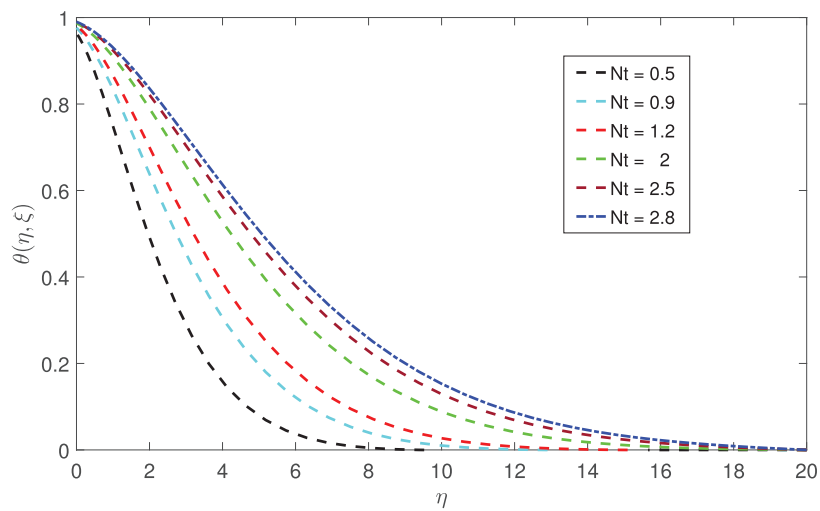


Figure 16: Influence of the thermophoresis parameter on temperature profile.

which explains the stability of the scheme. We additionally note that as long as time interval ε is kept small, accurate results are guaranteed when using overlapping grid spectral collocation method. Thus, the algorithm can be relied upon to give reliable solutions to highly nonlinear governing equations.

Figures 4 and 5 show the absolute difference for successive approximate values of (f, θ, ϕ) and (f', θ', ϕ') versus iterations, respectively. Both of the graphs converge after the sixth iteration. We further establish that the approximation error is relatively small, approximately 10^{-14} and 10^{-16} , respectively. We confirm the accuracy and fast convergence of the method resulting from the overlapping nature of the selected grid points. These results conclude that the overlapping grid spectral collocation method is efficient in solving highly nonlinear PDEs. Figure 6 displays the effects of the Reynolds number on the entropy generation. The irreversibility process increases with an increase in the Reynolds number. At higher Reynolds number, the flow tends to be almost turbulent. The turbulence results from differences in the flow speed and direction, which may sometimes intersect or even move counter to the main course of the flow. The eddy currents begin to churn the flow, using up energy in the process, which increases the chances of entropy production. We may use this to predict the transition from laminar to turbulent flows, scaling of similar but different-sized flow situations, design of fountain heads, pumps, and water pipes (Donnelly, 2012).

Figure 7 displays the influence of the Brinkman number on entropy generation. Entropy generation significantly grows close to the walls of the cylinder and fades away toward the center as we increase the Brinkman number. As the fluid flows in the channel, frictional forces between the walls and fluid layers grow, leading to heat transfer by conduction and viscous dissipation, causing a

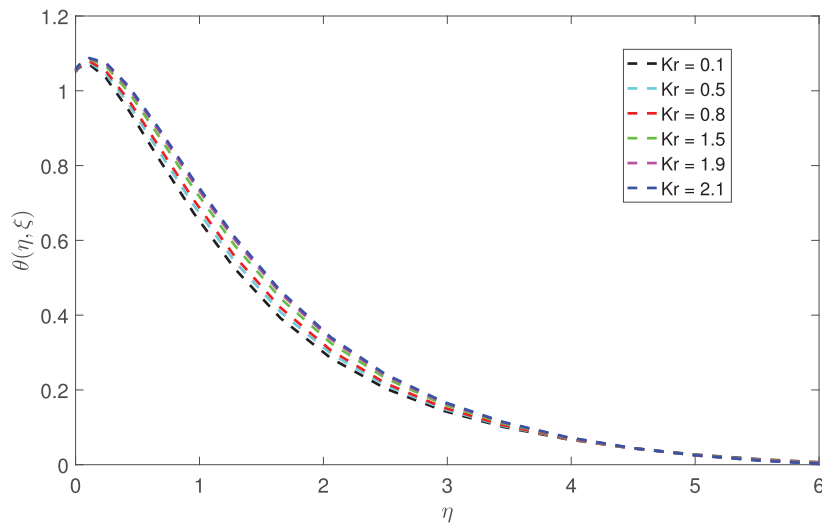


Figure 17: Influence of the chemical reaction parameter on temperature profile.

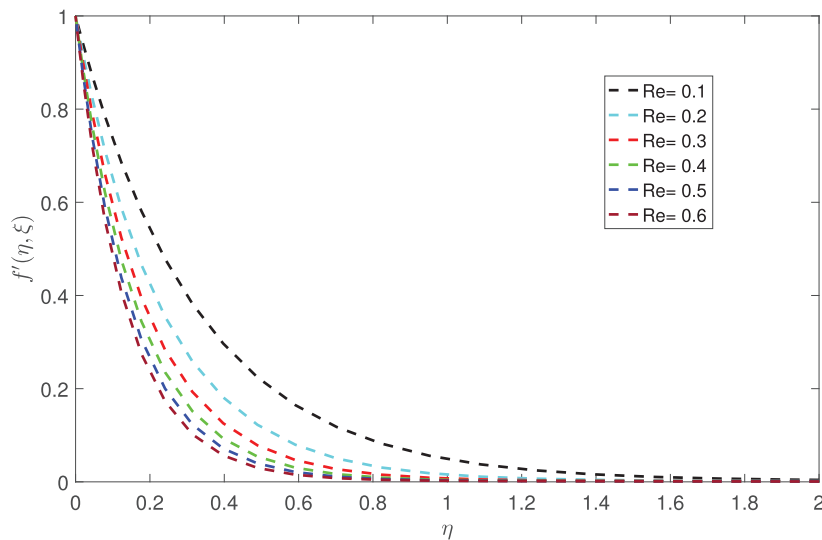


Figure 18: Influence of the Reynolds number on velocity profile.

rise in the temperature of the fluid. As a result, energy loss through entropy generation occurs an occurrence commonly found in polymer processing. Figure 8 shows the influence of the chemical reaction parameter on the entropy generation. An increase in the chemical reaction parameter suppresses entropy production in the flow. As the fluid flows in the conduit, kinetic energy is used up in the chemical bond-breaking process resulting in less entropy production. Figure 9 shows the influence of the magnetic number on entropy generation. The magnetic parameter increase has a positive effect on entropy generation. Increasing magnetic forces leads to a rise in the Lorentz forces, which, as a result, leads to an increase in shear stress, increasing the entropy generation. We can apply this concept in the electronic industry where the magnetic fields applied in the nanofluid can act as liquid seals to keep dust out of the computer hard drive.

Figure 10 shows the influence of the temperature difference parameter on the entropy generation. An increase in the temperature difference parameter suppresses the production of entropy due to the assumption that the temperature difference between the wall of the inclined cylinder and fluid layers is sufficiently small. Figure 11 displays the influence of the thermal radiation parameter on the entropy generation. A rise in the thermal radiation parameter leads to an increase in entropy generation. Heat is transferred from the stretching walls of the cylinder to the fluid layers by conduction, causing a rise in temperature within the conduit and thus generating more heat in the flow. We can apply this in the design heat exchangers, among other thermodynamic systems. Figure 12 shows the effect of the unsteadiness parameter on temperature. An increase in the unsteadiness parameter suppresses the temperature of the nanofluid. The stretching of the cylinder wall causes the unsteady flow to occur. As a result, the thermal energy used up causes a

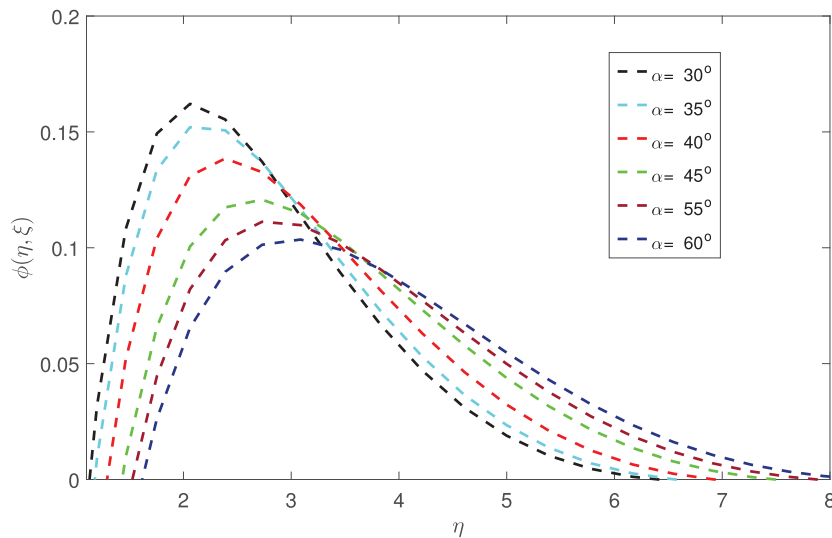


Figure 19: Influence of the angle of inclination to concentration profile.

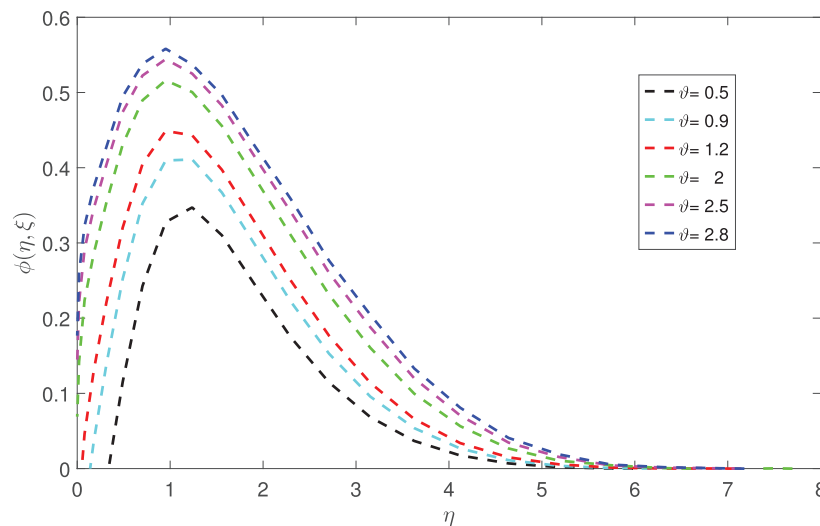


Figure 20: Influence of the curvature parameter on concentration profile.

reduction in the thermal boundary layer thickness suppressing the temperature growth. We can conclude that stretching the walls of a model can be used in stabilizing the temperatures of the thermodynamic system. Figure 13 shows the effect of the thermal radiation parameter on temperature. An increase in thermal radiation leads to a rise in the temperature of the fluid. The stretching walls of the cylinder emit thermal radiation in all directions causing the thermal boundary layer to thicken. We may apply this concept in controlling temperature emitted from radiant heat panels and in photography.

Figure 14 shows the influence of the Richardson number on the temperature profiles of the fluid. An increase in Richardson number leads to a decrease in temperature profiles of the nanofluid. As the fluid flows, the buoyancy forces increase, resulting in the shear thinning of the thermal boundary layer. These causes the temperature of the liquid to decrease, and we may apply this concept in weather forecasting, including finding the density of fluid currents in fluid pipes. Figure 15 illustrates the influence of the inclination angle of the cylinder on the temperature profiles. The increased angle of inclination causes the velocity of the flow to rise. As a result, frictional forces between the walls and flow layers increase, causing the temperature of the fluid to rise. The alteration of the fluid flow angle of will always affect the temperature pattern, a fundamental concept used in the transportation of oil in pipes laid on different terrains. Figure 16 shows an increase in the thermophoretic parameter leads to a rise in the temperature of the fluid. The thermophoretic forces build upon the walls of the stretching cylinder as the fluid flows, causing hot air to diffuse through the liquid. As a result, the thermal boundary layer thickens, leading to a rise in the temperature. We may apply this concept during the separation of different types of fluid mixtures moving in different velocities under the force of temperature gradient. The thermophoresis parameter has excellent potential in facilitating drug discovery in medicine. Figure 17 displays the effect of the

Table 2: Skin friction coefficient τ for different values of parameters.

t	Re	Pr	M	Kr	Sc	Nt	α	Nr	Kp	Gr	Ec	τ
0.3	1	0.71	0.5	2	0.5	0.16	30	5	2.18	0.61	0.01	0.348191
0.3	2	0.71	0.5	2	0.5	0.16	30	5	2.18	0.61	0.01	0.433628
0.3	3	0.71	0.5	2	0.5	0.16	30	5	2.18	0.61	0.01	0.532473
0.3	5	0.75	0.5	2	0.5	0.16	30	5	2.18	0.61	0.01	0.328147
0.3	5	0.79	0.5	2	0.5	0.16	30	5	2.18	0.61	0.01	0.513612
0.3	5	1.50	0.5	2	0.5	0.16	30	5	2.18	0.61	0.01	0.752707
0.3	5	0.71	0.4	2	0.5	0.16	30	5	2.18	0.61	0.01	0.037351
0.3	5	0.71	1.0	2	0.5	0.16	30	5	2.18	0.61	0.01	0.033223
0.3	5	0.71	2.0	2	0.5	0.16	30	5	2.18	0.61	0.01	0.021835
0.3	5	0.71	0.5	3	0.5	0.16	30	5	2.18	0.61	0.01	0.254516
0.3	5	0.71	0.5	5	0.5	0.16	30	5	2.18	0.61	0.01	0.247196
0.3	5	0.71	0.5	7	0.5	0.16	30	5	2.18	0.61	0.01	0.245231
0.3	5	0.71	0.5	2	0.7	0.16	30	5	2.18	0.61	0.01	1.678722
0.3	5	0.71	0.5	2	0.8	0.16	30	5	2.18	0.61	0.01	1.651064
0.3	5	0.71	0.5	2	1.0	0.16	30	5	2.18	0.61	0.01	1.613411
0.3	5	0.71	0.5	2	0.5	0.20	30	5	2.18	0.61	0.01	0.878638
0.3	5	0.71	0.5	2	0.5	0.45	30	5	2.18	0.61	0.01	0.777832
0.3	5	0.71	0.5	2	0.5	0.60	30	5	2.18	0.61	0.01	0.685048
0.3	5	0.71	0.5	2	0.5	0.16	0	5	2.18	0.61	0.01	0.087390
0.3	5	0.71	0.5	2	0.5	0.16	45	5	2.18	0.61	0.01	0.09915
0.3	5	0.71	0.5	2	0.5	0.16	60	5	2.18	0.61	0.01	1.271783
0.3	5	0.71	0.5	2	0.5	0.16	30	6	2.18	0.61	0.01	0.951711
0.3	5	0.71	0.5	2	0.5	0.16	30	7	2.18	0.61	0.01	0.988235
0.3	5	0.71	0.5	2	0.5	0.16	30	9	2.18	0.61	0.01	0.990745
0.3	5	0.71	0.5	2	0.5	0.16	30	5	5.10	0.61	0.01	1.025881
0.3	5	0.71	0.5	2	0.5	0.16	30	5	7.20	0.61	0.01	0.7433372
0.3	5	0.71	0.5	2	0.5	0.16	30	5	9.40	0.61	0.01	0.6213831
0.3	5	0.71	0.5	2	0.5	0.16	30	5	2.18	0.72	0.01	0.429104
0.3	5	0.71	0.5	2	0.5	0.16	30	5	2.18	0.85	0.01	0.684313
0.3	5	0.71	0.5	2	0.5	0.16	30	5	2.18	0.92	0.01	0.831831
0.3	5	0.71	0.5	2	0.5	0.16	30	5	2.18	0.61	0.04	0.571954
0.3	5	0.71	0.5	2	0.5	0.16	30	5	2.18	0.61	0.06	0.615956
0.3	5	0.71	0.5	2	0.5	0.16	30	5	2.18	0.61	0.09	0.713957
0.1	5	0.71	0.5	2	0.5	0.16	30	5	2.18	0.61	0.01	0.710751
0.2	5	0.71	0.5	2	0.5	0.16	30	5	2.18	0.61	0.01	1.202312
0.4	5	0.71	0.5	2	0.5	0.16	30	5	2.18	0.61	0.01	2.016981
0.6	5	0.71	0.5	2	0.5	0.16	30	5	2.18	0.61	0.01	2.126542

chemical reaction parameter on temperature profiles. An increase in the chemical reaction parameter suppresses the temperature profiles of the fluid. As the fluid flows past the cylinder, thermal diffusivity of the fluid decreases, causing shear thinning of the thermal boundary layer and consequently reducing the temperature of the nanofluid. We may apply this knowledge in both the textile industry and industrial chemistry. We further note that the chemical reaction parameter has a significant impact on both the Sherwood number and the Nusselt number, as depicted in Tables 3 and 4.

Figure 18 indicates that higher values of the Reynolds number affect the velocity profiles of the fluid positively. Inertia forces increase with higher Reynolds number causing less friction between fluid layers and the walls. As a result, the velocity profiles of the flow increase significantly. We may apply this in the design of the water piping system and aircraft wings to anticipate the occurrence of turbulent flows, which can cause havoc if not carefully handled. Figure 19 shows the effect of the inclination angle on concentration profiles. An increase in the curve leads to a decrease in the concentration profiles of the fluid. The flow conduit becomes more vertical when tilted, and the velocity upward is reduced due to the pull of gravity forces. As a result, the mass transfer is slowed in the fluid, causing a decrease in the concentration profiles. We further note that the no-slip condition leads to less mass transferred in the model. Figure 20 demonstrates the effect of the curvature parameter on concentration profiles. An increase in the curvature parameter has a positive impact on the concentration profiles of the fluid. The velocity of the fluid increases with an increase in the bending of the edges of the cylinder. As a result, the mass transfer of the flow increases.

Table 2 shows that increasing the Reynolds number, the inclination angle of the cylinder, thermal radiation, the Grashof number, the Prandtl number, the Eckert number, and time leads to an increase in skin friction coefficient. An increase in magnetic number, chemical reaction parameter, the Schmidt number, thermophoresis parameter, and permeability parameter leads to a decrease in the skin friction coefficient.

Table 3 shows that increasing the Reynolds number, magnetic number, chemical reaction parameter, thermophoresis parameter, the inclination angle of the cylinder, thermal radiation, and permeability parameter had a positive effect on the Nusselt number. Increasing the Prandtl number, the Schmidt number, the Eckert number, and time t suppressed the Nusselt number.

Table 3: The Nusselt number for different values of parameters.

t	Re	Pr	M	Kr	Sc	Nt	α	Nr	Kp	Gr	Ec	Nu
0.3	1	0.71	0.5	2	0.5	0.16	30	5	2.18	0.61	0.01	1.510982
0.3	2	0.71	0.5	2	0.5	0.16	30	5	2.18	0.61	0.01	1.628693
0.3	3	0.71	0.5	2	0.5	0.16	30	5	2.18	0.61	0.01	1.716734
0.3	5	0.75	0.5	2	0.5	0.16	30	5	2.18	0.61	0.01	1.205228
0.3	5	0.79	0.5	2	0.5	0.16	30	5	2.18	0.61	0.01	0.924675
0.3	5	1.50	0.5	2	0.5	0.16	30	5	2.18	0.61	0.01	0.638148
0.3	5	0.71	0.4	2	0.5	0.16	30	5	2.18	0.61	0.01	0.078158
0.3	5	0.71	1.0	2	0.5	0.16	30	5	2.18	0.61	0.01	0.282102
0.3	5	0.71	2.0	2	0.5	0.16	30	5	2.18	0.61	0.01	1.150223
0.3	5	0.71	0.5	3	0.5	0.16	30	5	2.18	0.61	0.01	0.185326
0.3	5	0.71	0.5	5	0.5	0.16	30	5	2.18	0.61	0.01	0.295332
0.3	5	0.71	0.5	7	0.5	0.16	30	5	2.18	0.61	0.01	0.385436
0.3	5	0.71	0.5	2	0.7	0.16	30	5	2.18	0.61	0.01	0.701773
0.3	5	0.71	0.5	2	0.8	0.16	30	5	2.18	0.61	0.01	0.501812
0.3	5	0.71	0.5	2	1.0	0.16	30	5	2.18	0.61	0.01	0.207178
0.3	5	0.71	0.5	2	0.5	0.20	30	5	2.18	0.61	0.01	0.586382
0.3	5	0.71	0.5	2	0.5	0.45	30	5	2.18	0.61	0.01	0.767835
0.3	5	0.71	0.5	2	0.5	0.60	30	5	2.18	0.61	0.01	0.895048
0.3	5	0.71	0.5	2	0.5	0.16	0	5	2.18	0.61	0.01	0.668204
0.3	5	0.71	0.5	2	0.5	0.16	45	5	2.18	0.61	0.01	0.670735
0.3	5	0.71	0.5	2	0.5	0.16	60	5	2.18	0.61	0.01	0.820725
0.3	5	0.71	0.5	2	0.5	0.16	30	6	2.18	0.61	0.01	0.078158
0.3	5	0.71	0.5	2	0.5	0.16	30	7	2.18	0.61	0.01	0.282102
0.3	5	0.71	0.5	2	0.5	0.16	30	9	2.18	0.61	0.01	1.150223
0.3	5	0.71	0.5	2	0.5	0.16	30	5	5.10	0.61	0.01	0.232139
0.3	5	0.71	0.5	2	0.5	0.16	30	5	7.20	0.61	0.01	0.332138
0.3	5	0.71	0.5	2	0.5	0.16	30	5	9.40	0.61	0.01	0.342138
0.3	5	0.71	0.5	2	0.5	0.16	30	5	2.18	0.61	0.01	0.429104
0.3	5	0.71	0.5	2	0.5	0.16	30	5	2.18	0.61	0.01	0.429104
0.3	5	0.71	0.5	2	0.5	0.16	30	5	2.18	0.61	0.01	0.429104
0.3	5	0.71	0.5	2	0.5	0.16	30	5	2.18	0.61	0.04	0.348674
0.3	5	0.71	0.5	2	0.5	0.16	30	5	2.18	0.61	0.06	0.274123
0.3	5	0.71	0.5	2	0.5	0.16	30	5	2.18	0.61	0.09	0.174168
0.1	5	0.71	0.5	2	0.5	0.16	30	5	2.18	0.61	0.01	0.710751
0.2	5	0.71	0.5	2	0.5	0.16	30	5	2.18	0.61	0.01	0.703287
0.4	5	0.71	0.5	2	0.5	0.16	30	5	2.18	0.61	0.01	0.661835
0.6	5	0.71	0.5	2	0.5	0.16	30	5	2.18	0.61	0.01	0.641742

Table 4 shows an increase in the Reynolds number, magnetic number, chemical reaction parameter, the Schmidt number, the inclination angle of the cylinder, thermal radiation, permeability parameter, the Grashof number, and the Eckert number leads to an increase in Sherwood number. An increase in the Prandtl number, thermophoresis parameter, and time t suppressed the Sherwood number. These findings can primarily be used in molecular diffusion and advection theory to assist the engineers in their designs of various systems and equipment.

7. Conclusion

This study presented a numerical analysis of entropy generation in an unsteady fluid flow past an inclined cylinder with combined thermal radiation and magnetic field effects. We have solved the transport equations governing the flow using an overlapping grid spectral collocation method, and the accuracy convergence of the algorithm was determined. We have reported on the effects of pertinent parameters on the coefficient of skin friction, the Nusselt number, and the Sherwood number. The following are the main conclusions drawn from this study:

- (i) Decreasing the values of thermal radiation parameter, the Nusselt number, and the chemical reaction parameter is significant in minimizing entropy generation.
- (ii) Entropy generation increased by increasing the magnetic number, the angle of cylinder inclination, the Brinkman number, and the Reynolds number.
- (iii) Increasing the thermal radiation parameter, the angle of inclination of the cylinder, and the thermophoresis parameter increases the temperature of the fluid.
- (iv) Increasing the Reynolds number of the flow leads to a rise in velocity profiles of the flow.
- (v) Growth in the curvature parameter leads to an increase in the concentration field.
- (vi) The overlapping grid spectral collocation method is accurate and converges fast.

Table 4: The Sherwood number for different values of parameters.

t	Re	Pr	M	Kr	Sc	Nt	α	Nr	Kp	Gr	Ec	Sh
0.3	1	0.71	0.5	2	0.5	0.16	30	5	2.18	0.61	0.01	1.610991
0.3	2	0.71	0.5	2	0.5	0.16	30	5	2.18	0.61	0.01	1.688692
0.3	3	0.71	0.5	2	0.5	0.16	30	5	2.18	0.61	0.01	1.691673
0.3	5	0.75	0.5	2	0.5	0.16	30	5	2.18	0.61	0.01	0.103128
0.3	5	0.79	0.5	2	0.5	0.16	30	5	2.18	0.61	0.01	0.024673
0.3	5	1.50	0.5	2	0.5	0.16	30	5	2.18	0.61	0.01	0.018141
0.3	5	0.71	0.4	2	0.5	0.16	30	5	2.18	0.61	0.01	0.103703
0.3	5	0.71	1.0	2	0.5	0.16	30	5	2.18	0.61	0.01	0.302421
0.3	5	0.71	2.0	2	0.5	0.16	30	5	2.18	0.61	0.01	0.350243
0.3	5	0.71	0.5	3	0.5	0.16	30	5	2.18	0.61	0.01	0.185418
0.3	5	0.71	0.5	5	0.5	0.16	30	5	2.18	0.61	0.01	0.200976
0.3	5	0.71	0.5	7	0.5	0.16	30	5	2.18	0.61	0.01	0.215872
0.3	5	0.71	0.5	2	0.7	0.16	30	5	2.18	0.61	0.01	2.158513
0.3	5	0.71	0.5	2	0.8	0.16	30	5	2.18	0.61	0.01	3.447662
0.3	5	0.71	0.5	2	1.0	0.16	30	5	2.18	0.61	0.01	4.640861
0.3	5	0.71	0.5	2	0.5	0.20	30	5	2.18	0.61	0.01	0.850256
0.3	5	0.71	0.5	2	0.5	0.45	30	5	2.18	0.61	0.01	0.751045
0.3	5	0.71	0.5	2	0.5	0.60	30	5	2.18	0.61	0.01	0.707963
0.3	5	0.71	0.5	2	0.5	0.16	0	5	2.18	0.61	0.01	1.668623
0.3	5	0.71	0.5	2	0.5	0.16	45	5	2.18	0.61	0.01	1.672482
0.3	5	0.71	0.5	2	0.5	0.16	60	5	2.18	0.61	0.01	1.712483
0.3	5	0.71	0.5	2	0.5	0.16	30	6	2.18	0.61	0.01	0.158730
0.3	5	0.71	0.5	2	0.5	0.16	30	7	2.18	0.61	0.01	0.158910
0.3	5	0.71	0.5	2	0.5	0.16	30	9	2.18	0.61	0.01	0.159300
0.3	5	0.71	0.5	2	0.5	0.16	30	5	5.10	0.61	0.01	0.175622
0.3	5	0.71	0.5	2	0.5	0.16	30	5	7.20	0.61	0.01	0.175959
0.3	5	0.71	0.5	2	0.5	0.16	30	5	9.40	0.61	0.01	0.176147
0.3	5	0.71	0.5	2	0.5	0.16	30	5	2.18	0.81	0.01	0.229104
0.3	5	0.71	0.5	2	0.5	0.16	30	5	2.18	0.91	0.01	0.338693
0.3	5	0.71	0.5	2	0.5	0.16	30	5	2.18	1.61	0.01	0.429104
0.3	5	0.71	0.5	2	0.5	0.16	30	5	2.18	0.61	0.04	1.822615
0.3	5	0.71	0.5	2	0.5	0.16	30	5	2.18	0.61	0.06	1.961072
0.3	5	0.71	0.5	2	0.5	0.16	30	5	2.18	0.61	0.09	2.117791
0.1	5	0.71	0.5	2	0.5	0.16	30	5	2.18	0.61	0.01	1.881366
0.2	5	0.71	0.5	2	0.5	0.16	30	5	2.18	0.61	0.01	1.670562
0.4	5	0.71	0.5	2	0.5	0.16	30	5	2.18	0.61	0.01	1.551875
0.6	5	0.71	0.5	2	0.5	0.16	30	5	2.18	0.61	0.01	1.451419

Acknowledgement

The authors appreciate the support offered by the University of KwaZulu-Natal, South Africa and Amity University Kolkata, India.

Conflict of interest statement

Authors do not have any conflict of interest to publish this article.

References

- Abdul Hakeem, A. K., Nayak, M. K., & Makinde, O. D. (2019). Effect of exponentially variable viscosity and permeability on Blasius flow of Carreau nano fluid over an electromagnetic plate through a porous medium. *Journal of Applied and Computational Mechanics*, 5(2), 390–401.
- Abolbashari, M. H., Freidoonimehr, N., Nazari, F., & Rashidi, M. M. (2014). Entropy analysis for an unsteady MHD flow past a stretching permeable surface in nano-fluid. *Powder Technology*, 267, 256–267.
- Abolbashari, M. H., Freidoonimehr, N., Nazari, F., & Rashidi, M. M. (2015). Analytical modeling of entropy generation for Casson nano-fluid flow induced by a stretching surface. *Advanced Powder Technology*, 26(2), 542–552.
- Acharya, N., Das, K., & Kundu, P. K. (2019). On the heat transport mechanism and entropy generation in a nozzle of liquid rocket engine using ferrofluid: A computational framework. *Journal of Computational Design and Engineering*, 6(4), 739–750.
- Aminian, E., Moghadasi, H., & Saffari, H. (2020). Magnetic field effects on forced convection flow of a hybrid nanofluid in a cylinder filled with porous media: A numerical study. *Journal of Thermal Analysis and Calorimetry*, 141, 2019–2031.
- Azam, M., Khan, M., & Alshomrani, A. S. (2017). Unsteady radiative stagnation point flow of MHD Carreau nanofluid over expanding/contracting cylinder. *International Journal of Mechanical Sciences*, 130, 64–73.

- Bahiraie, M., & Majd, S. M. (2016). Prediction of entropy generation for nanofluid flow through a triangular minichannel using neural network. *Advanced Powder Technology*, 27(2), 673–683.
- Bejan, A. (1982). *Entropy generation through heat and fluid flow*. New York: Wiley.
- Bejan, A. (2002). Fundamentals of exergy analysis, entropy generation minimization, and the generation of flow architecture. *International Journal of Energy Research*, 26(7), 0–43.
- Bellman, R. E., & Kalaba, R. E. (1965). Quasilinearization and nonlinear boundary-value problems. Santa Monica, CA: RAND Corporation, R-438-PR, <https://www.rand.org/pubs/reports/R438.html>.
- Bhatti, M. M., Abbas, T., & Rashidi, M. M. (2017). Entropy generation as a practical tool of optimisation for non-Newtonian nanofluid flow through a permeable stretching surface using slm. *Journal of Computational Design and Engineering*, 4(1), 21–28.
- Chamkha, A. J., & Aly, A. M. (2010). MHD free convection flow of a nanofluid past a vertical plate in the presence of heat generation or absorption effects. *Chemical Engineering Communications*, 198(3), 425–441.
- Clausius, R. (1867). *The mechanical theory of heat: With its applications to the steam-engine and to the physical properties of bodies*. London: J. van Voorst.
- Dalir, N. (2014). Numerical study of entropy generation for forced convection flow and heat transfer of a Jeffrey fluid over a stretching sheet. *Alexandria Engineering Journal*, 53(4), 769–778.
- Das, K., Sharma, R. P., & Sarkar, A. (2016). Heat and mass transfer of a second grade magnetohydrodynamic fluid over a convectively heated stretching sheet. *Journal of Computational Design and Engineering*, 3(4), 330–336.
- Das, S., Chakraborty, S., Jana, R. N., & Makinde, O. D. (2015). Entropy analysis of unsteady magneto-nanofluid flow past accelerating stretching sheet with convective boundary condition. *Applied Mathematics and Mechanics*, 36(12), 1593–1610.
- Delkosh, M., Parand, K., & Ganji, D. D. (2019). An efficient numerical method to solve the boundary layer flow of an Eyring–Powell non-Newtonian fluid. *Journal of Applied and Computational Mechanics*, 5(2), 454–467.
- Dhanai, R., Rana, P., & Kumar, L. (2016). MHD mixed convection nanofluid flow and heat transfer over an inclined cylinder due to velocity and thermal slip effects: Buongiorno's model. *Powder Technology*, 288, 140–150.
- Donnelly, R. J. (2012). *High Reynolds number flows using liquid and gaseous helium*. New York: Springer.
- Faghidian, S. A., Goudar, D., Farahi, G. H., & Smith, D. J. (2012). Measurement, analysis and reconstruction of residual stresses. *The Journal of Strain Analysis for Engineering Design*, 47(4), 254–264.
- Freidoonimehr, N., Rashidi, M., Abelman, S., & Lorenzini, G. (2016). Analytical modeling of MHD flow over a permeable rotating disk in the presence of Soret and Dufour effects: Entropy analysis. *Entropy*, 18(5), 131.
- Huminić, G., & Angel, (2020). Entropy generation of nanofluid and hybrid nanofluid flow in thermal systems: A review. *Journal of Molecular Liquids*, 302, 112533.
- Kargarnovin, M. H., Faghidian, S. A., Farjami, Y., & Farahi, G. H. (2010). Application of homotopy-padé technique in limit analysis of circular plates under arbitrary rotational symmetric loading using von-Mises yield criterion. *Communications in Nonlinear Science and Numerical Simulation*, 15(4), 1080–1091.
- Kataria, H. R., & Mittal, A. S. (2017). Velocity, mass and temperature analysis of gravity-driven convection nanofluid flow past an oscillating vertical plate in the presence of magnetic field in a porous medium. *Applied Thermal Engineering*, 110, 864–874.
- Mahanthesh, B., Gireesha, B. J., & Gorla, R. S. (2016). Heat and mass transfer effects on the mixed convective flow of chemically reacting nanofluid past a moving/stationary vertical plate. *Alexandria Engineering Journal*, 55(1), 569–581.
- Mahian, O., Kianifar, A., Kleinstreuer, C., Moh'd, A., Pop, I., Sahin, A. Z., & Wongwises, S. (2013). A review of entropy generation in nanofluid flow. *International Journal of Heat and Mass Transfer*, 65, 514–532.
- Mansour, M. A. (1990). Radiative and free-convection effects on the oscillatory flow past a vertical plate. *Astrophysics and Space Science*, 166(2), 269–275.
- Mondal, H., Almakki, M., & Sibanda, P. (2019). Dual solutions for three-dimensional magnetohydrodynamic nanofluid flow with entropy generation. *Journal of Computational Design and Engineering*, 6(4), 657–665.
- Motsa, S. S., Dlamini, P. G., & Khumalo, M. (2014). Spectral relaxation method and spectral quasilinearization method for solving unsteady boundary layer flow problems. *Advances in Mathematical Physics*, 2014, <https://doi.org/10.1155/2014/341964>.
- Muhammad, R., Khan, M. I., Khan, N. B., & Jameel, M. (2020). Magnetohydrodynamics (MHD) radiated nanomaterial viscous material flow by a curved surface with second order slip and entropy generation. *Computer Methods and Programs in Biomedicine*, 189, 105294.
- Periyadurai, K., Selvan, M., & Doh, D. H. (2019). Impact of magnetic field on convective flow of a micropolar fluid with two parallel heat source. *Journal of Applied and Computational Mechanics*, 5(4), 652–666.
- Pourmehran, O., Rahimi-Gorji, M., & Ganji, D. D. (2016). Heat transfer and flow analysis of nanofluid flow induced by a stretching sheet in the presence of an external magnetic field. *Journal of the Taiwan Institute of Chemical Engineers*, 65, 162–171.
- Rashidi, M. M., Ali, M., Freidoonimehr, N., & Nazari, F. (2013). Parametric analysis and optimization of entropy generation in unsteady MHD flow over a stretching rotating disk using artificial neural network and particle swarm optimization algorithm. *Energy*, 55, 497–510.
- Samuel, F. M., & Motsa, S. S. (2019). A highly accurate trivariate spectral collocation method of solution for two-dimensional nonlinear initial-boundary value problems. *Applied Mathematics and Computation*, 360, 221–235.
- Shamshuddin, M. D., Thirupathi, T., & Satya Narayana, P. V. (2019). Micropolar fluid flow induced due to a stretching sheet with heat source/sink and surface heat flux boundary condition effects. *Journal of Applied and Computational Mechanics*, 5(2), 816–826.
- Sheikholeslami, M., Jafaryar, M., Abohamzeh, E., Shafee, A., & Babazadeh, H. (2020a). Energy and entropy evaluation and two-phase simulation of nanoparticles within a solar unit with impose of new turbulator. *Sustainable Energy Technologies and Assessments*, 39, 100727.
- Sheikholeslami, M., Jafaryar, M., Shafee, A., & Babazadeh, H. (2020b). Acceleration of discharge process of clean energy storage unit with insertion of porous foam considering nanoparticle enhanced paraffin. *Journal of Cleaner Production*, 261, 121206.

- Siavashi, M., Yousofvand, R., & Rezanejad, S. (2018). Nanofluid and porous fins effect on natural convection and entropy generation of flow inside a cavity. *Advanced Powder Technology*, 29(1), 142–156.
- Trefethen, L. N. (2000). *Spectral methods in MATLAB*. Philadelphia: SIAM.
- Turkylmazoglu, M. (2018). Buongiorno model in a nanofluid filled asymmetric channel fulfilling zero net particle flux at the walls. *International Journal of Heat and Mass Transfer*, 126, 974–979.
- Yarmand, H., Ahmadi, G., Gharekhani, S., Kazi, S. N., Safaei, M. R., Alehashem, M. S., & Mahat, A. B. (2014). Entropy generation during turbulent flow of zirconia-water and other nanofluids in a square cross section tube with a constant heat flux. *Entropy*, 16(11), 6116–6132.

Chapter 4

Impact of irreversibility ratio and entropy generation on three-dimensional Oldroyd-B fluid flow with relaxation-retardation viscous dissipation

In Chapter 3, we investigated entropy generation, heat and mass transfer in an unsteady MHD nanofluid past an inclined cylinder using Buongiorno's model [135] with thermal radiation. This chapter extends the work in Chapter 3 by considering entropy production minimization in a three-dimensional MHD Oldroyd-B fluid flow subjected to relaxation and retardation viscous dissipation.

We further include the influence of source terms such as the mixed convection term, Cattaneo-Christov heat mass flux and a chemical reaction on the irreversibility ratio. The overlapping grid spectral collocation method is used to solve the transport equations.



Impact of irreversibility ratio and entropy generation on three-dimensional Oldroyd-B fluid flow with relaxation–retardation viscous dissipation

Z M Mburu¹, M K Nayak², S Mondal^{3*}  and P Sibanda¹

¹School of Mathematics, Statistics and Computer Science, University of KwaZulu-Natal, Private Bag X01, Scottsville, Pietermaritzburg 3209, South Africa

²Department of Physics, IHSE, Siksha O Anusandhan Deemed to be University, Bhubaneswar, Odisha, India

³Department of Mathematics, Amity University Kolkata, Newtown, West Bengal 700135, India

Received: 04 May 2020 / Accepted: 18 October 2020

Abstract: The study is concerned with entropy minimization on three-dimensional magnetohydrodynamic Oldroyd-B fluid flow with relaxation–retardation viscous dissipation and a mixed chemical reaction. A numerical solution of the nonlinear transport equations is obtained using an overlapping grid spectral collocation numerical scheme. We investigate strategies for entropy generation minimization in terms of system parameters such as the mixed convection parameter and changes in thermal and concentration fields under different conditions. Further, the findings on changes in the axial and transverse skin friction coefficients, the Nusselt number and the Sherwood number are presented.

Keywords: Oldroyd-B fluid; Relaxation–retardation viscous dissipation; Irreversibility ratio; Entropy generation; Overlapping grid spectral collocation method; Mixed chemical reaction

List of symbols

(u, v, w)	Velocity components along (x, y, z) directions	Γ_2	Deborah number in terms of retardation time
B_0	Uniform magnetic field strength	Sc	Schmidt number
λ_1	Relaxation time	M	Hartman number
λ_2	Retardation time	Gr_x	Thermal Grashof number
ν_f	Kinematic viscosity	Re	Reynolds number
Γ_e	Relaxation time for heat flux	Pr	Prandtl number
Γ_c	Relaxation time for mass flux	J	Mass flux
T	Fluid temperature in the boundary layer	ε	Thermal relaxation chemical reaction parameter
T_∞	Temperature of ambient fluid	ϕ	Irreversibility ratio
T_w	Surface temperature	D_B	Brownian diffusion coefficient
C	Fluid concentration in the boundary layer	γ	Chemical reaction parameter
C_∞	Concentration of ambient fluid	β	Ratio of stretching rates
C_w	Surface concentration	λ	Mixed convection parameter
g	Acceleration due to gravity	N	Concentration buoyancy parameter
k_f	Thermal conductivity	δ_e	Deborah number in terms of relaxation time of the heat flux
ρ_f	Density of the fluid	δ_c	Deborah number in terms of relaxation time of the mass flux
q	Heat flux	β_T	Volumetric coefficient thermal expansion
V	Velocity	β_T	Volumetric coefficient solutal expansion
Γ_1	Deborah number in terms of relaxation time	EG	Entropy generation
		VBL	Velocity boundary layer
		HTR	Heat transfer rate
		TBL	Thermal boundary layer

*Corresponding author, E-mail: sabya.mondal.2007@gmail.com

CPU	Central processing unit
QLM	Quasi-linearization method

1. Introduction

Non-Newtonian fluids are characterized by a nonlinear deformation on application of a shear stress. These fluids abound in industry and include adhesives, lubricating oils, slurries, mine tailing, and suspensions, biological fluids, polymer melts and pharmaceutical products.

The non-Newtonian fluids find use in diverse areas such as in petroleum drilling, the movement of biological fluids, polymer extrusion, crystal growing and wire drawing. The classical Navier–Stokes equations do not fully account for the typical properties of non-Newtonian fluids. A number of constitutive equations for non-Newtonian fluids have been established. Among many, Oldroyd [1] pioneered the development of a robust constitutive relationship for a fluid that is commonly known as the Oldroyd-B model that describes the behavior of certain types of nonlinear flows. The Oldroyd-B model characterizes the influence of both relaxation and retardation times. Many researchers have investigated the flow and heat transfer in an Oldroyd-B fluid for different flow configurations. These include the flow of an Oldroyd-B fluid flow induced by a free stream [2], the Oldroyd-B fluid flow with a decaying potential vortex [3], the Oldroyd-B fluid in a stratified stagnation point flow [4], the impact of heat absorption/generation in mixed convective flow of an Oldroyd-B fluid [5], and transient Oldroyd-B nanofluid thin film flow over a stretching sheet [6].

An applied magnetic field has a role in controlling momentum and heat transfers in the boundary flow of conducting fluids. For this reason, there are numerous studies on MHD effects in boundary layer flows, for instance studies on the impact of magnetohydrodynamics on a metachronal wave of particle–fluid suspension [7], fractional Oldroyd-B nanofluid flow [8], effects of mixed convection on MHD Eyring–Powell nanofluid flow past a stretching cylinder [9], MHD Eyring–Powell nanofluid flow past a rotating disc [10], impact of the Brownian motion on MHD nanofluid flow between plates [11] and MHD Oldroyd-B nanofluid flow with heat generation/absorption [12].

The concept of thermal inertia or thermal relaxation time in Fourier’s theory of heat flux was introduced by Cattaneo [13]. The Cattaneo model was further improved by Christov [14] with the partial time derivative replaced by upper convective differentiation. The resulting model is known as the Cattaneo–Christov heat flux model. Hosseinzadeh [15] reported on Maxwell fluid flow in a porous medium and found that the Prandtl number had a significant effect on the heat transfer coefficient and on the fluid temperature. The impact of thermal radiation and mixed convection on nanofluid flow past a vertical cylinder was analyzed by Gholinia [16]. They reported that the temperature of the fluid increased significantly due to the higher thermal conductivity of the nanoparticles. The boundary layer flow of the Oldroyd-B fluid flow was studied by Abbasi [17], stretched flow of the Oldroyd-B fluid [18], solidification process of a phase changing material in a thermal system using copper nanoparticles [19], and MHD flow of the Oldroyd-B fluid with homogeneous heterogeneous reactions [12, 20] influenced by Cattaneo–Christov double diffusion theory.

A number of entropy generation problems in the literature have been solved using various numerical methods. Sandeep [21] used the Runge–Kutta shooting technique to solve heat transfer in the Maxwell and Oldroyd-B nanofluid flow past a stretching surface, Shah [22] used the homotopy analysis scheme to solve the equations for entropy generation in a radiative MHD Casson nanofluid flow, Sumaira [23] reported on the analysis of entropy generation in a hyperbolic nanofluid flow using homotopy analysis method, Saeed [24] solved the influence of heat flux on MHD Jeffrey nanofluid flow using the homotopy analysis method, Shehzad [25] used the homotopy analysis method to find the magnetic field effects in an Oldroyd-B flow past a radiative surface, and Almakki [26] used the spectral relaxation method to solve the equations of entropy generation at a stagnation point. We have used an overlapping grid spectral collocation method to solve the highly nonlinear ordinary differential equations that describe the flow in this study. The method has not been used before in solving the boundary problem. The method is highly accurate and converges rapidly. It is described in detail in Sect. 4.

The minimization of entropy generation in fluid flow has been considered in many studies over the past several decades. This is important in order to maximize the thermal energy resources available to do useful work. Entropy generation leads to energy losses due to irreversibilities in thermal dynamic process. Several researchers have attempted to address this problem in order to intensify heat

transfer and minimize heat loss. Derakhshan [27] reported on the analysis of entropy generation analysis in MHD nanofluid flow between two rotating disks, and the optimization of plate fin heat sink was studied by Khan [28], entropy generation in nanofluid flow past a thin moving needle with nonlinear thermal radiation effects [29], optimal design of heat exchangers by using entropy generation minimization techniques [30] and optimization of solid gas reactors based on entropy generation minimization method [31].

The literature shows that there are few, if any studies on the three-dimensional MHD flow of an Oldroyd-B fluid with relaxation–retardation viscous dissipation. The objective is to analyze the entropy minimization on three-dimensional MHD flow of an Oldroyd-B fluid with relaxation–retardation viscous dissipation subject to Cattaneo–Christov heat mass flux and mixed chemical reaction. A numerical solution to the system of nonlinear equations has been obtained using a new overlapping grid spectral collocation technique. The influence of physical parameters on the fluid properties, entropy generation number and Bejan number is discussed (Fig. 1).

2. Formulation of the problem

We consider the flow of a three-dimensional incompressible Oldroyd-B fluid occupying the space $z > 0$ [32, 33].

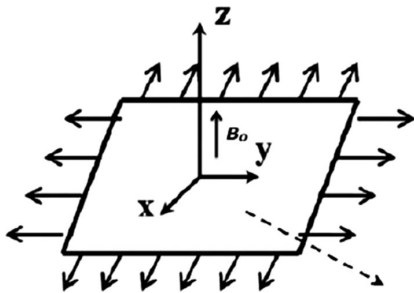


Fig. 1 Overlapping grid in η

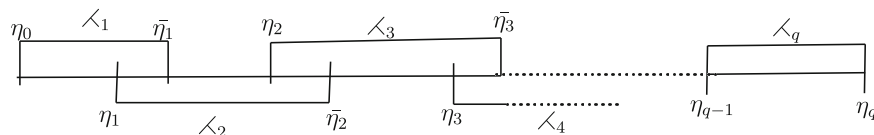


Fig. 2 The flow model

The flow configuration is shown in Fig. 2. The transport equations are given by

$$\frac{\partial u}{\partial x} + \frac{\partial v}{\partial y} + \frac{\partial w}{\partial z} = 0. \quad (1)$$

$$\begin{aligned} u \frac{\partial u}{\partial x} + v \frac{\partial u}{\partial y} + w \frac{\partial u}{\partial z} + \lambda_1 \left(u^2 \frac{\partial^2 u}{\partial x^2} + v^2 \frac{\partial^2 u}{\partial y^2} \right. \\ \left. + w^2 \frac{\partial^2 u}{\partial z^2} + 2uv \frac{\partial^2 u}{\partial x \partial y} + 2vw \frac{\partial^2 u}{\partial y \partial z} + \right. \\ \left. 2uw \frac{\partial^2 u}{\partial x \partial z} \right) = \nu_f \left[\frac{\partial^2 u}{\partial z^2} + \lambda_2 \left(u \frac{\partial^3 u}{\partial x \partial z^2} + v \frac{\partial^3 u}{\partial y \partial z^2} + w \frac{\partial^3 u}{\partial z^3} - \frac{\partial u}{\partial x} \frac{\partial^2 u}{\partial z^2} - \frac{\partial u}{\partial y} \frac{\partial^2 u}{\partial z^2} \right. \right. \\ \left. \left. - \frac{\partial u}{\partial z} \frac{\partial^2 u}{\partial z^2} \right) \right] - \frac{\sigma B_0^2}{\rho} \left(u + \lambda_1 w \frac{\partial u}{\partial z} \right) + g[\beta_r(T - T_\infty) + \beta_c(C - C_\infty)]. \end{aligned} \quad (2)$$

$$\begin{aligned} u \frac{\partial v}{\partial x} + v \frac{\partial v}{\partial y} + w \frac{\partial v}{\partial z} + \lambda_1 \left(u^2 \frac{\partial^2 v}{\partial x^2} + v^2 \frac{\partial^2 v}{\partial y^2} + w^2 \frac{\partial^2 v}{\partial z^2} + 2uv \frac{\partial^2 v}{\partial x \partial y} + 2vw \frac{\partial^2 v}{\partial y \partial z} + \right. \\ \left. 2uw \frac{\partial^2 v}{\partial x \partial z} \right) = \nu_f \left[\frac{\partial^2 v}{\partial z^2} + \lambda_2 \left(u \frac{\partial^3 v}{\partial x \partial z^2} + v \frac{\partial^3 v}{\partial y \partial z^2} + w \frac{\partial^3 v}{\partial z^3} - \frac{\partial v}{\partial x} \frac{\partial^2 u}{\partial z^2} - \frac{\partial v}{\partial y} \frac{\partial^2 v}{\partial z^2} \right. \right. \\ \left. \left. - \frac{\partial v}{\partial z} \frac{\partial^2 w}{\partial z^2} \right) \right] - \frac{\sigma B_0^2}{\rho_f} \left(v + \lambda_1 w \frac{\partial v}{\partial z} \right). \end{aligned} \quad (3)$$

The Cattaneo–Christov diffusion model describing the thermal and concentration diffusion with relaxation of heat and mass fluxes is given by Khan [34]

$$q + \Gamma_e \left[\frac{\partial q}{\partial t} + V \cdot \Delta q - q \cdot \Delta V + (\Delta \cdot V)q \right] = -k_f \Delta T. \quad (4)$$

$$J + \Gamma_c \left[\frac{\partial J}{\partial t} + V \cdot \Delta J - J \cdot \Delta J + (\Delta \cdot V)J \right] = -D_B \Delta C. \quad (5)$$

For $\Gamma_e = 0$ and $\Gamma_c = 0$, Eqs. (4) and (5) reduce to law due to Fourier for an incompressible fluid

$$q + \Gamma_e [V \cdot \Delta q - q \cdot \Delta V + (\Delta \cdot V)q] = -k_f \Delta T. \quad (6)$$

$$J + \Gamma_c [V \cdot \Delta J - J \cdot \Delta J + (\Delta \cdot V)J] = -D_B \Delta C. \quad (7)$$

With these relations, the temperature and concentration equations are

$$\begin{aligned} u \frac{\partial T}{\partial x} + v \frac{\partial T}{\partial y} + w \frac{\partial T}{\partial z} + \Omega_e \Gamma_e = \frac{k_f}{(\rho C_p)_f} \left(\frac{\partial^2 T}{\partial z^2} \right) \\ + \frac{\lambda_2}{\lambda_1} \left(\frac{\nu_f}{c_p} \right) \left[\left(\frac{\partial u}{\partial z} \right)^2 + \left(\frac{\partial v}{\partial z} \right)^2 \right]. \end{aligned} \quad (8)$$

$$u \frac{\partial C}{\partial x} + v \frac{\partial C}{\partial y} + w \frac{\partial C}{\partial z} + \Omega_c \Gamma_c = D_B \frac{\partial^2 C}{\partial z^2} + K_0 \left[\Gamma_c \left(u \frac{\partial C}{\partial x} + v \frac{\partial C}{\partial y} + w \frac{\partial C}{\partial z} \right) + (C - C_\infty) \right]. \quad (9)$$

$$\Omega_e = u^2 \frac{\partial^2 T}{\partial x^2} + v^2 \frac{\partial^2 T}{\partial y^2} + w^2 \frac{\partial^2 T}{\partial z^2} + \left(u \frac{\partial u}{\partial x} + v \frac{\partial u}{\partial y} + w \frac{\partial u}{\partial z} \right) \frac{\partial T}{\partial x} + \left(u \frac{\partial v}{\partial x} + v \frac{\partial v}{\partial y} + w \frac{\partial v}{\partial z} \right) \frac{\partial T}{\partial y} + \left(u \frac{\partial w}{\partial x} + v \frac{\partial w}{\partial y} + w \frac{\partial w}{\partial z} \right) \frac{\partial T}{\partial z} + 2uv \frac{\partial^2 T}{\partial x \partial y} + 2uw \frac{\partial^2 T}{\partial y \partial z} + 2vw \frac{\partial^2 T}{\partial x \partial z}. \quad (10)$$

$$\Omega_c = u^2 \frac{\partial^2 C}{\partial x^2} + v^2 \frac{\partial^2 C}{\partial y^2} + w^2 \frac{\partial^2 C}{\partial z^2} + \left(u \frac{\partial u}{\partial x} + v \frac{\partial u}{\partial y} + w \frac{\partial u}{\partial z} \right) \frac{\partial C}{\partial x} + \left(u \frac{\partial v}{\partial x} + v \frac{\partial v}{\partial y} + w \frac{\partial v}{\partial z} \right) \frac{\partial C}{\partial y} + \left(u \frac{\partial w}{\partial x} + v \frac{\partial w}{\partial y} + w \frac{\partial w}{\partial z} \right) \frac{\partial C}{\partial z} + 2uv \frac{\partial^2 C}{\partial x \partial y} + 2uw \frac{\partial^2 C}{\partial y \partial z} + 2vw \frac{\partial^2 C}{\partial x \partial z}. \quad (11)$$

The required boundary conditions are

$$u = U_w = 0, \quad v = V_w, \quad w = 0; \quad T = T_w, \quad C = C_w, \quad \text{at } z = 0. \\ u \rightarrow 0, \quad v \rightarrow 0, \quad T \rightarrow T_\infty, \quad C \rightarrow C_\infty, \quad \text{as } z \rightarrow \infty. \quad (12)$$

Here, $U_w = U_0 \exp[(x+y)/L]$ and $V_w = V_0 \exp[(x+y)/L]$ are stretching velocities with U_0 and V_0 as reference velocities, and $T_w = T_\infty + T_0 \exp[A(x+y)/2L]$ and $C_w = C_\infty + C_0 \exp[B(x+y)/2L]$ are surface temperature and concentration, respectively. The transformations used to reduce the equations to ordinary differentials are

$$u = U_0 \exp[(x+y)/L] f'(\eta), \quad v = U_0 \exp[(x+y)/L] g'(\eta),$$

$$w = -\sqrt{\frac{v_f U_0}{2L}} \exp[A(x+y)/2L],$$

$$[f(\eta) + \eta f'(\eta) + g(\eta) + \eta g'(\eta)], \quad \theta(\eta) = \frac{T - T_\infty}{T_w - T_\infty},$$

$$\phi(\eta) = \frac{C - C_\infty}{C_w - C_\infty},$$

$$\eta = \sqrt{\frac{U_0}{2v_f L}} \exp[(x+y)/2L] z. \quad (13)$$

Using Eqs. (13), (2), (3), (8), (9) and (12) become

$$f'''' + (f+g)f'' - 2(f'+g')f' + \Gamma_1 \left\{ (3f'' + \eta f''') \right. \\ \left. [(f+g)(f'+g') + \eta((f')^2 + (g')^2) \right. \\ \left. + 2\eta f'g'] - f'g'(4f' + 5\eta f'' + \eta^2 f''') \right. \\ \left. - ((f')^2 + (g')^2)(2f' + 2.5\eta f'' + 0.5\eta^2 f''') \right. \\ \left. - 2f''''[(f+g) + \eta(f'+g')]^2 \right\} \\ + \Gamma_2 \left\{ 2(f'+g')f''' + [\eta(f'+g') + 0.5(f+g)]f^{iv} \right. \\ \left. - (f'''' + g''')f' - [1.5(f'' + g'')f'' + \eta(f'''' + g''')f'''] \right\} \\ - 2Mf' + M\Gamma_1 f''[(f+g) + \eta(f'+g')] + 2\lambda[\theta(\eta) + N\phi(\eta)] = 0. \quad (14)$$

$$g'''' + (f+g)g'' - 2(f'+g')g' + \Gamma_1 \left\{ (3g'' + \eta g''') \right. \\ \left. [(f+g)(f'+g') + \eta((f')^2 + (g')^2) \right. \\ \left. + 2\eta f'g'] - f'g'(4g' + 5\eta g'' + \eta^2 g''') \right. \\ \left. - ((f')^2 + (g')^2)(2g' + 2.5\eta g'' + 0.5\eta^2 g''') \right. \\ \left. - 2g''''[(f+g) + \eta(f'+g')]^2 \right\} + \Gamma_2 \left\{ 2(f'+g')g''' + [\eta(f'+g') + 0.5(f+g)] \right. \\ \left. g^{iv} - (f'''' + g''')g' - [1.5(f'' + g'')g'' + \eta(f'''' + g''')g'''] \right\} \\ - 2Mg' + M\Gamma_1 g''[(f+g) + \eta(f'+g')] = 0. \quad (15)$$

$$\frac{1}{Pr} \theta'' + (f+g)\theta' - \delta_c \left\{ [(f+g) + \eta(f'+g')]^2 \theta'' + (f+g)(f'+g'+f''+g'')\theta' \right. \\ \left. + [(f+g)(f'+g') + 2\eta((f')^2 + (g')^2 + f'g')] (\theta' + \eta\theta'') + \eta[(f'+g')^2 \right. \\ \left. - (f+g+f'+g')(f''+g'')] \theta' \right\} + E_{cm} [(f'')^2 + (g'')^2] = 0. \quad (16)$$

$$\begin{aligned} & \frac{1}{Sc} \phi'' + (f+g)\phi' - \delta_c \left\{ \left[(f+g) + \eta(f'+g') \right]^2 \phi'' + (f+g)(f'+g'+f''+g'')\phi' \right. \\ & \left. + \left[(f+g)(f'+g') + 2\eta(f'^2 + (g')^2 + f'g') \right] (\phi' + \eta\phi'') + \eta \left[(f'+g')^2 \right. \right. \\ & \left. \left. - (f+g+f'+g')(f''+g'') \right] \phi' \right\} + \varepsilon(f+g)\phi' - 2\gamma\phi = 0. \end{aligned} \quad (17)$$

The boundary conditions are reduced to

$$\begin{aligned} & f(0) = 0, g(0) = 0, f'(0) = 1, g'(0) = \beta; \theta(0) = 1, \phi(0) = 1, \text{ at } \eta = 0. \\ & f' \rightarrow 0, g' \rightarrow 0, f'' \rightarrow 0, g'' \rightarrow 0, \theta \rightarrow 0, \phi \rightarrow 0, \text{ as } \eta \rightarrow \infty. \end{aligned} \quad (18)$$

Here,

$$\begin{aligned} \Gamma_1 &= \frac{\lambda_1 U_0 \exp[(x+y)/L]}{L}, \\ \Gamma_2 &= \frac{\lambda_2 U_0 \exp[(x+y)/L]}{L}, M = \frac{2L\sigma B_0^2}{\rho U_0 \exp[(x+y)/L]}, \\ \lambda &= \frac{g\beta_t(T_w - T_\infty)L^3}{(U^2 x^2/v^2)} = \frac{Gr_x}{Re_x^2}, Gr_x = \frac{g\beta_t(T_w - T_\infty)L^3}{v^2}, \\ Re_x &= \frac{U_x}{v}, N = \frac{\beta_c(C_w - C_\infty)}{\beta_t(T_w - T_\infty)}, \\ \delta_e &= \frac{\Gamma_e U_0 \exp[(x+y)/L]}{2L}, \delta_c = \frac{\Gamma_c U_0 \exp[(x+y)/L]}{2L} \\ E_{cm} &= \frac{\lambda_2 U^2}{\lambda_1 c_p (T_w - T_\infty)}, \\ Pr &= \frac{\nu_f}{\alpha_f}, \beta = \frac{V_0}{U_0}, \gamma = \frac{K_0 L}{U}, Sc = \frac{\nu_f}{D_B}, \varepsilon = K_0 \Gamma_c. \end{aligned} \quad (19)$$

For practical purpose, the following variables are important, namely the

$$\text{Axial skin friction coefficient, } \left(\frac{Re}{2}\right)^{\frac{1}{2}} C_{fx} = \mathbf{F}''(0), \quad (20)$$

$$\text{Transverse skin friction coefficient, } \left(\frac{Re}{2}\right)^{\frac{1}{2}} C_{fy} = \mathbf{G}''(0), \quad (21)$$

$$\text{Local Nusselt number, } \left(\frac{Re}{2}\right)^{-\frac{1}{2}} Nu_x = -\frac{x}{L} \Theta'(0), \quad (22)$$

$$\text{Local Sherwood number, } \left(\frac{Re}{2}\right)^{-\frac{1}{2}} Sh_x = -\frac{x}{L} \Phi'(0), \quad (23)$$

where $Re = \frac{U_w L}{\nu_f}$ is the local Reynolds number.

3. Entropy generation analysis

The entropy generation in three-dimensional Oldroyd-B fluid with relaxation-retardation viscous dissipation is given by Hafeez [35]

$$\begin{aligned} S_{gen}''' &= \frac{k_f}{T_\infty^2} \left[\left(\frac{\partial T}{\partial x} \right)^2 + \left(\frac{\partial T}{\partial y} \right)^2 + \left(\frac{\partial T}{\partial z} \right)^2 \right] \\ &\quad \text{Thermal irreversibility} \\ &+ \frac{\lambda_2 \mu}{\lambda_1 T_\infty} \left[\left(\frac{\partial u}{\partial y} \right)^2 + \left(\frac{\partial u}{\partial z} \right)^2 \right] \\ &\quad \text{Relaxation-retardation fluid friction irreversibility} \\ &+ \frac{RD_B}{C_\infty} \left(\frac{\partial C}{\partial z} \right)^2 + \frac{RD_B}{T_\infty} \left(\frac{\partial T}{\partial z} \frac{\partial C}{\partial z} \right) \\ &\quad \text{Mass transfer irreversibility} \end{aligned} \quad (24)$$

The entropy generation number represents the ratio between the actual entropy generation rate S_{gen}''' and characteristic entropy generation rate S_0''' expressed as

$$\begin{aligned} N_G &= \frac{S_{gen}'''}{S_0'''} = \frac{1}{2}(\eta^2 + Re)(\Phi')^2 + \frac{AB_r}{\Omega_e} \left\{ (\mathbf{F}')^2 \right. \\ &\quad \left. + \frac{1}{4}(\eta^2 + 2Re)(\mathbf{F}'')^2 \right\} + \frac{1}{2}\gamma Re \left\{ \left(\frac{\Omega_c}{\Omega_e} \right)^2 (\Phi')^2 \right. \\ &\quad \left. + \left(\frac{\Omega_c}{\Omega_e} \right) \Theta' \Phi' \right\}, \end{aligned} \quad (25)$$

where $\Omega_e = \frac{T_w - T_\infty}{T_\infty}$, $\Omega_c = \frac{C_w - C_\infty}{C_\infty}$, $\gamma = \frac{RD_B C_w}{k_f}$, $B_r = \frac{\mu u_w^2}{k_f T_w - T_\infty}$, $A = \frac{\lambda_2}{\lambda_1}$, $Re = \frac{u_w L}{v}$ and $S_0''' = \frac{k_f (T_w - T_\infty)^2}{T_\infty^2 L^2}$.

The irreversibility ratio, introduced by Bejan [36] is defined as

$$\phi = \frac{\text{Dissipation}}{\text{Conduction}} = \frac{\frac{AB_r}{\Omega_e} \left\{ (\mathbf{F}')^2 + \frac{1}{4}(\eta^2 + 2Re)(\mathbf{F}'')^2 \right\}}{\frac{1}{2}(\eta^2 + Re)(\Theta')^2}. \quad (26)$$

4. Method of solution

The section describes a spectral collocation numerical scheme with overlapping grids used in solving the nonlinear ordinary differential Eqs. (14–17). The nonlinear system of ODEs is simplified by using the quasi-linearization method (QLM) of Bellman and Kalaba [37]. Applying the QLM scheme to Eqs. (14–17) we obtained the following linearized system

$$\begin{aligned}
& aa_{0,r}f_{r+1}^{iv} + aa_{1,r}f_{r+1}''' + aa_{2,r}f_{r+1}'' + aa_{3,r}f_{r+1}' + aa_{4,r}f_{r+1} \\
& + aa_{5,r}g_{r+1}''' + aa_{6,r}g_{r+1}'' + aa_{7,r}g_{r+1}' + aa_{8,r}g_{r+1} \\
& + aa_{9,r}\theta_{r+1} + aa_{10,r}\phi_{r+1} = Rr_{1,r}.
\end{aligned} \tag{27}$$

$$\begin{aligned}
& bb_{0,r}g_{r+1}''' + bb_{1,r}g_{r+1}'' + bb_{2,r}g_{r+1}' + bb_{3,r}g_{r+1} \\
& + bb_{4,r}f_{r+1}''' + bb_{5,r}f_{r+1}'' + bb_{6,r}f_{r+1}' \\
& + bb_{7,r}f_{r+1} = Rr_{2,r}.
\end{aligned} \tag{28}$$

$$\begin{aligned}
& cc_{0,r}\theta_{r+1} + cc_{1,r}\theta_{r+1}' \\
& + cc_{2,r}f_{r+1}'' + cc_{3,r}f_{r+1}' + cc_{4,r}f_{r+1} \\
& + cc_{5,r}g_{r+1}'' + cc_{6,r}g_{r+1}' + \\
& cc_{7,r}g_{r+1} = Rr_{3,r}.
\end{aligned} \tag{29}$$

$$\begin{aligned}
& dd_{0,r}\phi_{r+1} + dd_{1,r}\phi_{r+1}' + dd_{2,r}\phi_{r+1} \\
& + dd_{3,r}f_{r+1}'' + dd_{4,r}f_{r+1}' + dd_{5,r}f_{r+1} + dd_{6,r}g_{r+1}'' \\
& + dd_{7,r}g_{r+1}' + dd_{8,r}g_{r+1} = Rr_{4,r}.
\end{aligned} \tag{30}$$

The boundary conditions are expressed as

$$\begin{aligned}
& f' = 1, f = 0, g' = \beta, g = 0, \theta = 1, \phi = 1, \text{ at } \eta = 0, \\
& f' \rightarrow 0, f'' \rightarrow 0, g' \rightarrow 0, g'' \rightarrow 0, \theta \rightarrow 0, \phi \rightarrow 0 \text{ as } \eta \rightarrow \infty.
\end{aligned} \tag{31}$$

Equations (27–30) are the linearized system of the ordinary differential equations where $aa_{i,r}, bb_{i,r}, cc_{i,r}$ and $dd_{i,r}, i = 0, 1, 2, \dots, n$ represent the variable coefficients. $Rr_{i,r}, i = 1, 2, \dots, n$ represent the right side of the system of ODEs, while r is the iteration level. Equations (27–30) are solved iteratively starting with an initial approximation until the desired accuracy tolerance is realized. The spatial domain $\eta \in [0, \infty)$ is first truncated to $[0, L_\eta]$ where L_η is large enough to approximate conditions at infinity and $[0, L_\eta]$ is broken down into q overlapping subintervals of equal lengths with

$$\langle \cdot \rangle_l = [\eta_{l-1}, \bar{\eta}_l], \quad \eta_{l-1} < \eta_l < \bar{\eta}_l, \quad \eta_0 = 0, \quad \eta_q = L_\eta, \quad l = 1, 2, 3, \dots, q, \tag{32}$$

where $\eta_l < \bar{\eta}_l$ depicts the overlapping points. Pictorially the overlapping domain decomposition in η can be represented as

The computational domain $[\eta_{l-1}, \bar{\eta}_l]$ in the l^{th} subinterval is transformed into $\eta^* \in [-1, 1]$ where the standard Chebyshev differential matrix is defined by applying the linear map

$$\eta^* = \frac{2}{\bar{\eta}_l - \eta_{l-1}} \left[\eta - \frac{1}{2}(\bar{\eta}_l + \eta_{l-1}) \right], \quad \eta \in [\eta_{l-1}, \bar{\eta}_l]. \tag{33}$$

Further, each subinterval is divided into $N_\eta + 1$ Chebyshev–Gauss–Lobatto points. The subintervals of the decomposed domain are made to overlap in such a way that the last two points in the $\langle \cdot \rangle_l$ subinterval overlap with the first two points of the $\langle \cdot \rangle_{l+1}$ subinterval and they remain common. The collocation nodes in the l^{th} subinterval in η are as defined by Trefethen [38] and expressed as

$$\eta_i = \cos\left(\frac{\pi i}{N_\eta}\right), \quad \text{for } i = 0, 1, 2, \dots, N_\eta, \quad \eta \in [-1, 1]. \tag{34}$$

To obtain an explicit expression for the length of each subinterval given by $L = \bar{\eta}_l - \eta_{l-1}$ in η in terms of the number of subintervals q we solve for L in Eq. (35) expressed as

$$qL - L(q-1) \left(\frac{1}{2} - \frac{1}{2} \cos\left\{ \frac{\pi}{N_\eta} \right\} \right) = b - a, \tag{35}$$

to obtain

$$L = \frac{b - a}{q + (1 - q) \left(\frac{1}{2} - \frac{1}{2} \cos\left\{ \frac{\pi}{N_\eta} \right\} \right)}. \tag{36}$$

From Eq. (33) η_l and $\bar{\eta}_l$ have the following relation

$$\bar{\eta}_l = \eta_l + L \left(\frac{1}{2} - \frac{1}{2} \cos\left\{ \frac{\pi}{N_\eta} \right\} \right). \tag{37}$$

Equation (37) is used in defining the boundaries of the overlapping subintervals of the domain. The system of ODEs Eqs. (14–17) is approximated using Lagrange bivariate interpolating polynomials expressed as

$$\begin{aligned}
f(\eta) &\approx \sum_{q=0}^{N_\eta} f(\eta_q) L_q(\eta), \quad g(\eta) \approx \sum_{q=0}^{N_\eta} g(\eta_q) L_q(\eta), \\
\theta(\eta) &\approx \sum_{q=0}^{N_\eta} \theta(\eta_q) L_q(\eta), \\
\phi(\eta) &\approx \sum_{q=0}^{N_\eta} \phi(\eta_q) L_q(\eta),
\end{aligned} \tag{38}$$

where $L_q(\eta)$ denotes the cardinal standard Lagrange polynomial. The $F(f, g, \theta, \phi)$ derivatives in respect of η in the l^{th} subinterval for $l = 1, 2, 3, \dots, q$ are approximated at the grid points (η_i) for $i = 0, 1, 2, \dots, N_\eta$ as

$$\frac{\partial^n F_{r+1}(\eta_i)}{\partial \eta^n} = \mathbf{D}^n \mathbf{F}_{i,r+1} = \left(\frac{2}{L_\eta} \right)^n \sum_{h=0}^{N_\eta} \mathbf{D}_{i,h}^n F_{r+1}(\eta_h), \tag{39}$$

where

5. Interpolation errors and validation of results

Theorem 1 [39] *If $F(\eta)$ is a polynomial function of degree N which interpolates $f(\eta)$ at $N + 1$ grid points $\eta_0, \eta_1, \eta_2, \dots, \eta_N, \eta \in [a, b]$ and if the $(N + 1)$ th derivatives of $f(\eta)$ exist and are continuous, then there exists an error function ϵ_η for which*

$$|f(\eta) - F(\eta)| \leq \frac{1}{(N+1)!} f^{(N+1)}(\epsilon_\eta) \prod_{j=0}^N (\eta - \eta_j), \quad (47)$$

where $F(\eta)$ is the $(N + 1)$ th degree interpolating polynomial that approximates $f(\eta)$. If the values of higher ordered derivatives increase indefinitely without bound, then the approximation error may grow as the number of grid points N increases. The product term in Eq. (47) can be made as small as possible by making a suitable choice of grid points, Griffiths [40]. To find the error bound we note that the Chebyshev–Gauss–Lobatto nodes in the interval $\eta \in [a, b]$ are defined as

$$\begin{aligned} \{\bar{\eta}_j\}_{j=0}^N &= \cos\left(\frac{j\pi}{N}\right), \\ \bar{\eta}(\eta) &= \frac{2}{b-a} \left[\eta - \frac{1}{2}(a+b) \right], \quad \eta \in [a, b]. \end{aligned} \quad (48)$$

The grid points are relative extremes of the N th degree Chebyshev polynomial, $T_N(\bar{\eta})$, $\bar{\eta} \in [-1, 1]$ [41]. To obtain the interior Gauss–Lobatto nodes we solve the equation $T'_N(\bar{\eta}) = 0$, where the prime represents differentiation with respect to η . The exterior nodes -1 and 1 are solutions of $(1 - \bar{\eta}^2) = 0$. Thus, the complete set of Gauss–Lobatto points Eq. (48) are the roots of $(N + 1)$ th degree polynomial expressed as

$$L_{N+1}(\bar{\eta}) = (1 - \bar{\eta}^2) T'_N(\bar{\eta}). \quad (49)$$

The error bound obtained when Chebyshev–Gauss–Lobatto points $\{\bar{\eta}_j\}_{j=0}^N \in [a, b]$ are used in a polynomial interpolation is expressed as

$$E(\eta) \leq \frac{4}{2^N (N+1)!} \left(\frac{b-a}{2} \right)^{N+1} f^{(N+1)}(\eta). \quad (50)$$

This result can be shown by first constructing the $(N + 1)$ th degree polynomial, L_{N+1} given by Salzer [42]

$$L_{N+1}(\bar{\eta}) = (1 - \bar{\eta}^2) T'_N(\bar{\eta}) = -N\bar{\eta} T_N(\bar{\eta}) + N T_{N-1}(\bar{\eta}). \quad (51)$$

For $\bar{\eta} \in [-1, 1]$, $|T_N(\bar{\eta})| \leq 1$, hence applying the triangle inequality Eq. (51) we have

$$\begin{aligned} |L_{N+1}(\bar{\eta})| &= | -N\bar{\eta} T_N(\bar{\eta}) + N T_{N-1}(\bar{\eta}) | \leq | \\ & -N\bar{\eta} T_N(\bar{\eta}) | + | N T_{N-1}(\bar{\eta}) | \leq 2N. \end{aligned} \quad (52)$$

The absolute value of the leading coefficient of $L_{N+1}(\bar{\eta})$ is $2^{N-1}N$. The components 2^{N-1} and N , respectively, come from the $T_N(\bar{\eta})$ leading coefficient of and the N th differentiation law applied to $T_N(\bar{\eta})$. The product term in error bound expression Eq. (47) can thus be written as

$$\prod_{j=0}^N (\bar{\eta} - \bar{\eta}_j) = \frac{L_{N+1}(\bar{\eta})}{2^{N-1}N}. \quad (53)$$

The polynomial Eq. (53) is bounded by

$$\left| \prod_{j=0}^N (\bar{\eta} - \bar{\eta}_j) \right| = \left| \frac{L_{N+1}(\bar{\eta})}{2^{N-1}N} \right| \leq \frac{2N}{2^{N-1}N} = \frac{4}{2^N}. \quad (54)$$

For a general interval $\eta \in [a, b]$ the product term is bounded above by

$$\begin{aligned} & \max_{a \leq \eta \leq b} \left| \prod_{j=0}^N (\eta - \eta_j) \right| \\ &= \max_{-1 \leq \bar{\eta} \leq 1} \left| \prod_{j=0}^N \frac{(b-a)^{N+1}}{2} (\bar{\eta} - \bar{\eta}_j) \right| \\ &= \left(\frac{b-a}{2} \right)^{N+1} \max_{-1 \leq \bar{\eta} \leq 1} \left| \prod_{j=0}^N (\bar{\eta} - \bar{\eta}_j) \right| \\ &= \left(\frac{b-a}{2} \right)^{N+1} \max_{-1 \leq \bar{\eta} \leq 1} \left| \frac{L_{N+1}(\bar{\eta})}{2^{N-1}N} \right| \leq \frac{4}{2^N} \left(\frac{b-a}{2} \right)^{N+1}. \end{aligned} \quad (55)$$

Using Eq. (55) in Eq. (47) the proof is completed.

Sensitivity analysis is carried out on the coefficient matrix that is used to solve the system of differential equations. The analysis is important in testing the robustness of the algorithm and to check if the matrix is well conditioned. The reciprocal condition number of the matrix and the results obtained are presented in Table 1. The condition number is relatively close to unity implying that the matrix is symmetric and well conditioned. Further, the CPU time is small implying that the method converges rapidly. It can therefore be assumed that the method is a suitable numerical tool for solving systems of highly nonlinear ordinary differential equations. To determine the convergence of the numerical method, the error is computed between two successive iterations as

$$|E_{r+1}|_{\infty} = \max_{0 \leq \eta \leq T} |F_{r+1}^N - F_r^N|, \quad (56)$$

where r is the number of iterations. From Table 2 it is evident that after the sixth iteration, the solution error is of the order 10^{-16} implying that the numerical tool used is

Table 1 Reciprocal condition number

Time	CPU time	Condition number
0.4	0.40869	2.31642e+05
0.9	0.52877	2.47164e+04
1.5	0.59214	2.51287e+03
1.9	0.69153	2.51371e+02
2.5	0.73419	2.42654e+02
3.0	0.81735	2.47342e+02

accurate with fast convergence. The method can be relied upon to give accurate solutions to highly nonlinear governing equations.

The numerical results for the minimization of entropy generation and fluid properties are computed for various fluid and physical parameters including the Deborah numbers, the Prandtl number, chemical reaction parameter, stretching parameter, mixed convection parameter, concentration buoyancy parameter, time ratio parameter, the Reynolds number, the Brinkman number, temperature ratio parameter and concentration ratio parameter. A comparison of the Nusselt number with the reported literature is given in Table 3 when $\Gamma_1 = 0, \Gamma_2 = 0, \gamma, \lambda = 0, \delta_c = 0, \Omega_e = 0, \beta_1 = 0.2, \beta_2 = 0.4, Sc = 1.0,$ and $Pr = 1.2.$ The results are comparable to those reported by Hayat [12] showing the accuracy of the numerical scheme.

6. Numerical results and discussion

Figure 3 shows that reducing the Brinkman number, entropy production is reduced. As the Brinkman number increases, heat energy produced by viscous dissipation from the surface of the plate is transferred by conduction to the fluid leading to a growth in the thermal boundary thickness. This may be the case, for example, in a screw extruder where the energy supplied to the polymer comes

from heat conduction from the wall. Figure 4 shows the influence of the Reynolds number on entropy generation. A 30% decrease in the Reynolds number leads to increased entropy generation, while the opposite trend is observed when the Reynolds number is increased. Reducing the Reynolds number leads to a decrease in inertia forces resulting in less friction between fluid layers that consequently leads to a thin thermal boundary layer and so minimizing entropy production. Figure 5 shows that increased values of the time ratio parameter lead to a growth in entropy production. Long contact time between the wall and the fluid particles increases the frictional forces between the wall and the fluid layers which leads to thickening of the thermal boundary layer causing entropy production to increase. Minimal entropy production in our model can therefore be achieved by reducing contact time and this can be done, for example, by increasing the velocity of the fluid. Figure 6 shows entropy production can be minimized by reducing the concentration ratio parameter by 20% as less deposits are made on the surface of the plate resulting in lower frictional forces between the fluid layers and the surface. This leads to a thin thermal boundary layer and thus minimal production of entropy. The mixed convection parameter has minimal effects on entropy generation.

Figure 7 shows that growth in the Hartman number leads to a decrease in the velocity profiles. The Hartman number is the ratio of electromagnetic forces to the viscous forces experienced as the fluid flows through magnetic fields. The electromagnetic forces increase, causing the drag forces between the flow layers and the surface to increase. As a result, the velocity is reduced depending on the strength of the applied magnetic fields. The Hartman number is important, for example, in the design of liquid metallic devices such as MHD generators, electromagnetic pumps and water meters. Figure 8 indicates that an increase in the mixed convection parameter leads to an

Table 2 Overlapping grid spectral collocation approximations using $N_\eta = 30, q = 5$

Iterations	Residual error			
	$\ f_{r+1} - f_r\ _\infty$	$\ g_{r+1} - g_r\ _\infty$	$\ \theta_{r+1}\ _\infty$	$\ \phi_{r+1}\ _\infty$
1.0	4.03161e-1	5.03121e-3	2.91641e-2	2.96312e-4
2.0	3.13943e-4	2.24022e-4	2.82065e-4	2.77216e-6
3.0	2.72152e-7	2.03187e-6	2.43282e-8	1.52971e-12
4.0	2.03474e-14	1.23321e-15	1.24378e-14	1.32873e-14
5.0	2.13122e-14	1.13726e-15	1.04762e-15	1.02343e-15
6.0	1.13720e-15	1.05627e-16	0.14371e-15	1.00143e-15
CPU time (s)	0.23321	0.22360	0.15362	0.11342

Table 3 Axial skin friction coefficient τ for different values of parameters

Γ_1	Γ_2	M	λ	N	δ_e	δ_c	Re	Pr	Sc	τ
0.01	0.03	0.01	0.2	0.5	0.2	0.1	0.1	0.75	0.61	1.53304051
0.02										1.53710323
0.03										1.54112027
0.05										1.55675488
	0.04									1.28346965
	0.05									1.30296704
	0.07									1.32226539
	0.09									1.36044052
		0.02								0.92775416
		0.03								0.93702861
		0.50								1.25522136
		0.70								1.32981918
			0.3							1.32980485
			0.4							1.28482929
			0.6							1.19086891
			0.8							1.14025734
				0.2						1.32656583
				0.4						1.32293946
				0.7						1.31559995
				0.9						1.30437283
					0.1					1.20551931
					0.4					1.20164271
					0.5					1.19260784
					0.7					1.18700290
						0.01				1.20945152
						0.04				1.21043567
						0.07				1.21229940
						0.10				1.21518649
							0.4			1.21520717
							0.7			1.21520749
							0.9			1.21520037
							1.2			1.21479999
								0.01		1.09863018
								0.03		1.09460680
								0.05		1.08465255
								0.06		1.07717397
									0.1	1.26421389
									0.3	1.26427880
									0.7	1.26435190
									1.1	1.26485890

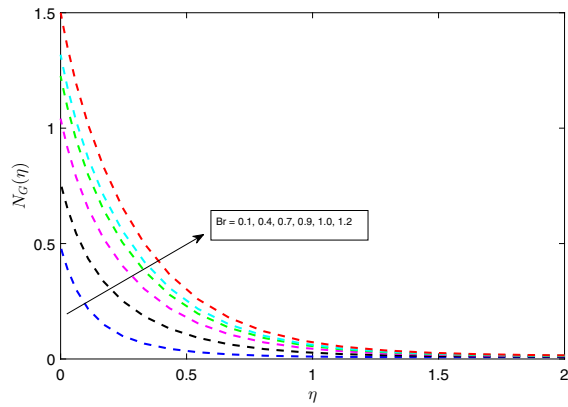


Fig. 3 Varying Brinkman number on entropy generation

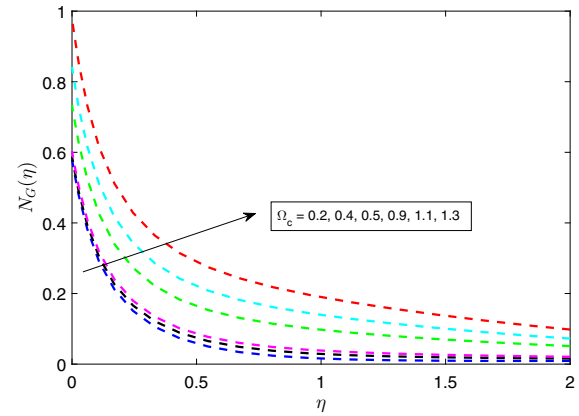


Fig. 6 Influence of concentration ratio parameter on entropy generation

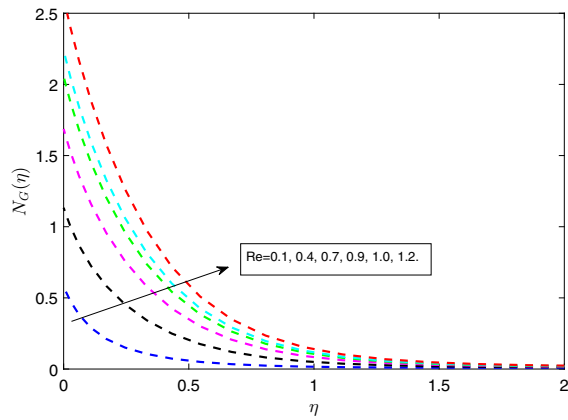


Fig. 4 Influence of Reynolds number on entropy generation

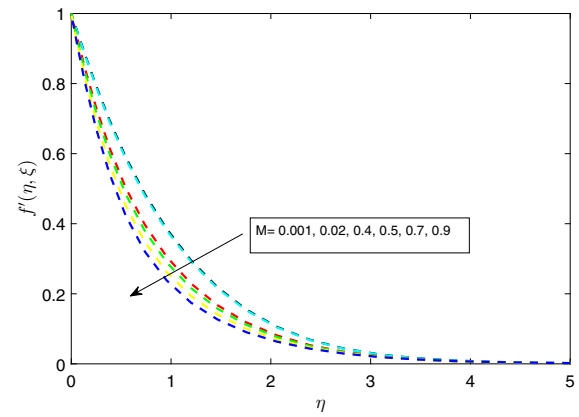


Fig. 7 Influence of the Hartman number on primary velocity profile

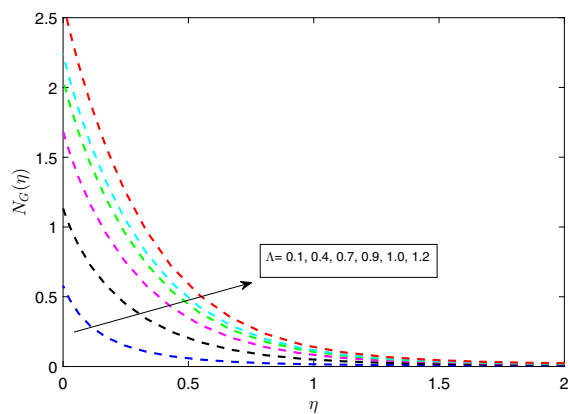


Fig. 5 Influence of time ratio parameter on entropy generation

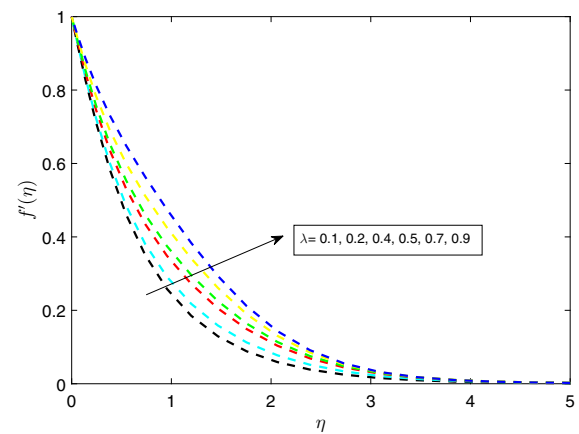


Fig. 8 Influence of mixed convection parameter on primary velocity profile

increase in the velocity profiles. The Deborah numbers in terms of relaxation and retardation time have minimal effects on the primary and secondary velocity profiles. Figure 9 shows that an increase in the Hartman number leads to a reduction in the secondary velocity profiles. The electromagnetic forces increase with increased Hartman number, causing the drag force between the flow layers and the surface to increase. For this reason, the fluid velocity is reduced depending on the strength of the applied magnetic field.

Figure 10 indicates that growth in the Deborah number in terms of relaxation time heat flux contributes to an increase in temperature profiles. The temperature is higher on the surface of the plate and lower far from the surface. Increasing the Deborah number leads to less contact time between fluid particles and the surface of the plate, leading to thickening of the thermal boundary layer. Figure 11

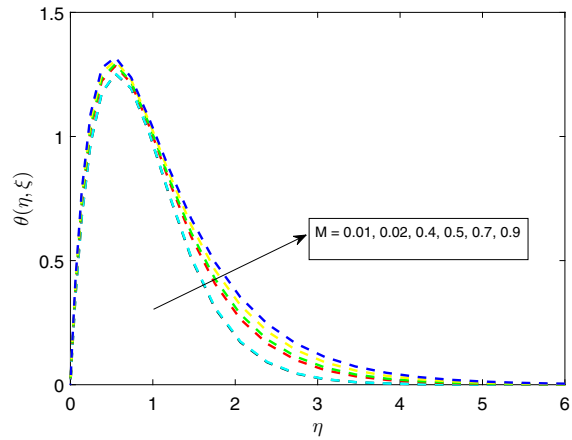


Fig. 11 Influence of the Hartman number on temperature profile

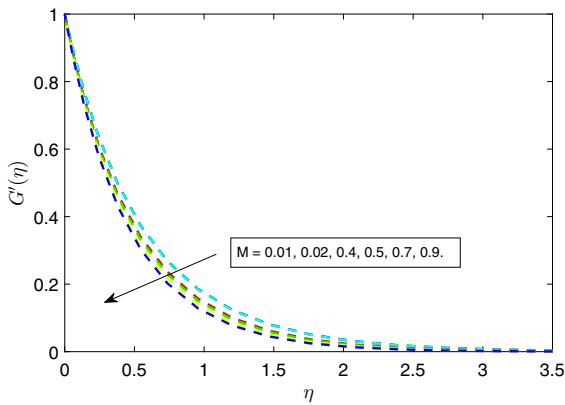


Fig. 9 Influence of Hartman number on secondary velocity profile

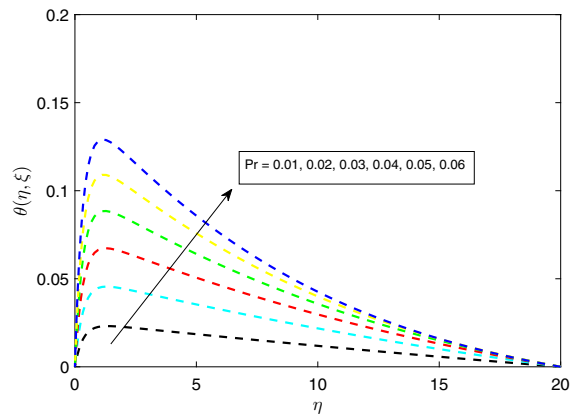


Fig. 12 Influence of Prandtl number on temperature profile

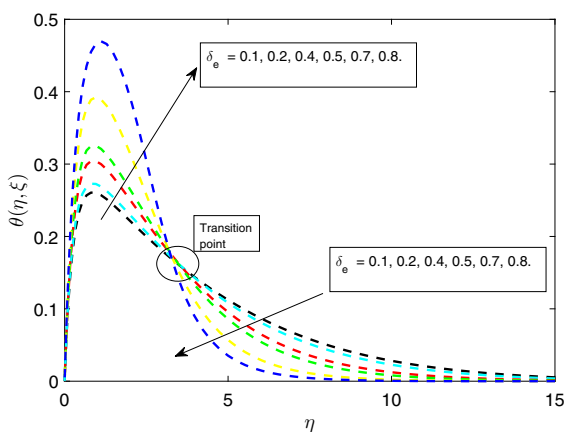


Fig. 10 Influence of Deborah number in terms of relaxation time heat flux on temperature profile

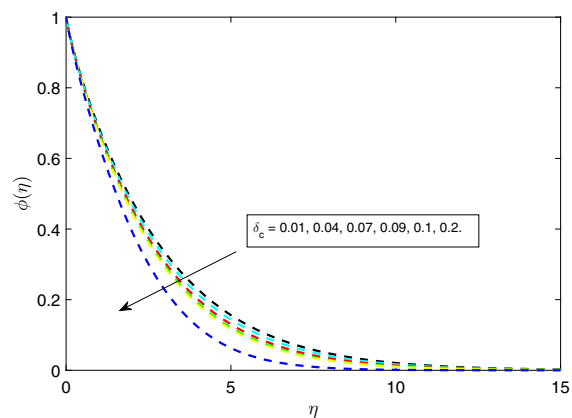


Fig. 13 Influence of Deborah number in terms of relaxation time of mass flux on concentration profile

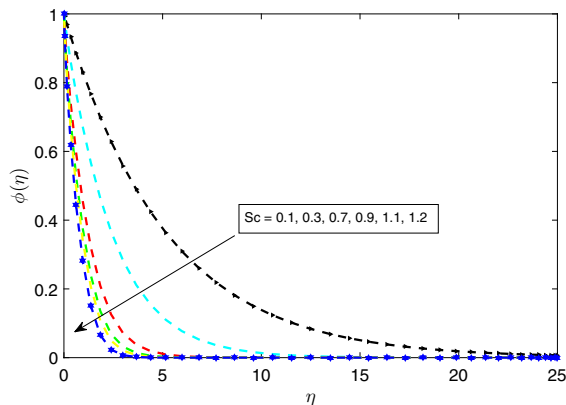


Fig. 14 Influence of Schmidt number on concentration profile

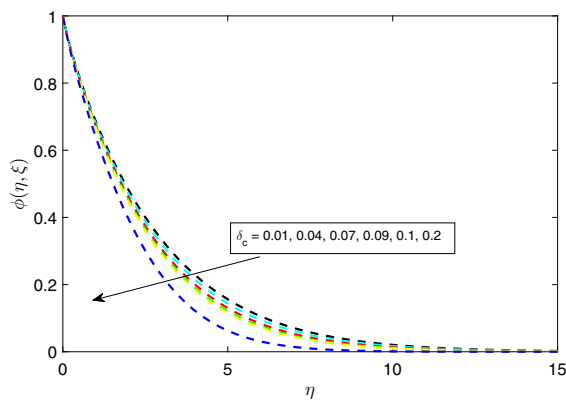


Fig. 15 Influence of Deborah number in terms of relaxation time on concentration profile

shows that increased Hartman number leads to a rise in the temperature profiles. The electromagnetic forces increases when the Hartman number is increased which causes the frictional forces between fluid layers and surface to rise, resulting in thickening of the thermal boundary layer. Figure 12 shows that an increase in the Prandtl number leads to temperature profile rise. The Prandtl number is the ratio of momentum diffusivity to thermal diffusivity. Both the dynamic viscosity and the specific heat capacity of the fluid increases as the Prandtl number increases which leads to a thickening of the thermal boundary layer causing the temperature of the fluid to rise.

Figure 13 shows that an increase in the Deborah number in terms of mass flux relaxation time leads to a decline in the concentration profiles. Figure 14 shows that a rise in the Schmidt number has a negative impact on concentration profiles. Growth in the Schmidt number means an increase in the dynamic viscosity of the fluid, meaning that the mass flow rate will increase leading to a decrease in

mass deposits on the surface. This has applications, in, for example in stirling engines that work by cyclic compression and expansion of gasses at various temperatures where the Schmidt number relates to particular temperatures. Figure 15 shows that a growth in the Deborah number in mass flux relaxation time leads to a decline in the concentration profile.

Tables 3, 4, 5 and 6 give the results of the axial skin and transverse skin friction coefficients, Nusselt number and Sherwood number, respectively, for various parameters. The Deborah number, the Hartman number and the Schmidt number all contribute to an increase in the skin friction coefficient. The fluid flow generates frictional forces at the surface which impede the forward movement of the fluid and as a result energy is generated at the surface. Entropy generation can be minimized in this case by reducing these fluid parameters. The Nusselt number is the ratio of heat transfer by convection to conduction. Small values of the Nusselt number are significant in minimizing entropy generation and this can be achieved by increasing the Deborah numbers in both relaxation and retardation time, mixed convection parameter and the Schmidt number. The Sherwood number is the ratio of convective mass transfer to the rate of diffusive mass transport. Entropy generation for this model can be minimized by reducing the Deborah number in both relaxation and retardation time, mixed convection parameter, the Reynolds number and the Schmidt number. These results are in line with those of [12] (i.e., see Table 7).

7. Conclusion

The study presented an analysis of irreversibility and entropy minimization on three-dimensional MHD Oldroyd-B fluid with relaxation-retardation viscous dissipation and a chemical reaction. The flow equations were solved using an overlapping grid spectral collocation method. The accuracy convergence was determined. The following are findings in this study:

1. *Minimizing entropy generation can be achieved by increasing the Deborah numbers in both relaxation and retardation time, mixed convection parameter and the Schmidt number.*
2. *An increase in the Reynolds number increases entropy generation.*
3. *Increasing the Hartman number reduces the velocity boundary layer thickness while increasing the thermal boundary layer thickness.*
4. *Increasing the mixed convection parameter increases the primary and the secondary velocity fields substantially.*

Table 4 Transverse skin friction coefficient τ for different values of parameters

Γ_1	Γ_2	M	λ	N	δ_e	δ_c	Re	Pr	Sc	τ
0.01	0.03	0.01	0.2	0.1	0.2	0.1	0.1	0.75	0.61	2.16834340
0.02										2.20506147
0.03										2.24156164
0.05										2.31393387
	0.04									2.12488711
	0.05									2.11416064
	0.07									2.10406024
	0.09									2.08561731
		0.02								1.89077893
		0.03								1.89553935
		0.50								2.07236866
		0.70								2.11742394
			0.3							2.11742452
			0.4							2.12460412
			0.6							2.13784511
			0.8							2.14426587
				0.2						2.11806805
				0.4						2.11877920
				0.7						2.12018975
				0.9						2.12088941
					0.1					2.16867356
					0.4					2.16938688
					0.5					2.17104413
					0.7					2.17206869
						0.01				2.16049660
						0.04				2.16033526
						0.07				2.16018144
						0.10				2.16008294
							0.4			2.01136676
							0.7			2.01136676
							0.9			2.01136676
							1.2			2.01136676
								0.01		2.00130784
								0.03		2.00253425
								0.05		2.00358147
								0.06		2.00526550
									0.1	2.13547319
									0.3	2.13544287
									0.7	2.13541478
									1.1	2.13536397

Impact of irreversibility ratio

Table 5 Nusselt number for different values of parameters

Γ_1	Γ_2	M	λ	N	δ_e	δ_c	Re	Pr	Sc	$-\theta'(0)$
0.01										5.60055304
0.02										5.56598545
0.03										5.53256056
0.05										5.40887984
	0.03									14.46604447
	0.05									14.47294138
	0.07									14.49395524
	0.09									14.52838779
		0.01								6.71318928
		0.02								6.72997786
		0.50								7.35535581
		0.70								7.51670807
			0.2							7.51640856
			0.4							7.33722237
			0.6							7.08093919
			0.8							6.98801474
				0.5						7.49060447
				0.7						7.46242334
				0.9						7.40752933
				1.1						7.38077975
					0.1					1.26891346
					0.2					1.29019166
					0.4					1.34077832
					0.5					1.37174221
						0.01				1.20576271
						0.04				1.21970592
						0.07				1.23328235
						0.10				1.24215526
							0.1			1.28907541
							0.4			1.28907538
							0.7			1.28907743
							1.0			1.28914025
								0.01		14.46604447
								0.03		14.46767511
								0.05		14.47294138
								0.06		14.49395524
									0.1	2.13547319
									0.3	2.13544287
									0.7	2.13541478
									1.1	2.13536397

Table 6 Sherwood number for different values of parameters

Γ_1	Γ_2	M	λ	N	δ_e	δ_c	Re	Pr	Sc	$-\phi'(0)$
0.01	0.03	0.01	0.2	0.1	0.2	0.1	0.1	0.75	0.61	0.19326450
0.02										0.19354058
0.03										0.19381857
0.05										0.19495088
	0.03									0.48239094
	0.05									0.48055316
	0.07									0.47856901
	0.09									0.47417871
		0.01								0.52841418
		0.02								0.52696373
		0.50								0.48134856
		0.70								0.47176532
			0.2							0.47167893
			0.4							0.48152048
			0.6							0.49937250
			0.8							0.50800160
				0.5						0.47305212
				0.7						0.47455960
				0.9						0.47751976
				1.1						0.47897389
					0.1					0.44011411
					0.2					0.53477154
					0.4					0.70907197
					0.5					0.79055353
						0.01				0.50331720
						0.04				0.50705514
						0.07				0.51114458
						0.10				0.51408883
							0.1			0.684313
							0.4			0.831831
							0.7			0.571954
							1.0			0.615956
								0.01		0.41403964
								0.03		0.41633007
								0.05		0.41826619
								0.06		0.41826619
									0.1	0.07056240
									0.3	0.09106629
									0.7	0.11157308
									1.1	0.15278081

Table 7 Comparison of existing literature results with present results for the Nusselt number (Nu) when

Hayat et al. [12]. Nu $1-\theta'$	Present Nu $1-\theta'$
0.2836	0.283152
0.2790	0.278480
0.2780	0.277631
0.2741	0.273692
0.2727	0.272692
0.2672	0.2671571
0.2648	0.2647821

5. The concentration field reduces with an increase in the Schmidt number.

Acknowledgements The authors are grateful to the University of KwaZulu-Natal, South Africa, and Amity University Kolkata, India, for necessary support.

Compliance with ethical standards

Conflict of interest The authors declare that they have no conflict of interest.

References

- [1] J Oldroyd *Proc. R. Soc. Lond.* **200** 523 (1950)
- [2] R K Bhatnagar, G Gupta and K R Rajagopal *Int. J. Nonlinear Mech.* **30** 391 (1995)
- [3] C Fetecau and C Fetecau *Int. J. Eng. Sci.* **43** 340 (2005)
- [4] T Hayat, Z Hussain, M Farooq, A Alsaedi and M Obaid *Int. J. Nonlinear Sci. Numer. Simul.* **15** 77 (2014)
- [5] T Hayat, M Ijaz, Khan, M Waqas and A Alsaedi *Nuclear Eng. Nuclear Eng. Technol.* **49** 1645 (2017)
- [6] Y Zhang, M Zhang and Y Bai *J. Mol. Liq.* **220** 665 (2016)
- [7] M M Bhatti, A Zeeshan and M M Rashidi *Int. J. Eng. Sci. Technol.* **20** 265 (2017)
- [8] Y Zhang, J Jiang and Y Bai *Comput. Math. Appl.* (2019)
- [9] S S Ghadikolaei, K h Hosseinzadeh and D D Ganji *World J. Eng.* (2019)
- [10] M Gholinia, K H Hosseinzadeh, H Mehrzadi, D D Ganji, and A A Ranjbar *Case Stud. Therm. Eng.* **13** 100356 (2019)
- [11] Kh Hosseinzadeh, A Jafarian Amiri, S Saedi Ardahaie and D D Ganji *Case Stud. Therm. Eng.* **10** 595 (2017)
- [12] T Hayat, T Muhammad, S A Shehzad and A Alsaedi *Int. J. Therm. Sci.* **111** 274 (2017)
- [13] C Cattaneo *Atti Sem. Mat. Fis. Univ. Modena* **3** 83 (1948)
- [14] C I Christov *Mech. Res. Commun.* **36** 481 (2009)
- [15] K H Hosseinzadeh, M Gholinia, B Jafari, A Ghanbarpour, H Olfian, and D D Ganji *Heat Transf. Asian Res.* **48** 744 (2019)
- [16] M Gholinia, S Gholinia, K H Hosseinzadeh, and D D Ganji *Results Phys.* **9** 1525 (2018)
- [17] F M Abbasi, M Mustafa, S A Shehzad, M S Alhuthali and T Hayat *Chin. Phys. B* **25** 147 (2015)
- [18] T Hayat, M Waleed, A Khan, A Alsaedi, M Ayub, and M I Khan *Results Phys.* **7** 2470 (2017)
- [19] K H Hosseinzadeh, A R Mogharrebi, A Asadi, M Paikar and D D Ganji *J. Mol. Liq.* **300** 112347 (2020)
- [20] T Hayat, M Imtiaz, A Alsaedi and S Almezal *J. Magn. Magn. Mater.* **401** 296 (2016)
- [21] N Sandeep and C Sulochana *Ain Shams Eng. J.* **9** 517 (2018)
- [22] Z Shah, P Kumam and W Deebani *Sci. Rep.* **10** 14 (2020)
- [23] M I Sumaira, K Qayyum, T Hayat, M I Khan, A Alsaedi and T Khan *Phys. Lett. A* **382** 2026 (2018)
- [24] A Saeed, S Islam, A Dawar, Z Shah, P Kumam and W Khan *Symmetry* **11** 439 (2019)
- [25] S A Shehzad, Z Abdullah, F M Abbasi, T Hayat and A Alsaedi *J. Magn. Magn. Mater.* **399** 97 (2016)
- [26] M Almakki, S K Nandy, S Mondal, P Sibanda and D Sibanda *Heat Transf. Asian Res.* **48** 24 (2019)
- [27] K H Hosseinzadeh, A Asadi, A R Mogharrebi, J Khalesi, S Mousavisani and D D Ganji *Case Stud. Therm. Eng.* **14** 100482 (2019)
- [28] W A Khan, M M Yovanovich and J R Culham *Twenty-Second Annual IEEE Semiconductor Thermal Measurement and Management Symposium* 78 (2006)
- [29] M W Khan, M I Khan, T Hayat and A Alsaedi *Phys. B Condens. Matter* **534** 113 (2018)
- [30] S Huang, Z Ma, and P Cooper *Energy Convers. Manag.* **87** 128 (2014)
- [31] H Feng, J You, L Chen, Y Ge, and S Xia *Eur. Phys. J. Plus* **135** 257 (2020)
- [32] S A Shehzad, A Alsaedi, T Hayat and M S Alhuthali *J. Taiwan Inst. Chem. Eng.* **45** 787 (2014)
- [33] T Hayat, T Muhammad, S A Shehzad, M S Alhuthali and J Lu *J. Mol. Liq.* **212** 272 (2015)
- [34] W A Khan, M Irfan and M Khan *Results Phys.* **7** 3583 (2017)
- [35] A Hafeez, M Khan and J Ahmed *Comput. Methods Prog. Biomed.* **191** 105342 (2020)
- [36] A Bejan *Second Law Anal. Heat Transf.* **5** 720 (1980)
- [37] R Bellman, R Kalaba and B Kotkin *Math. Comput.* **17** 155 (1963)
- [38] L N Trefethen *Spectral Methods MATLAB v.10* (2000)
- [39] G Birkhoff and A Priver *J. Math. Phys.* **46** 440 (1967)
- [40] D V Griffiths and I M Smith *Numer. Methods Eng.* (2006)
- [41] B Fischer and R Freund *J. Approx. Theory* **65** 261 (1991)
- [42] H E Salzer *Math. Comput.* **30** 295 (1976)

Publisher's Note Springer Nature remains neutral with regard to jurisdictional claims in published maps and institutional affiliations.

Chapter 5

Entropy generation in double-diffusive convective magnetic nanofluid flow in the stagnation region of a rotating sphere with viscous dissipation

In Chapter 4, we reported on the three-dimensional MHD flow with relaxation and retardation viscous dissipation, in considering the impact on the irreversibility ratio and entropy minimization. The model equations were solved using the overlapping grid spectral collocation method.

In this chapter, we investigate entropy generation in a double-diffusive convective magnetic nanofluid flow in the stagnation region of a rotating sphere with viscous dissipation. The flow is subjected to thermal radiation, a chemical reaction and rotational effects. The bivariate spectral quasilinearization method is used to solve the system of highly coupled partial differential equations. The impact of physical and chemical parameters on entropy production, heat and mass transfer is determined and discussed.

Entropy generation in double-diffusive convective magnetic nanofluid flow in the stagnation region of a rotating sphere with viscous dissipation

M.Almakki¹, H. Mondal^{2*}, Z.Mburu¹ and P. Sibanda¹

¹*Department of Mathematics, University of KwaZulu-Natal, Private Bag X01, Scottsville 3209, Pietermaritzburg, South Africa*

²*Department of Mathematics, Brainware University, 398 Ramkrishnapur Road, Barasat, North 24 Parganas, Kolkata-700125, India*

Abstract

We investigate the entropy generation for an unsteady magnetic nanofluid flow in the stagnation region of an impulsively rotating sphere, in the presence of thermal radiation, viscous dissipation and chemical reaction effects. Employing the similarity technique, the equations modeling the flow are transformed into highly nonlinear differential equations for boundary layer flow. These equations are numerically executed using the bivariate spectral quasilinearization method. The effect of varying various pertinent parameters on entropy generation, and the velocity, temperature and concentration profiles are investigated and the results analyzed graphically. The rate of entropy generation and temperature profiles increased with increased values of thermal radiation, chemical reaction and rotation parameters while increased values of the magnetic number had a negative impact on rate of entropy generation. Variables of engineering interest, which include the skin friction coefficient, the Nusselt number and the Sherwood number were also analyzed in a table. These numerical results will be valuable for physicists, chemists, biologists and engineers interested in the theory and applications of entropy generation.

Keywords: Viscous dissipation; entropy generation; double diffusive; chemical reaction.

Nomenclature

c_p	heat capacity of the fluid
λ	rotation parameter
ρ	density of the fluid
σ	electrical conductivity of the nanofluid
k	thermal conductivity of the nanofluid
k^*	mean absorption coefficient
Nt	thermophoresis parameter

β_c	concentration expansion coefficients
β_t	temperature expansion coefficients
χ	dimensionless concentration difference parameter
η	dimensionless space variable
Γ	diffusive parameter
γ	buoyancy parameter
ν	kinematic viscosity
ν	viscosity of the fluid
$\phi(\xi, \eta)$	dimensionless concentration variables
Σ	dimensionless temperature difference parameter
σ^*	Stefan-Boltzmann constant
τ	ratio of heat capacity of the nanoparticle material to heat capacity of the fluid
$\theta(\xi, \eta)$	dimensionless temperature variable
ξ	dimensionless time variable
B_0	magnetic field factor
Br	Brinkman number
C_∞	ambient concentration
C_w	constant concentration at the surface
D_B	Brownian diffusion coefficient
D_T	thermophoresis diffusion coefficient
Ec	Eckert number
$f'(\xi, \eta)$	dimensionless velocity components along x -axis
g	acceleration due to gravity
G_r	Grashoff number
Le	Lewis number
M	magnetic field parameter
N	buoyancy ratio
$N_G(\eta, \xi)$	entropy generation number
Nb	Brownian motion parameter
Nr	thermal radiation parameter

Pr	Prandtl number
R	chemical reaction parameter
r	radius of the sphere
R_0	dimensionless chemical reaction parameter
Re	Reynolds number
$S(\xi, \eta)$	dimensionless velocity components along z -axis
S_0'''	characteristic entropy generation
S_{gen}'''	local entropy generation
T_∞	ambient temperature
T_w	constant temperature at the surface
\mathbf{v}	velocity of the fluid
a	constant
C	concentration of the fluid
MHD	Magnetohydrodynamics
T	temperature of the fluid
t	time
u, v, w	velocity components
x, y, z	Cartesian coordinates

1 Introduction

Double-diffusive convection is a fluid dynamics phenomenon that describes a form of convection driven by two different density gradients. The gradients may be due to differences in the composition of the fluid, or differences in temperature causing thermal expansion. The two density gradients may cause different rates of diffusion. Double-diffusive convection is important in understanding flow evolution in systems that have multiple causes of density variations; examples include convection in the atmosphere and oceans. Similar trends are observed in various manufacturing devices such as heat exchangers, gas turbines, atomic plants, and thermal energy storage devices.

Nayak and Bhattacharyya [1] discovered the important fluid outcomes in a cubical lid-driven cavity with opposing temperature gradients causing double-diffusive convection. Their equations were solved using a control volume approach. Further, they found that the transverse velocity occurs at a higher flow Reynolds number, which disturbs the two-dimensional nature in the flow. Double-diffusion natural convection in a rectangular enclosure filled with a binary fluid saturated porous media was discussed by Mohamad et al. [2]. The influence of the lateral aspect ratio on the flow properties was considered to be significant. Hayat et al. [3] studied 3D double-diffusion Cattaneo-Christov nanofluid flow. The flow equations with boundary layer flow were numerically solved using the optimal homotopy analysis method. The results showed

that both temperature and concentration distributions were decreasing functions of thermal and concentration relaxation parameters.

Khan et al. [4] discussed the impact of chemical processes on a 3D Burgers fluid utilizing Cattaneo-Christov double-diffusion. The coupled nonlinear ordinary differential equations were solved by means of the homotopy analysis method. It was deduced that temperature and concentration profiles decay as the non-dimensional thermal and concentration relaxation time parameters are enhanced. Ferdows et al. [5] discussed the variable diffusivity and variable viscosity in double diffusion convection. The resulting highly nonlinear ordinary differential equations were solved numerically using the fourth order Runge-Kutta method and showed an increase of thermal slip boundary layer. Related additional studies include [6–9].

Magnetic nanofluid are a special type of fluid that exhibit both magnetic and fluid properties. They are generated by having magnetic nanoparticles suspended in a base fluid. Recently, these fluid have attracted attention and been studied due to their perceived valuable properties and current applications in a variety of fields. For instance, during surgery it may be necessary to drop blood flow and reduce temperature, which can be achieved by using a magnetic field. Furthermore, the concentration of particles that are delivered to the targeted regions increases with an increase in the magnetic field strength. Yousofvand et al. [10] discussed MHD transverse mixed convection and entropy generation in an electromagnetic pump, including a nanofluid, using a three-dimensional simulation. This type of flow is utilized in power generation systems where heat energy is converted into electric energy. The influence of the angle of inclination on unsteady MHD Casson fluid flow past a vertical surface filled by a porous medium in presence of constant heat flux, chemical reaction and viscous dissipation was investigated by Raju et al. [11]. The results indicated that heat transfer performance is improved when the Hartmann number was increased. Time dependent MHD flow of a conducting Newtonian fluid was analyzed by Makinde and Sibanda [12]. Additional studies on MHD fluid flow are reported in the references [13–15].

Numerous researchers have carried out theoretical and experimental investigations on the effect of radiation in the type fluid flow in which the Rosseland approximation is linear. Its impact is of considerable interest in various non-isothermal conditions, as discussed by Sheikholeslami et al. [16]. Radiation effects for the fluid flow and heat transfer over an unsteady stretching sheet were investigated by Raptis et al. [17]. The results indicated that the temperature profiles increased with a rise in the radiation parameter and magnetic number. Related studies on the effect of radiation on fluid flow were undertaken in the references [18, 19].

Entropy generation in fluid flow has generated special interest and recent investigations in view of its industrial and engineering applications. Entropy generation is a measure of the magnitudes of the irreversibilities present during the process. The performance of almost all engineering systems is degraded by the presence of irreversibility processes and thus there is a need for research on ways by which the rate of entropy generation may be managed so as to improve the efficiency of machines. The effects of entropy generation on miscellaneous applications was first investigated by Bejan [20]. Entropy generation in parallel flow of a power-law liquid was investigated by Haro et al. [21]. Entropy generation due to mixed convection over vertical permeable cylinders using nanofluid was reported in [22]. The entropy generation and couple stress fluid through a channel, including the effect of non-uniform wall temperature, was recently presented in [23]. Ahmed and Mahdy [24] examined the 2D unsteady flow through the stagnation region in double-diffusive convection. The results indicated that the rotational parameter has a positive effect on the flow, heat and mass transfer rates.

In the various research studies cited above, less emphasis has been put on the numerical study of entropy generation in double diffusive convective magnetic nanofluid flow near the stagnation region of a rotating sphere with viscous dissipation forming the basis of this study. The current study aims to investigate entropy generation, heat and mass transfer for MHD laminar boundary layer flow in a nanofluid flow near the stagnation point, determine the convergence and accuracy of the spectral quasilinearization numerical scheme used in solving the relevant PDEs directly, and to investigate the effect of different parameters on the skin friction coefficient, Nusselt and Sherwood numbers.

2 Problem formulation

We consider an unsteady three-dimensional laminar stagnation point of flow an incompressible viscous MHD nanofluid with chemical reaction. The physical model as shown in Figure 1. The velocity of the nanofluid is given by $\mathbf{v} = (u, v, w, t)$. However, It is assumed that $\mathbf{v} = (u, v, w, t)$ is the velocity of the nanofluid, and $u \rightarrow U(x) = ax$ is the distribution of the velocity in regions close to the surface, where $a > 0$. The magnetic field B_0 is applied perpendicular to the flow, which is along the z -axis. The flow is subject to both the viscous dissipation, and chemical reaction. Thermophoresis and the Brownian motion are assumed to be significant.

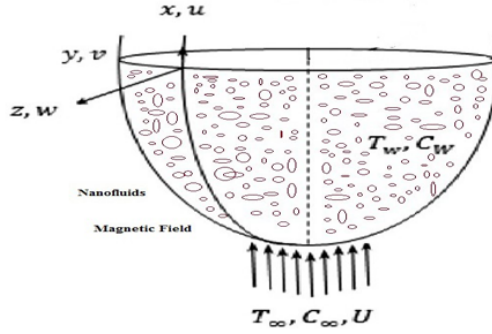


Figure 1: Physical model and coordinate system (see [24])

The equations that describe such convective magnetic nanofluid flow are (see [24, 25])

$$\frac{\partial(xu)}{\partial x} + \frac{\partial(xw)}{\partial z} = 0 \quad (2.1)$$

$$\begin{aligned} \frac{\partial u}{\partial t} + u \frac{\partial u}{\partial x} + w \frac{\partial u}{\partial z} - \frac{v^2}{x} = U \frac{\partial U}{\partial x} + \nu \frac{\partial^2 u}{\partial z^2} + \left[\beta_t (T - T_\infty) + \beta_c (C - C_\infty) \right] g \frac{x}{r} \\ - \frac{\sigma B_0^2}{\rho} (u - v) \end{aligned} \quad (2.2)$$

$$\frac{\partial v}{\partial t} + u \frac{\partial v}{\partial x} + w \frac{\partial v}{\partial z} + \frac{uv}{x} = \nu \frac{\partial^2 v}{\partial z^2} - \frac{\sigma B_0^2}{\rho} v, \quad (2.3)$$

$$\begin{aligned} \frac{\partial T}{\partial t} + u \frac{\partial T}{\partial x} + w \frac{\partial T}{\partial z} &= \frac{k}{\rho c_p} \frac{\partial^2 T}{\partial z^2} + \frac{1}{(\rho c)_f} \frac{16\sigma^* T_\infty^3}{3k^*} \frac{\partial^2 T}{\partial z^2} + \frac{\mu}{\rho c_p} \left(\frac{\partial u}{\partial z} \right)^2 + \\ &\quad \tau \left[D_B \frac{\partial c}{\partial z} \frac{\partial T}{\partial z} + \frac{D_T}{T_\infty} \left(\frac{\partial T}{\partial z} \right)^2 \right], \end{aligned} \quad (2.4)$$

$$\frac{\partial C}{\partial t} + u \frac{\partial C}{\partial x} + w \frac{\partial C}{\partial z} = D_B \frac{\partial^2 C}{\partial z^2} + \frac{D_T}{T_\infty} \frac{\partial^2 T}{\partial z^2} - R(C - C_\infty). \quad (2.5)$$

Equations (2.1)–(2.5) are solved subject to the following boundary conditions (see [24, 25])

$$\begin{aligned} U(x) &= u(t, x, \infty), \quad v = v(t, x, \infty) = 0, \\ T_\infty &= T(t, x, \infty), \quad C_\infty = C(t, x, \infty) \quad \text{at } t \geq 0, \\ u(t, x, z) &= 0, \quad v(t, x, z) = w(t, x, z) = 0, \\ T_\infty &= T(t, x, z), \quad C_\infty = C(t, x, z) \quad \text{at } t < 0. \end{aligned} \quad (2.6)$$

The conservation equations (2.1)–(2.5) require the following transformation variables (see [24, 25])

$$\begin{aligned} U(x) &= ax, \quad \eta = \sqrt{2a/\nu} \xi^{-1/2} z, \quad \xi = 1 - \exp(-at), \quad u = ax f'(\eta, \xi), \\ w &= -(2a\nu)^{1/2} \xi^{1/2} f(\eta, \xi), \quad v(t, x, z) = \Omega x S(\eta, \xi,) \quad \text{at } t > 0 \\ \theta(\eta, \xi,) &= \frac{T - T_w}{T_w - T_\infty}, \quad \phi(\eta, \xi,) = \frac{C - C_w}{C_w - C_\infty}. \end{aligned} \quad (2.7)$$

The set of equations (2.1)–(2.5) are reduced to PDEs using the transformations variables in equation (2.7), resulting to the following set of equations:

$$\begin{aligned} f''' + \xi f f'' + 0.25\eta(1 - \xi) f'' + 0.5\xi(1 - f'^2 + \lambda S^2) + 0.5\xi(1 - f')M + 0.5\xi(\theta + N\phi)\gamma \\ = 0.5\xi(1 - \xi) \frac{\partial f'}{\partial \xi}, \end{aligned} \quad (2.8)$$

$$S'' + \xi(fS' - f'S) + 0.25\eta(1 - \xi)S' - 0.5\xi MS = 0.5\xi(1 - \xi) \frac{\partial S}{\partial \xi}, \quad (2.9)$$

$$\frac{1 + Nr}{Pr} \theta'' + 0.25\eta(1 - \xi)\theta' + \xi f \theta' + Ec f''^2 + Nb \theta' \phi' + Nt \theta'^2 = 0.5\xi(1 - \xi) \frac{\partial \theta}{\partial \xi}, \quad (2.10)$$

$$\frac{1}{Le} \phi'' + 0.25\eta(1 - \xi)\phi' + \xi f \phi' + \frac{1}{Le} \frac{Nt}{Nb} \theta'' - R_0 \phi = 0.5\xi(1 - \xi) \frac{\partial \phi}{\partial \xi}. \quad (2.11)$$

Similarly, using the same transformation variables in equation (2.7), the boundary conditions are reduced to

$$\begin{aligned} f(0, \xi) &= 0, \quad f'(0, \xi) = 0, \quad S(0, \xi) = \theta(0, \xi) = \phi(0, \xi) = 1, \\ f'(\infty, \xi) &= 1, \quad S(\infty, \xi) = 0, \quad \theta(\infty, \xi) = \phi(\infty, \xi) = 0, \end{aligned} \quad (2.12)$$

where the primes denotes differentiation with respect to η or ξ . The parameters obtained in equations (2.8)–(2.11) are defined as follows:

$$\begin{aligned}\lambda &= \left(\frac{\Omega}{a}\right)^2, \quad \gamma = \frac{Gr_R}{Re_R^2}, \quad M = \frac{\sigma B_0^2}{\rho a}, \quad N = \frac{Gr_{Rc}}{Gr_R}, \quad Nr = \frac{16\sigma^* T_\infty^3}{3kk^*}, \\ Pr &= \frac{\mu c_p}{k}, \quad Ec = \frac{\nu^2}{c_p(T_w - T_\infty)}, \quad Nb = \frac{\tau D_B(C_w - C_\infty)}{\nu}, \quad Le = \frac{\nu}{D_B} \\ Nt &= \frac{\tau D_T(T_w - T_\infty)}{\nu T_\infty}, \quad R_0 = \frac{R}{2a},\end{aligned}\quad (2.13)$$

where $\gamma > 0$ and $\gamma < 0$ are the heat source and sink respectively.

3 Entropy Generation

Energy is a quantitative property that is transferred to an object, enabling it to perform work or to heat the object. Entropy generation is a measure of dissipated energy, which reduces the performance of engineering systems, such as transport or rate processes. Entropy is always generated whenever heat enters or exists from a system. The positive entropy generated when heat enters the system is always equal, but opposite in sign, to the negative entropy generated when heat exits the system. Entropy generation can also be defined as the difference between the heat energy entering a system from the high temperature heat source and that which exits to the low temperature heat sink of the system. Entropy generation occurs due to irreversibility of processes or due to friction associated with a process (which increases temperature). Entropy generation is zero for reversible process [20]. The entropy generation with nanoparticles were discovered by [26]. The volumetric rate of local entropy generation for our three-dimensional flow is defined by the following equations (see [27]);

$$\begin{aligned}S_{gen}''' &= \underbrace{\frac{k_f}{T_\infty^2} \left[\left(\frac{\partial T}{\partial z}\right)^2 + \frac{16\sigma^* T_\infty^3}{3k_f k^*} \left(\frac{\partial T}{\partial z}\right)^2 \right]}_{S_{th}} + \underbrace{\frac{\sigma B_0^2}{T_\infty} (u^2 + v^2)}_{S_m} + \underbrace{\frac{\mu}{T_\infty} \left\{ 2 \left[\left(\frac{\partial u}{\partial x}\right)^2 + \left(\frac{\partial w}{\partial z}\right)^2 \right] \right.}_{S_{dis}} \\ &\quad \left. + \left(\frac{\partial v}{\partial x}\right)^2 + \left(\frac{\partial u}{\partial z}\right)^2 + \left(\frac{\partial v}{\partial z}\right)^2 \right\}}_{S_{dis}} + \underbrace{\frac{RD}{T_\infty} \left[\left(\frac{\partial T}{\partial z}\right) \left(\frac{\partial C}{\partial z}\right) \right]}_{S_{dif}} + \underbrace{\frac{RD}{C_\infty} \left(\frac{\partial C}{\partial z}\right)^2}_{S_{dif}}.\end{aligned}\quad (3.1)$$

Equation (3.1) can be written as

$$S_{gen}''' = S_{th} + S_m + S_{dis} + S_{dif} \quad (3.2)$$

where (S_{th}) is the heat transfer, (S_m) is the magnetic field, (S_{dis}) is viscous dissipation and (S_{dif}) is mass transfer. The characteristic entropy generation rate obtained as (see [28])

$$S_0''' = \frac{k_f(T_w - T_\infty)^2}{T_\infty^2 x^2}.\quad (3.3)$$

S_0''' is the optimization problem [29]. The entropy generation number is obtained by dividing equation (3.1) by equation (3.3) to have

$$N_G(\eta, \xi) = \frac{S_{gen}'''}{S_0'''} = 2Re(1 + Nr)\xi^{-1}\theta'^2 + \frac{MReBr}{\Sigma}(f'^2 + \lambda S^2) + 2Re\Gamma\left(\frac{\chi}{\Sigma}\right)^2 \xi^{-1}\phi'^2 + 2Re\Gamma\left(\frac{\chi}{\Sigma}\right)\theta'\phi' + \frac{Br}{\Sigma} \left[10f'^2 + \lambda S^2 + 2Re\xi^{-1}(f''^2 + \lambda S'^2) \right]. \quad (3.4)$$

The equation (3.4) is obtained as

$$Re = \frac{U(x)x}{\nu}, \quad Br = \frac{\mu U^2(x)}{k_f \Delta T}, \quad \Sigma = \frac{\Delta T}{T_\infty} = \frac{T_w - T_\infty}{T_\infty}, \\ \Gamma = \frac{C_\infty RD}{k_f}, \quad \chi = \frac{C_w - C_\infty}{C_\infty}. \quad (3.5)$$

Equation (3.4) can be written as $N_G = S_{th} + S_m + S_{dis} + S_{dif}$, where

$$S_{th} = 2Re(1 + Nr)\xi^{-1}\theta'^2, \quad S_m = \frac{MReBr}{\Sigma}(f'^2 + \lambda S^2), \quad S_{dif} = 2Re\Gamma\left(\frac{\chi}{\Sigma}\right)^2 \xi^{-1}\phi'^2 \\ + 2Re\Gamma\left(\frac{\chi}{\Sigma}\right)\theta'\phi', \quad S_{dis} = \frac{Br}{\Sigma} \left[10f'^2 + \lambda S^2 + 2Re\xi^{-1}(f''^2 + \lambda S'^2) \right]. \quad (3.6)$$

4 Method of solution

In this section, the numerical method used to solve equations (2.8)–(2.12), is described and then the solution so obtained is used in solving the entropy generation equation (3.4). The system of equations is simplified using the quasilinearization scheme and the resulting linear partial differential equations are solved using the spectral collocation method. This approach has been applied with success in solving nonlinear evolution PDEs [30]. Spectral methods produce approximations of high accuracy using comparatively few grid points since they construct the desired approximations from all available function values [31, 32].

The quasilinearization method is an iterative procedure derived from the Taylor series that approximates the unknown functions and their derivatives. The iterative nature of the quasilinearization method implies that previous estimates are denoted using the subscript r and new estimates are denoted by the subscript $r + 1$. Using the quasilinearization method on equations (2.8)–(2.12), leads to the following PDEs:

$$a_{0,r}f_{r+1}''' + a_{1,r}(\eta, \xi)f_{r+1}'' + a_{2,r}(\eta, \xi)f_{r+1}' + a_{3,r}(\eta, \xi)f_{r+1} + a_{4,r}(\eta, \xi)S_{r+1} + a_{5,r}(\eta, \xi)\theta_{r+1} \\ + a_{6,r}(\eta, \xi)\phi_{r+1} - 0.5\xi(1 - \xi)\frac{\partial f'}{\partial \xi} = R_1(\eta, \xi), \quad (4.1)$$

$$a_{0,r}f_{r+1}''' + a_{1,r}(\eta, \xi)f_{r+1}'' + a_{2,r}(\eta, \xi)f_{r+1}' + a_{3,r}(\eta, \xi)f_{r+1} + a_{4,r}(\eta, \xi)S_{r+1} + a_{5,r}(\eta, \xi)\theta_{r+1} + a_{6,r}(\eta, \xi)\phi_{r+1} - 0.5\xi(1-\xi)\frac{\partial f'}{\partial \xi} = R_1(\eta, \xi), \quad (4.2)$$

$$b_{0,r}S'' + b_{1,r}(\eta, \xi)S' + b_{2,r}(\eta, \xi)S + b_{3,r}(\eta, \xi)f_{r+1}' + b_{4,r}(\eta, \xi)f_{r+1} - 0.5\xi(1-\xi)\frac{\partial S}{\partial \xi} = R_{2,r}(\eta, \xi), \quad (4.3)$$

$$c_{0,r}\theta_{r+1}'' + c_{1,r}(\eta, \xi)\theta_{r+1}' + c_{2,r}(\eta, \xi)f_{r+1} + c_{3,r}(\eta, \xi)f_{r+1}' + c_{4,r}(\eta, \xi)\theta_{r+1}' - 0.5\xi(1-\xi)\frac{\partial \phi}{\partial \xi} = R_{3,r}(\eta, \xi), \quad (4.4)$$

$$d_{0,r}\phi_{r+1}'' + d_{1,r}(\eta, \xi)\phi_{r+1}' + d_{2,r}(\eta, \xi)\phi_{r+1} + d_{3,r}(\eta, \xi)f_{r+1} + d_{4,r}(\eta, \xi)\theta_{r+1}' - 0.5\xi(1-\xi)\frac{\partial \phi}{\partial \xi} = R_{4,r}(\eta, \xi). \quad (4.5)$$

The boundary conditions can be expressed as

$$\begin{aligned} f_{r+1}(0, \xi) = 0, \quad f_{r+1}'(0, \xi) = 0, \quad S_{r+1}(0, \xi) = \theta_{r+1}(0, \xi) = \phi_{r+1}(0, \xi) = 0, \\ f_{r+1}'(\infty, \xi) = 1, \quad S_{r+1}(\infty, \xi) = 1, \quad \theta_{r+1}(\infty, \xi) = \phi_{r+1}(\infty, \xi) = 1. \end{aligned} \quad (4.6)$$

The coefficients in equations (4.1)–(4.5) are

$$a_{0,r} = 1, \quad a_{1,r}(\eta, \xi) = \xi f + 0.25(1-\xi)\eta, \quad a_{2,r}(\eta, \xi) = -(\xi f_r' + 0.5\xi M), \quad (4.7)$$

$$a_{3,r}(\eta, \xi) = \xi f_r'', \quad a_{4,r}(\eta, \xi) = \lambda \xi S, \quad a_{5,r}(\eta, \xi) = 0.5\xi \gamma, \quad a_{6,r}(\eta, \xi) = 0.5\xi \gamma N,$$

$$b_{0,r} = 1, \quad b_{1,r}(\eta, \xi) = \xi f_r + 0.25(1-\xi)\eta, \quad b_{2,r}(\eta, \xi) = -\xi f_r' - 0.5\xi \eta, \quad b_{3,r}(\eta, \xi) = -\xi S_r, \quad (4.8)$$

$$b_{4,r}(\eta, \xi) = \xi S_r',$$

$$c_{0,r} = \frac{1 + Nr}{Pr}, \quad c_{1,r}(\eta, \xi) = 0.25(1-\xi)\eta + \xi f_r' + Nb\phi_r' + 2Nt\theta_r', \quad c_{2,r}(\eta, \xi) = \xi \theta_r', \quad (4.9)$$

$$c_{3,r}(\eta, \xi) = 2Ec f_r'', \quad c_{4,r}(\eta, \xi) = Nb\theta_r',$$

$$d_{0,r} = \frac{1}{Le}, \quad d_{1,r}(\eta, \xi) = 0.25(1-\xi)\eta + \xi f_r, \quad d_{2,r}(\eta, \xi) = \xi \phi_r', \quad d_{3,r}(\eta, \xi) = -R_0, \quad (4.10)$$

$$d_{4,r}(\eta, \xi) = \left(\frac{Nt}{Nb}\right)\frac{1}{Le},$$

$$\begin{aligned} R_{1,r}(\eta, \xi) &= \xi f_r f_r'' + 0.5\xi(\lambda S_r^2 - f_r^2) - 0.5\xi(1+M), \quad R_{2,r}(\eta, \xi) = \xi(f_r S_r' - f_r' S_r), \\ R_{3,r}(\eta, \xi) &= \xi f_r \theta_r' + Ec f_r''^2 + Nt \theta_r'^2 + Nb \theta_r' \phi_r', \quad R_{4,r}(\eta, \xi) = \xi f_r \phi_r'. \end{aligned} \quad (4.11)$$

A variety of numerical methods exist that can be used to solve the linear system of equations (4.1)–(4.5). In this analysis, the Chebyshev spectral collocation with bivariate Lagrange interpolation methods was chosen due to the high precision associated with it. Accordingly, the physical domain $(\eta, \xi) \in (0, L) \times (0, 1)$ is transformed into a computational domain $[-1, 1] \times [-1, 1]$ using the linear transformation

$$\eta = \frac{L\eta}{2}(1+L), \quad \xi = \frac{L\xi}{2}(1+L). \quad (4.12)$$

Discretization is done using the Chebyshev Gauss-Lobatto collocation points defined by

$$\begin{aligned} \tau_i &= \cos\left(\frac{i\pi}{N_\eta}\right), \quad \zeta_j = \cos\left(\frac{j\pi}{N_\xi}\right) \\ \text{for } i &= 0, 1, \dots, N_\eta \text{ and } j = 0, 1, \dots, N_\xi. \end{aligned} \quad (4.13)$$

The solution to the system of differential equations is approximated by the functions given below,

$$f(\eta, \xi) \approx \sum_{i=0}^{N_\eta} \sum_{j=0}^{N_\xi} f(\tau_i, \zeta_j) L_i(\tau) L_j(\zeta), \quad (4.14)$$

$$S(\eta, \xi) \approx \sum_{i=0}^{N_\eta} \sum_{j=0}^{N_\xi} h(\tau_i, \zeta_j) L_i(\tau) L_j(\zeta), \quad (4.15)$$

$$\theta(\eta, \xi) \approx \sum_{i=0}^{N_\eta} \sum_{j=0}^{N_\xi} \theta(\tau_i, \zeta_j) L_i(\tau) L_j(\zeta), \quad (4.16)$$

$$\phi(\eta, \xi) \approx \sum_{i=0}^{N_\eta} \sum_{j=0}^{N_\xi} \phi(\tau_i, \zeta_j) L_i(\tau) L_j(\zeta), \quad (4.17)$$

where L_i and L_j denote the standard Lagrange interpolation polynomials. The derivatives with respect to η and ξ are approximated at the collocation points using the Chebyshev differentiation matrices. The resulting approximation of the p^{th} derivative of f can be expressed as

$$\left. \frac{\partial^p f_{r+1,i}}{\partial^p \eta} \right|_{\eta=\eta_i} = \left(\frac{2}{\eta_e}\right)^p \sum_{k=0}^{N_\eta} D_{j,k}^p f_{r+1,i}(\tau_k, \zeta_i) = \mathbf{D}^p \mathbf{f}_{r+1,i}, \quad (4.18)$$

$$\mathbf{F}_{r+1,i} = \left[F_{r+1,i}(\tau_0), F_{r+1,i}(\tau_1), \dots, F_{r+1,i}(\tau_{N_\eta}) \right]^T. \quad (4.19)$$

The approximations of the derivative with respect to ξ at the collocation points are computed similarly as:

$$\left. \frac{\partial f_{r+1}}{\partial \xi} \right|_{\xi=\xi_i} = 2 \sum_{k=0}^{N_\xi} d_{i,k} f_{r+1}(\tau_k, \zeta_k), \quad (4.20)$$

where $[d_{i,k}]$ represents an $(N_\xi + 1) \times (N_\xi + 1)$ Chebyshev derivative matrix.

The procedure detailed above is used to compute approximations for the derivatives of h, θ and ϕ with respect to η and ξ at the collocation points.

Equations (4.1)–(4.5) can be written as

$$A_{1,1}^i \mathbf{F}_{r+1,i} - \xi(1-\xi) \sum_{j=0}^{N_\xi} d_{i,j} \mathbf{D} \mathbf{F}_{r+1,j} + A_{1,2}^i \mathbf{S}_{r+1,i} + A_{1,3}^i \mathbf{\Theta}_{r+1,i} + A_{1,4}^i \mathbf{\Phi}_{r+1,i} = \mathbf{R}_{1,r}, \quad (4.21)$$

$$A_{2,1}^i \mathbf{F}_{r+1,i} + A_{2,2}^i \mathbf{S}_{r+1,i} - \xi(1-\xi) \sum_{j=0}^{N_\xi} d_{i,j} \mathbf{S}_{r+1,j} = \mathbf{R}_{2,r}, \quad (4.22)$$

$$A_{3,1}^i \mathbf{F}_{r+1,i} + A_{3,3}^i \mathbf{\Theta}_{r+1,i} + A_{3,4}^i \mathbf{\Phi}_{r+1,i} - \xi(1-\xi) \sum_{j=0}^{N_\xi} d_{i,j} \mathbf{\Theta}_{r+1,j} = \mathbf{R}_{3,r}, \quad (4.23)$$

$$A_{4,1}^i \mathbf{F}_{r+1,i} + A_{4,3}^i \mathbf{\Theta}_{r+1,i} + A_{4,4}^i \mathbf{\Phi}_{r+1,i} - \xi(1-\xi) \sum_{j=0}^{N_\xi} d_{i,j} \mathbf{\Phi}_{r+1,j} = \mathbf{R}_{4,r}, \quad (4.24)$$

where

$$\begin{aligned} A_{1,1}^i &= a_{0,r}^i \mathbf{D}^3 + a_{1,r}^i \mathbf{D}^2 + a_{2,r}^i \mathbf{D} + a_{3,r}^i, & A_{1,2}^i &= a_{4,r}, & A_{1,3}^i &= a_{5,r}, & A_{1,4}^i &= a_{6,r}, \\ A_{2,2}^i &= b_{0,r}^i \mathbf{D}^2 + b_{1,r}^i \mathbf{D} + b_{2,r}^i, & A_{2,1}^i &= b_{3,r}^i \mathbf{D} + b_{4,r}^i, & A_{3,3}^i &= c_{0,r}^i \mathbf{D}^2 + c_{1,r}^i \mathbf{D}, \\ A_{3,1}^i &= c_{2,r}^i + c_{3,r}^i \mathbf{D}^2, & A_{3,4}^i &= c_{4,r}^i \mathbf{D}, & A_{4,4}^i &= d_{0,r}^i \mathbf{D}^2 + d_{1,r}^i \mathbf{D} + d_{2,r}^i, \\ A_{4,1}^i &= d_{3,r}^i, & A_{4,3}^i &= d_{4,r}^i \mathbf{D}^2, \end{aligned} \quad (4.25)$$

with $a_{k,r}^i$ ($k = 0, 1, 2, \dots, 6$) and $R_{1,r} = [R_{1,r}(\tau_0), R_{1,r}(\tau_1), \dots, R_{1,r}(\tau_{N_x})]^T$.

Equations (4.21)–(4.24) can be written in matrix notation (see Appendix A) and their solution is determined by solving the equation of the form

$$\mathbf{F}\mathbf{F} = \mathbf{A}\mathbf{A}^{-1}\mathbf{R}\mathbf{R}, \quad (4.26)$$

where

$$\begin{aligned} B_{1,1}^{(i,i)} &= A_{1,1}^i - \xi(1-\xi)d_{i,i}\mathbf{D}, & B_{1,2}^{(i,i)} &= A_{1,2}^i, & B_{1,3}^{(i,i)} &= A_{1,3}^i, & B_{1,4}^{(i,i)} &= A_{1,4}^i, \\ B_{2,1}^{(i,i)} &= A_{2,1}^i, & B_{2,2}^{(i,i)} &= A_{2,2}^i - \xi(1-\xi)d_{i,i}\mathbf{I}, & B_{2,3}^{(i,i)} &= A_{2,3}^i, & B_{2,4}^{(i,i)} &= A_{2,4}^i, \\ B_{3,1}^{(i,i)} &= A_{3,1}^i, & B_{3,2}^{(i,i)} &= A_{3,2}^i, & B_{3,3}^{(i,i)} &= A_{3,3}^i - \xi(1-\xi)d_{i,i}\mathbf{I}, & B_{3,4}^{(i,i)} &= A_{3,4}^i, \\ B_{4,1}^{(i,i)} &= A_{4,1}^i, & B_{4,2}^{(i,i)} &= A_{4,2}^i, & B_{4,3}^{(i,i)} &= A_{4,3}^i, & B_{4,4}^{(i,i)} &= A_{4,4}^i - \xi(1-\xi)d_{i,i}\mathbf{I}, \\ B_{1,1}^{(i,j)} &= -\xi(1-\xi)d_{i,j}\mathbf{D}, & B_{2,2}^{(i,j)} &= -\xi(1-\xi)d_{i,j}\mathbf{I}, & B_{3,3}^{(i,j)} &= -\xi(1-\xi)d_{i,j}\mathbf{I}, \\ B_{4,4}^{(i,j)} &= -\xi(1-\xi)d_{i,j}\mathbf{I}, & & & & & & i \neq j, \end{aligned} \quad (4.27)$$

and \mathbf{I} represents $(N_\eta + 1) \times (N_\eta + 1)$ the identity matrix. The results obtained after solving the system of equations (4.26), that the fluid flow variables (f , h , θ and ϕ), are used in solving the entropy generation equation (3.4) by substituting the variables obtained directly. The equations are solved using the MATLAB software and the results are presented in graphs and tables. Convergence analysis for the numerical scheme is also performed.

5 Convergence analysis

In this section, we have determined the accuracy of the successive approximations and their derivatives. Figure 2(a) reflects the velocity, entropy generation, temperature and concentration profiles for $f(\eta, \xi)$, $S(\eta, \xi)$, $\theta(\eta, \xi)$, and $\phi(\eta, \xi)$ according to the number of iterations. It is seen that the error decreases smoothly to $\approx 10^{-14}$ when the iterations lie between $5 \leq \xi \leq 6$. The absolute error shown in Figure 2(b) reflects smooth convergence after the sixth iteration. The results of the convergence analysis clearly affirm that the method is accurate and can be used as a numerical tool to solve even the more complex fluid dynamic problems.

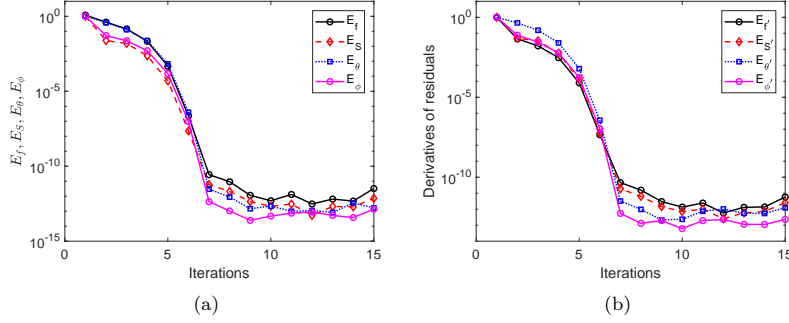


Figure 2: Convergence graph of (a) $f(\eta, \xi)$, $S(\eta, \xi)$, $\theta(\eta, \xi)$ and $\phi(\eta, \xi)$ and (b) $f'(\eta, \xi)$, $S'(\eta, \xi)$, $\theta'(\eta, \xi)$ and $\phi'(\eta, \xi)$.

6 Results and discussion

In our investigation of three-dimensional MHD nanofluid flow near the stagnation point with entropy generation, the bivariate spectral quasilinearisation method (BSQLM) has been applied to solve for the different parameter values. For boundary layer problems, this method gives more accurate results than do finite differences methods [30, 33]. In this section, we first evaluate the influence of the key parameters of interest to determine the effect of Nr , Nb , Nt and Ec on both the temperature and concentration profiles, the influence of N on both the velocity along the x - axis and the temperature profiles, and the effect of ξ on the velocity, temperature and concentration profiles. Finally, we evaluate the effect of varying both Nr and Pr on variables of engineering interest, which include the skin- friction coefficient, the Nusselt number and Sherwood number, the results of which are presented in a tabular format in appendix B.

The system of PDEs (2.8)–(2.11) and the entropy equation (3.4) are solved numerically using BSQLM for selected parameter values. The iterations begin from an initial approximation that satisfies the boundary conditions (2.12), as expressed

$$\begin{aligned} f_0(\eta, \xi) &= \eta + \exp(-\eta) - 1, & S_0(\eta, \xi) &= \exp(-\eta), \\ \theta_0(\eta, \xi) &= \exp(-\eta), & \phi_0(\eta, \xi) &= \exp(-\eta). \end{aligned} \quad (6.1)$$

From the initial approximation, the set of PDEs (2.8)–(2.11) is coupled and solved iteratively

until results with the desired accuracy are obtained, which are presented in both graphical and tabular forms.

Figure 3(a) displays the increase in entropy generation with increase in the Reynolds number. Physically, the Reynolds number influence on the heat transfer, which increases due to a rise in random eddies and flow fluctuations in the fluid. The decrease in the Reynolds number results in reduced entropy production. Figure 3(b) displays how increased temperature difference negatively affects the generation of entropy.

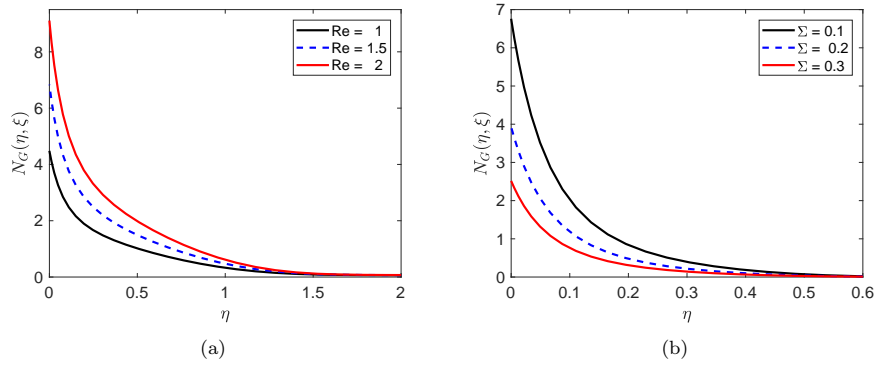


Figure 3: The Influence of (a) the Reynolds number and (b) dimensional temperature difference parameter on entropy generation.

The importance of viscous dissipation and fluid conduction are indicated by variations in the Brinkman number, as demonstrated Figure 4(a). Chemical reaction's influence on entropy generation is displayed in Figure 4(b). It is noted that an increased rate of chemical reaction has a negative effect on the rate of entropy generation as less heat is generated from the reactions as they are reduced, while the opposite trend is observed further away from the sheet.

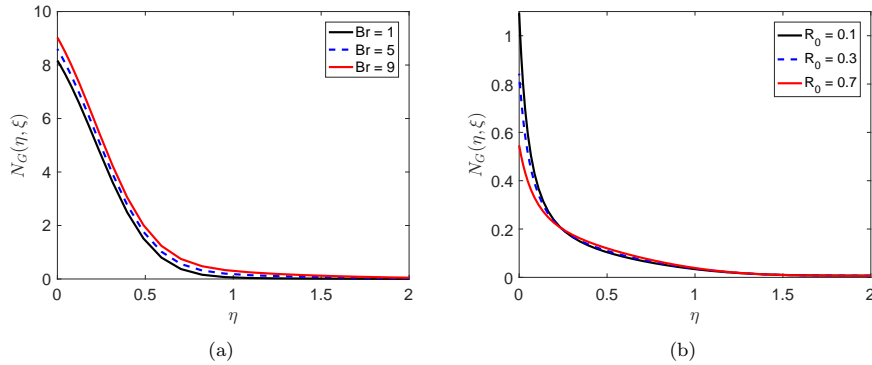


Figure 4: The influence of (a) the Brinkman number and (b) dimensionless chemical reaction parameter on entropy generation.

Figure 5(a) shows how increased values of the double diffusive number affect the rate of entropy generation positively. This is attributed to the increased convection currents driven by the differences in the densities of the nanofluid under the influence of gravitational forces, leading to increased heat production. The rate of entropy generation is also affected positively by increased values of the concentration difference parameter, as indicated in Figure 5(b). A greater mass is deposited on the surface of the spherical plate as concentration increases, resulting in higher pressure being exerted on the walls of the sphere, which causes higher rates of entropy generation at the surface.

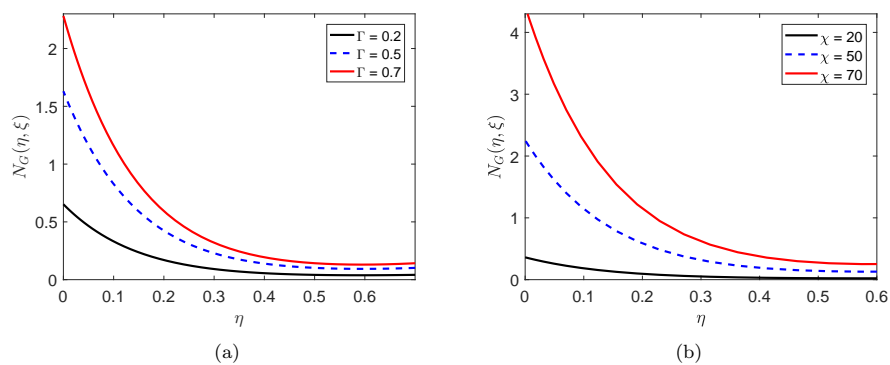


Figure 5: The influence of (a) double diffusive parameter and (b) concentration difference parameter on entropy generation.

Increased magnetic number was observed to affect entropy production negatively, as results show in Figure 6(a). The increased magnetic field strength slows down the rate of fluid flow, which leads to a reduced rate of entropy generation. Similarly, the positive effect of increased thermal radiation on entropy generation is displayed in Figure 6(b). Increased thermal radiation increases the fluid temperature leading to increased rate of heat generation.

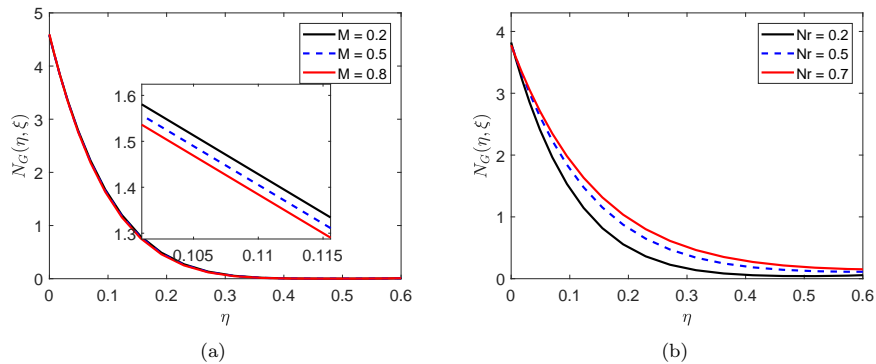


Figure 6: The influence of (a) magnetic number and (b) thermal radiation parameter on entropy generation.

The temperature and concentration profiles for different values of thermal radiation parameter are shown in Figure 7. Figure 7(a) indicates that increased thermal radiation has a positive effect on the temperature gradient of the fluid, which is consistent with the literature reported; see for instance [34]. The thermal limit layer thickness increased with the amount of thermal radiation, which means that the radiation parameter should be decreased in order to reduce the cooling rate in a given thermodynamic system. Figure 7(a) indicates that an increment in Nr leads to a reduction in the concentration profiles near the surface of the rotating sphere, while far from the surface ($\eta > 2$), the concentration profiles increased with increasing values of thermal radiation number.

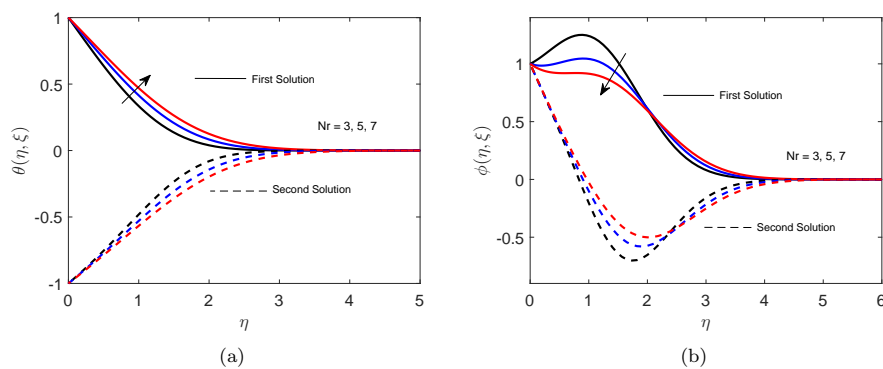


Figure 7: The influence of thermal radiation parameter on (a) temperature and (b) concentration profiles.

The influence of different values of the Brownian motion number on the temperature and concentration profiles is depicted in Figure 8 (a) and (b), respectively. Increasing the Brownian motion parameter has a positive effect on temperature profiles and a negative impact on the

species concentration.

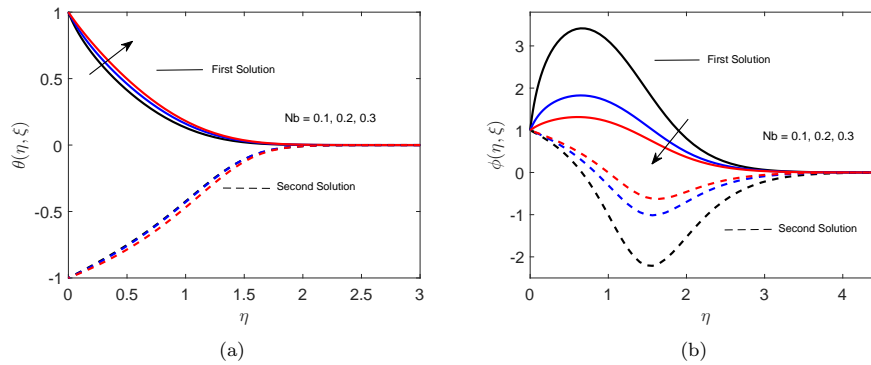


Figure 8: The influence of the Brownian motion parameter on (a) the temperature and (b) the concentration profiles.

Changes in the temperature and concentration profiles with increased values of thermophoresis number are given in Figure 9. Figure 9 (a) shows that the temperature profiles rise for increased values of Nt . The thermophoresis parameter is positively correlated with the temperature variable, from equation (2.10), thus increased thermophoresis number has a positive effect on the fluid temperature. In addition, near the surface of the sheet, the concentration profiles decrease with an increasing thermophoresis parameter close to the value of $0 \leq \eta \leq 1.5$, while a reverse trend occurred away from the sheet where the value of $\eta \geq 1.5$. Figure 9(b) indicates that the concentration profiles decrease for larger values of Nt until they reach the lowest values at $\eta = 1.5$ and then they continue to increase for $\eta > 1.5$.

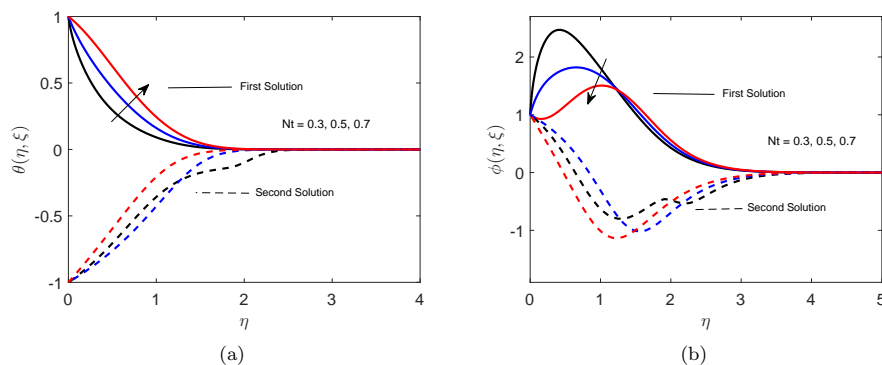


Figure 9: The influence of thermophoresis parameter on (a) temperature profile and (b) concentration profile.

Figure 10 shows the effect of buoyancy ratio on the velocity profiles of the fluid. Increased

values in the buoyancy ratio number have a positive effect on the velocity profiles along the x -axis. Increased buoyancy ratio number tends to reduce the viscous forces, thereby causing a rise in the velocity of the fluid flow.

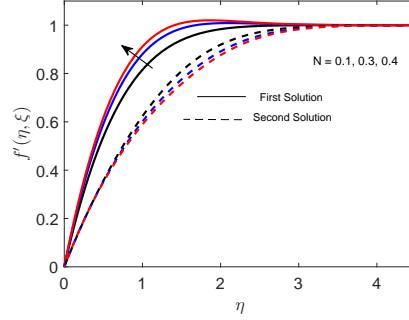


Figure 10: The influence of buoyancy ratio parameter on velocity profile.

Figures 11 (a), (b) and (c) illustrate the effect of the dimensionless time parameter ξ on velocity along the z -axis, temperature and concentration profile, respectively, temperature and concentration profiles, respectively. It is observed that ξ causes the distribution of velocity along the z -axis to deteriorate slightly, as shown in Figure 11 (a). From Figure 11 (b), it can be seen that the temperature distribution is influenced positively by increased values of the dimensionless parameter between $0 < \eta < 0.5$, while an opposite pattern is observed for $\eta > 0.5$. Figure 11 (c) indicates that between $0 < \eta < 0.5$ the dimensionless parameter is inversely related to the concentration distribution. However, the concentration distribution is influenced positively while close to the surface for $0 < \eta < 1.5$ while the opposite trend is observed when $\eta > 1.5$.

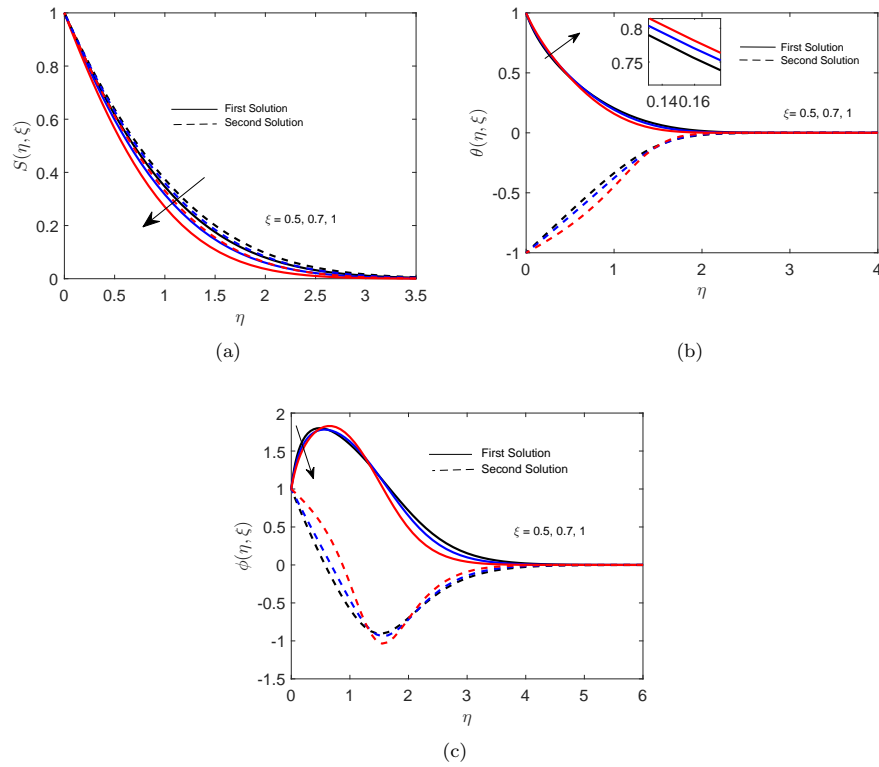


Figure 11: The influence of dimensionless time parameter on (a) velocity profile, (b) temperature and (c) concentration profiles.

In Figure 12(a) and (b) show the effects of the Eckert parameter on both temperature and concentration profiles of the fluid. From Figure 12(a) it can be seen that increased values of the Eckert number affects the temperature of the fluid flow positively while increasing the same number leads to a significant reduction in the concentration profiles, as shown in Figure 12(b). This effect can be due to the rise in fluid velocity as the Joule parameter is proportional to the velocity of the sheet, which consequently causes the nanoparticles. The opposite pattern for the concentration profiles is observed far from the sheet, when $\eta > 1.5$.

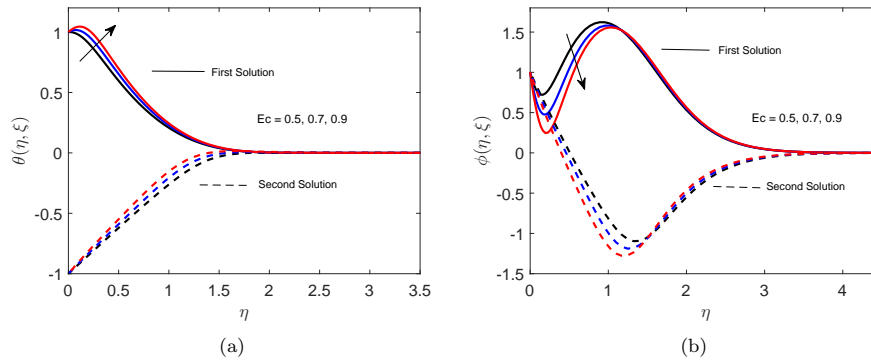


Figure 12: The influence of Eckert number on (a) the temperature profile and (b) the concentration profile.

The variations in concentration profiles with chemical reaction number is displayed in Figure 13. It is noted that increasing the chemical reaction parameter leads to a decrease in the concentration profiles.

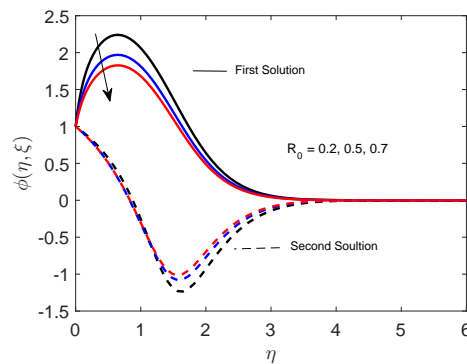


Figure 13: The influence of dimensionless chemical reaction parameter on the concentration profile.

The variations in the skin-friction coefficient, $f''(0, \xi)$, the Nusselt number $\theta'(0, \xi)$, and Sherwood number, $\phi'(0, \xi)$ with the Prandtl number, for different values of thermal radiation parameter are shown in Figure 14 (a), (b) and (c), respectively. It can be seen in Figures 14 (a) and (b) that increasing the values of Prandtl number, Pr , improves $f''(0, \xi)$ and degrades $\theta'(0, \xi)$ for all the values of Nr . Moreover, Nr has a positive relation with $f''(0, \xi)$, while in Figure 14 (b) the opposite trend is observed in the case of the local Nusselt number. From Figure 14 (c), it is evident that the Sherwood number has a positive relationship with the Prandtl number and the thermal radiation parameter.

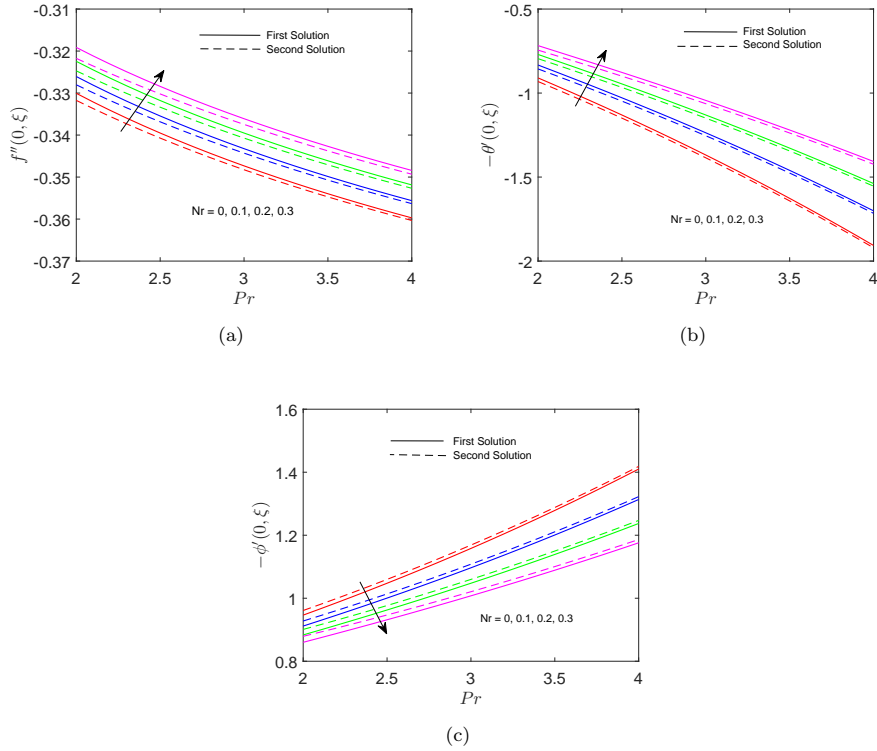


Figure 14: The influence of thermal radiation parameter and the Prandtl number on (a) coefficient of skin friction, (b) the Nusselt number, and (c) the Sherwood numbers.

7 Conclusion

We have successfully solved the generalized model for determining the entropy generation in an unsteady incompressible three-dimensional MHD boundary layer flow, with heat and mass transfer in a nanofluid near a stagnation point. The modeled equations were solved numerically using the bivariate spectral quasilinearization method, which has proven to be an accurate method that converges quickly. The effect of various parameters has been determined and presented graphically. The main observations made for this analysis are as follows.

- Increased values of thermal radiation number, double-diffusive parameter, chemical reaction parameter, Brinkman number and rotational parameters have a positive effect on entropy generation.
- Increasing values of the temperature difference parameter and the magnetic number have a negative effect on the entropy production.
- The velocity and concentration profiles increase when the buoyancy ratio parameter increases.

- The thermal radiation parameter increased in the thermal boundary layer.
- The Eckert number has a positive impact on the temperature profiles whereas an increase in the Eckert number deteriorates the concentration profiles.

References

- [1] A. Nayak and S. Bhattacharyya, “Double-diffusive convection in a cubical lid-driven cavity with opposing temperature and concentration gradients,” *Theoretical and Computational Fluid Dynamics*, vol. 26, no. 6, pp. 565–581, 2012.
- [2] A. Mohamad, R. Bennacer, and J. Azaiez, “Double diffusion natural convection in a rectangular enclosure filled with binary fluid saturated porous media: The effect of lateral aspect ratio,” *Physics of Fluids*, vol. 16, no. 1, pp. 184–199, 2004.
- [3] T. Hayat, T. Muhammad, A. Alsaedi, and B. Ahmad, “Three-dimensional flow of nanofluid with Cattaneo–Christov double-diffusion,” *Results in Physics*, vol. 6, pp. 897–903, 2016.
- [4] W. A. Khan, M. Khan, and A. S. Alshomrani, “Impact of chemical processes on 3D Burgers fluid utilizing Cattaneo–Christov double-diffusion: Applications of non-Fourier’s heat and non-Fick’s mass flux models,” *Journal of Molecular Liquids*, vol. 223, pp. 1039–1047, 2016.
- [5] M. Ferdows, M. J. Uddin, and T. S. Khaleque, “Double diffusion, slips and variable diffusivity effects on combined heat mass transfer with variable viscosity via a point transformation,” *Progress in Computational Fluid Dynamics, an International Journal*, vol. 13, no. 1, pp. 54–64, 2013.
- [6] D. A. Nield, A. Bejan, *et al.*, *Convection in Porous Media*, vol. 3. Springer, 2006.
- [7] M. Ferdows, M. Bangalee, J. Crepeau, and M. Seddeek, “The effect of variable viscosity in double diffusion problem of MHD from a porous boundary with internal heat generation,” *Progress in Computational Fluid Dynamics, an International Journal*, vol. 11, no. 1, pp. 54–65, 2010.
- [8] M. J. Martin and I. D. Boyd, “Falkner–Skan flow over a wedge with slip boundary conditions,” *Journal of Thermophysics and Heat Transfer*, vol. 24, no. 2, pp. 263–270, 2010.
- [9] C.-Y. Cheng, “Double diffusion from a vertical truncated cone in a non-Newtonian fluid saturated porous medium with variable heat and mass fluxes,” *International Communications in Heat and Mass Transfer*, vol. 37, no. 3, pp. 261–265, 2010.
- [10] R. Yousofvand, S. Derakhshan, K. Ghasemi, and M. Siavashi, “MHD transverse mixed convection and entropy generation study of electromagnetic pump including a nanofluid using 3D LBM simulation,” *International Journal of Mechanical Sciences*, vol. 133, pp. 73–90, 2017.
- [11] R. S. Raju, B. M. Reddy, and G. J. Reddy, “Influence of angle of inclination on unsteady MHD Casson fluid flow past a vertical surface filled by porous medium in presence of constant heat flux, chemical reaction and viscous dissipation,” *Journal of Nanofluids*, vol. 6, no. 4, pp. 668–679, 2017.
- [12] O. D. Makinde and P. Sibanda, “Effects of chemical reaction on boundary layer flow past a vertical stretching surface in the presence of internal heat generation,” *International Journal of Numerical Methods for Heat & Fluid Flow*, vol. 21, no. 6, pp. 779–792, 2011.

- [13] M. M. Rashidi, B. Rostami, N. Freidoonimehr, and S. Abbasbandy, "Free convective heat and mass transfer for MHD fluid flow over a permeable vertical stretching sheet in the presence of the radiation and buoyancy effects," *Ain Shams Engineering Journal*, vol. 5, no. 3, pp. 901–912, 2014.
- [14] H. R. Kataria and H. R. Patel, "Soret and heat generation effects on MHD Casson fluid flow past an oscillating vertical plate embedded through porous medium," *Alexandria Engineering Journal*, vol. 55, no. 3, pp. 2125–2137, 2016.
- [15] I. Khan, M. Malik, A. Hussain, and T. Salahuddin, "Effect of Homogenous-Heterogeneous reactions on MHD Prandtl fluid flow over a stretching sheet," *Results in Physics*, vol. 7, pp. 4226–4231, 2017.
- [16] M. Sheikholeslami, D. D. Ganji, M. Y. Javed, and R. Ellahi, "Effect of thermal radiation on magnetohydrodynamics nanofluid flow and heat transfer by means of two phase model," *Journal of Magnetism and Magnetic Materials*, vol. 374, pp. 36–43, 2015.
- [17] A. Raptis, C. Perdikis, and H. S. Takhar, "Effect of thermal radiation on MHD flow," *Applied Mathematics and Computation*, vol. 153, no. 3, pp. 645–649, 2004.
- [18] M. Nawaz, A. Zeeshan, R. Ellahi, S. Abbasbandy, and S. Rashidi, "Joules and Newtonian heating effects on stagnation point flow over a stretching surface by means of genetic algorithm and Nelder-Mead method," *International Journal of Numerical Methods for Heat & Fluid Flow*, vol. 25, no. 3, pp. 665–684, 2015.
- [19] T. Hayat, M. Shafique, A. Tanveer, and A. Alsaedi, "Magnetohydrodynamic effects on peristaltic flow of hyperbolic tangent nanofluid with slip conditions and Joule heating in an inclined channel," *International Journal of Heat and Mass Transfer*, vol. 102, pp. 54–63, 2016.
- [20] A. Bejan, "Entropy generation minimization: The new thermodynamics of finite-size devices and finite-time processes," *Journal of Applied Physics*, vol. 79, no. 3, pp. 1191–1218, 1996.
- [21] M. L. de Haro, S. Cuevas, and A. Beltrán, "Heat transfer and entropy generation in the parallel plate flow of a power-law fluid with asymmetric convective cooling," *Energy*, vol. 66, pp. 750–756, 2014.
- [22] S. E. Ahmed, Z. Raizah, and A. M. Aly, "Entropy generation due to mixed convection over vertical permeable cylinders using nanofluids," *Journal of King Saud University-Science*, vol. 31, no. 3, pp. 352–361, 2019.
- [23] J. Falade, S. Adesanya, J. Ukaegbu, and M. Osinowo, "Entropy generation analysis for variable viscous couple stress fluid flow through a channel with non-uniform wall temperature," *Alexandria Engineering Journal*, vol. 55, no. 1, pp. 69–75, 2016.
- [24] S. E. Ahmed and A. E. S. Mahdy, "Unsteady MHD double diffusive convection in the stagnation region of an impulsively rotating sphere in the presence of thermal radiation effect," *Journal of the Taiwan Institute of Chemical Engineers*, vol. 58, pp. 173–180, 2016.
- [25] H. S. Takhar, A. J. Chamkha, and G. Nath, "Unsteady laminar MHD flow and heat transfer in the stagnation region of an impulsively spinning and translating sphere in the presence of buoyancy forces," *Heat and Mass Transfer*, vol. 37, no. 4-5, pp. 397–402, 2001.

- [26] A. Malvandi, D. Ganji, F. Hedayati, and E. Y. Rad, "An analytical study on entropy generation of nanofluids over a flat plate," *Alexandria Engineering Journal*, vol. 52, no. 4, pp. 595–604, 2013.
- [27] S. Aïboud and S. Saouli, "Entropy analysis for viscoelastic magnetohydrodynamic flow over a stretching surface," *International Journal of Non-Linear Mechanics*, vol. 45, no. 5, pp. 482–489, 2010.
- [28] M. A. Abbas, Y. Bai, M. M. Rashidi, and M. M. Bhatti, "Analysis of entropy generation in the flow of peristaltic nanofluids in channels with compliant walls," *Entropy*, vol. 18, no. 3, p. 90, 2016.
- [29] A. Bejan, *Advanced Engineering Thermodynamics*. John Wiley & Sons, 2016.
- [30] S. Motsa, V. Magagula, and P. Sibanda, "A bivariate Chebyshev spectral collocation quasi-linearization method for nonlinear evolution parabolic equations," *The Scientific World Journal*, vol. 2014, 2014.
- [31] J. S. Hesthaven, S. Gottlieb, and D. Gottlieb, *Spectral Methods for Time-Dependent Problems*, vol. 21. Cambridge University Press, 2007.
- [32] J. Boyd, "Chebyshev and Fourier Spectral Methods, (2nd edition)," 2001.
- [33] G. Makanda, S. Shaw, and P. Sibanda, "Effects of radiation on MHD free convection of a Casson fluid from a horizontal circular cylinder with partial slip in non-Darcy porous medium with viscous dissipation," *Boundary Value Problems*, vol. 2015, no. 1, p. 75, 2015.
- [34] W. Ibrahim and B. Shankar, "MHD boundary layer flow and heat transfer of a nanofluid past a permeable stretching sheet with velocity, thermal and solutal slip boundary conditions," *Computers & Fluids*, vol. 75, pp. 1–10, 2013.

Appendix B

Table 1: Computed values of $f''(0)$, $-\theta'(0)$ and $-\phi'(0)$ with different values of K, Nt, Nb and R_0 when $\xi = 0.2, \omega_t = \omega_c = 1, Nr = 0.2, Ha = 0.5, Sc = 0.94, Pr = 6.8, s = 1, Ec = 0.1, Q_0 = 0.1, n = 0.5$

K	Nt	Nb	R_0	$C_{f_x} R^{1/2}$	$Re^{-1/2} Nu_x$	$Re^{-1/2} Sh_x$
0.2				-0.915452	1.519181	0.853184
1	0.5	0.5	0.3	-0.858733	1.541030	0.850256
2.5				-0.792516	1.562133	0.848537
	0.5			-0.858733	1.541030	0.850256
1	1	0.5	0.3	-0.848969	1.286133	0.751045
	1.5			-0.839054	1.132108	0.707963
		0.2		-0.848848	1.652673	0.528010
1	0.5	0.5	0.3	-0.858733	1.541030	0.850256
		1		-0.860131	1.345855	0.979923
			0.1	-0.858106	1.542271	0.834545
1	0.5	0.5	0.3	-0.858733	1.541030	0.850256
			1	-0.861379	1.531537	0.909714

Chapter 6

A numerical study of the fluid velocity, heat, and mass transfer in an unsteady nanofluid flow past parallel porous plates

In Chapter 5 we reported on entropy production in a double-diffusive convective magnetic nanofluid flow in the stagnation region of a spinning sphere. The flow was subjected to thermal radiation, chemical reaction and rotational effects of the sphere. We extend the work in Chapter 5 to unsteady flow past inclined porous plates.

We determine the impact of chemical reaction, momentum diffusivity, permeability and the magnetic fields on the fluid velocity, heat and mass transfer in an unsteady nanofluid flow over parallel porous plates. The system of equations governing the flow are solved using the bivariate spectral quasilinearization method. The results are compared with those in the literature and the impact of the physical and chemical parameters on fluid properties is discussed.

A numerical study of the fluid velocity, heat and mass transfer in an unsteady nanofluid flow past parallel porous plates

Z. M. Mburu^{*}, S. Mondal^{**} and P. Sibanda^{*}

^{*}*Department of Mathematics, University of KwaZulu-Natal, Private Bag X01, Scottsville 3209, Pietermaritzburg, South Africa*

^{**}*Department of Mathematics, Amity University Kolkata, Newtown - 700135, West Bengal, India, Corresponding Author's email id: sabya.mondal.2007@gmail.com*

Abstract

This problem of an electrically conducting nanofluid flow has applications in engineering and industry, such as designing cooling systems and aerodynamics. This article analyzes the fascinating and novel characteristics of the fluid velocity, and thermal and mass transfer for such a fluid flowing past parallel porous plates with varying temperature and concentration boundary conditions. The combined influence of chemical reaction, applied magnetic field, momentum diffusivity and permeability on the nanofluid flow characteristics are investigated. The governing flow equations are solved using the bivariate spectral quasilinearization method (BSQLM). The findings show a significant increase in the profiles for fluid velocity, temperature and concentration with an increase in chemical reaction, applied magnetic field, and thermal radiation. Further, the numerical method converges fast and solves the boundary value problem efficiently. Excellent agreement is found between our results and those previously published.

Keywords: *Nanofluid; Porous plates; Bivariate spectral collocation method; Chemical reaction; Unsteady flow.*

1 Introduction

Over the last several decades, the thermophysical characteristics of nanofluid flow through porous surfaces have created much research interest due to their practical engineering applications, which include heating and cooling of nuclear power plants, regulating the thermal boundary layer in aircraft structures and manufacturing food products. Furthermore, optimal temperature control in manufacturing polymers is a key factor in determining the quality of the final product. It is, therefore, important to investigate the physical and chemical parameters that affect the flow properties of such a fluid.

Heat and mass flux in various models with different boundary conditions have been studied extensively. In the analysis of heat dissipation, the target is to improve the efficiency of a thermal dynamic system in order to minimize energy losses and maximize the limited energy resources available. Wang *et al.* [1] investigated heat and mass flux in two nanofluids, having either copper oxide or aluminium oxide nanoparticles. They applied homotopy analysis to analyze the thermal conductivity properties of the two fluid mixtures and found that both had greater heat transfer properties than base fluids, such as water, alone. Rundora and Makinde [2] investigated the thermal effects for an unsteady temperature-dependent third grade nanofluid flow in a permeable conduit. The walls of the channel were subjected to convective heat from the fluid with chemical reaction taking place in the system. The results indicated that increasing the Reynolds number and permeability parameter each reduced the fluid velocity and temperature profiles. The thermal diffusion rate was much smaller than the viscous diffusivity rate, which explains the reduced temperature and velocity gradients. Ireka *et al.* [3] analyzed the fluid dynamics of gases that needed to be blown during the chemical process to manufacture polymers. The differential equations were solved using the finite-volume technique and it was found that the wall-slip parameter significantly decreased the production of fumes during the manufacturing process.

There is abundant research on the effect of magnetic field on nanofluid flow. The effect of the magnetic field on turbulent flow in an annular pipe with conducting walls was researched by Zhang *et al.* [4]. They found that the magnetic field applied transverse to the flow direction

suppressed the turbulent velocity profiles fluctuations and the thermal conductivity reduced with an increment in the Reynolds number. Zhong *et al.* [5] considered the effectiveness of a magnetic field in circulating nanofluids in flow channels made of high temperature ceramic tapes. The magnetic field generated the Lorentz forces, which decreased the flow rate and increased the fluid temperature within the MHD pump. When Ahmed *et al.* [6] studied the unsteady natural convective nanofluid flow over a vertical pervious channel, taking into consideration thermal dissipation and the Hall current effects, they found that increasing the values of the Hall parameter increased the concentration profiles while decreasing the Soret number, resulted in higher velocity profiles of the fluid.

In a steady MHD flow along a tilted plate with thermodiffusion Alam *et al.* [7] considered the effect of internal friction and heat transfer and established that thermal conductivity was directly proportional to the increase in the inclination angle of the channel walls and it could be decreased by increasing either the Lorentz force or the Grashof number. Mbeledogu and Ogulu [8] investigated unsteady MHD fluid flow along a rotating porous plane with heat transfer. They deduced that by increasing the Prandtl number, the hydrodynamic boundary layer increased, causing a rise in the temperature profiles and, at the same time reducing the momentum diffusivity that would have decreased the fluid velocity.

In their study of thermal radiation effects for a steady natural convection from a circular pipe to a nanofluid saturated with pervious medium, El-Amin *et al.* [9] found that increasing the permeability of the surface significantly increased the temperature of the fluid. For an MHD nanofluid flow over a permeable tilted plate with varying boundary domains, Chen [10] showed that increasing permeability led to reduced fluid velocity profiles and increasing the inclination angle of the plate reduced the conducting thermal properties of the fluid.

For the unsteady boundary layer flow of a heat absorbing nanofluid over semi-infinite vertical porous moving plates with radiation effects, Dharmiah *et al.* [11] deduced that increasing the Grashof number had a positive influence on velocity profiles, while increasing the permeability parameter reduced the thermal conductivity of the fluid. Rosca *et al.* [12] investigated heat

flux in a mixed convection nanofluid flow over a horizontal porous surface with a heat sink and observed that increasing the mixed convection number led to more heat diffusing from the air to the nanofluid, causing a rise in fluid's temperature. Chandrasekhara *et al.* [13] investigated mass flux of a buoyancy induced nanofluid flow through a porous medium that was adjacent to a semi-permeable parallel surface. Their results indicated that the fluid velocity and thermal distribution were inversely proportional to the permeability parameter. A related study on heat transfer for viscous flow was reported by Kishan and Amrutha [14], who investigated thermal dissipation effects on MHD flow past a shrinking surface. The velocity profiles increased with increased thermal dissipation parameter, chemical reaction number, and were reduced by the applied magnetic field. For a mixed nanofluid MHD flow over two moving horizontal plates with thermal radiation effects, Mukhopadhyay *et al.* [15] noticed that a slight movement of the plates increased the vibrations on the fluid molecules, which led to a rise in both fluid velocity and temperature. Subhashini *et al.* [16] investigated the diffusive convection heat from a porous vertical wall with velocity-slip conditions. The buoyancy forces caused an overshoot in the flow velocity while an increment in the Schmidt number caused a temperature rise.

To determine the effect of thermal radiation on the fluid flow through a porous conduit, Lee *et al.* [17] applied the Lie group analysis method. They found that the fluid motion generated electromagnetic radiation, which then increased the acceleration of the flow charges leading to an increase in the temperature of the fluid. Parveen and Alim [18] applied the finite differences technique to solve the differential equations that model MHD fluid flow along an inclined plane. Their solutions showed that heat flux increased with Joule heating and the resulting increased fluid particles collisions generated heat in the micro-scale, causing a rise in both the temperature and velocity of the fluid. Khan and Pop [19] extended this research by analyzing the effects of magnetic flux on the fluid flow past a stretching plane. The Lorentz force arising from the magnetic field reduced the velocity of the fluid. Then, Reddy *et al.* [20] applied similarity transformations in the Runge–Kutta method to solve the differential equations modelling heat flux for natural convection MHD nanofluid flow along an inclined surface, while considering the influences of the Lorentz forces, thermal conductivity and

porosity on the fluid flow variables. Their results indicated that increasing the magnetic force reduced the flow rate, and that the fluid temperature reduced gradually as the fluid viscosity or permeability increased.

The inspiration for this research work is to explore numerically the impact of chemical reaction, convected heat, permeability and the Lorentz force on MHD flow past parallel porous plates. The convective model of Reddy *et al.* [20] is revised to incorporate the combined effects of thermal dissipation, chemical reaction, permeability and the magnetic flux. The governing equations are solved using the bivariate spectral quasilinearization method (BSQLM) along with varying thermal and concentration boundary conditions. The BSQLM method is an innovative technique that uses the Newton-Raphson algorithm to linearize the system of nonlinear PDEs. The linearized system is then solved using the Chebyshev spectral collocation method with the Lagrange polynomials being applied as the basis functions. The BSQLM is time-economic and convergence rapidly with high accuracy.

2 Mathematical Formulation

The unsteady, MHD, electrical conducting and incompressible fluid flow past parallel porous plates is considered. The flow velocity is taken to be along the semi-infinite inclined permeable surface in the direction of x -, with y -axis perpendicular to it. The two surfaces are taken to be H units apart. The magnetic field B_0 is applied orthogonally to the direction of fluid flow motion as shown in Figure 1. The Reynolds number is assumed to be less than one unit; as such, the induced magnetic field is trivial compared to the external magnetic flux. The thermal properties are taken to be constant, except for the effect of density variation on the body force terms. Wall temperature T_w is set to be greater than the free stream temperature T_∞ and the surface concentration C_w is also set to be larger than the free stream concentration C_∞ . The foreign mass concentration is presumed to be high, such that both the Dufour and Soret influences are felt. From the approximations of Boussinesq with varying boundary domains, the equations governing our flow model are (see Reddy *et al.* [20])

$$\frac{\partial u}{\partial x} + \frac{\partial v}{\partial y} = 0. \quad (1)$$

$$\frac{\partial u}{\partial t} + u \frac{\partial u}{\partial x} + v \frac{\partial u}{\partial y} = \nu \frac{\partial^2 u}{\partial y^2} + g\hat{\beta}(T - T_\infty) \cos \hat{\alpha}^* + g\hat{\beta}^*(C - C_\infty) \cos \hat{\alpha}^* - \frac{\sigma\beta_0^2}{\rho}u - \frac{v}{K_p}u. \quad (2)$$

$$\begin{aligned} \frac{\partial T}{\partial t} + u \frac{\partial T}{\partial x} + v \frac{\partial T}{\partial y} &= \frac{\alpha_k}{\rho C_p} \frac{\partial^2 T}{\partial y^2} - \frac{16\sigma^* T_\infty^3}{3\rho C_p k^*} \frac{\partial^2 T}{\partial y^2} + \frac{Q_0}{\rho C_p}(T - T_\infty) + \frac{\mu}{\rho C_p} \left(\frac{\partial u}{\partial y} \right)^2 + \\ &\frac{D_m k_t}{c_s \rho C_p} \frac{\partial^2 C}{\partial y^2}. \end{aligned} \quad (3)$$

$$\frac{\partial C}{\partial t} + u \frac{\partial C}{\partial x} + v \frac{\partial C}{\partial y} = D_m \frac{\partial^2 C}{\partial y^2} + \frac{D_m k_t}{c_s C_p} \frac{\partial^2 T D_m}{\partial y^2} - K_r(C - C_\infty). \quad (4)$$

Eqs. (1-4) are solved under the following boundary domains

$$t = (0) : \quad u = 0, \quad v = 0, \quad T = T_w, \quad C = C_w,$$

$$t > (0) : \quad u = \lambda u_w, \quad v = s v_w, \quad T = T_w, \quad C = C_w, \quad \text{at } y = H,$$

$$t > (0) : \quad u \rightarrow 0, \quad T \rightarrow T_\infty, \quad C \rightarrow C_\infty \quad \text{at } y \rightarrow \infty,$$

where u , v , t , C , T , ρ , μ , ν , C_p , c_s , σ , σ^* , g , Q_0 , α_k , β_0^2 , K_p , K_r , k_t , k^* , D_m , and λ , represent velocity in x, y directions, time, fluid concentration, fluid temperature, density, viscosity, kinematic viscosity of the nanofluid, specific heat of the fluid at constant pressure, concentration susceptibility, electrical conductivity, Stefan-Boltzmann constant, acceleration due to gravity, heat generation constant, thermal diffusivity, magnetic field induction, permeability constant, chemical reaction parameter, thermal conductivity, mean absorption coefficient, mass diffusivity coefficient and dimensionless stretching/shrinking parameter, respectively. In addition, s is the mass flux number, where $s > 0$ represents suction and $s < 0$ represents injection; $\hat{\beta}$ is the volumetric heat expansion coefficient, and $\hat{\beta}^*$ is the volumetric concentration expansion coefficient, expressed as $\hat{\beta} = -\frac{1}{\rho}(\frac{\partial \rho}{\partial T})_P$ and $\hat{\beta}^* = -\frac{1}{\rho}(\frac{\partial \rho}{\partial C})_P$,

respectively. The following non-dimensional quantities are used to reduce Eqs. (1-4) to dimensionless form

$$\hat{x}^* = \frac{x \hat{U}_\infty}{v}, \quad \hat{t}^* = \frac{t u_0^2}{v}, \quad \hat{y}^* = \frac{y \hat{U}_\infty}{v}, \quad \hat{u}^* = \frac{u}{\hat{U}_\infty}, \quad \hat{v}^* = \frac{v}{\hat{U}_\infty}. \quad (5)$$

Using Eq. (5) and dropping the asterisks, Eqs. (1-4) are simplified and expressed as

$$\frac{\partial u}{\partial x} + \frac{\partial v}{\partial y} = 0. \quad (6)$$

$$\frac{\partial u}{\partial t} + u \frac{\partial u}{\partial x} + v \frac{\partial u}{\partial y} = \frac{1}{Re} \frac{\partial^2 u}{\partial y^2} + Gr \theta \cos \alpha^* + Gm \phi \cos \alpha^* - \left(M + \frac{1}{Kp} \right) u. \quad (7)$$

$$\frac{\partial \theta}{\partial t} + u \frac{\partial \theta}{\partial x} + v \frac{\partial \theta}{\partial y} = \frac{1}{Re} \frac{1}{Pr} \frac{\partial^2 \theta}{\partial y^2} - \frac{4}{3Nr Re Pr} \frac{\partial^2 T}{\partial y^2} + Hg \theta + \frac{Ec}{Re} \left(\frac{\partial u}{\partial y} \right)^2 + Df Re \frac{\partial^2 c}{\partial y^2}. \quad (8)$$

$$\frac{\partial \phi}{\partial t} + u \frac{\partial \phi}{\partial x} + v \frac{\partial \phi}{\partial y} = \frac{1}{Re} \frac{1}{Sc} \frac{\partial^2 \phi}{\partial y^2} + \frac{Sr}{Re} \frac{\partial^2 \theta}{\partial y^2} - Kr \phi. \quad (9)$$

Here, Gr , Gm , Sc , Sr , Re , Nr , Df , Hg , Ec , M and Pr represent the temperature Grashof number, mass Grashof number, Schmidt parameter, Soret parameter, Reynolds number, thermal radiation number, Dufour parameter, heat generation number, Eckert parameter,

magnetic parameter, and Prandtl number, respectively. These parameters are expressed as

$$\begin{aligned}
K_p &= \frac{Kp\hat{U}_\infty^3}{V^3}, & Gr &= \frac{vg\hat{\beta}(T_w - T_\infty)}{\hat{U}_\infty^3}, & Gm &= \frac{vg\hat{\beta}^*(C_w - C_\infty)}{\hat{U}_\infty^3}, \\
Sc &= \frac{\mu}{\rho D_m}, & Sr &= \frac{\rho D_m K_f (T_w - T_\infty)}{\mu T_m (C_w - C_\infty)}, & Kr &= \frac{Kr' V}{V^2}, \\
Re &= \frac{\hat{U}_\infty H}{v}, & Nr &= \frac{16\sigma^* T_\infty^3}{3k_f K^*}, & Df &= \frac{D_m k_t (C_w - C_\infty)}{c_s K (T_w - T_\infty)}, \\
Hg &= \frac{Q_0 v (C_w - C_\infty)}{V_0^2 (T_w - T_\infty)}, & Ec &= \frac{\hat{U}_\infty^2}{C_p (T_w - T_\infty)}, & M &= \frac{\sigma \beta_0^2 v}{\hat{U}_\infty^3}, \\
Pr &= \frac{\mu c_p}{k_f}.
\end{aligned}$$

The transformed boundary conditions are expressed as

$$\begin{aligned}
t \geq 0: \quad u &= \hat{U}_w(x), \quad v = v_w, \quad T = T_w, \quad C = C_w \quad \text{at} \quad y = 0 \\
t > 0: \quad u &= \hat{U}_\infty(x), \quad v = 0, \quad T = T_\infty, \quad C = C_\infty \quad \text{at} \quad y \rightarrow \infty.
\end{aligned}$$

Applying the stream functions $u = \frac{\partial \psi}{\partial y}$ and $v = -\frac{\partial \psi}{\partial x}$ to Eqs. (7-9) yields

$$\frac{\partial^2 \psi}{\partial t \partial y} + \frac{\partial \psi}{\partial y} \frac{\partial^2 \psi}{\partial x \partial y} - \frac{\partial \psi}{\partial x} \frac{\partial^2 \psi}{\partial y^2} = \frac{1}{Re} \frac{1}{Pr} \frac{\partial^3 \psi}{\partial y^3} + Gr \theta \cos \alpha^* + Gm \phi \cos \alpha^* - \left(M + \frac{1}{K_p} \right) \frac{\partial \psi}{\partial y} \quad (10)$$

$$\frac{\partial \theta}{\partial t} + \frac{\partial \psi}{\partial y} \frac{\partial \theta}{\partial x} - \frac{\partial \psi}{\partial x} \frac{\partial \theta}{\partial y} = \frac{1}{Pr} \frac{\partial^2 \theta}{\partial y^2} + \frac{4}{3NRePr} \frac{\partial^2 T}{\partial y^2} + Hg\theta + \frac{Ec}{Re} \left(\frac{\partial \psi}{\partial x} \frac{\partial^2 \psi}{\partial y^2} \right)^2 + D_f Re \frac{\partial^2 c}{\partial y^2} \quad (11)$$

$$\frac{\partial \phi}{\partial t} + \frac{\partial \phi}{\partial y} \frac{\partial \phi}{\partial x} - \frac{\partial \psi}{\partial x} \frac{\partial \phi}{\partial y} = \frac{1}{Re} \frac{1}{Sc} \frac{\partial^2 \phi}{\partial y^2} + \frac{Sr}{Re} \frac{\partial^2 \theta}{\partial y^2} - Kr \phi. \quad (12)$$

We apply the similarity transformations given in Eq. 13 to Eqs. (10-12).

$$\psi = x^{\frac{2}{3}} f(\eta, \varepsilon), \quad \varepsilon = x^{\frac{-2}{3}} t, \quad \eta = x^{\frac{-1}{3}} y, \quad \theta(\varepsilon, \eta) = \frac{T - T_w}{T_w - T_\infty}, \quad \phi(\varepsilon, \eta) = \frac{C - C_w}{C_w - C_\infty}. \quad (13)$$

Substituting Eq. (13) into Eqs. (10-12) yields the more simplified partial differential equations:

$$\frac{1}{Re}(f''') + \frac{4}{12}(ff'') + \frac{3}{9}(f')^2 - M(f') - \frac{1}{K_p}f' + Gr\theta \cos \alpha + Gm\phi \cos \alpha = \frac{\partial f'}{\partial \varepsilon} - \frac{4}{12}\varepsilon \left(f' \frac{\partial f'}{\partial \varepsilon} + f'' \frac{\partial f}{\partial \varepsilon} \right) \quad (14)$$

$$\frac{1}{Pr} \frac{1}{Re} \left(1 - \frac{4}{3Nr} \right) \theta'' + \frac{Ec}{Re} f'' + D_f Re \phi'' + Hg\theta + 2f\theta' = \frac{\partial \theta}{\partial \varepsilon} - \frac{2}{3}\varepsilon \left(f' \frac{\partial \theta}{\partial \varepsilon} - \phi' \frac{\partial f}{\partial \varepsilon} \right) \quad (15)$$

$$\frac{1}{ReSc} \phi'' + \frac{Sr}{Re} \phi'' + \frac{2}{3} f \phi' - K_r \phi = \frac{\partial \phi}{\partial t} - \frac{2}{3}\varepsilon \left(f' \frac{\partial \phi}{\partial \varepsilon} + \phi' \frac{\partial f}{\partial \varepsilon} \right). \quad (16)$$

The respective boundary domains are expressed as follows

$$f(0, \varepsilon) = f_w, \quad f'(0, \varepsilon) = \lambda, \quad \theta(0, \varepsilon) = 1, \quad \phi(0, \varepsilon) = 1, \quad \text{at } \eta = 0, \quad \varepsilon \geq 0$$

$$f'(\infty, \varepsilon) = 1, \quad \theta(\infty, \varepsilon) = 0, \quad \phi(\infty, \varepsilon) = 0 \quad \text{as } \eta \rightarrow \infty.$$

Where the primes denote the derivatives with respect to (η) and f_w is the suction/injection constant. In our case, suction $f_w > 0$ and injection $f_w < 0$.

3 Method of Solution

We apply the BSQLM to solve the system of Eqs. (14-16) under the specified limiting conditions. The BSQLM was previously used in solving the unsteady boundary value flow problems as reported by Motsa et al. [21]. The two main components of the BSQLM are the approximating function and the weight function. The approximating function is a linear combination of the basis functions; these provide an approximate representation of the solution. The weight function ensures the boundary conditions are fulfilled. The BSQLM version considered in this study uses the bivariate Lagrange interpolating polynomials as a basis function interpolating the solutions at given Chebyshev-Gauss-Lobatto grid points in η

and ε . The BSQLM achieves highly accurate results with comparatively fewer grid points as it utilizes all available functional values to set up the required approximating functions for solutions of the system of PDEs. Using the quasilinearization technique [21], Eqs. (14-16) are linearized to obtain

$$a_{3r}f_{r+1}''' + a_{2r}f_{r+1}'' + a_{1r}f_{r+1}' + a_{0r}f_{r+1} + a_{1r}^* \frac{\partial f_{r+1}'}{\partial \varepsilon} + a_{0r}^* \frac{\partial f_{r+1}}{\partial \varepsilon} + \hat{a}_{0r}\theta_{r+1} + \hat{\hat{a}}_{0r}\phi_{r+1} = R_{1r}, \quad (17)$$

$$b_{2r}f_{r+1}'' + b_{1r}f_{r+1}' + b_{0r}f_{r+1} + \hat{b}_{0r}^* \frac{\partial f_{r+1}}{\partial \varepsilon} + \hat{b}_{2r}\theta_{r+1}'' + \hat{b}_{1r}\theta_{r+1}' + \hat{b}_{0r}\theta_{r+1} + \hat{\hat{b}}_{0r}^* \frac{\partial \theta_{r+1}}{\partial \varepsilon} + \hat{\hat{b}}_{2r}\phi_{r+1}'' = R_{2r}, \quad (18)$$

$$c_{1r}f_{r+1}' + c_{0r}f_{r+1} + \hat{c}_{0r}^* \frac{\partial f_{r+1}}{\partial \varepsilon} + \hat{c}_{2r}\phi_{r+1}'' + \hat{c}_{1r}\phi_{r+1}' + \hat{c}_{0r}\phi_{r+1} + c_{0r}^* \frac{\partial \phi_{r+1}}{\partial \varepsilon} = R_{3r}. \quad (19)$$

The asterisks are used for coefficients of terms associated with derivatives with respect to ε , whereas the hat $\hat{}$ and the double hat $\hat{\hat{}}$ have been used to distinguish coefficients of θ and ϕ , respectively. The boundary conditions are expressed as

$$\begin{aligned} f_{r+1}(0, \varepsilon) = f_w, \quad f_{r+1}'(0, \varepsilon) = \lambda, \quad \theta_{r+1}(0, \varepsilon) = 1.0, \quad \phi_{r+1}(0, \varepsilon) = 1.0; \\ f_{r+1}'(\infty, \varepsilon) = 1.0, \quad \theta_{r+1}(\infty, \varepsilon) = 0, \quad \phi_{r+1}(\infty, \varepsilon) = 0. \end{aligned} \quad (20)$$

The variable coefficients in Eqs. (17)-(19) are defined as

$$\begin{aligned} a_{3r} &= \frac{1}{Re}, \quad a_{2r} = \frac{2}{3}f_r + \frac{2}{3}\varepsilon \frac{\partial f_r}{\partial \varepsilon}, \quad a_{1r} = \frac{2}{3}(f_r' + \varepsilon \frac{\partial f_r}{\partial \varepsilon}) - M - \frac{1}{K_p}, \quad a_{0r} = \frac{2}{3}f_r'', \\ a_{1r}^* &= -1 + \frac{2}{3}\varepsilon f_r', \quad a_{0r}^* = \frac{2}{3}\varepsilon f_r'', \quad \hat{a}_{0r} = G_r \cos \alpha^*, \quad \hat{\hat{a}}_{0r} = G_m \cos \alpha^*, \quad b_{2r} = \frac{E_c}{Re}, \\ b_{1r} &= \frac{2}{3}\varepsilon \frac{\partial \theta_r}{\partial \varepsilon}, \quad b_{0r} = 2\theta_r', \quad \hat{b}_{0r}^* = \frac{-2}{3}\varepsilon \phi_r', \quad \hat{b}_{2r} = \frac{1}{P_r Re} \left(1 - \frac{4}{3N_r}\right), \quad \hat{b}_{0r} = H_g, \\ \hat{b}_{1r} &= 2f_r - \frac{2}{3}\varepsilon \frac{\partial f_r}{\partial \varepsilon}, \quad \hat{\hat{b}}_{0r}^* = \frac{2}{3}\varepsilon f_r' - 1, \quad \hat{\hat{b}}_{2r} = D_f Re, \quad c_{1r} = \frac{2}{3}\varepsilon \frac{\partial \phi_r}{\partial \varepsilon}, \quad c_{0r} = \frac{2}{3}\phi_r', \\ \hat{c}_{0r}^* &= \frac{2}{3}\varepsilon \phi_r', \quad \hat{c}_{2r} = \frac{1}{Re Sc} + \frac{Sr}{Re}, \quad \hat{c}_{0r} = -K_r, \quad \hat{c}_{1r} = \frac{2}{3}f_r + \frac{2}{3}\varepsilon \frac{\partial f_r}{\partial \varepsilon}, \quad c_{0r}^* = \frac{2}{3}\varepsilon f_r' - 1, \\ R_{1r} &= \frac{2}{3}f_r f_r'' + \frac{1}{3}f_r'^2 + \frac{2}{3}\varepsilon \left(f_r' \frac{\partial f_r'}{\partial \varepsilon} + f_r'' \frac{\partial f_r}{\partial \varepsilon} \right), \quad R_{2r} = 2f_r \theta_r' + \frac{2}{3}\varepsilon \left(f_r' \frac{\partial \theta_r}{\partial \varepsilon} - \theta_r' \frac{\partial f_r}{\partial \varepsilon} \right), \\ R_{3r} &= \frac{2}{3}f_r \phi_r' + \frac{2}{3}\varepsilon \left(f_r' \frac{\partial \phi_r}{\partial \varepsilon} - \phi_r' \frac{\partial f_r}{\partial \varepsilon} \right). \end{aligned}$$

The physical domain $(\eta, \varepsilon) \in [0, \infty) \times [0, \infty)$ is first truncated to $[0, L_\eta] \times [0, L_\varepsilon]$, where L_η and L_ε are sufficiently large to estimate the infinity boundary domains in η and ε , respectively. We then convert the abridged domain $(0, L_\eta) \times (0, L_\varepsilon)$ into a computational domain $(\eta^i, \varepsilon^i) \in [-1, 1] \times [-1, 1]$ using the following transformations

$$\eta = \frac{L_\eta}{2}(1 + \eta^i), \quad \varepsilon = \frac{L_\varepsilon}{2}(1 + \varepsilon^i). \quad (21)$$

The discretization is performed at the Chebyshev-Gauss Lobatto nodes defined by

$$\eta_i = \cos\left(\frac{\pi i}{N_\eta}\right), \quad \varepsilon_j = \cos\left(\frac{\pi j}{N_\varepsilon}\right), \quad \text{for } i = 0, 1, 2, \dots, N_\eta, \quad j = 0, 1, 2, \dots, N_\varepsilon, \quad \eta, \varepsilon \in [-1, 1]. \quad (22)$$

The PDEs solutions are then approximated by the bivariate Lagrange interpolating polynomials represented by

$$\begin{aligned} f(\eta, \varepsilon) &\approx \sum_{i=0}^{N_\eta} \sum_{j=0}^{N_\varepsilon} f(\eta_i, \varepsilon_j) \bar{L}_i(\eta) \bar{L}_j(\varepsilon), \quad \theta(\eta, \varepsilon) \approx \sum_{i=0}^{N_\eta} \sum_{j=0}^{N_\varepsilon} \theta(\eta_i, \varepsilon_j) \bar{L}_i(\eta) \bar{L}_j(\varepsilon), \\ \phi(\eta, \varepsilon) &\approx \sum_{i=0}^{N_\eta} \sum_{j=0}^{N_\varepsilon} \phi(\eta_i, \varepsilon_j) \bar{L}_i(\eta) \bar{L}_j(\varepsilon). \end{aligned} \quad (23)$$

Here, $\bar{L}_i(\eta)$ and $\bar{L}_j(\varepsilon)$ represent the standard cardinal Lagrange polynomials in η and ε , respectively. We use the interpolating polynomial to illustrate the approximation of discrete derivatives to the unknown functions. The derivatives of f are obtained at the collocation points (η_i, ε_j) for $j = 0, 1, 2, 3, \dots, N_{\varepsilon_j}$ as:

$$\frac{\partial^p f_{r+1}(\eta_i, \varepsilon_j)}{\partial \eta^p} = \left(\frac{2}{L_\eta}\right)^p \sum_{\hat{k}=0}^{N_\eta} D_{i,\hat{k}}^p f_{r+1}(\eta_{\hat{k}}, \varepsilon_j) = \mathbf{D}^p \mathbf{F}_{j,r+1}, \quad (24)$$

where

$$\mathbf{D} = \left(\frac{2}{L_\eta}\right) D_{i,\hat{k}} \quad \text{for } i, \hat{k} = 0, 1, 2, \dots, N_\eta. \quad (25)$$

Here, $D_{j,\hat{k}}$, $i, \hat{k} = 0, 1, 2, \dots, N_\eta$ denotes $(N_\eta + 1) \times (N_\eta + 1)$ standard Chebyshev differentiation matrices and the term $\left(\frac{2}{L_\eta}\right)$ is as a result of applying the chain rule. The term $\mathbf{F}_{j,r+1}$ is defined

as

$$\mathbf{F}_{j,r+1} = [f_{r+1}(\eta_0, \varepsilon_j), f_{r+1}(\eta_1, \varepsilon_j), f_{r+1}(\eta_2, \varepsilon_j), \dots, f_{r+1}(\eta_{N_\eta}, \varepsilon_j)]^{\hat{T}} \quad (26)$$

here \hat{T} represent the matrix transpose. Derivatives with respect to ε are obtained at the collocation points (η_i, ε_j) for $i = 0, 1, 2, \dots, N_\eta$ as

$$\frac{\partial f_{r+1}(\eta_i, \varepsilon_j)}{\partial \varepsilon} = \frac{2}{L_\varepsilon} \sum_{q=0}^{N_\varepsilon} \hat{d}_{j,q} f_{r+1}(\tau_i, \varepsilon_q) = \sum_{q=0}^{N_\varepsilon} d_{j,q} f_{r+1}(\tau_i, \varepsilon_q), \quad (27)$$

where $\hat{d}_{j,q}$, $\left(\hat{d}_{j,q} = \frac{N_\varepsilon}{2} d_{j,q}\right)$, $j, q = 0, 1, 2, 3, 4, \dots, N_\varepsilon$ denotes the entries of an $(N_\varepsilon + 1) \times (N_\varepsilon + 1)$ standard Chebyshev differentiation matrix. A similar approach is applied to compute derivatives of (θ) and (ϕ) . Using the discrete derivatives, Eqs. (17-19) are expressed as

$$\mathbf{A}_{1,1}^i \mathbf{F}_{i,r+1} + \mathbf{a}_{1r}^* \sum_{j=0}^{N_\varepsilon-1} d_{i,j} \mathbf{D} \mathbf{F}_{j,r+1} + \mathbf{a}_{0r}^* \sum_{j=0}^{N_\varepsilon-1} d_{i,j} \mathbf{F}_{j,r+1} + \mathbf{A}_{1,2}^i \mathbf{\Theta}_{i,r+1} + \mathbf{A}_{1,3}^i \mathbf{\Phi}_{i,r+1} = \mathbf{B}_{1,r}^i, \quad (28)$$

$$\mathbf{A}_{2,1}^i \mathbf{F}_{i,r+1} + \hat{\mathbf{b}}_{0r}^* \sum_{j=0}^{N_\varepsilon-1} d_{i,j} \mathbf{F}_{j,r+1} + \mathbf{A}_{2,2}^i \mathbf{\Theta}_{i,r+1} + \hat{\mathbf{b}}_{0r} \sum_{j=0}^{N_\varepsilon-1} d_{i,j} \mathbf{\Theta}_{j,r+1} + \mathbf{A}_{2,3}^i \mathbf{\Phi}_{i,r+1} = \mathbf{B}_{2,r}^i, \quad (29)$$

$$\mathbf{A}_{3,1}^i \mathbf{F}_{i,r+1} + \mathbf{c}_{0r}^* \sum_{j=0}^{N_\varepsilon-1} d_{i,j} \mathbf{F}_{j,r+1} + \mathbf{A}_{3,2}^i \mathbf{\Theta}_{i,r+1} + \mathbf{A}_{3,3}^i \mathbf{\Phi}_{i,r+1} + \hat{\mathbf{c}}_{0r}^* \sum_{j=0}^{N_\varepsilon-1} d_{i,j} \mathbf{\Phi}_{j,r+1} = \mathbf{B}_{3,r}^i. \quad (30)$$

Here,

$$\begin{aligned} \mathbf{A}_{1,1}^i &= \mathbf{a}_{3r} \mathbf{D}^3 + \mathbf{a}_{2r} \mathbf{D}^2 + \mathbf{a}_{1r} \mathbf{D} + \mathbf{a}_{0r} \mathbf{I}, \quad \mathbf{A}_{1,2}^i = \hat{a}_{0r} \mathbf{I}, \quad \mathbf{A}_{1,3}^i = \hat{\mathbf{a}}_{0r} \mathbf{I}, \\ \mathbf{A}_{2,1}^i &= \mathbf{b}_{2r} \mathbf{D}^2 + \mathbf{b}_{1r} \mathbf{D} + \mathbf{b}_{0r} \mathbf{I}, \quad \mathbf{A}_{2,2}^i = \hat{\mathbf{b}}_{2r} \mathbf{D}^2 + \hat{\mathbf{b}}_{1r} \mathbf{D} + \hat{\mathbf{b}}_{0r} \mathbf{I}, \quad \mathbf{A}_{2,3}^i = \hat{\mathbf{b}}_{2r} \mathbf{D}^2 + \hat{\mathbf{b}}_{1r} \mathbf{D}, \\ \mathbf{A}_{3,1}^i &= \mathbf{c}_{1r} \mathbf{D} + \mathbf{c}_{0r} \mathbf{I}, \quad \mathbf{A}_{3,2}^i = \mathbf{0}, \quad \mathbf{A}_{3,3}^i = \hat{\mathbf{c}}_{2r} \mathbf{D}^2 + \hat{\mathbf{c}}_{1r} \mathbf{D} + \hat{\mathbf{c}}_{0r} \mathbf{I}, \\ \mathbf{B}_{1,r}^i &= \mathbf{R}_{1,r} - [\mathbf{a}_{1r}^* \mathbf{D} + \mathbf{a}_{0r}^*] (d_{i,N_\varepsilon} \mathbf{F}_{N_\varepsilon,r+1}), \\ \mathbf{B}_{2,r}^i &= \mathbf{R}_{2,r} - [\hat{\mathbf{b}}_{0r}^* d_{i,N_\varepsilon} \mathbf{F}_{N_\varepsilon,r+1} + \hat{\mathbf{b}}_{0r} d_{i,N_\varepsilon} \mathbf{\Theta}_{N_\varepsilon,r+1}], \\ \mathbf{B}_{3,r}^i &= \mathbf{R}_{3,r} - [\mathbf{c}_{0r}^* d_{i,N_\varepsilon} \mathbf{F}_{N_\varepsilon,r+1} + \hat{\mathbf{c}}_{0r}^* d_{i,N_\varepsilon} \mathbf{\Phi}_{N_\varepsilon,r+1}]. \end{aligned}$$

Here, \mathbf{I} represent the size of the identity matrix $[N_\eta + 1] \times [N_\eta + 1]$. The boundary conditions defined in Eq. (20) are estimated at the collocation points and expressed as

$$\begin{aligned} f_{r+1}(N_\eta, \varepsilon_j) &= f_w, \quad \mathbf{D}f_{r+1}(N_\eta, \varepsilon_j) = \lambda, \quad \theta_{r+1}(N_\eta, \varepsilon_j) = 1.0, \quad \phi_{r+1}(N_\eta, \varepsilon_j) = 1.0, \\ \mathbf{D}f_{r+1}(0, \varepsilon_j) &= 1.0, \quad \theta_{r+1}(0, \varepsilon_j) = 0, \quad \phi_{r+1}(0, \varepsilon_j) = 0. \end{aligned}$$

The boundary domains are imposed on the system of Eqs. (28-30) yielding a $3N_\varepsilon \times (N_\eta + 1)$ system of linear equations denoted as a matrix system,

$$\mathbf{A}\mathbf{U} = \mathbf{B}. \tag{31}$$

Here, \mathbf{A} is a matrix system of size $3N_\varepsilon(N_\eta + 1) \times 3N_\varepsilon(N_\eta + 1)$, \mathbf{U} is the solution vector of unknowns of size $3N_\varepsilon(N_\eta + 1) \times 1$ and \mathbf{B} is known vector of size $3N_\varepsilon(N_\eta + 1) \times 1$. Starting with the initial approximation, the system of Eqs. (28-30) are solved recursively until an approximate solution of desired precision is realized. These results are presented in the next section, as graphs and tables for the pertinent parameters, and are discussed.

4 Results

The flow problem having been successfully solved by using the BSQLM, as described above, we first report on the accuracy and convergence of the approximate solutions. Then we will discuss the influence of the most significant chemical and physical parameters on the behavior of fluid flow variables. The accuracy and convergence of the approximate solutions are evaluated by determining the absolute difference for the estimated solutions and for their derivatives. Figure 2 and 3 illustrate these absolute differences versus the number of iterations for f , θ , ϕ and for f' , θ' , ϕ' respectively. It can be seen that after the sixth iteration, the absolute differences for f , θ and ϕ decrease to approximately 10^{-10} , while for f' , θ' and ϕ' they decrease to approximately 10^{-11} . Further, Table 1 shows a validation of these results with those of Reddy *et al.* [20] for $K_r = 0$, $N_r = 0$, $M = 0$, $R_e = 0$, $D_f = 0$. There is excellent agreement between the two sets. These results confirm that the proposed BSQLM is accurate with a high convergence rate.

Table 2 displays the effect of varying the skin-friction coefficient, the Nusselt number and the Sherwood number. For the model, an increase in thermal radiation leads to an increment of these three parameters. Such results are expected because, as thermal radiation increases, the internal energy of the fluid tends to rise and so surrounding temperature gradient increases, resulting in the upward shift of the three parameters. The permeability parameter is inversely related to the coefficient of skin-friction and is directly proportional to the rates of heat and mass flux. This is because increased permeability leads to a higher inflow of fluid, which causes increased drag on fluid movement due to increased frictional and gravitational forces with the resulting positive effect on mass and heat flux. We also observe that the coefficient of skin-friction was reduced by an increase in the magnetic field, which is due to the reduced shear stresses within the boundary layer region. The magnetic flux increases the concentration boundary layer, causing a rise in the mass transfer rate. Thermal boundary layer thickness for the model thickens with increased magnetic number due to increased Lorentz forces which causes increase the collisions between fluid particles and the walls leading to the temperature rise. The rise in the chemical reaction process leads to smaller values of the coefficient of skin-friction and an increment of the model's heat and mass flux. This can, of course, be explained by the chemical reactions causing more significant collisions of the nanofluid particles, which slows down the flow motion and subsequently reduces both the heat and mass flux for the model, as depicted in Table 2.

Figure 4 indicates the upward shift of the Reynolds number causing an increase in fluid motion down the inclined surface. This would be expected as the Reynolds number is a ratio of inertial forces to viscous forces. The inertial forces increase downstream causing less friction between the walls and fluid particles, resulting in higher fluid velocity. Similar results were obtained by Mohebbi *et al.* [22]. Figure 5 and 6 clearly indicate that the Reynolds number is directly related to the temperature profiles and indirectly related to the concentration profiles, respectively. As fluid motion increases, greater collisions occur between nanofluid particles and walls, resulting in an increase in frictional forces, and thereby causing an increase in temperature profiles. When more species are transported in a time unit down the inclined plate, this increased flow rate reduces the concentration profiles, as shown in Figure 6.

Figure 7 shows that as the Prandtl number increases from 7 to 15, the nanofluid velocity decreases. Notably, beyond $Pr = 10$, the reduction in the velocity profile is significantly small. This is due to higher values for the Prandtl number giving increased momentum diffusivity for the nanofluid, making it more viscous, and so leading to a decline in velocity profiles, as observed. Figure 8 shows the temperature of the nanofluid being decreased with increased Prandtl number values. Due to the reduced velocity of the nanofluid as observed in Figure 7, less frictional forces are present, and further, the thermal conductivity reduces, leading to a lower rate of heat transfer from the plates to the nanofluid. Figure 9 indicates that the concentration of the fluid is directly related to the Prandtl number. With a reduced fluid velocity, less mass is transported in the conduit, which increases the concentration boundary layer as predicted by our model. These outcomes correspond to those reported by Oyelakin *et al.* [23].

The influence of a chemical reaction on the temperature is displayed in Figure 10. In our model, the temperature of the fluid rises with the chemical reaction rate. This is of course due to chemical reaction being an exothermic process. Figure 11 shows that the nanofluid concentration is inversely proportional to the chemical reaction parameter. The flow velocity reduces due to the higher collision of particles with the plate walls causing low species transfer in the flow conduit, as observed in the graph.

Figure 12 shows a decrease in the flow rate when the magnetic number increases. Such an outcome is expected because the Lorentz force slows down the flow as the applied magnetic field increases. Similar results were reported by Mburu *et al.* [24]. Figure 13 shows that the magnetic number is directly related to the temperature of the fluid. The applied magnetic field produces Lorentz forces, which cause high friction between the walls of the plate and the layers of the fluid, leading to a rise of fluid temperature. Figure 14 indicates that the nanofluid concentration is directly related to the magnetic number. The reduced motion of the fluid caused by the increased applied magnetic field leads to fewer species being transported per unit time, which results in increased concentration profiles.

Increased thermal radiation leads is inversely related to the temperature profiles, as shown in Figure 15. The motion of the fluid particles generates electromagnetic radiation and so thermal energy is transferred from the nanofluid to the walls resulting in a drop in the temperature profiles. This confirms similar results by Sithole *et al.* [25]. Figure 16 indicates that the flow velocity reduces with increased permeability parameter. Increased porosity would lead to either more inflow into the conduit or outflow from the conduit. As a result, the mainstream flow velocity will be retarded due to gravitational forces on the fluid. Lastly, Figure 17 shows that the temperature of the nanofluid is significantly increased by a slight rise in the heat generation number. This outcome is expected as the plates' walls are heated up, leading to heat being transferred to the nanofluid by convection. This results in the temperature of the nanofluid rising.

5 Conclusion

We have successfully studied the combined effects of chemical reaction, thermal radiation, permeability and magnetic forces on velocity, heat, and mass transfer for unsteady MHD flow past parallel porous plates. The system of PDEs alongside the varying boundary domains has been solved using the BSQLM, and the results found to be coherent with those reported in the literature. The numerical scheid used have proved to be efficient with rapid convergence, making it an appropriate tool for solving partial differential equations with applications in real-life problems. The essential numerical findings drawn from our model include:

- Heat flux is directly related to thermal radiation, the applied magnetic field, permeability, and the chemical reaction involved.
- Mass flux increases with increased chemical reaction, permeability and the magnetic parameter.
- The skin-friction coefficient reduces with higher values of magnetic field and permeability parameters and increases with an increment in thermal radiation and chemical reaction.

- The velocity of the fluid is inversely proportional to the magnetic number, permeability and the Prandtl number.
- The temperature of the nanofluid increases with an increase in chemical reaction parameter, magnetic parameter, Reynolds number, and the heat generation parameter. It is inversely proportional to the Prandtl number.
- The nanofluid concentration is directly related to the Prandtl and magnetic numbers and inversely related to the Reynolds number and chemical reaction.
- The BSQLM has a high convergence rate with high accuracy.

6 Acknowledgment

The authors are grateful to the University of KwaZulu-Natal for their support.

7 Conflict of Interest

The authors state that they do not have a conflict of interest.

References

- [1] X Wang, X Xianfan, S Choi, and U Stephen. Thermal conductivity of nanoparticle-fluid mixture. *Journal of Thermophysics and Heat Transfer*, 13(4):474–480, 1999.
- [2] L Rundora and O D Makinde. Effects of suction/injection on unsteady reactive variable viscosity non-Newtonian fluid flow in a channel filled with porous medium and convective boundary conditions. *Journal of Petroleum Science and Engineering*, 108:328–335, 2013.
- [3] I E Ireka. *Computational analysis of non-isothermal flow of non-Newtonian fluids*. Unpublished PhD thesis, University of Cape Town, 2015.
- [4] X Zhang, C Pan, and Z Xu. Experimental investigations on liquid metal MHD turbulent flows through a circular pipe with a conductive wall. *Fusion Engineering and Design*, 125:647–652, 2017.

- [5] J Zhong, M Yi, and H H Bau. Magneto hydrodynamic (MHD) pump fabricated with ceramic tapes. *Sensors and Actuators A: Physical*, 96(1):59–66, 2002.
- [6] N Ahmed, H Kalita, and D P Barua. Unsteady MHD free convective flow past a vertical porous plate immersed in a porous medium with hall current, thermal diffusion and heat source. *International Journal of Engineering, Science and Technology*, 2(6), 2010.
- [7] M S Alam, M M Rahman, and M A Sattar. On the effectiveness of viscous dissipation and Joule heating on steady magnetohydrodynamic heat and mass transfer flow over an inclined radiate isothermal permeable surface in the presence of thermophoresis. *Communications in Nonlinear Science and Numerical Simulation*, 14(5):2132–2143, 2009.
- [8] I U Mbeledogu and A Ogulu. Heat and mass transfer of an unsteady MHD natural convection flow of a rotating fluid past a vertical porous flat plate in the presence of radiative heat transfer. *International Journal of Heat and Mass Transfer*, 50(9-10):1902–1908, 2007.
- [9] M F El-Amin, A Salama, and S Sun. A conditionally stable scheme for a transient flow of a non-Newtonian fluid saturating a porous medium. *Procedia Computer Science*, 9:651–660, 2012.
- [10] C H Chen. Heat and mass transfer in MHD flow by natural convection from a permeable, inclined surface with variable wall temperature and concentration. *Acta Mechanica*, 172(3-4):219–235, 2004.
- [11] G Dharmiah, R Baby, N Vedavathi, and K S Balamurugan. Heat and mass transfer on MHD fluid flow over a semi infinite flat plate with radiation absorption, heat source and diffusion thermo effect. *Frontiers in Heat and Mass Transfer*, 11, 2018.
- [12] A V Rosca, N C Rosca, T Grosan, and I Pop. Non-Darcy mixed convection from a horizontal plate embedded in a nanofluid saturated porous media. *International Communications in Heat and Mass Transfer*, 39(8):1080–1085, 2012.
- [13] B C Chandrasekhara, P Namboodiri, and A R Hanumanthappa. Similarity solutions for buoyancy induced flows in a saturated porous medium adjacent to impermeable horizontal surfaces. *Wärme-und Stoffübertragung*, 18(1):17–23, 1984.

- [14] N Kishan and P Amrutha. Effects of viscous dissipation on MHD flow with heat and mass transfer over a stretching surface with heat source, thermal stratification and chemical reaction. *Journal of Naval Architecture and Marine Engineering*, 7(1):11–18, 2010.
- [15] S Mukhopadhyay, K Bhattacharyya, and G C Layek. Steady boundary layer flow and heat transfer over a porous moving plate in presence of thermal radiation. *International Journal of Heat and Mass Transfer*, 54(13-14):2751–2757, 2011.
- [16] S V Subhashini, N Samuel, and I Pop. Double-diffusive convection from a permeable vertical surface under convective boundary condition. *International Communications in Heat and Mass Transfer*, 38(9):1183–1188, 2011.
- [17] J Lee, P Kandaswamy, M Bhuvaneshwari, and S Sivasankaran. Lie group analysis of radiation natural convection heat transfer past an inclined porous surface. *Journal of Mechanical Science and Technology*, 22(9):1779–1784, 2008.
- [18] N Parveen and M A Alim. Joule heating effect on magnetohydrodynamic natural convection flow along a vertical wavy surface with viscosity dependent on temperature. *Journal of Naval Architecture and Marine Engineering*, 9(1):11-24, 2011.
- [19] W A Khan and I Pop. Boundary-layer flow of a nanofluid past a stretching sheet. *International Journal of Heat and Mass Transfer*, 53(11-12):2477–2483, 2010.
- [20] G Reddy, S M Ibrahim, and V S Bhagavan. Similarity transformations of heat and mass transfer effects on steady MHD free convection dissipative fluid flow past an inclined porous surface. *Journal of Naval Architecture and Marine Engineering*, 11(2):157–166, 2014.
- [21] S S Motsa, P Dlamini, and M Khumalo. Spectral relaxation method and spectral quasilinearization method for solving unsteady boundary layer flow problems. *Advances in Mathematical Physics*, 2014, 2014.
- [22] R Mohebbi, M M Rashidi, M Izadi, N Azwadi C Sidik, and H W Xian. Forced convection of nanofluids in an extended surfaces channel using lattice Boltzmann method. *International Journal of Heat and Mass Transfer*, 117:1291–1303, 2018.

- [23] I S Oyelakin, P C Lalramneihmawii, S Mondal, S K Nandy, and P Sibanda. Thermophysical analysis of three-dimensional magnetohydrodynamic flow of a tangent hyperbolic nanofluid. *Engineering Reports*, 2(4): e12144, 2020.
- [24] Z M Mburu, S Mondal, and P Sibanda. Numerical study on combined thermal radiation and magnetic field effects on entropy generation in unsteady fluid flow past an inclined cylinder. *Journal of Computational Design and Engineering*, 8(1):149–169, 2021, <https://doi.org/10.1093/jcde/qwaa068>.
- [25] H Sithole, H Mondal, S Goqo, P Sibanda, and S Motsa. Numerical simulation of couple stress nanofluid flow in magneto-porous medium with thermal radiation and a chemical reaction. *Applied Mathematics and Computation*, 339:820–836, 2018.

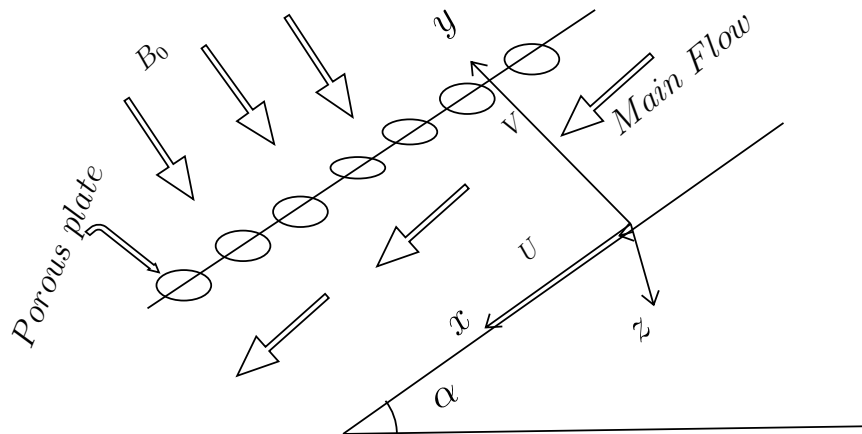


Figure 1: Physical model of the flow

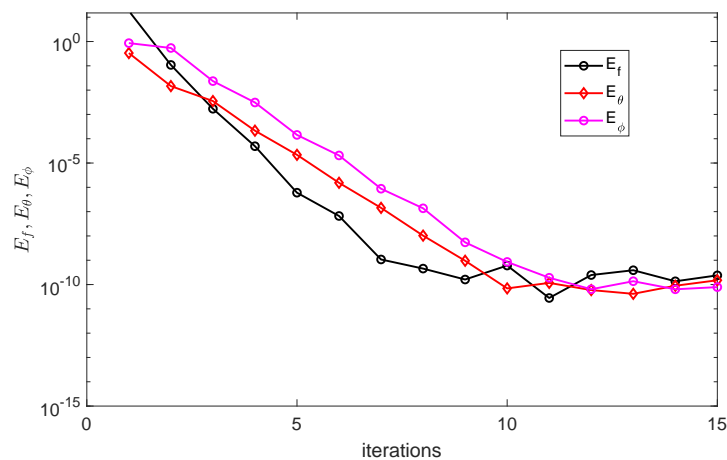


Figure 2: Convergence graph for (f, θ, ϕ)

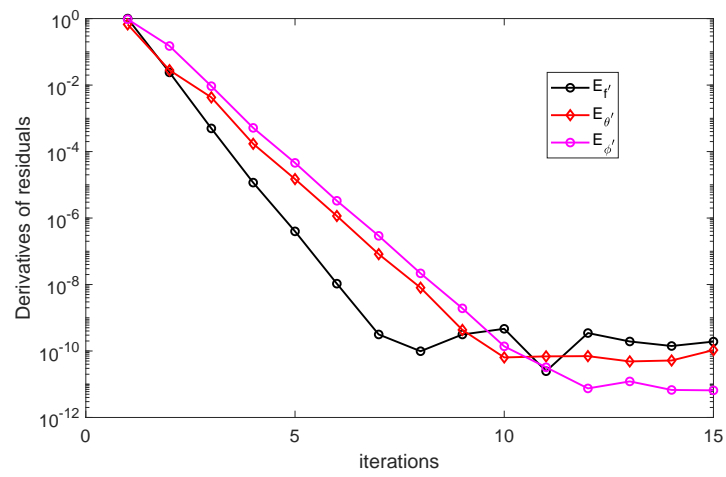


Figure 3: Convergence graph for (f', θ', ϕ')

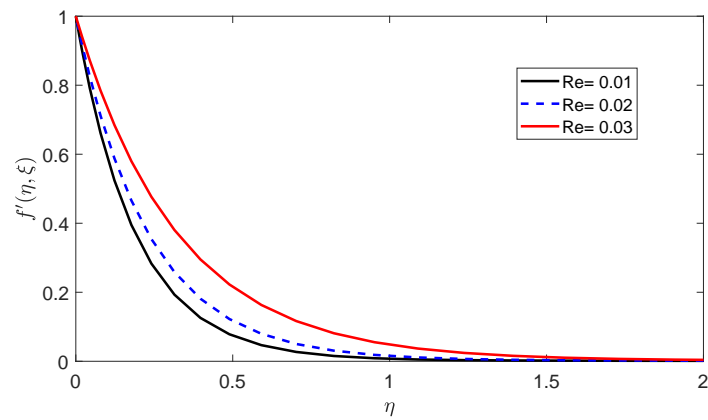


Figure 4: Velocity profiles variation with the Reynolds number

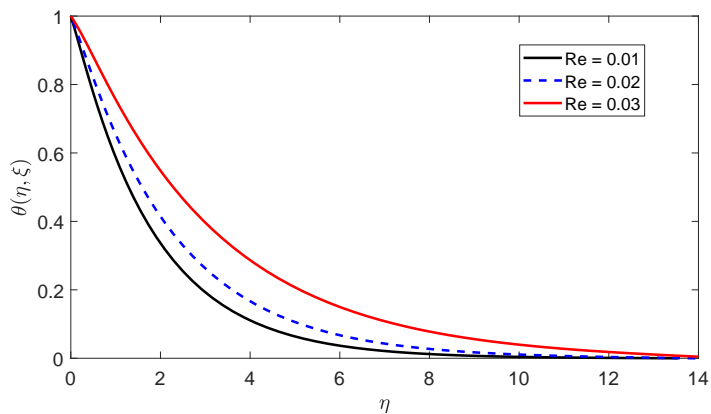


Figure 5: Temperature profiles variation with the Reynolds number

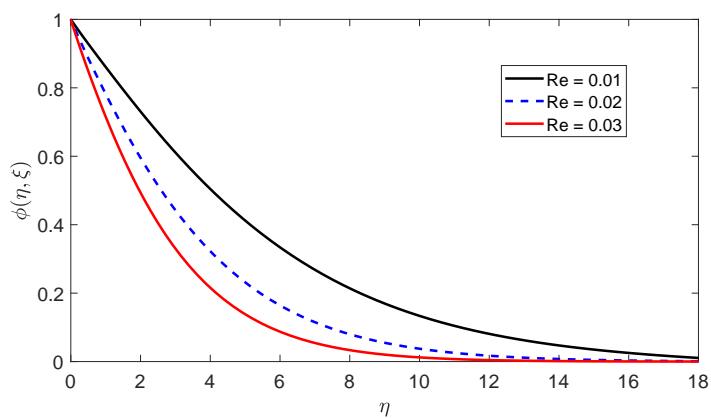


Figure 6: Concentration profiles variation with the Reynolds number

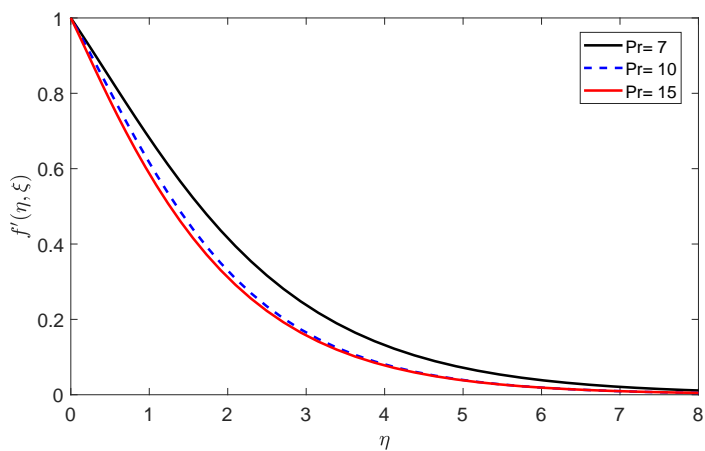


Figure 7: Velocity profiles variation with the Prandtl number

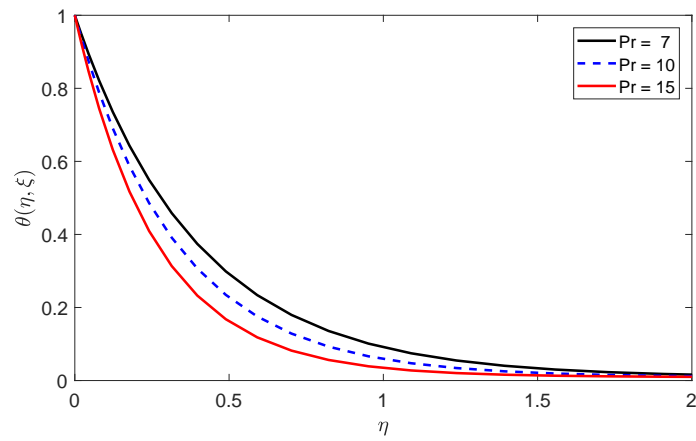


Figure 8: Temperature profiles variation with the Prandtl number

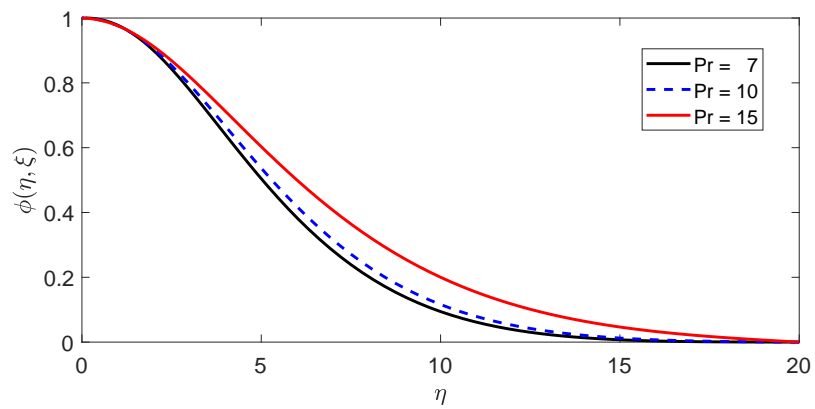


Figure 9: Concentration profiles variation with the Prandtl number

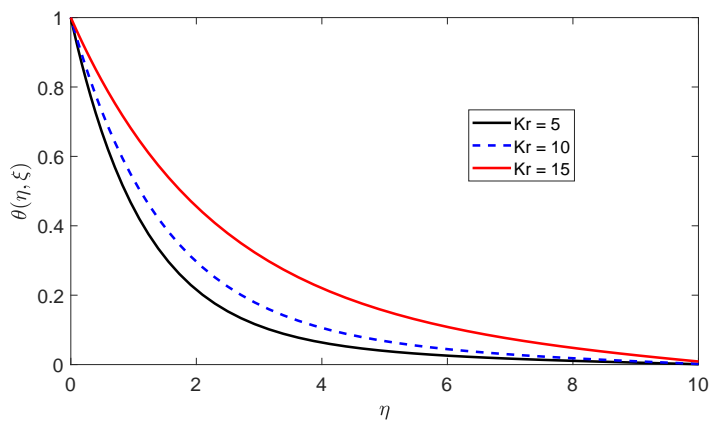


Figure 10: Temperature profiles variation with the chemical reaction parameter

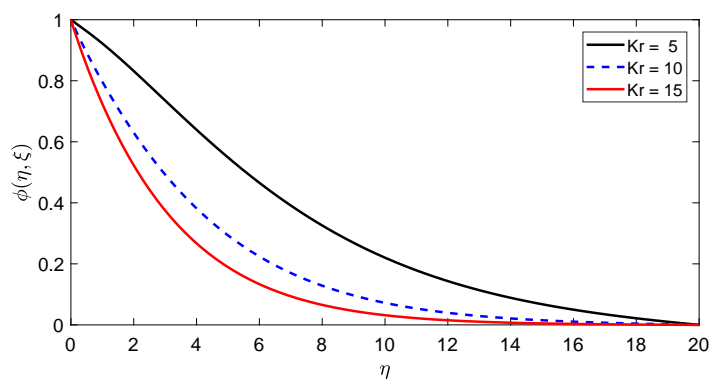


Figure 11: Concentration profiles variation with the chemical reaction parameter

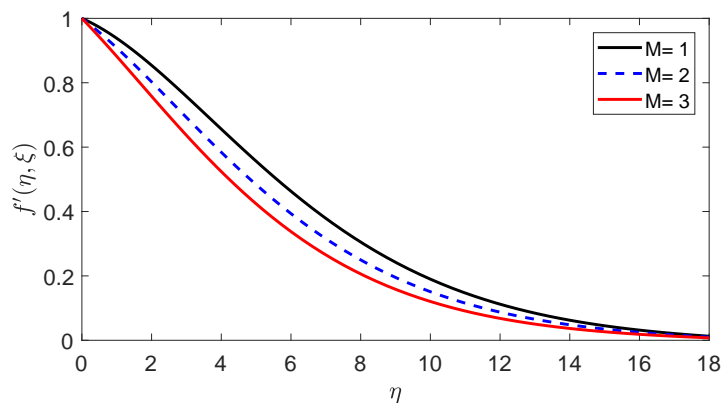


Figure 12: Velocity profiles variation with the magnetic number

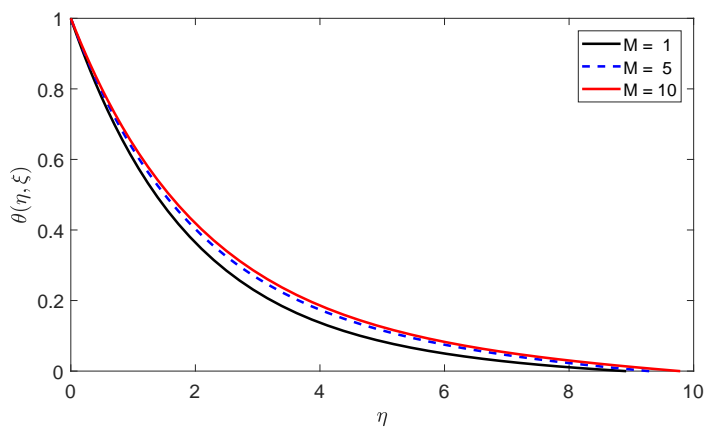


Figure 13: Temperature profiles variation with the magnetic number

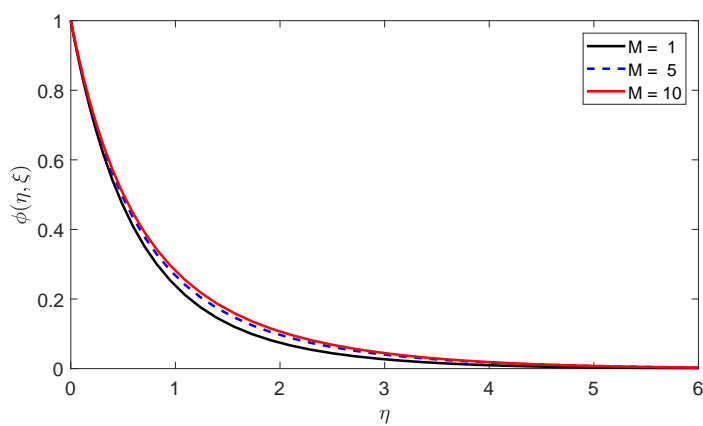


Figure 14: Concentration profiles variation with the magnetic number

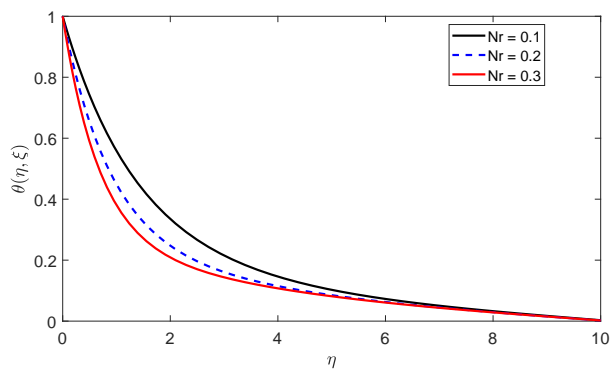


Figure 15: Temperature profile variation with thermal radiation number

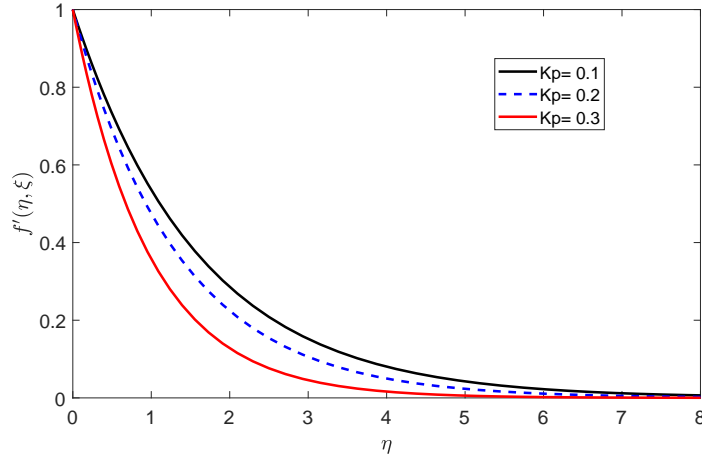


Figure 16: Velocity profiles variation with the permeability parameter

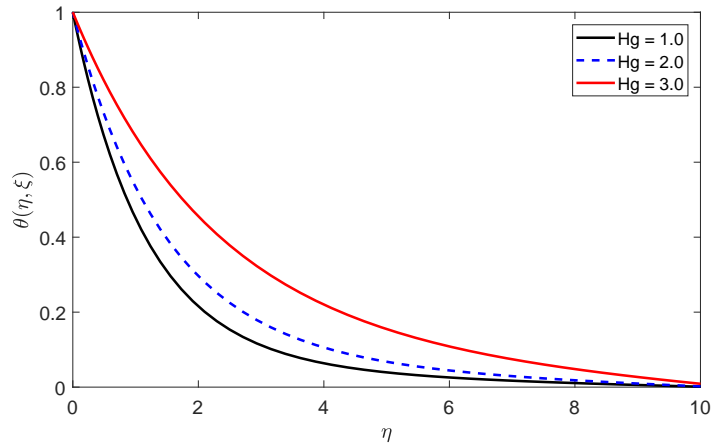


Figure 17: Temperature profiles variation with the heat generation parameter

Table 1: Variation of Coefficients of friction, Sherwood and Nusselt numbers with various parameters.

Pr	Ec	α	Reddy <i>et al.</i> [22]			Current results		
			$f''[0]$	$-\theta'[0]$	$-\phi'[0]$	$f''[0]$	$-\theta'[0]$	$-\phi'[0]$
0.71	0.01	30^0	1.67872	0.37536	0.632846	1.67871789	0.37535726	0.63282437
		1.0	1.64902	0.429375	0.629509	1.64901535	0.42937331	0.62950324
		2.0	1.57721	0.570278	0.622038	1.57721245	0.57027652	0.62202731
0.70	0.10	30^0	1.68425	0.337882	0.633256	1.68424091	0.33788455	0.63325547
		0.20	1.69051	0.29549	0.633719	1.69050412	0.29548671	0.63371892
0.71	0.10	45^0	1.39653	0.352877	0.621139	1.39651967	0.35287683	0.62113884
		60^0	1.01526	0.318826	0.60434	1.01525725	0.31882558	0.60433169

Chapter 7

Conclusion

In this thesis, we have investigated entropy generation, heat and mass transfer in nanofluid flow using different mathematical models and boundary conditions. This was achieved by solving highly coupled systems of nonlinear ordinary and partial differential equations using the overlapping grid spectral collocation and the bivariate spectral quasilinearization methods. We have conducted numerical simulations and determined the accuracy and computational performance of the solution methods. The overlapping grid spectral collocation method was shown to perform better than the bivariate spectral quasilinearization method in terms of accuracy and ease of use. The overlapping grid points lead to sparsity in the spatial differential matrices, thereby rendering a stable numerical scheme with shorter computational times. The significance of varying both chemical and physical parameters on entropy generation, velocity, heat and mass transport is presented.

In Chapter 2, we investigated entropy production due to the unsteady boundary layer flow of an Oldroyd-B nanofluid past a Riga plate. Approximate numerical solutions were constructed using the overlapping grid spectral collocation method. The effects of the varying dimensions of the Riga plates, the Brinkman number, the Prandtl number and the Brownian motion parameter on entropy production, velocity, temperature and concentration profiles were determined. Two essential aspects of this study were determining factors that reduce energy loss from a thermodynamic system and evaluating the accuracy of the method. We have shown that entropy generation is significantly reduced by using small values of the Brownian motion parameter, the Brinkman number and the width of the Riga plate. The opposite trend occurs with increased Prandtl number. Finally, the numerical methods gave accurate results and rapid convergence with the small residual errors.

In Chapter 3, we investigated entropy generation of an incompressible nanofluid past an

inclined contracting permeable cylinder with velocity slip and convective boundary conditions. The buoyancy force due to temperature difference between the walls caused the fluid to accelerate upwards. The overlapping grid spectral collocation method was used to solve the highly nonlinear partial differential equations governing the flow model. The numerical method was found to be accurate with a high rate of convergence. Among other findings, we have shown that the chemical reaction parameter, thermal radiation parameter, unsteadiness parameter and the angle of inclination of the cylinder significantly suppressed the rate of entropy generation. The Nusselt number, Sherwood number and skin friction coefficient increased with an increase in the Reynolds number, magnetic number, thermal radiation and with increased angle of inclination for the cylinder. The most significant finding from the chapter is that increased vortices and flow fluctuations in the fluid associated with increased Reynolds number lead to enhanced entropy generation.

In Chapter 4, we examined the impact of the irreversibility ratio and entropy generation on a three-dimensional Oldroyd-B fluid with relaxation-retardation viscous dissipation and no-slip boundary conditions. In the flow model, we included chemical reaction, buoyancy force, Deborah number for relaxation and retardation time, magnetic induction and momentum diffusivity. The transport equations were solved using the overlapping grid spectral collocation method. We found that the rate of irreversibility increased with a rise in viscous dissipation, chemical reaction parameter and the Reynolds number. The velocity of the fluid increased with a rise in the Deborah number for relaxation time and in the Prantl number. Increasing the mixed convection parameter increased the primary and secondary velocity fields substantially. The concentration of the fluid decreased with an increase in the Schmidt number. The overlapping grid spectral collocation method was found to be accurate and converged fast.

In Chapter 5, we investigated entropy generation in a double-diffusive convective magnetic nanofluid flow in the stagnation region of a rotating sphere with viscous dissipation. The bivariate spectral quasilinearization method was used to solve the system of highly coupled partial differential equations. The impact of various physical parameters on entropy production, heat and mass transfer was determined and discussed. Increased thermal radiation number, double-diffusive parameter, chemical reaction parameter, Brinkman number and

rotational parameters all increased the rate of entropy generation. The velocity and concentration profiles increased with the buoyancy ratio parameter. The approximate numerical solutions indicated that the method is efficient in terms of accuracy and computational speed.

In Chapter 6, we analyzed the boundary layer problem for an unsteady and electrically conducting nanofluid over inclined porous plates. The combined effects of chemical reaction, thermal radiation, permeability and magnetic field on velocity, heat and mass transfer of the flow were investigated. The model equations were solved using the bivariate spectral quasilinearization method. The outcomes indicated that the fluid velocity decreased with increased intensity of the magnetic field. Heat transfer was found to increase with thermal radiation, the magnetic and permeability parameters and chemical reaction. The skin friction decreased with increases in the magnetic field and the permeability parameter while it increased with increasing thermal radiation and chemical reaction number.

The study presented focused mainly on theoretical aspects of entropy generation, heat and mass transfer in different flow geometries with varying boundary conditions. Our findings show that, firstly, there is room for experimental validation of entropy generation, heat and mass transfer studies in non-Newtonian and higher order fluids. Secondly, although we only considered the overlapping grid and the bivariate spectral methods, there are numerous numerical such as the finite difference method, finite volume, fourth order Runge Kutta method and spectral methods available to solve differential equations, so our methods, may be improved. Furthermore, some methods may be more suitable for certain types of equations, while others may give a better accuracy. This point requires checking methods for some properties such as stability and consistency. In future studies, one of the areas to be considered is developing more accurate numerical schemes to solve highly nonlinear differential equations, such as those that describe the flow of fluids.

References

- [1] A. F. Miguel. A study of entropy generation in tree-shaped flow structures. *International Journal of Heat and Mass Transfer*, 92:349–359, 2016.
- [2] N. Foong, L. K. and Shirani, D. Toghraie, M. Zarringhalam, and M. Afrand. Numerical simulation of blood flow inside an artery under applying constant heat flux using Newtonian and non-Newtonian approaches for biomedical engineering. *Computer Methods and Programs in Biomedicine*, 190:105375, 2020.
- [3] T. Hayat and S. Siddiqui, A. M. and Asghar. Some simple flows of an Oldroyd-B fluid. *International Journal of Engineering Science*, 39(2):135–147, 2001.
- [4] N. Galanis and M. M. Rashidi. Entropy generation in non-Newtonian fluids due to heat and mass transfer in the entrance region of ducts. *Heat and Mass Transfer*, 48(9):1647–1662, 2012.
- [5] Y. M. Hung. Viscous dissipation effect on entropy generation for non-Newtonian fluids in microchannels. *International Communications in Heat and Mass Transfer*, 35(9): 1125–1129, 2008.
- [6] J. Escandón, O. Bautista, and F. Méndez. Entropy generation in purely electroosmotic flows of non-Newtonian fluids in a microchannel. *Energy*, 55:486–496, 2013.
- [7] S. Rehman, R. Haq, Z. H. Khan, and C. Lee. Entropy generation analysis for non-Newtonian nanofluid with zero normal flux of nanoparticles at the stretching surface. *Journal of the Taiwan Institute of Chemical Engineers*, 63:226–235, 2016.
- [8] M. Pakdemirli and B. S. Yilbas. Entropy generation for pipe flow of a third grade fluid with Vogel model viscosity. *International Journal of Non-Linear Mechanics*, 41(3): 432–437, 2006.
- [9] N. Dalir, M. Dehsara, and S. S. Nourazar. Entropy analysis for magnetohydrodynamic flow and heat transfer of a Jeffrey nanofluid over a stretching sheet. *Energy*, 79:351–362, 2015.

- [10] K. Lee, H. Tsai, and W. Yan. Mixed convection heat and mass transfer in vertical rectangular ducts. *International Journal of Heat and Mass Transfer*, 40(7):1621–1631, 1997.
- [11] C. L. Iandoli, E. Sciubba, and N. Zeoli. The computation of the entropy generation rate for turbomachinery design applications: some theoretical remarks and practical examples. *International Journal of Energy Technology and Policy*, 6(1-2):64–95, 2008.
- [12] A. Sciacovelli, V. Verda, and E. Sciubba. Entropy generation analysis as a design tool. *Renewable and Sustainable Energy Reviews*, 43:1167–1181, 2015.
- [13] E. H. Lieb and J. Yngvason. The physics and mathematics of the second law of thermodynamics. *Physics Reports*, 310(1):1–96, 1999.
- [14] U. Lucia. Maximum or minimum entropy generation for open systems. *Statistical Mechanics and its Applications*, 391(12):3392–3398, 2012.
- [15] K. Pruess. Enhanced geothermal systems (EGS) using carbon dioxide as working fluid—a novel approach for generating renewable energy with simultaneous sequestration of carbon. *Geothermics*, 35(4):351–367, 2006.
- [16] M. Abolbashari, N. Freidoonimehr, F. Nazari, and M. Rashidi. Analytical modeling of entropy generation for Casson nano-fluid flow induced by a stretching surface. *Advanced Powder Technology*, 26(2):542–552, 2015.
- [17] M. Siavashi, R. T. Hamid, and H. Saffari. Numerical investigation of flow characteristics, heat transfer and entropy generation of nanofluid flow inside an annular pipe partially or completely filled with porous media using two-phase mixture model. *Energy*, 93:2451–2466, 2015.
- [18] A. S. Butt, S. Munawar, A. Ali, and A. Mehmood. Entropy generation in hydrodynamic slip flow over a vertical plate with convective boundary. *Journal of Mechanical Science and Technology*, 26(9):2977–2984, 2012.
- [19] O. D. Makinde and A. S. Eegunjobi. Effects of convective heating on entropy generation rate in a channel with permeable walls. *Entropy*, 15(1):220–233, 2013.

- [20] T. Chinyoka and O. D. Makinde. Analysis of entropy generation rate in an unsteady porous channel flow with Navier slip and convective cooling. *Entropy*, 15(6):2081–2099, 2013.
- [21] M. Qasim, Hayat K., K. Zafar, and Q. M. Al-Mdallal. Analysis of entropy generation in flow of methanol-based nanofluid in a sinusoidal wavy channel. *Entropy*, 19(10):490, 2017.
- [22] A. Reveillere and A. C. Baytas. Minimum entropy generation for laminar boundary layer flow over a permeable plate. *International Journal of Exergy*, 7(2):164–177, 2010.
- [23] M. R. Mahpeykar, A. R. Teymourtash, and Amiri R. E. Reducing entropy generation by volumetric heat transfer in a supersonic two-phase steam flow in a Laval nozzle. *International Journal of Exergy*, 9(1):21–39, 2011.
- [24] M. Hassan, R. Sadri, G. Ahmadi, M. B. Dahari, S. N. Kazi, M. R. Safaei, and E. Sadeghinezhad. Numerical study of entropy generation in a flowing nanofluid used in micro and minichannels. *Entropy*, 15(1):144–155, 2013.
- [25] M. A. Sheremet, H. F. Oztop, I. Pop, and N. Abu-Hamdeh. Analysis of entropy generation in natural convection of nanofluid inside a square cavity having hot solid block: Tiwari and Das' model. *Entropy*, 18(1):9, 2016.
- [26] A. Jery, N. Hidouri, M. Magherbi, and A. B. Brahim. Effect of an external oriented magnetic field on entropy generation in natural convection. *Entropy*, 12(6):1391–1417, 2010.
- [27] R. Weijermars and H. Schmeling. Scaling of Newtonian and non-Newtonian fluid dynamics without inertia for quantitative modelling of rock flow due to gravity (including the concept of rheological similarity). *Physics of the Earth and Planetary Interiors*, 43(4):316–330, 1986.
- [28] U. Besson. The cooling law and the search for a good temperature scale, from Newton to Dalton. *European Journal of Physics*, 32(2):343, 2011.

- [29] B. Li, L. Zheng, and X. Zhang. Heat transfer in pseudo-plastic non-Newtonian fluids with variable thermal conductivity. *Energy Conversion and Management*, 52(1):355–358, 2011.
- [30] R. Mehri, C. Mavriplis, and M. Fenech. Red blood cell aggregates and their effect on non-Newtonian blood viscosity at low hematocrit in a two-fluid low shear rate microfluidic system. *PLoS One*, 13(7):e0199911, 2018.
- [31] M. Hojjat, S. G. Etemad, R. Bagheri, and J. Thibault. Rheological characteristics of non-Newtonian nanofluids: experimental investigation. *International Communications in Heat and Mass Transfer*, 38(2):144–148, 2011.
- [32] S. Z. Heris, S. G. Etemad, and M. N. Esfahany. Convective heat transfer of a Cu/water nanofluid flowing through a circular tube. *Experimental Heat Transfer*, 22(4):217–227, 2009.
- [33] M. A. Akhavan-Behabadi, M. Shahidi, M. R. Aligoodarz, and M. Fakoor-Pakdaman. An experimental investigation on rheological properties and heat transfer performance of MWCNT-water nanofluid flow inside vertical tubes. *Applied Thermal Engineering*, 106:916–924, 2016.
- [34] H. Eshgarf and M. Afrand. An experimental study on rheological behavior of Newtonian hybrid nano-coolant for application in cooling and heating systems. *Experimental Thermal and Fluid Science*, 76:221–227, 2016.
- [35] S. Rostami, A. Nadooshan, and A. Raisi. The effect of hybrid nano-additive consists of graphene oxide and copper oxide on rheological behavior of a mixture of water and ethylene glycol. *Journal of Thermal Analysis and Calorimetry*, 139(3):2353–2364, 2020.
- [36] M. Khan, A. Shahid, M. El Shafey, T. Salahuddin, and F. Khan. Predicting entropy generation in flow of non-Newtonian flow due to a stretching sheet with chemically reactive species. *Computer Methods and Programs in Biomedicine*, 187:105246, 2020.
- [37] A. Riaz, M. M. Bhatti, R. Ellahi, A. Zeeshan, and S. Sait. Mathematical analysis on

- an asymmetrical wavy motion of blood under the influence entropy generation with convective boundary conditions. *Symmetry*, 12(1):102, 2020.
- [38] J. Wang, W. A. Khan, Z. Asghar, M. Waqas, M. Ali, and M. Irfan. Entropy optimized stretching flow based on non-Newtonian radiative nanoliquid under binary chemical reaction. *Computer Methods and Programs in Biomedicine*, 188:105274, 2020.
- [39] M. Shojaeian and A. Kosar. Convective heat transfer and entropy generation analysis on Newtonian and non-Newtonian fluid flows between parallel-plates under slip boundary conditions. *International Journal of Heat and Mass Transfer*, 70:664–673, 2014.
- [40] M. Waqas. A mathematical and computational framework for heat transfer analysis of ferromagnetic non-Newtonian liquid subjected to heterogeneous and homogeneous reactions. *Journal of Magnetism and Magnetic Materials*, 493:165646, 2020.
- [41] M. Yoshino, Y. Hotta, T. Hirozane, and M. Endo. A numerical method for incompressible non-Newtonian fluid flows based on the lattice Boltzmann method. *Journal of Non-Newtonian Fluid Mechanics*, 147(1-2):69–78, 2007.
- [42] A. Moisala, A. G. Nasibulin, and E. I. Kauppinen. The role of metal nanoparticles in the catalytic production of single-walled carbon nanotubes—a review. *Journal of Physics Condensed Matter*, 15(42):S3011, 2003.
- [43] L. Chen, H. Xie, Y. Li, and W. Yu. Nanofluids containing carbon nanotubes treated by mechanochemical reaction. *Thermochimica acta*, 477(1-2):21–24, 2008.
- [44] U. S. Choi. Nanofluid technology current status and future research. Technical report, Argonne National Lab, 1998. <https://www.osti.gov/servlets/purl/11048>.
- [45] G. Saha and M. C. Paul. Analysis of heat transfer and entropy generation of TiO_2 -water nanofluid flow in a pipe under transition. *Procedia Engineering*, 105:381–387, 2015.
- [46] G. Domairry and M. Hatami. Squeezing Cu–water nanofluid flow analysis between parallel plates by DTM-Padé method. *Journal of Molecular Liquids*, 193:37–44, 2014.

- [47] M. Hatami and D. D. Ganji. Heat transfer and flow analysis for SA-TiO₂ non-Newtonian nanofluid passing through the porous media between two coaxial cylinders. *Journal of Molecular Liquids*, 188:155–161, 2013.
- [48] R. Derakhshan, A. Shojaei, K. H. Hosseinzadeh, M. Nimafar, and D. D. Ganji. Hydrothermal analysis of magneto hydrodynamic nanofluid flow between two parallel by AGM. *Case Studies in Thermal Engineering*, 14:100439, 2019.
- [49] M. Waqas, S. Jabeen, T. Hayat, M. I. Khan, and A. Alsaedi. Modeling and analysis for magnetic dipole impact in nonlinear thermally radiating Carreau nanofluid flow subject to heat generation. *Journal of Magnetism and Magnetic Materials*, 485:197–204, 2019.
- [50] F. Garoosi, L. Jahanshaloo, M. M. Rashidi, A. Badakhsh, and M. E. Ali. Numerical simulation of natural convection of the nanofluid in heat exchangers using a Buongiorno model. *Applied Mathematics and Computation*, 254:183–203, 2015.
- [51] J. Li and C. Kleinstreuer. Entropy generation analysis for nanofluid flow in microchannels. *Journal of Heat Transfer*, 132(12):122401, 2010.
- [52] Z. Shah, S. Islam, H. Ayaz, and S. Khan. Radiative heat and mass transfer analysis of micropolar nanofluid flow of Casson fluid between two rotating parallel plates with effects of Hall current. *Journal of Heat Transfer*, 141(2):022401, 2019.
- [53] P. Li, D. Zhang, and Y. Xie. Heat transfer and flow analysis of aluminium oxide–water nanofluids in microchannel with dimple and protrusion. *International Journal of Heat and Mass Transfer*, 73:456–467, 2014.
- [54] P. K. Kameswaran, S. Shaw, P. Sibanda, and N. Murthy. Homogeneous–heterogeneous reactions in a nanofluid flow due to a porous stretching sheet. *International Journal of Heat and Mass Transfer*, 57(2):465–472, 2013.
- [55] I. S. Oyelakin, S. Mondal, and P. Sibanda. Unsteady Casson nanofluid flow over a stretching sheet with thermal radiation, convective and slip boundary conditions. *Alexandria Engineering Journal*, 55(2):1025–1035, 2016.

- [56] M. Dhlamini, P. K. Kameswaran, P. Sibanda, S. Motsa, and H. Mondal. Activation energy and binary chemical reaction effects in mixed convective nanofluid flow with convective boundary conditions. *Journal of Computational Design and Engineering*, 6(2):149–158, 2019.
- [57] M. D. Losego, M. E. Grady, N. R. Sottos, D. G. Cahill, and P. V. Braun. Effects of chemical bonding on heat transport across interfaces. *Nature Materials*, 11(6):502–506, 2012.
- [58] S. D. Brorson, J. G. Fujimoto, and E. P. Ippen. Femtosecond electronic heat-transport dynamics in thin gold films. *Physical Review Letters*, 59(17):1962, 1987.
- [59] R. S. Abiev. A new form of the heat-and mass-transfer and fluid-flow equations. *Theoretical Foundations of Chemical Engineering*, 39(2):184–189, 2005.
- [60] S. O. Salawu and S. I. Oke. Inherent irreversibility of exothermic chemical reactive third-grade Poiseuille flow of a variable viscosity with convective cooling. *Journal of Applied and Computational Mechanics*, 4(3):167–174, 2018.
- [61] L. Mejlbro. The complete solution of Fick’s second law of diffusion with time-dependent diffusion coefficient and surface concentration. *Durability of Concrete in Saline Environment*, pages 127–158, 1996.
- [62] P. N. Dwivedi and S. N. Upadhyay. Particle-fluid mass transfer in fixed and fluidized beds. *Industrial & Engineering Chemistry Process Design and Development*, 16(2):157–165, 1977.
- [63] O. D. Makinde, W. A. Khan, and Z. H. Khan. Buoyancy effects on MHD stagnation point flow and heat transfer of a nanofluid past a convectively heated stretching/shrinking sheet. *International Journal of Heat and Mass Transfer*, 62:526–533, 2013.
- [64] I. Tlili, N. N. Hamadneh, and W. A. Khan. Thermodynamic analysis of MHD heat and mass transfer of nanofluids past a static wedge with Navier slip and convective boundary conditions. *Arabian Journal for Science and Engineering*, 44(2):1255–1267, 2019.

- [65] W. A. Khan, J. R. Culham, and O. D. Makinde. Combined heat and mass transfer of third-grade nanofluids over a convectively-heated stretching permeable surface. *The Canadian Journal of Chemical Engineering*, 93(10):1880–1888, 2015.
- [66] A. O. Ali, O. D. Makinde, and Y. Nkansah. Numerical study of unsteady MHD Couette flow and heat transfer of nanofluids in a rotating system with convective cooling. *International Journal of Numerical Methods for Heat & Fluid Flow*, 26(5):1567–1597, 2016.
- [67] F. Mabood, S. Shateyi, M. M. Rashidi, E. Momoniat, and N. Freidoonimehr. MHD stagnation point flow heat and mass transfer of nanofluids in porous medium with radiation, viscous dissipation and chemical reaction. *Advanced Powder Technology*, 27(2):742–749, 2016.
- [68] M.I. Anwar, I. Khan, S. Sharidan, and M. Z. Salleh. Conjugate effects of heat and mass transfer of nanofluids over a nonlinear stretching sheet. *International Journal of Physical Sciences*, 7(26):4081–4092, 2012.
- [69] L. Yang, K. Du, and Z. Zhang. Heat transfer and flow optimization of a novel sinusoidal minitube filled with non-Newtonian SiC/EG-water nanofluids. *International Journal of Mechanical Sciences*, 168:105310, 2020.
- [70] P. S. Reddy, P. Sreedevi, and A. J. Chamkha. MHD boundary layer flow, heat and mass transfer analysis over a rotating disk through porous medium saturated by Cu-water and Ag-water nanofluid with chemical reaction. *Powder Technology*, 307:46–55, 2017.
- [71] A. Wakif, Z. Boualahia, F. Ali, M. R. Eid, and R. Sehaqui. Numerical analysis of the unsteady natural convection MHD Couette nanofluid flow in the presence of thermal radiation using single and two-phase nanofluid models for Cu–water nanofluids. *International Journal of Applied and Computational Mathematics*, 4(3):1–27, 2018.
- [72] C. Qi, J. Tang, F. Fan, and Y. Yan. Effects of magnetic field on thermo-hydraulic behaviors of magnetic nanofluids in CPU cooling system. *Applied Thermal Engineering*, 179:115717, 2020.

- [73] B. C. Sakiadis. Boundary-layer behavior on continuous solid surfaces and boundary-layer equations for two-dimensional and axisymmetric flow. *AIChE Journal*, 7(1):26–28, 1961.
- [74] K. Gangadhar, T. Kannan, G. Sakthivel, and K. Dasaradha. Unsteady free convective boundary layer flow of a nanofluid past a stretching surface using a spectral relaxation method. *International Journal of Ambient Energy*, 41(6):609–616, 2020.
- [75] J. Rahimi, D. D. Ganji, M. Khaki, and K. Hosseinzadeh. Solution of the boundary layer flow of an Eyring-Powell non-Newtonian fluid over a linear stretching sheet by collocation method. *Alexandria Engineering Journal*, 56(4):621–627, 2017.
- [76] D. E. Loper. Turbulent boundary-layer flow beneath a vortex. Part 1: Turbulent Bödewadt flow. *Journal of Fluid Mechanics*, 892:A16, 2020.
- [77] O. D. Makinde. Second law analysis for variable viscosity hydromagnetic boundary layer flow with thermal radiation and Newtonian heating. *Entropy*, 13(8):1446–1464, 2011.
- [78] A. Hussanan, Z. Ismail, I. Khan, A. G. Hussein, and S. Shafie. Unsteady boundary layer MHD free convection flow in a porous medium with constant mass diffusion and Newtonian heating. *The European Physical Journal Plus*, 129(3):46, 2014.
- [79] M. I. Afridi and M. Qasim. Entropy generation and heat transfer in boundary layer flow over a thin needle moving in a parallel stream in the presence of nonlinear Rosseland radiation. *International Journal of Thermal Sciences*, 123:117–128, 2018.
- [80] G. Rasool, T. Zhang, A. J. Chamkha, A. Shafiq, I. Tlili, and G. Shahzadi. Entropy generation and consequences of binary chemical reaction on MHD Darcy–Forchheimer Williamson nanofluid flow over non-linearly stretching surface. *Entropy*, 22(1):18, 2020.
- [81] H. Berrehal, F. Mabood, and O. D. Makinde. Entropy-optimized radiating water/FCNTs nanofluid boundary-layer flow with convective condition. *The European Physical Journal Plus*, 135(7):1–21, 2020.

- [82] H. Mondal, S. Mishra, P. K. Kundu, and P. Sibanda. Entropy generation of variable viscosity and thermal radiation on magneto nanofluid flow with dusty fluid. *Journal of Applied and Computational Mechanics*, 6(1):171–182, 2020.
- [83] S. Mir, O. A. Akbari, D. Toghraie, G. Sheikhzadeh, A. Marzban, S. Mir, and P. Talebizadehsardari. A comprehensive study of two-phase flow and heat transfer of water/Ag nanofluid in an elliptical curved minichannel. *Chinese Journal of Chemical Engineering*, 28(2):383–402, 2020.
- [84] T. R. Vijaybabu. Influence of permeable circular body and CuO- H₂O nanofluid on buoyancy-driven flow and entropy generation. *International Journal of Mechanical Sciences*, 166:105240, 2020.
- [85] S. Aghakhani, A. H. Pordanjani, M. Afrand, M. Sharifpur, and J. P. Meyer. Natural convective heat transfer and entropy generation of alumina/water nanofluid in a tilted enclosure with an elliptic constant temperature: Applying magnetic field and radiation effects. *International Journal of Mechanical Sciences*, 174:105470, 2020.
- [86] A. Aziz and M. Shams. Entropy generation in MHD Maxwell nanofluid flow with variable thermal conductivity, thermal radiation, slip conditions, and heat source. *AIP Advances*, 10(1):015038, 2020.
- [87] M. M. Rashidi, S. Abelman, and N. F. Mehr. Entropy generation in steady MHD flow due to a rotating porous disk in a nanofluid. *International journal of Heat and Mass Transfer*, 62:515–525, 2013.
- [88] M. R. Eid and F. Mabood. Entropy analysis of a hydromagnetic micropolar dusty carbon-kerosene nanofluid with heat generation. *Journal of Thermal Analysis and Calorimetry*, 1:1–18, 2020.
- [89] A. Lopez, G. Ibanez, J. Pantoja, J. Moreira, and O. Lastres. Entropy generation analysis of MHD nanofluid flow in a porous vertical microchannel with nonlinear thermal radiation, slip flow and convective-radiative boundary conditions. *International Journal of Heat and Mass Transfer*, 107:982–994, 2017.

- [90] S. Baag, S. R. Mishra, G. C. Dash, and M. Acharya. Entropy generation analysis for viscoelastic MHD flow over a stretching sheet embedded in a porous medium. *Ain Shams Engineering Journal*, 8(4):623–632, 2017.
- [91] D. A. Nield and A. V. Kuznetsov. The onset of double-diffusive convection in a nanofluid layer. *International Journal of Heat and Fluid Flow*, 32(4):771–776, 2011.
- [92] Y. Yang, W. Chen, R. Verzicco, and D. Lohse. Multiple states and transport properties of double-diffusive convection turbulence. *Proceedings of the National Academy of Sciences*, 117(26):14676–14681, 2020.
- [93] J. Turner. Double-diffusive phenomena. *Annual Review of Fluid Mechanics*, 6(1):37–54, 1974.
- [94] H. Mondal, S. Mishra, P. K. Kundu, and P. Sibanda. Entropy generation of variable viscosity and thermal radiation on magneto nanofluid flow with dusty fluid. *Journal of Applied and Computational Mechanics*, 6(1):171–182, 2020.
- [95] S. Chen, B. Yang, X. Xiao, and C. Zheng. Analysis of entropy generation in double-diffusive natural convection of nanofluid. *International Journal of Heat and Mass Transfer*, 87:447–463, 2015.
- [96] M. Sohail, Z. Shah, A. Tassaddiq, P. Kumam, and P. Roy. Entropy generation in MHD Casson fluid flow with variable heat conductance and thermal conductivity over non-linear bi-directional stretching surface. *Scientific Reports*, 10(1):1–16, 2020.
- [97] M. Siavashi, V. Bordbar, and P. Rahnama. Heat transfer and entropy generation study of non-Darcy double-diffusive natural convection in inclined porous enclosures with different source configurations. *Applied Thermal Engineering*, 110:1462–1475, 2017.
- [98] S. H. Hussain. Analysis of heatlines and entropy generation during double-diffusive MHD natural convection within a tilted sinusoidal corrugated porous enclosure. *Engineering Science and Technology*, 19(2):926–945, 2016.
- [99] Z. Chen, M. P. Burke, and Y. Ju. Effects of Lewis number and ignition energy on the

- determination of laminar flame speed using propagating spherical flames. *Proceedings of the Combustion Institute*, 32(1):1253–1260, 2009.
- [100] M. Torabi, M. Torabi, and G. P. Peterson. Entropy generation of double diffusive forced convection in porous channels with thick walls and Soret effect. *Entropy*, 19(4):171, 2017.
- [101] G. R. Kefayati. Simulation of double diffusive natural convection and entropy generation of power-law fluids in an inclined porous cavity with Soret and Dufour effects. *International Journal of Heat and Mass Transfer*, 94:582–624, 2016.
- [102] S. Khan, T. Hayat, M. Khan, and A. Alsaedi. Salient features of Dufour and Soret effect in radiative MHD flow of viscous fluid by a rotating cone with entropy generation. *International Journal of Hydrogen Energy*, 45(28):14552–14564, 2020.
- [103] G. C. Shit, R. Haldar, and S. Mandal. Entropy generation on MHD flow and convective heat transfer in a porous medium of exponentially stretching surface saturated by nanofluids. *Advanced Powder Technology*, 28(6):1519–1530, 2017.
- [104] G. Seth, A. Bhattacharyya, R. Kumar, and A. Chamkha. Entropy generation in hydromagnetic nanofluid flow over a non-linear stretching sheet with Navier’s velocity slip and convective heat transfer. *Physics of Fluids*, 30(12):122003, 2018.
- [105] F. Oueslati, B. Ben, and T. Lili. Double-diffusive natural convection and entropy generation in an enclosure of aspect ratio four with partial vertical heating and salting sources. *Alexandria Engineering Journal*, 52(4):605–625, 2013.
- [106] A. Mchirgui, N. Hidouri, M. Magherbi, and A. Brahim. Entropy generation in double-diffusive convection in a square porous cavity using Darcy–Brinkman formulation. *Transport in Porous Media*, 93(1):223–240, 2012.
- [107] D. Jing, S. Hu, M. Hatami, Y. Xiao, and J. Jia. Thermal analysis on a nanofluid-filled rectangular cavity with heated fins of different geometries under magnetic field effects. *Journal of Thermal Analysis and Calorimetry*, 139(6):3577–3588, 2020.

- [108] S. E. Ahmed, M. A. Mansour, A. Mahdy, and S. S. Mohamed. Entropy generation due to double diffusive convective flow of Casson fluids over nonlinearity stretching sheets with slip conditions. *Engineering Science and Technology, an International Journal*, 20(6):1553–1562, 2017.
- [109] L. Song, P. W. Li, Y. Gu, and C. M. Fan. Generalized finite difference method for solving stationary 2D and 3D Stokes equations with a mixed boundary condition. *Computers & Mathematics with Applications*, 80(6):1726–1743, 2020.
- [110] R. Eymard, T. Gallouët, and R. Herbin. Finite volume methods. In J. L. Lions; P. Ciarlet (Editors). *Solution of Equation in R^n (Part 3), Handbook of Numerical Analysis*, 7: 713–1018, 2000.
- [111] J. Fish. The s-version of the finite element method. *Computers & Structures*, 43(3): 539–547, 1992.
- [112] F. Bassi and S. Rebay. A high-order accurate discontinuous finite element method for the numerical solution of the compressible Navier–Stokes equations. *Journal of Computational Physics*, 131(2):267–279, 1997.
- [113] V. Selmin. The node-centred finite volume approach: bridge between finite differences and finite elements. *Computer Methods in Applied Mechanics and Engineering*, 102(1): 107–138, 1993.
- [114] C. Shu. High-order finite difference and finite volume WENO schemes and discontinuous Galerkin methods for CFD. *International Journal of Computational Fluid Dynamics*, 17(2):107–118, 2003.
- [115] S. Zhang, A. Zhang, P. Cui, and T. Li. Simulation of air gun bubble motion in the presence of air gun body based on the finite volume method. *Applied Ocean Research*, 97:102095, 2020.
- [116] H. Wang and X. Zhang. A high-accuracy preserving spectral Galerkin method for the Dirichlet boundary-value problem of variable-coefficient conservative fractional diffusion equations. *Journal of Computational Physics*, 281:67–81, 2015.

- [117] F. Yin, T. Tian, J. Song, and M. Zhu. Spectral methods using Legendre wavelets for nonlinear Klein Sine-Gordon equations. *Journal of Computational and Applied Mathematics*, 275:321–334, 2015.
- [118] M. Izadkhah and J. Saberi. Gegenbauer spectral method for time-fractional convection–diffusion equations with variable coefficients. *Mathematical Methods in the Applied Sciences*, 38(15):3183–3194, 2015.
- [119] P. Amodio, L. Brugnano, and F. Iavernaro. Analysis of spectral Hamiltonian boundary value methods (SHBVMs) for the numerical solution of ODE problems. *Numerical Algorithms*, 1:1–20, 2019.
- [120] S. Motsa and Z. Makukula. On spectral relaxation method approach for steady Von Kármán flow of a Reiner-Rivlin fluid with Joule heating, viscous dissipation and suction/injection. *Open Physics*, 11(3):363–374, 2013.
- [121] E. Doha, A. Bhrawy, and S. Eldien. A Chebyshev spectral method based on operational matrix for initial and boundary value problems of fractional order. *Computers & Mathematics with Applications*, 62(5):2364–2373, 2011.
- [122] Y. Qin and H. Ma. Legendre-tau-Galerkin and spectral collocation method for nonlinear evolution equations. *Applied Numerical Mathematics*, 153:52–65, 2020.
- [123] J. Shen. Efficient spectral-Galerkin method I. Direct solvers of second-and fourth-order equations using Legendre polynomials. *SIAM Journal on Scientific Computing*, 15(6):1489–1505, 1994.
- [124] Y. Saad. Least squares polynomials in the complex plane and their use for solving nonsymmetric linear systems. *SIAM Journal on Numerical Analysis*, 24(1):155–169, 1987.
- [125] C. Zhang, L. Wang, D. Gu, and W. Liu. On approximate inverse of Hermite and Laguerre collocation differentiation matrices and new collocation schemes in unbounded domains. *Journal of Computational and Applied Mathematics*, 344:553–571, 2018.

- [126] Z. Liu and L. Shujuan. Rational Chebyshev pseudospectral method for long-short wave equations, 2017.
- [127] S. S. Motsa, P. Dlamini, and M. Khumalo. A new multistage spectral relaxation method for solving chaotic initial value systems. *Nonlinear Dynamics*, 72(1):265–283, 2013.
- [128] V. M. Magagula, S. S. Motsa, P. Sibanda, and P. G. Dlamini. On a bivariate spectral relaxation method for unsteady magneto-hydrodynamic flow in porous media. *Springer Plus*, 5(1):1–15, 2016.
- [129] S. S. Motsa and I. L. Animasaun. Bivariate spectral quasi-linearisation exploration of heat transfer in the boundary layer flow of micropolar fluid with strongly concentrated particles over a surface at absolute zero due to impulsive. *International Journal of Computing Science and Mathematics*, 9(5):455–473, 2018.
- [130] I. S. Oyelakin, S. Mondal, P. Sibanda, and S. S. Motsa. A multi-domain bivariate approach for mixed convection in a Casson nanofluid with heat generation. *Walailak Journal of Science and Technology (WJST)*, 16(9):681–699, 2019.
- [131] M. Samuel. Computational and numerical analysis of differential equations using spectral based collocation method. Unpublished PhD thesis, University of KwaZulu-Natal, Durban South Africa, 2019.
- [132] M. P. Mkhathshwa, S. S. Motsa, and P. Sibanda. Numerical solution of time-dependent Emden-Fowler equations using bivariate spectral collocation method on overlapping grids. *Nonlinear Engineering*, 9(1):299–318, 2020.
- [133] M. P. Mkhathshwa, S. S. Motsa, and P. Sibanda. Overlapping multi-domain spectral method for conjugate problems of conduction and MHD free convection flow of nanofluids over flat plates. *Mathematical and Computational Applications*, 24(3):75, 2019.
- [134] M. P. Mkhathshwa, S. S. Motsa, and P. Sibanda. MHD mixed convective radiative flow of Eyring-Powell fluid over an oscillatory stretching sheet using bivariate spectral method on overlapping grids. *Heat Transfer*, 50(1):655–687, 2021.

- [135] M Mustafa. MHD nanofluid flow over a rotating disk with partial slip effects: Buongiorno model. *International Journal of Heat and Mass Transfer*, 108:1910–1916, 2017.